

University of Alberta

**Experimental and Numerical Investigations of Sand-Water Slurry
Jets in Water**

by

Amir Hossein Azimi

A thesis submitted to the Faculty of Graduate Studies and Research in partial
fulfillment of the requirements for degree of Doctor of Philosophy

in

Water Resources Engineering

Department of Civil and Environmental Engineering

© Amir Hossein Azimi

Fall 2012

Edmonton, Alberta

Permission is hereby granted to the University of Alberta Libraries to reproduce single copies of this thesis and to lend or sell such copies for private, scholarly or scientific research purposes only. Where the thesis is converted to, or otherwise made available in digital form, the University of Alberta will advise potential users of the thesis of these terms.

The author reserves all other publication and other rights in association with the copyright in the thesis and, except as herein before provided, neither the thesis nor any substantial portion thereof may be printed or otherwise reproduced in any material form whatsoever without the author's prior written permission.

To my wife Elham,

Abstract:

Sand-laden jets can be found in many engineering applications, such as, marine bed capping, mining operations, hydro-transport, dredging material disposal, and discharge of industrial and domestic wastewater. Understanding the dynamic interactions of the sand particles and its ambient are important for proper design and optimizing the engineering systems. Mass, momentum and energy of the system can be influenced by interactions of the suspended particles within the jet. As a result, the hydrodynamics of the flow of particle and fluid velocities, turbulence, and shear stresses are affected by particle interaction mechanisms which increase the complexity of the system and mixing phenomenon. The conducted experimental studies and numerical modeling in this thesis are new in terms of the fundamental understanding, flow characteristics and numerical techniques in simulation of sediment laden jets in water. The obtained results of this study can be used in many other environmental problems, such as marine construction, building artificial islands, deep ocean mining and discharge of sewage sludge into water bodies.

Part of this thesis focused on the numerical investigation of sand and slurry jets. Effects of the controlling parameters of the jets such as, particle size, nozzle diameter, initial velocity and particle concentration were investigated and it was found that in contrast with single-phase water jet, the water-phase spreading of slurry jets is function of nozzle size and particle concentration. Numerical experiments revealed that the water-phase centreline velocity of slurry jets increased with increasing particle concentration. Empirical formulations were introduced to show these strong correlations between densimetric Froude number, particle concentration and the velocity decay of slurry jets.

Particle-laden jets are commonly observed when particles are released instantaneously into water bodies but less attention has been devoted to study the starting of particle-laden jets and jet front with relatively high particle concentrations. It was found that the jet front terminal velocities, $u_{f\infty}$, of small particles were as large as 5 times of the individual particle settling velocity, u_{∞} . Experimental investigation of sand jet front revealed that the slope of correlation between the normalized frontal velocity and axial distance was found to be $1/5$ whereas this slope for a single-phase water jet was known to be $1/3$.

An interesting flow feature that has long been associated with starting jets is the formation of the vortex structure. The formation of the vortex is largely due to the roll up of the jet shear layer as it is introduced into the ambient. Vortex structure of sand jet front was studied experimentally by employing the Galilean decomposition and the swirling strength techniques. In study of the turbulent modulation, it was found that smaller particles attenuate the turbulence much faster than larger particles and logarithmic formulations were developed for prediction of turbulent modulation on solid-gas and solid-liquid turbulent jets.

Effect of particle size on turbulence modulation of sand and slurry jets were investigated with numerical simulation and it was found that the turbulent kinetic energy of the water phase decreases with increasing particle size. Grouping effect of particles on variation of the drag coefficient of the slurry jets was studied by employing the fundamental conservation of mass and momentum equations. It was found that particle concentration can reduce the drag coefficient of particle cloud since particles tend to travel behind the wake generated by frontal particles.

Part of this thesis focused on the physical characteristics and underlying dynamics of particles for designing purposes such as designing the nozzle size of the jet, choosing the most suitable jet velocity, and the initial sand concentration of the slurry jet for a given particle size range. In order to optimize slurry disposal and capping thickness, laboratory experiments were conducted to understand the structure and dynamics of slurry jets and the development of sand deposition with time. Variations of the aspect ratios with time were studied and power law correlations were introduced for prediction of the mound dimensions. Proposed models can be employed for estimating the mound dimensions on slopes up to 10 degrees with the average error of 4.8%.

Acknowledgements

I gratefully acknowledge my supervisors Dr. David Zhu and Dr. Nallamuthu Rajaratnam for their guidance, encouragement and friendship. Their support throughout the entire course of my studies helped me overcome many obstacles. It was rewarding experience and a privilege to work under their supervision. I am thankful to Perry Fedun and Chris Kraft for building the experimental arrangements and for their willingness to help.

I deeply thank my wife Elham, my parents Ali and Fatemeh and my parents in-law, Davood and Shohre for their love; encouragement and support that always provide me the strength to become a better person and to achieve my aspirations.

Table of Contents

Chapter 1:

General Introduction	1
1.1 Motivation and Background.....	1
1.2 Overview of Thesis Content.....	6

Chapter 2:

Effect of Particle Size on the Characteristics of Sand Jets in Water	11
2.1 Introduction.....	11
2.2 Governing Equations.....	14
2.3 Modeling Background and Model Validation.....	17
2.4 Effect of Particle Size on the Mean Properties of the Sand Jets.....	28
2.5 Effect of Particle Size on the Turbulent Characteristics of the Sand Jets.....	32
2.6 Summary and Conclusion.....	40
2.7 Notation.....	42

Chapter 3:

Computational Investigation on Vertical Slurry Jets in Water	45
3.1 Introduction.....	45
3.2 Model Convergence and Validation.....	50
3.3 Results of Numerical Experiments.....	62
3.4 Spreading of the Jet.....	64
3.5 Centreline Velocity.....	70
3.6 Ambient Entrainment of Slurry Jets.....	79
3.7 Drag Reduction of Group Particles.....	82

3.8 Turbulence Characteristics of Slurry Jets.....	85
3.9 Summary and Conclusion.....	92
3.10 Notation.....	95
Chapter 4:	
Experimental Study of Sand Jet Front in Water.....	97
4.1 Introduction.....	97
4.2 Laboratory Experiment.....	102
4.3 Dimensional Analysis.....	107
4.4 Evolution of Sand Jet Front.....	111
4.5 Frontal Velocity of the Sand Jets.....	115
4.6 The Growth Rate of Jet Front Width.....	124
4.7 Axial and Radial Velocities.....	126
4.8 Vortex Structure.....	134
4.9 Turbulence Modulation.....	140
4.10 Summary and Conclusion.....	144
4.11 Notation.....	148
Chapter 5:	
An Experimental Study of Sand Deposition from Slurry Wall Jets.....	151
5.1 Introduction.....	151
5.2 Experimental Setup.....	155
5.3 Dimensional Consideration and Flow Visualization.....	159
5.4 Effect of Initial Momentum.....	164
5.5 Effect of Bed Slope.....	168

5.6 Effect of Sediment Concentration.....	172
5.7 Summary and Conclusion.....	181
5.8 Notation.....	183
Chapter 6:	
General Conclusions and Recommendations for Future Research.....	185
6.1 General Conclusion.....	185
6.2 Future Research Studies.....	191
Appendix 1: Slurry Jet Visualization.....	196
Appendix 2: Mass Flux Measurements.....	200
References.....	202

List of Tables

Table 2-1: Mesh characteristics and cell size of the sand jet in different mesh structure.....	20
Table 2-2: Time scales and non-dimensional properties of sand jets.....	35
Table 3-1: Experimental conditions under which previous two-phase solid-gas and solid-liquid turbulent jet investigations were conducted.....	46
Table 3-2: Domain characteristics and mesh refinement properties of the numerical simulation.....	51
Table 3-3: Selected computational domain and the initial flow characteristics of laboratory measurements.....	63
Table 4-1: Experimental details of Series A with the particle size of $D_{50} = 206 \mu\text{m}$	103
Table 4-2: Properties of the sand particles of Series B with the nominal nozzle size of 4 mm.....	104
Table 4-3: Principal characteristics of the two-phase solid-gas and solid-liquid turbulent jets.....	142
Table 5-1: Details of the laboratory experiments and jet characteristics (sediment size $D = 0.21 \text{ mm}$, water depth $h = 0.20 \text{ m}$).....	158

List of Figures

Figure 1-1: Oil-sand slurry flow disposed into tailing ponds. Single pipe (a) or a series of pipes (b) may be used for slurry disposal. (Photographed by (a) Domenick Yoney and (b) Peter Essick).....	2
Figure 1-2: Images of sand jet with the initial volumetric concentration of 60%. a) Jet with 9 mm nozzle diameter. b) Jet with 13.25 mm nozzle diameter and c) Jet with 15.5 mm nozzle diameter.....	4
Figure 1-3: Raw images of sand jet front taken for velocity field measurement using Particle Image Velocimetry (PIV). The green light is the laser light passed through the axis of the jet for eliminating the background water. a) Jet with 3 mm nozzle diameter. b) Jet with 5 mm nozzle diameter.....	5
Figure 1-4: Sediment deposition formed by a horizontal slurry wall jet.....	6
Figure 2-1: a) Simulation domain of the turbulent sand jet in water. b) Schematic of control volume of sand jet.....	21
Figure 2-2: Mesh sensitivity plots of sand velocity and concentration for sand jet; a) $x/d = 30$; b) $x/d = 50$	22
Figure 2-3: Comparison of the simulation outputs of the sand jets with the measurements using different mesh set up; a) Sand velocity; b) Sand concentration.....	24
Figure 2-4: Variation of centerline sand velocity and concentration in the axial direction $d = 8.2$ mm; a) Normalized axial sand velocity; b) Centerline concentration.....	25
Figure 2-5: Variations of the measured sand and water momentum fluxes along the jet axis compared with the simulation outputs, $d = 8.2$ mm; (Open symbols are measurements and lines are simulation results).....	27
Figure 2-6: Effect of particle size on the axial velocity of the sand phase and the water phase; a) Sand phase velocity; b) Water phase velocity.....	29
Figure 2-7: Effect of particle size on the radial sand and water phase velocity distributions at different cross sections, $x/d = 16, 32, 48, 64$, ($d = 8.2$ mm); a) Sand velocity distributions; b) Water velocity distributions.....	30
Figure 2-8: Contour plots of the sand phase velocity with different particle size, a) $D = 210 \mu\text{m}$, b) $D = 460 \mu\text{m}$, c) $D = 780 \mu\text{m}$	31

Figure 2-9: Effect of particle size on variations of the water phase turbulent characteristics along the jet axis; a) Rate of turbulent energy dissipation; b) Turbulent kinetic energy; c) Turbulent eddy frequency; d) Turbulence intensity.....33

Figure 2-10: Effect of particle size on turbulent characteristics of the water phase at different cross sections; a) Rate of turbulent energy dissipation; b) Turbulent kinetic energy.....37

Figure 2-11: A comparison on turbulence modulation of sand jets with different particle size and experimental data collected by Crowe (2000).....39

Figure 3-1: Schematic of a slurry jet with computational boundary conditions and computational domain. a) Definition sketch of a jet with coordinate system. b) Computational elements arrangement at the nozzle. Top: Experiment No. 1, Middle: Experiment No. 2, Bottom: Experiment No. 3. b) Half cylindrical computational domain with mesh resolution used for simulation of Experiment No. 2.....53

Figure 3-2: Mesh sensitivity analysis and correlations of the computed parameters with mesh structure and residual target level of Experiment No. 1. a) Turbulent viscosity. b) Radial velocities.....54

Figure 3-3: Effect of total computational time steps on the accuracy level of numerical simulation. a) Validation of axial and radial velocities, Experiment No. 1. b) Validation of turbulent kinetic energy per unit mass, Experiment No. 2. c) Validation of sand concentration, Experiment No. 3.....55

Figure 3-4: Comparison of the simulation outputs of the axial velocity using different mesh resolution with measurements of Experiment No. 1 (Arai et al., 2003) at three cross sections. a) At the injection pipe, $x/d = 0$. b) $x/d = 3$. c) $x/d = 15$56

Figure 3-5: Comparison between numerical results and laboratory measurements of sand-phase and water-phase radial velocities of Experiment No. 1 (Arai et al., 2003). a) $x/d = 3$. b) $x/d = 15$58

Figure 3-6: Model performance on prediction of the sand-phase axial velocity (Left) and the sand volumetric concentration (Right) of Experiment No. 2 (Hall et al., 2010) at three cross-sections. a) $x/d = 12.9$. b) $x/d = 25.8$. c) $x/d = 38.7$59

Figure 3-7: Comparison between model outputs and experimental observations of the normalized water-phase axial velocity and turbulent kinetic energy per unit mass (i.e., TKE) of Experiment No. 3 (Parthasarathy & Faeth, 1987) at three cross sections and two different initial concentration of $c_o = 2.4\%$ (Left) and $c_o = 4.8\%$ (Right). a) Axial velocity at $x/d = 16$. b) TKE at $x/d = 8$. c) TKE at $x/d = 16$. d) TKE at $x/d = 40$60

Figure 3-8: Effects of sand concentration and nozzle size on spreading of slurry jet. The spreading is calculated from the water-phase velocity profile width at $\frac{1}{2}$ the maximum velocity. a) Variation of the jet half-width along the axis of the jet for particle concentration of 2.4%. b) The jet spreading was normalized with nozzle diameter ($c_o=2.4\%$). c) Effect of sand concentration on the spreading of the jet for nozzle diameter of $d=5$ mm. Numerical results were compared with spreading of a single-phase water jets.....65

Figure 3-9: Normalized concentration, sand-phase and water-phase velocity profiles at $x/d=160$ for numerical test of c8 ($D=0.505$ mm and $c_o=12\%$). The radial distances of the sand-phase were normalized with b_s and the radial distances of the water-phase and particle concentration were normalized with b_w67

Figure 3-10: Variation of the ratio between the spreading rate of the concentration, b_c and the spreading rate of the water-phase velocity profiles, b_w (i.e., $\lambda=b_c/b_w$) along the axis of the jet with the effects of sand volumetric concentration and particle size on λ in slurry jets. a) Effect of particle size on λ for slurry jets with $c_o=2.4\%$ (Series D). b) Effect particles size on λ for very dilute slurry jets with $c_o = 0.3\%$ (Series S). c) Effect of particle concentration on λ for slurry jets with small particle size ($D=0.1$ mm). d) Effect of particle concentration on λ for slurry jets with relatively large particle size with $D=0.505$ mm (Series C).....69

Figure 3-11: Variation of the sand-phase and water-phase centerline velocities of slurry jets along the axis of the jet. a) Velocities along the axis of the jet were compared with those single-phase water jets and plumes. b) Axial distance was normalized with nozzle diameter and centerline velocities were normalized with the initial velocity of the jets.....72

Figure 3-12: Correlations of the water-phase velocity along the axis of the jet with the effects of nozzle size variation (Series d), sand particle size variation (Series D) and initial velocity variation (Series U). a) Variation of the centerline velocity with distance from the nozzle. b) Variation of the normalized centerline velocity with normalized axial distance. c) Correlations of the centerline velocity of the water-phase with Froude number, F_r74

Figure 3-13: Correlations of the water-phase velocity along the axis of the jet with the effects of sand volumetric concentration (Series c). a) Numerical results were compared with the centerline velocity decay of a single-phase water jet and plume. b) Variation of the normalized centerline velocity with normalized distance from the nozzle. c) Centerline velocity of the water-phase was normalized with Froude number, F_r76

Figure 3-14: Centerline decay of the water-phase velocity and the mean sand concentration along the axis of the jet. Computational results were compared with proposed curve fit for buoyant jets used by Wang and Law (2002). a) Variation of the

centerline water-phase velocity with x/l_m in log-log scale. b) Variation of centerline volumetric concentration with x/l_m in log-log scale.....78

Figure 3-15: Schematic of the change on the mass and momentum fluxes of slurry jets in differential form for prediction of a) Entrainment coefficient and b) Averaged drag coefficient of the particle cloud along the axis of the jet.....79

Figure 3-16: Effect of sand volumetric concentration on variation of entrainment coefficient along the axis of the jet. The computed entrainment coefficients were compared with the entrainment coefficient of a single-phase water jet.....80

Figure 3-17: Effects of sand volumetric concentration, nozzle size, sand particle size and initial velocity on variation of the absolute entrainment coefficient, α_o along the axis of the jet. The absolute entrainment coefficient of slurry jets were compared with α_o of a single-phase water jet.....81

Figure 3-18: Effects of sand volumetric concentration, nozzle size and sand particle size on variation of the averaged drag coefficient with Reynolds number, R . a) Variations of the averaged drag of particle cloud with R in logarithmic scale. b) Effects of particle concentration, nozzle size and initial velocity of the jet on variation of C_D with R84

Figure 3-19: Effect of nozzle size, sand particle size and sand volumetric concentration on the normalized turbulent kinetic energy per unit mass and normalized turbulent length scale. a) Effect of nozzle size. b) Effect of particle size. c) Effect of sand volumetric concentration.....86

Figure 3-20: Contour plots of the computed turbulent viscosity of the sand-phase, $\mu_{t(s)}$ show the effect of particles volumetric concentration on $\mu_{t(s)}$. a) $c_o=0.3\%$, a) $c_o=1.2\%$, a) $c_o=2.4\%$, a) $c_o=4.8\%$ and a) $c_o=12\%$88

Figure 3-21: Cross-sectional variation of the computed normalized water-phase turbulent shear stress at a) $x/d = 16$. b) $x/d = 40$. The computed turbulent shear stresses were compared with experimental results of slurry jets (Parthasarathy & Faeth, 1987) and single-phase water jets (Wynanski & Fiedler, 1969).....90

Figure 3-22: Cross-sectional variation of the computed normalized sand-phase turbulent shear stress at a) $x/d = 16$. b) $x/d = 40$. c) $x/d = 50$ and d) $x/d = 60$. The computed turbulent shear stresses were compared with experimental results of dilute slurry jets ($c_o=0.19\%$), (Jiang et al., 2005) and single-phase buoyant jets (Wang & Law, 2002).....91

Figure 4-1: A schematic view of the experimental setup.....102

Figure 4-2: Images of the sand jets with different nozzle sizes in water at $t = 2$ sec. [Exp. A1 - A4] a) $d = 2$ mm; b) $d = 3$ mm; c) $d = 4.75$ mm; d) $d = 10$ mm. Images turned to negative for better visualization.....112

Figure 4-3: Effect of particle size on sand jet front behavior of experiments B1 – B8 at $t^* = 60$. a) Experiment B1 ($D=137.5 \mu\text{m}$), b) Experiment B2 ($D=165 \mu\text{m}$), c) Experiment B3 ($D=196 \mu\text{m}$), d) Experiment B4 ($D=231 \mu\text{m}$), e) Experiment B5 ($D=275 \mu\text{m}$), f) Experiment B6 ($D=327 \mu\text{m}$), g) Experiment B7 ($D=389.5 \mu\text{m}$), h) Experiment B8 ($D=507 \mu\text{m}$). Particles fall out of the cloud and the front head become narrower and sharper in experiments B5 – B8. Images turned to negative for better visualization.....113

Figure 4-4: The evolution of sand jet front at $t^* = 10, 30, 50$ and 70 for experiments B3, B5 and B7. a) Experiment B3 ($D=196 \mu\text{m}$), b) Experiment B5 ($D=275 \mu\text{m}$), c) Experiment B7 ($D=389.5 \mu\text{m}$). Images turned to negative for better visualization.....114

Figure 4-5: Effect of nozzle size on the frontal velocity of the sand jets, u_f , along the jet axis, x for experiments A1 ($d=2$ mm), A2 ($d=3$ mm), A3 ($d=4.75$ mm) and A4 ($d=10$ mm). a) Variations of the frontal velocity along the jet axis. b) Correlations of the frontal velocity normalized with the sand terminal velocity, u_∞ with the normalized distance of x/d . The proposed logarithmic equation of 4.14 corresponding for experiments A3 and A4 were included for comparison.....116

Figure 4-6: Effect of particle size on the frontal velocity of the sand jets, u_f , normalized with sand terminal velocity, u_∞ , for experiments B1 to B8.....118

Figure 4-7: Variations of the settling velocity of the sand jet front, $u_{f\infty}$ with the effect of particle, D and particle Reynolds number, Re_p corresponding to experiments B1 to B8.....119

Figure 4-8: Effect of nozzle size and particle size on the frontal velocity of the sand jets, u_f , normalized with the frontal velocity of the water jet, u_b . a) Variations of the normalized frontal velocity along the jet axis for experiments A1 to A4. b) Correlations of the normalized frontal velocity along the jet axis for experiments B1 to B8. c) Effect of nozzle size on variations of the normalized frontal velocity plotted in logarithmic scale. d) Effect of particle size on development of the frontal velocity plotted in logarithmic scale.....120

Figure 4-9: Effect of nozzle size on the correlation between normalized frontal velocity and normalized buoyancy at a) $10 < x < 30$ cm and b) $30 < x < 60$ cm. Dashed line distinguishes from the swarm and the thermal regimes.....121

Figure 4-10: The growth rate of a sand jet front. Solid line is the growth rate of a starting water jet and dashed line is the growth rate of the thermal of a heavy salt. Numbers in brackets are the particles payload.....	125
Figure 4-11: Axial frontal velocity at three fixed points located at $x/d = 75, 100,$ and 125 corresponding to cases B2, B4, B6 and B8. Solid line represents the axial velocity at the jet centreline and dashed line represents the maximum axial velocity at the cross section. The parallel lines indicate the times when the frontal head entered to and exited from those fixed locations of $x/d = 75, 100,$ and 125	126
Figure 4-12: Instantaneous axial (left) and radial (right) velocities of experiments B2, B4, B5 and B8 at $t^* = 70$. a) $x/d = 75,$ b) $x/d = 100$ and c) $x/d = 125$	129
Figure 4-13: Variations of the axial (left) and the radial (right) water velocities with normalized time at a) $x/d = 75,$ b) $x/d = 100,$ and c) $x/d = 125$	131
Figure 4-14: (Color online) Contour plots of the axial velocity, $u,$ and the radial velocity, $v,$ and effect of particle Reynolds number on the shape and speed of jet front at $t^* = 60$. a-h) Experiments B1 to B8.....	133
Figure 4-15: Two-dimensional velocity vector field obtained from PIV measurement technique at $t^* = 60$. a) B2, b) B4, c) B5 and d) B7.....	134
Figure 4-16: Velocity vector fields in transient turbulent sand jets illustrated at $t^* = 60$ (Exp B4).....	136
Figure 4-17: (Color online) Identification of vortices in sand jet front at $t^* = 60$ (Exp. B4).....	138
Figure 4-18: (Color online) Vortex structures generated by interactions of particles into the water bodies at $t^* = 60$. a) B2, b) B4, c) B5 and d) B7.....	139
Figure 4-19: Turbulent attenuation of the two-phase turbulent jets. a) Change in turbulent intensity of a general two-phase system as a function of $D/L_e,$ and the effect of particle size $D,$ on turbulent modulation of solid-liquid jets. Dashed lines show the modulation of turbulence of the solid-liquid and the solid-air two-phase turbulent jets. b) Turbulent attenuation of the two-phase turbulent jets as a function of $D/L_e.$ Open symbols are solid-air turbulent jets and solid symbols are solid-liquid turbulent jets. c) Effect of Stokes number on the turbulence modulation of the two-phase turbulent jets.....	141
Figure 5-1: a) Experimental setup and coordinate system, b) Sketch for deposition length scales.....	156

Figure 5-2: Images of the sediment deposition and ripples formed at different times for experiment C2. a) $t = 3$ min. b) $t = 6$ min. c) $t = 12$ min. d) $t = 21$ min. e) $t = 27$ min. f) $t = 32$ min. Images turned to negative for better visualization.....161

Figure 5-3: Raw images taken from experiment A1 show development of sediment deposition with time and illustrate different classifications of mound formation. a) Deposition in developing regime, b) Sediment mound development at the end of developing regime, c) Three-dimensional view of the spreading regime, d) End stage of the spreading regime, e) Beginning of the backup regime, f) Advancement of sediments toward the nozzle, g) End stage of the backup regime, h) Three-dimensional side view of the sediment deposition at the end of experiment, i) Top-view at the end of experiment shows the area of mound cone (1) versus the deposition area formed in the backup regime (2).....163

Figure 5-4: Correlation of the normalized deposition length scales with densimetric Froude number, F . a) Variation of the normalized length of the maximum deposition height from the nozzle, x_m with F . b) Variation of the normalized deposition length normalized with the nozzle diameter with F165

Figure 5-5: Effects of sediment concentration and densimetric Froude number, F on development of the mound angle of deposition, β , for experiments A1-A7. a) Growth of the angle of deposition with time. b) Effects of sediment concentration and F on correlation of the angle of deposition with normalized time.....167

Figure 5-6: Development of the deposition base area with time for experiments A1-A7. Mound base area was normalized with the cone area of the mound, $(\pi b_m^2/4)$ and time was normalized with the time scale of the slurry jet. Influence of sediment concentration on mound development was included in this plot (I is the developing regime, II is the spreading regime).....168

Figure 5-7: Contour plots of the sediment deposition at different times and effect of bed slope on the size and shape of the deposition. a) $S = 2.5^\circ$, b) $S = 5^\circ$, c) $S = 7.5^\circ$, d) $S = 10^\circ$. Contour lines were shown at one minute time interval.....169

Figure 5-8: Effect of initial velocity and bed slope on development of the sediment mound length scales (Top: Maximum mound height, Middle: Mound width, Bottom: Mound length), a) Effect of initial velocity, b) Effect of bed slope. (I is the developing regime, II is the spreading regime).....170

Figure 5-9: Variations of the longitudinal profiles of the sediment deposition with time and bed slope. a) $S = 0^\circ$, b) $S = 2.5^\circ$, c) $S = 5^\circ$, d) $S = 7.5^\circ$, e) $S = 10^\circ$171

Figure 5-10: Effects of sediment concentration, C and densimetric Froude number, F on development of the characteristic length scales of the sediment deposition. a) Correlations

of the maximum deposition height with normalized time, C and F . b) Variations of the mound width with time, C and F173

Figure 5-11: Variations of the mound aspect ratio and sediment base area with time at different regimes. (I is the developing regime, II is the spreading regime and III is the backup regime.) Deposition aspect ratios and the normalized mound base area were correlated with the mound time scale, T , sediment concentration, C , and densimetric Froude number, F175

Figure 5-12: Comparison between predictions of the proposed equations and experimental measurements. a) Model performance on prediction of the maximum deposition height, y_m . b) Comparison between the computed deposition widths, b with measurements. c) Comparison of the computed mound length, L , with measurements.....178

Figure 5-13: Comparison between the measured initiation of the sediment deposition and the location of bed erosion close to the nozzle with calculations for experiments series A, B and C. Open symbols show the initiation of deposition and solid symbols show the locations of erosion. Dash lines represent the $\pm 30\%$ accuracy of calculations.....180

Figure A1-1: Photographical observation of the turbulent sand jet in water from the water surface to the 72 cm downstream; Left, $d = 6$ mm; Middle $d = 12.5$ mm; Right, $d = 19.2$ mm.....196

Figure A1-2: Observation results on the growth of the turbulent sand jets.....198

Figure A1-3: Correlation of the spreading rate of the turbulent sand jets with F_o . (ph) in the legend stands for the photographical observation, (m) stands for the measurement and (s) stands for the numerical simulation.....199

Figure A2-1: Mass - Time relationship for different particle sizes. a) $D=125-150$ μm , b) $D=150-180$ μm , c) $D=180-212$ μm , d) $D=212-250$ μm , e) $D=250-300$ μm , f) $D=300-354$ μm , g) $D=354-425$ μm , and h) $D=425-589$ μm200

Figure A2-2: Effect of nozzle diameter on the mass flux of sand particles. a) $D = 210$ μm , b) $D = 300 - 425$ μm , c) $D = 425 - 707$ μm , and d) $D = 707 - 850$ μm201

Chapter 1

General Introduction

1.1 Motivation and Background

One of the largest oil deposits in the world with a reserve of 174 billion barrels of bitumen is located in northern Alberta, Canada (Alberta Energy and Utilizes Board, 2005). Because of the increasing global demand for natural resources, the average daily production of oil-sand mines has reached about 1 million barrels of oil and it is projected to become triple over the next decade (National Energy Board, 2006). Since oil-sand mines consume large volumes of water (i.e. 1 m³ of water for 1 barrel of oil) and the intake of freshwater from rivers is limited to less than 2% of the annual flow, oil-sand operators have to store the processed waters and tailings on-site to recycle and reuse. This limitation has resulted in the construction of over 70 km² of tailings pond with a total volume of 700 million m³ (Dominski, 2007).

The oil-sands tailings contain between 70 to 80 % of water and approximately 20-30% of solid materials. According to regulations of the Alberta Department of Energy (1995), oil-sand operators must reclaim tailing ponds and other disturbed lands to a self-sustaining ecosystem similar to its original landscape. The reclamation processes of tailing ponds can be achieved by many techniques such as capping the fine residuals and wastes by a layer of sand. Another efficient way of reclaiming those tailing ponds is to remove the non-settling particles by discharging new slurries from the plant at certain locations of tailing ponds. In this method, sediment discharge from slurry jets can break up the structure of non-settling tailings and causes settling of the fine particles. This way, the volume of the fine tailings will be reduced and the pond will be capped with a sand layer. By employing these techniques the pond could eventually be reclaimed. Sediment

deposition in the end-pit lakes (EPLs) is expected to form a buffer layer at the water-tailings interface to reduce the transfer of contaminants from the tailings to the water (FTFC, 1995). The shape and the thickness of this sediment layer are related to many parameters which are investigated experimentally in part of this thesis.



Figure 1-1: Oil-sand slurry flow disposed into tailing ponds. Single pipe (a) or a series of pipes (b) may be used for slurry disposal. (Photographed by (a) Domenick Yoney and (b) Peter Essick)

The middle layer of tailing ponds has poor consolidation and water release properties. It was observed that the tailings can reach to 20 wt% solids within a few weeks but finer sediment require several years to gain 30-35 wt% solids to form mature fine tailings (MFT) (Scott et al., 1985). From observation of Syncrude tailing ponds, MacKinnon (2001) reported that a settling time of 10 years is required to consolidate MFT from 30 to 44 wt% solids.

Many physical and chemical processes have been developed to increase the settling rates of fine particles and shorten the consolidation processing time. Settling of fine particles can be enhanced by centrifugation, pH adjustment, inorganic coagulants and organic flocculants (Kasperski, 1992). These additives must be mixed properly with tailings by slurry flow to enhance coagulation and form larger flocs. The mixing mechanism can be carried out by injecting slurry flow as a vertical sand-laden jet into the tailing ponds.

Since the sand concentration and its size in slurry flow vary during the time of operation, effects of those parameters in mixing and turbulent properties of the jets can be studied by laboratory experiments and numerical modeling. This chapter introduces the applications of sediment-laden jets and provides a brief description of experimental and numerical techniques. It also outlines the investigations presented in this thesis.

Sand-laden jets can be found in many engineering applications, such as, marine bed capping, mining operations, hydro-transport, dredging material disposal, and discharge of industrial and domestic wastewater. Understanding the dynamic interactions of the sand particles and its ambient is important for efficient design and for optimizing the engineering systems. Mass, momentum and energy of the system can be influenced by interactions of the suspended particles within the jets.

As a result, particle motion and the surrounding fluid velocities, turbulence, and the shear stresses are affected by particle interaction mechanisms. The interaction between two phases enhances the complexity of the system and mixing phenomenon. For instance, information obtained from experimental investigation on solid-liquid jets (Parthasarathy and Faeth, 1987; Tsuji et al., 1988; Sheen et al., 1994; Virdung and Rasmuson, 2007) has shown that the particle-laden jets exhibit higher turbulence level.

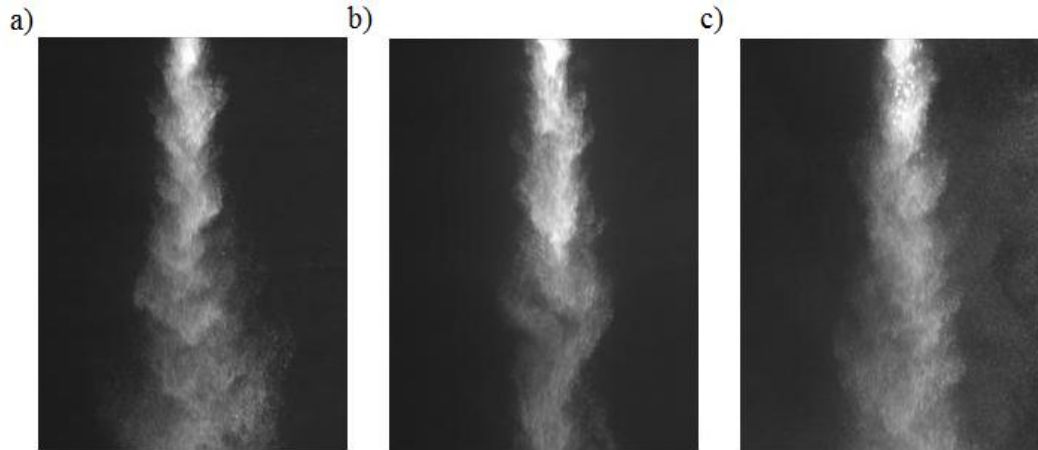


Figure 1-2: Images of sand jet with the initial volumetric concentration of 60%. a) Jet with 9 mm nozzle diameter. b) Jet with 13.25 mm nozzle diameter and c) Jet with 15.5 mm nozzle diameter.

The initial particle volume fractions of the turbulent slurry jets in most of the previous experiments were limited to 5% (Parthasarathy and Faeth, 1987; Muste et al., 1998; Arai et al., 2003; Jiang et al., 2005; Virdung and Rasmuson, 2007; Cuthbertson and Davies, 2008). In these circumstances, the effects of particle-particle interactions can be neglected and the flow structure can be treated as a homogeneous two-phase flow system. In many engineering applications, however, particle-laden jets can have higher particle concentration. Therefore, particle-particle interaction can play a dominant role in the dynamics of these systems. In addition, effects of particle size, particle concentration and initial jet velocities on mixing properties of the sediment-laden jets are not completely understood at this time and require more investigation.

Particle-laden jets are commonly observed when particles are released instantaneously into water bodies such as aqueous industrial waste disposal (Buhler and Papantoniou, 1991; Bush et al., 2003). Less attention has been devoted to study of the fronts of particle-laden jets with relatively high particle concentration. An interesting flow feature that has long been associated with starting jets is the formation of the vortex structure. The formation of vortex is largely due to the roll up of the jet shear layer as it is

introduced into the ambient. Vortex structures and eddies can be extracted from two dimensional velocity vector field to provide more information about the effect of particles on the mixing mechanism and frontal entrainment of the starting sand jets. Detailed simulation of the unsteady behaviour of the sediment-laden jets with high initial concentration is a challenge for CFD modellers. Consequently, the results provided in this thesis can also be used for validation of numerical models.

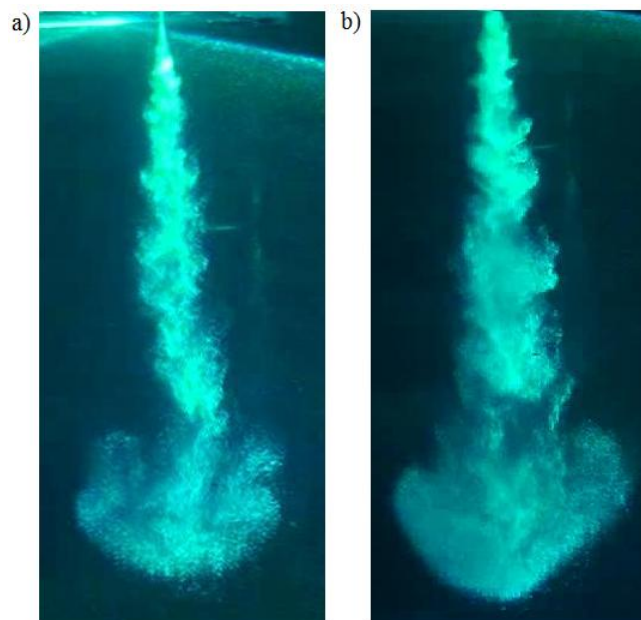


Figure 1-3: Raw images of sand jet front taken for velocity field measurement using Particle Image Velocimetry (PIV). The green light is the laser light passed through the axis of the jet for eliminating the background water. a) Jet with 3 mm nozzle diameter. b) Jet with 5 mm nozzle diameter.

Sediment deposition can be used as a method to cover the underwater waste materials for the purpose of recycling the top layer of water and enhance the consolidation process. These layers of sediment can prevent the mixing of those waste materials with the surface water. Sediment deposition can be formed and developed by the release of particle-laden jets into either co-flow or stagnant ambient water. The deposition shape, size and development rate can be directly related to the flow configuration. Sediment-laden jets

can be introduced into the ambient either vertically or horizontally or at an angle. Many experimental investigations have been carried out to provide information about the settling of particle cloud and flow entrainment of slurry flow into stagnant ambient (Ruggaber, 2000; Bush et al., 2003; Nicolas, 2002).



Figure 1-4: Sediment deposition formed by a horizontal slurry wall jet.

The location of sediment deposition can be affected by many parameters such as ambient current, sediment size and its concentration. According to experimental studies on the dynamics of particle cloud in cross flow, the shape and development of the particle cloud can be influenced by the release variables such as, particle size, release height and water content (Gu et al., 2008; Bhuiyan et al., 2010; Gensheimer III, 2010).

1.2 Overview of Thesis Content

This thesis is composed of two numerical studies and two experimental investigations including the general conclusion and topics for future fundamental and applied research. Each contribution is presented in a separate chapter and following is a brief introduction to each chapter.

1.2.1 Dynamics of Particles in Vertical Sand Jets

Lack of detailed research studies on the topic of sediment-laden jets with high particle concentration clearly demonstrates the importance of the investigation of such systems. Thus, in order to understand the dynamics of particle interaction in sediment-laden jets, detailed numerical modeling of sand and slurry jets in water was conducted at high initial sand concentration. In this numerical study ANSYS CFX 11.0 was employed which is considered as one of the well-known and acceptable numerical packages. This model is able to simulate the turbulent flow systems and it has been verified both theoretically and experimentally in the literature (Ansys, 2008).

Chapter 2 describes a detailed numerical modelling of sand jets in water at high initial sand concentration. In this chapter, the performance of the numerical model is evaluated by comparing the model outputs with results of some recent laboratory experiments. Simulations are then conducted to investigate the effect of sand particle sizes on velocity distribution, concentration profile and turbulent properties. In order to study the turbulent modification by the presence of particles, turbulent flow characteristics like turbulent kinetic energy, turbulence intensity, rate of energy dissipation, and turbulent eddy frequency are evaluated in this chapter and the trend compared with the previous studies in the literature.

1.2.2 Investigation on Vertical Slurry Jets

In Chapter 3, effects of controlling parameters such as, nozzle size, particle size, initial velocity and particle concentration on the characteristics of slurry jets in water are investigated by a validated numerical model (CFX 11.0). To validate the numerical model in these conditions, predictions of the main properties of these jets such as axial and radial velocities and particle concentration are compared with laboratory measurements. The effect of sand particles on slurry jet spreading rate, axial velocity

decay, decay of concentration and turbulence properties are studied, and the results are compared with the corresponding single-phase water jets and plumes. Effects of controlling parameters on the axial velocity decay of slurry jets can be described by suitable empirical formulations. Effect of particles on parameters such as entrainment and drag coefficients can be computed from some integral properties of the numerical results. The absolute entrainment coefficient is introduced and effects of controlling parameters on variations of the absolute entrainment coefficient are studied. Some detailed turbulence properties such as turbulent shear stresses of both sand-phase and water-phase can be estimated from the computed velocity and concentration profiles.

1.2.3 Front of Sand Jet in Water

Chapter 4 deals with the behaviour of the fronts of particle-laden turbulent jets in still water with special emphasis on the effects of nozzle diameter and particle size on the hydrodynamics of the particle-laden jets. Effect of nozzle diameter and particle size on the shape and velocity of the front can help to understand the changes on vortex formation and the mixing capacity of the jet fronts. Since many factors are involved in this study such as unsteadiness (i.e., time dependency), particle concentration, nozzle diameter, particle size and the excess momentum generated by particles, a close comparison between the results of this study with the results of the classical experimental studies (i.e., the single-phase jet front, single-phase vortex, particle-laden turbulent jets and particle thermals) can address the effect of each parameter on the characteristics of the jet fronts.

In Chapter 4, series of experimental studies are conducted and effects of different sand particle sizes and initial sand jet diameters are studied. The frontal axial and radial velocities, vortices and turbulence of the jet front and its surrounding water are measured

with Particle Image Velocimetry (PIV) technique. The PIV system is one of the efficient and effective measurement techniques used to measure two dimensional velocities and turbulence levels in a flow. The PIV technique has been used by many researchers to measure the structure of two-phase liquid-solid turbulent jets (Muste et al., 1998; Wu and Christensen, 2006). This system consists of a continuous 6W argon ion laser to generate a light sheet to illuminate the flow and a high resolution CCD camera to capture the images of flow. Two-dimensional velocities of the flow field are computed from the displacements between subsequent images (La Vision, 2007).

Chapter 4 shows the results obtained from PIV measurements of the sand jet front and a comparison of the sand jet front with those single-phase buoyant jets and particle thermals. To understand the underlying vortex structure of the sand jet front, local vortex identification techniques such as Galilean velocity decomposition were used. Evolution of vortices and its structures can be extracted from velocity fields by employing these techniques. For example in Galilean velocity decomposition, the magnitude of the radial convection velocity shows the shape of the vortices. The large radial convection velocity indicates the semi-circular and the elongated ellipsoid vortices.

Effects of particles on the turbulence of the water phase are studied in this chapter. The influence of particles on the modulation of turbulence can be described by the Stokes number along the axis of the jet. Classifications are made for solid-liquid and solid-gas turbulent jets and new formulations are proposed to show the correlation between Stokes number and the turbulence attenuation of the particle-laden turbulent jets.

1.2.4 Sand Deposition from Circular Slurry Jets

Chapter 5 presents the results of an exploratory laboratory study on the deposition of sand particles. In this study, sand particles are injected from sediment-laden circular jets in to horizontal and inclined beds. To investigate the effects of jet characteristics and controlling parameters such as, initial velocity of jets, bed slope and sediment concentration on the development of sediment deposition, three series of experiments were carried out. Reynolds numbers, R based on the jet exit conditions are defined ranging from 9,600 to 19,200 and the densimetric Froude number, F ranging from 11.8 to 28.3.

In this chapter, effects of controlling parameters on the jet spreading rate and the sediment deposition length scales are studied. Deposition length scales, mound base area and the angle of deposition were measured. Since deposition of sediment is time dependent, experimental results in this chapter can be used to predict the mound development with time. The impact of the initial jet velocity and particle size can be formulated by employing the densimetric Froude number and the settling velocity of particle. A correlation between the variation of the axial velocity of the wall jets and the initiation of suspended load can be used to estimate the location of the initiation of sediment deposition.

Chapter 6 presents general conclusions and recommendations for future research.

Chapter 2

Effect of Particle Size on the Characteristics of Sand Jets in Water

2.1 Introduction

Sand-laden turbulent jet is a type of two-phase flow, which can be found in many engineering applications, such as, marine bed capping, mining operations, hydro-transport, dredging material disposal, and discharge of industrial and domestic wastewater. Understanding the dynamic interactions of the particle phase (i.e. sand) and turbulent water jets are important in order to properly design and optimize the mentioned engineering systems. The interactions of the suspended particles within the jet change the mass, momentum and energy transfers of the system. Flow properties such as the velocity, turbulence intensity, and Reynolds stresses are affected by particle interaction mechanism which leads to increase the complexity of the system and mixing phenomenon.

Obtained information from experimental investigation on solid-liquid jets (i.e., time averaged velocities and turbulent fluctuations of both phases) indicates that the particle-laden jets exhibited higher turbulence. This resulted in significant increases in particle drag from estimates based on the standard drag curve (Parthasarathy and Faeth, 1987). To estimate the axial particle velocity of the slurry jets, Jiang et al. (2005) proposed a correlation based on the summation of the fluid velocity and the settling velocity of particles. The formulation was obtained based on the experimental study of low concentrated (0.19%) slurry jets with 75 μm particles.

A paper based on the content of this chapter has been published in the *Journal of Engineering Mechanics*, ASCE, as Azimi et al., (2011), Vol. 137, No. 12, pp. 822-834.

Particle volume fraction has a prominent role in the structure and behaviour of the solid-liquid jets. Investigation on the effect of particle volume fraction indicates that by increasing the volume fraction of the particle phase, the spreading rate of both phases will increase (Virdung and Rasmuson, 2007). The results were obtained from experimental and numerical study of solid-liquid jets with low volume fractions (less than 2%). The initial particle volume fractions of the turbulent jets in most of the previous experiments were limited to less than 5% (Parthasarathy and Faeth, 1987; Muste et al., 1998; Arai et al., 2003; Jiang et al., 2005; Virdung and Rasmuson, 2007; Cuthbertson and Davies, 2008). In these cases, the effect of particle-particle interaction is ignored and the flow structure is treated as a homogeneous two-phase flow system. In many engineering applications, however, the particle-laden jets can have high particle concentrations where particle-particle interaction plays a dominant role in the dynamics of such jets.

A recent experimental investigation on highly concentrated slurry jets was conducted to observe the impact of particle-particle interaction on jet spreading and rate of change on the axial concentration (Hall et al., 2010). In this study, the averaged particle velocity and concentration were measured using a novel optical probe for highly concentrated sand jets. These experimental results can be used to calibrate and validate numerical models. Consequently, through numerical modeling, we will be able to capture the detailed information in the areas where the measurement techniques have encountered some difficulty, in particular, the effect of particle-particle interaction and the turbulent dynamics of sand jets.

Commercial packages have been successfully employed to model multiphase flows. Virdung and Rasmuson (2007) simulated their experiments of the particle-laden jets using a commercial CFD solver (Fluent 6.2) with $k - \varepsilon$ model for the turbulence modeling. However, in their study only mean properties of the jets were presented. Lain

and Garcia (2006) employed ELSA22 to study particle-laden jet flow. Angst et al. (2001 & 2003) also conducted computational simulation on the behaviour of the particles in jet loop reactors and stirred vessels using the CFX solver package with the $k - \varepsilon$ turbulent model. Mathiesen et al. (2000) used FLOTRANS-MP-3D for predictions of gas-solid flow.

This chapter consists of two parts. In the first part, the results from the numerical simulation of the sand jets are compared with the experimental measurements of Hall et al. (2010). Ansys CFX solver package with modified $k-\varepsilon$ turbulent model and inter-particle relations was applied for simulation of the water phase, and zero-equation model was used for simulation of the dispersed phase (Ansys, 2009). The computed results consist of time averaged axial velocity of sand phase, sand concentration profiles at different cross sections and momentum fluxes of both sand and water phases.

In order to identify proper boundary conditions, a single phase water jet was numerically simulated. The convergence criteria of the simulation were carefully monitored and a reasonable mesh structure and maximum residual were introduced for this type of simulation. The computed axial velocity distribution and concentration were compared with the experimental measurements on sand jets.

In the second part, effect of particle size on particle-laden jets structure was studied. Detailed information on the effects of particle size was presented as well. The effect of the mentioned parameters on mean properties of the sand jets was considered, and detailed information of the turbulence were extracted from the numerical simulation.

2.2 Governing Equations

It is possible to model the motion of large number of solid particles in liquid as an Eulerian-Eulerian two-phase flow (Ansys, 2009). Using of the two-fluid model in CFX provides one solution field for each separate phase. The formulation of the continuity equation for both the homogeneous and the two-fluid models is identical. By volume averaging over a small control volume as shown by Wörner (2003), one can obtain the continuity equation for continuous phase:

$$\frac{\partial(r_c \rho_c)}{\partial t} + \frac{\partial(r_c \rho_c u_{ci})}{\partial x_i} = 0 \quad , \quad r_c + r_D = 1 \quad (2.1)$$

where r_c is the volume fraction of the continuous phase and r_D is the volume fraction of the dispersed phase. ρ_c is density of the continuous phase; u_{ci} ($i=1,2,3$) represent the velocity of phase c . According to Wörner (2003), the momentum equation for the continuous phase can be presented as

$$\frac{\partial(r_c \rho_c u_{ci})}{\partial t} + \frac{\partial(r_c \rho_c u_{ci} u_{cj})}{\partial x_j} = r_c \rho_c g_i - r_c \frac{\partial p_c}{\partial x_i} + \frac{\partial}{\partial x_j} \left(r_c \mu_c \frac{\partial u_{ci}}{\partial x_j} \right) + M_c \quad (2.2)$$

Here M_c describes the interfacial forces acting on the continuous phase due to the presence of the particles which include drag force, virtual mass force and turbulent dispersion force. The effect lift force is negligible in our study. In solid-liquid flow the major source of the inter-phase momentum transfer is the inter-phase drag force, which is expressed as:

$$F_c^D = \frac{1}{8} C_D A_{CD} \rho_c |u_D - u_c| (u_D - u_c) \quad (2.3)$$

Here F_c^D is the drag force per unit volume (vector); u is the velocity vector; C_D is the drag coefficient and A_{CD} is the interfacial area density, the interfacial area per unit volume between the continuous phase and the dispersed phase. For a particle of simple shape, immersed in a Newtonian fluid and which is not rotating relative to the

surrounding free stream, the drag coefficient, C_D , depends only on the particle Reynolds number. Schiller and Naumann drag model was used for dispersed solid particles in this study.

$$C_D = \frac{24}{Re_p} (1 + 0.15 Re_p^{0.687}) \quad 0.2 < Re_p < 1000 \quad (Re_p = u_c D / \mu_c) \quad (2.4)$$

In vertical downward turbulent sand jets, the particles accelerate from their initial velocities by the effect of gravity. The following expression is used for considering the effect of particle acceleration.

$$F_C^{VM} = -F_D^{VM} = r_D \rho_C C_{VM} \left(\frac{D u_D}{Dt} - \frac{D u_C}{Dt} \right) \quad (2.5)$$

The coefficient of virtual mass force is related to the particle shape and for a group of particles it also depends on the particles volume fractions. Using the conventional definition of the added-mass force (Eq. 2.5) for particles and fluid accelerating independently, the added mass coefficient of Zhang & Prosperetti (1994) to first order is:

$$C_{VM} = 1/2 (1 - \alpha) \quad (2.6)$$

where α is the particles volume fractions. In the present numerical study, by assuming that the sand particles are spherical and the maximum volume fraction of a domain was around 4% the value of $C_{VM} = 0.48$ was selected for the present simulation. As mentioned by Loth (2009) the added mass force can be quite important for particle with low density which the virtual mass effects dominates the particle inertia effect and leads to an increased effective gravitational acceleration of $-2g$. The reaction of the particulate phase to the turbulent fluctuations can be simulated with different models (Lopez de Bertodano, 1998). In presence of turbulent fluctuation, the dispersed particles follow the continuous phase eddies by the effect of interphase drag which result in

additional dispersion from high to low concentration. In this study, the Favre Averaged Drag Model was used to simulate the turbulent dispersion.

$$F_C^{TD} = -F_D^{TD} = C_{TD} C_D \frac{\nu_{iC}}{\sigma_{iC}} \left(\frac{\nabla r_D}{r_D} - \frac{\nabla r_C}{r_C} \right)$$

(2.7)

where F^{TD} is the Favre Averaged Drag Force; ν_{iC} is the turbulent viscosity of the continuous phase; σ_{iC} is the turbulent Schmidt number for continuous phase. C_{TD} was selected equal to 0.75. Two-equation turbulence models are very widely used, as they offer a good compromise between numerical effort and computational accuracy. The transport equations for turbulent kinetic energy, k , and dissipation rate, ε , are employed for the continuous phase:

$$\frac{\partial}{\partial t} (r_C \rho_C k_C) + \nabla \cdot \left(r_C \left(\rho_C u_C k_C - \left(\mu + \frac{\mu_{iC}}{\sigma_K} \right) \nabla k_C \right) \right) = r_C (P_C - \rho_C \varepsilon_C) + T_{CD}^{(k)} \quad (2.8)$$

$$\frac{\partial}{\partial t} (r_C \rho_C \varepsilon_C) + \nabla \cdot \left(r_C \rho_C u_C \varepsilon_C - \left(\mu + \frac{\mu_{iC}}{\sigma_\varepsilon} \right) \nabla \varepsilon_C \right) = r_C \frac{\varepsilon_C}{k_C} (C_{\varepsilon 1} P_C - C_{\varepsilon 2} \rho_C \varepsilon_C) + T_{CD}^{(\varepsilon)} \quad (2.9)$$

Here, the parameter σ is a turbulent Schmidt number relating the dispersed phase kinematic eddy viscosity ν_{iD} . The additional terms $T_{CD}^{(k)}$ and $T_{CD}^{(\varepsilon)}$ represent inter-phase transfer for k and ε , respectively and they are omitted in CFX by default. For the k - ε model the turbulent viscosity is modelled as:

$$\mu_{iC} = C_\mu \rho_C \left(k_C^2 / \varepsilon_C \right) \quad (2.10)$$

The total pressure in two-phase simulation is defined as:

$$P_{tot} = P_{stat} + \sum_a \frac{1}{2} r_a \rho_a u_a^2$$

(2.11)

where P_{tot} is the total pressure and P_{stat} is the static pressure. In the presence of buoyancy, the buoyancy production term P_{kb} is included in the k equation and modeled as:

$$P_{kb} = -\frac{\mu_t}{\rho\sigma_p} g \cdot \nabla\rho \quad (2.12)$$

2.3 Modeling Background and Model Validation

Two-fluid models are theoretically more advanced compared to the homogeneous models, as they describe the mechanics of each phase. Each phase of the two-fluid model has its own velocity field and is described by an individual set of continuity and momentum equations (see section 2.2). The interactions between two phases known as inter-phase relations significantly change the structure of the flow system. Adding the inter-phase forces to the momentum equations of each phase requires more closure relations. Due to the complexity of the problem and limited knowledge of the physics in the phase interaction, many empirical expressions are added to the equations of motion. For two-fluid models separate sets of governing equations (i.e., continuity and momentum equations) are numerically solved for each phase using finite volume scheme. Two averaging methods have been used in modeling the above mentioned equations. Governing equations can be volume-averaged over each control volume named as one-average method. The present model employs one-average method in simulation of sand jets as a dilute mixture. The second method takes another average over turbulence. In this method the governing equations are averaged over a region in which the characteristic length scale is substantially larger than the inter-particle distance and smaller than the system dimensions. The two-average method has been used to model two-phase flow by many researchers [(Hrenya and Sinclair (1997), Lopez de Bertodano (1998), and Bombardelli and Jha (2009)].

The mentioned equations were integrated over each control volume. Then, the discretized integral equations were numerically solved using CFD solver. In order to discretize the advection term in Navier-Stokes equations, the variable ϕ_{ip} must be approximated in terms of the nodal values of ϕ .

$$\phi_{ip} = \phi_{up} + \beta \nabla \phi \cdot \Delta \vec{r} \quad (2.13)$$

where ϕ_{up} is the value at the upwind node, $\nabla \phi$ is the gradient of ϕ and $\Delta \vec{r}$ is the vector from the upwind node to the ip . Particular choices of β give rise to different schemes. For $\beta = 0$ the scheme is called first order upwind and for $\beta = 1$ it is a second order scheme. The High Resolution Scheme computes β locally to be as close to 1 as possible without introducing local oscillation and sets $\nabla \phi$ equal to the control volume gradient at the upwind node. This scheme is both accurate and bounded since it only reduces to first order scheme near discontinuities. In order to close the closure problem a well-known turbulent model ($k - \varepsilon$) was used for the water phase (Lauder and Spalding, 1974).

The only model available for the dispersed phase in turbulent flow was the Dispersed Phase Zero Equation (Ansys, 2009). In this model the dispersed phase kinematic viscosity ν_{iD} is related to the continuous phase kinematic viscosity ν_{iC} using the parameter of turbulent Schmidt number σ , ($\nu_{iC} = \sigma \nu_{iD}$). A number of numerical simulations on solid-liquid two-phase flow have been carried out to study the particle movement in stirred tank. Wang et al. (2006) used 10% glass beads with the particle size of 110 μm and selected $\sigma = 1.0$ for their CFD simulations. Hartmann et al. (2006) studied similar phenomenon using the same particle volume fraction and particle size of 300 μm and employed Schmidt number of 0.7. Montante and Magelli (2007) used $\sigma = 0.8$ and mentioned that the effect of turbulent Schmidt number in steady state solid-liquid flow is

negligible. Bombardelli and Jha (2009) studied the sediment-laden, open channel flows using the complete two-fluid models (CTFM) and partial two-fluid models (PTFM), and found that turbulent Schmidt number can effect on particle spreading. Effect of the Schmidt number will be studied in this chapter.

The drag coefficient was predicted using the Schiller & Neumann model (Wörner, 2003). The Favre Averaged Drag Force coefficient, which accounts for the influence of velocity fluctuations on the particle dispersion, was selected as 0.75. Virtual mass coefficient is a function of particle shape and is also related to the particle concentration. Considering the effect of particle concentration and assuming spherical shape for all particles, the virtual mass coefficient was set to 0.48 (see section 2.2).

In the present numerical study, simulations were performed on a desktop computer with an Intel Pentium dual 2.8 GHz process and a random access memory of 3 GB. The computation domain was similar to the laboratory experiment of sand jet in water (Hall et al., 2010). In Hall et al (2010) experiments, the nozzle sizes were 19 mm and 12.5 mm and located 75 mm above the water surface. Falling through the air, the diameter of the sand jet reduces from 19 to 12.5 mm and from 12.5 to 8.2 mm at the water surface, respectively. The water surface was selected as the top boundary of the computation domain. Nozzles with a diameter of $d = 12.5$ and 8.2 mm were generated representing the nozzle at the water surface. Sand particles have a median size, D , of 210 μm and injected into the tank by the effect of their weight.

To prevent wall effects, it was assumed that the domain was cut by four imaginary planes that both the liquid phase and the dispersed phase can enter and exit through them. The solver package CFX 11.0 has an option called opening boundary condition that allows the fluid to cross the boundary surface in either direction and this option was selected for the boundaries of the domain. The relative total pressure was assigned for the inflow boundary and the relative static pressure for the outflow

boundary. The magnitude of the velocity at the opening boundary was then part of the solution (see section 2.2 and Ansys 2009). Relative pressure was specified in opening boundaries to satisfy the conservation equations. The direction of the flow is also accounted normal to the boundary. The top boundary condition was selected as free slip wall boundary condition.

Given the symmetry of the problem, only a portion of the experimental tank was chosen as the computational domain. While the experimental tank had a width of 125 cm and a depth of 100 cm, the computational domain was selected to be 30 x 30 x 100 cm. The selected domain was based on the photographic observation of the laboratory experiments, as well as the comparison with the preliminary simulation using the experimental size. The water density, ρ_w , was set to 998 kg/m³ and sand density, ρ_s , was set to 2540 kg/m³.

Table 2-1: Mesh characteristics and cell size of the sand jet in different mesh structure.

Mesh Type	Cell size (mm)	Number of Nodes	Number of Elements
Cube 1	10.00	145,534	811,242
Cube 2	8.75	218,882	1,221,682
Cube 3	7.62	329,638	1,845,952
Cube 4	7.00	425,350	2,398,471
¼ Cube 1	4.50	401,312	2,245,906
¼ Cube 2	4.20	492,734	2,765,825
¼ Cube 3	3.80	492,206	2,733,894

The mesh had unstructured grids forming elements of tetrahedral, pyramids and wedges. One quarter of the cubic domain and 1/12 of a cylinder with a diameter of 30 cm and height of 100 cm were also generated to provide higher resolution and approach the simulation results to mesh independent condition. Seven different mesh sizes were used

for examining the effect of cell size and convergence criteria named, cube 1 to 4, ¼ cube 1 and 2, and 1/12 cylinder, see Table 2-1. Figure 2-1a illustrates the mesh structure of the domain in three dimensional views.

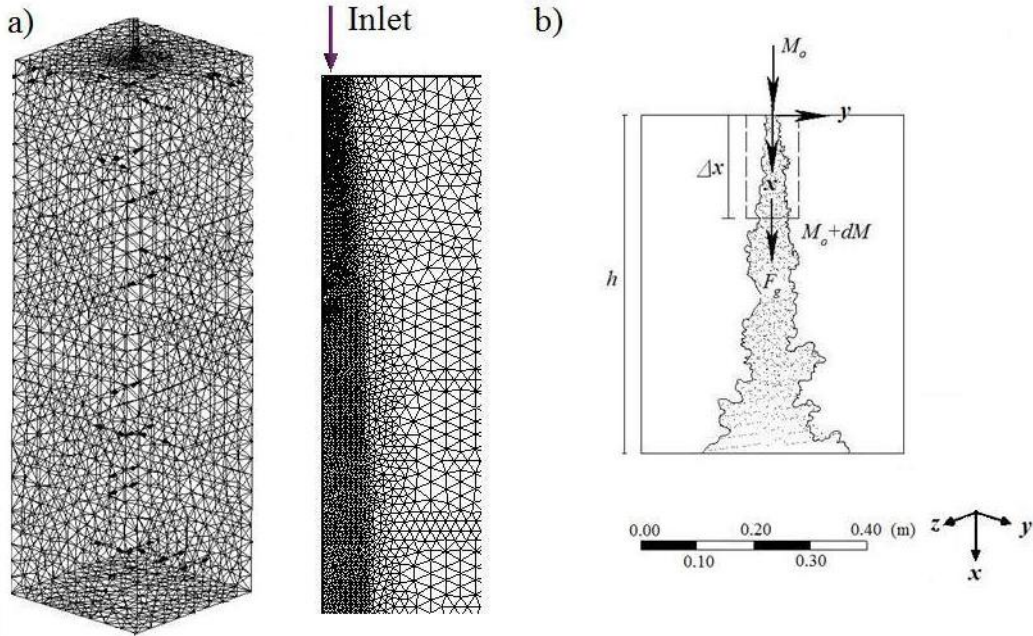


Figure 2-1: a) Simulation domain of the turbulent sand jet in water. b) Schematic of control volume of sand jet.

Figure 2-2 illustrates the effect of the mesh refinement and the magnitude of the computational residual changes on the normalized dispersed velocity and the concentration of sand jet. The residual is a measure of the local imbalance between the right-hand side and the left-hand side of conservative control volume equation. The solution would be “exact” if the residual becomes zero. The root mean square value of the residuals normalized with a representative range of the variable in the domain. Convergence is assessed when the normalized residual in discrete equations reaches a specified level. Three different target levels, 5×10^{-4} , 10^{-4} , and 5×10^{-5} were selected at two different sections, $x/d = 30$ and $x/d = 50$, where x is measured from the water surface. The computed sand velocity, u_s , was normalized with the initial sand velocity, $u_o = 0.69$ m/s, at the nozzle which was obtained from laboratory experiment. The jet sand concentration,

c_s , was also normalized with the initial volumetric concentration at the nozzle of $c_o=60\%$, therefore the initial void fraction of the sand jets can be calculated as 0.4. The obtained values from the 1/12 cylinder at the target level of 8.43×10^{-6} indicate that simulation reached the asymptotic regime. Accordingly, the 1/12 cylinder was used in this study, which has 2,637,457 elements constructed by 479,491 nodes with the maximum spacing of 2.8 mm. The domain contained four local mesh refinement regions: in the first 1 cm of the jet, computational cells was reduced from 3.8 mm to 0.5 mm ($\approx 1/16 d$); in the region from 1cm to 10 cm downstream of the jet, the cell size was reduced to 1 mm; in the region from 10 cm to 30 cm from the nozzle, cell size was reduced to 2 mm and in the region from 30 cm to 60 cm from the nozzle, cell size was reduced to 2 mm. The radius of mesh refinement in the region from 30 cm to 60 cm from the nozzle was 50 mm. It is interesting to note that, the model converges to the lower r.m.s residual for simulation of the larger particles. Each computational run, using the r.m.s residual target of 8.43×10^{-6} , took between 16-18 hours.

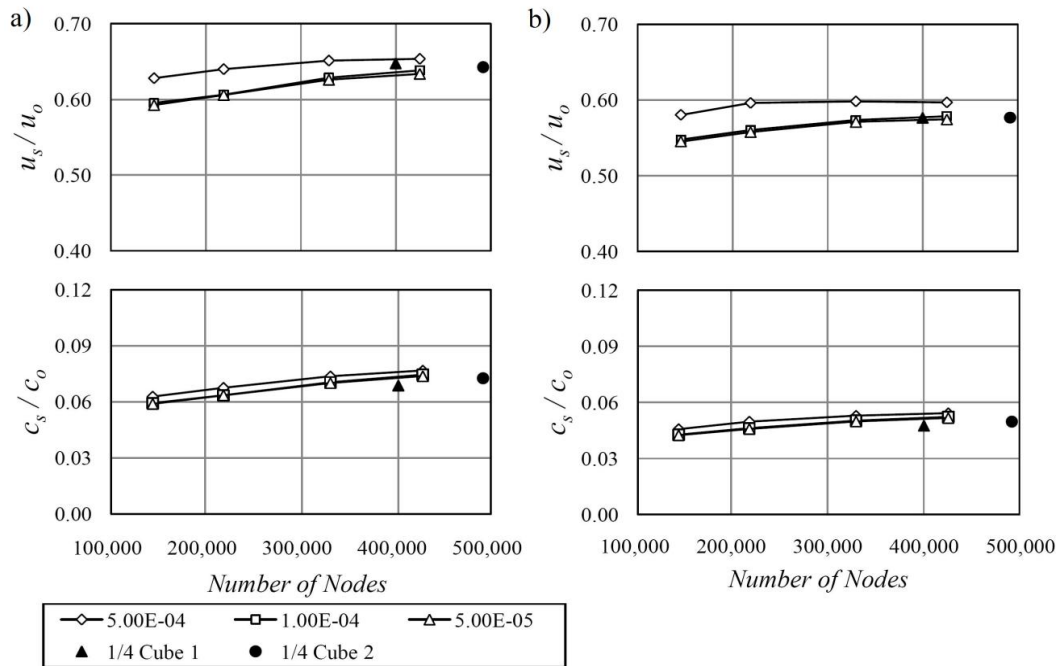


Figure 2-2: Mesh sensitivity plots of sand velocity and concentration for sand jet; a) $x/d = 30$; b) $x/d = 50$.

The size and the resolution of the present computational domain were compared with those found in the literature. A 12 mm particle-laden gas jet was simulated by employing ELSA22 numerical model (Lain and Garcia, 2006). They used a mesh size of 0.5 mm close to the nozzle and reported that such resolution is sufficient for producing grid-independent results. Uchiyama and Naruse (2003) proposed a vortex method to simulate a 4 mm gas-particle two-phase jet. The domain width in their simulation was $37d$ and the bottom boundary condition was located $50d$ downstream. A grid size of 4 mm was used in their simulation. They found that the result was not affected by finer grids. The momentum length scale can be defined based on the momentum flux, $M_o = (\pi d^2/4) \cdot \rho_s \cdot c_o \cdot u_o^2$, and the buoyancy flux, $B_o = (\pi d^2/4) \cdot g \cdot (\rho_s - \rho_w) \cdot c_o \cdot u_o$, where g is the acceleration due to gravity.

$$l_m = \frac{(M_o / \rho_w)^{3/4}}{(B_o / \rho_w)^{1/2}} \quad (2.14)$$

The momentum length scale was 2.7 cm for our experiments, which indicated the jet was in buoyancy dominant regime after about 10 cm. For single-phase buoyant jets, Papanicolaou and List (1988) suggested that the centreline velocity, u_m , and the centreline mass concentration, c_m , along the jet axis

$$u_m = 3.85 B_o^{1/3} x^{-1/3} \quad (2.15)$$

$$c_m = 11.0 c_o B_o^{-1/3} x^{-5/3} \quad (2.16)$$

Comparison of the measured sand velocity with the simulation at different cross sections was shown in Figure 2-3a. The jet half-width, b , close to the nozzle ($x/d = 24.4$) decreased slightly as the resolution of the mesh increased. The peak value of the sand velocity at this section increased with mesh resolution since the mass imbalance approached to zero. The simulated centreline velocity at this location over-estimated the measurement by 12%. At the middle of the jet ($x/d = 48.8$), the simulated centreline

velocity over-estimated by 8%, and far from the nozzle the model under estimated by 1.6%. The model outputs of sand concentration were shown in Figure 3b. The model over-estimated the concentration by 12% near the nozzle. At $x/d = 48.8$, model overestimated the peak value by 15%. At $x/d = 73.1$, the model over-estimated the peak value of sand concentration only by 3%.

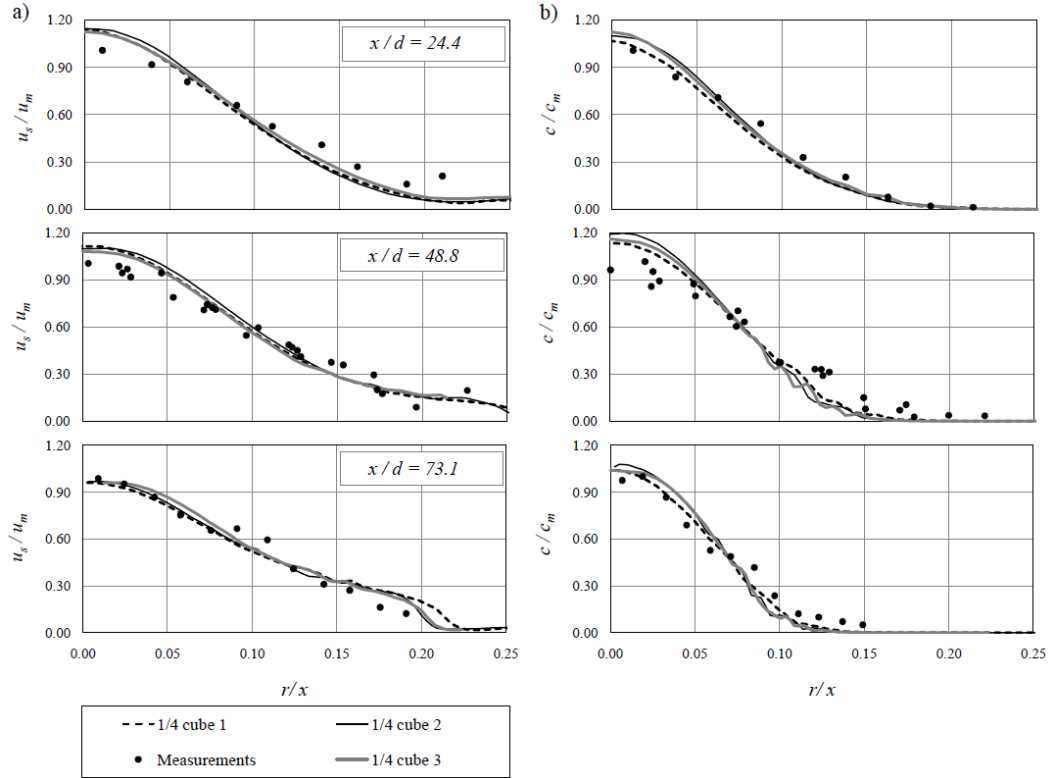


Figure 2-3: Comparison of the simulation outputs of the sand jets with the measurements using different mesh set up; a) Sand velocity; b) Sand concentration.

To evaluate the model performance, the experimental measurement uncertainties in Hall et al. (2010) are reported here. The measurement errors in jet width and concentration were 8% and 15% respectively. The standard deviation of the measurements were 4% of the average value within the inner 60% of the jet. Outside of this region, the errors were found to be much larger than the inner region, due to measurement difficulties between large eddies of particles. Considering the measurement

uncertainty, and the numerical model assumption, a difference of 15% between the predictions and measurements is considered to be acceptable. The above comparisons of the numerical results of sand velocity and concentration with laboratory measurements show that the modified $k-\varepsilon$ turbulent model is capable of simulation at those locations, the CFD mode performs well (i.e., error is less than 15%). Far away from the nozzle, the influence of the cell size was less significant on the sand velocity prediction compared to the sand concentration.

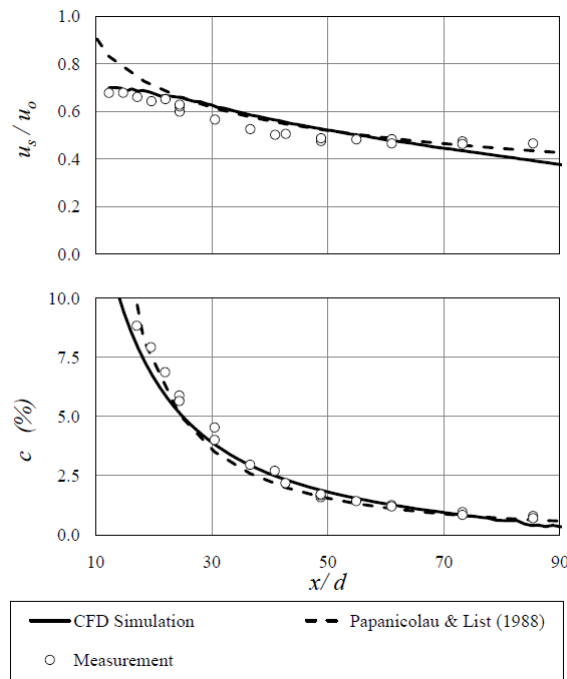


Figure 2-4: Variation of centerline sand velocity and concentration in the axial direction $d=8.2$ mm; a) Normalized axial sand velocity; b) Centerline concentration.

Figure 2-4 illustrates the variation of the axial velocity and concentration of sand jets with 8.2 mm nozzle diameter. The velocity data was normalized with the initial sand velocity, $u_o = 0.69$ m/sec. CFD simulation results were compared with laboratory measurements of Hall et al. (2010) in sand jets. Experimental measurements of Papanicolaou and List (1988) in single-phase buoyant plume were also included for comparison. The sand velocity from the nozzle up to the location $x/d = 25$ was over-

predicted by an average of 5.4%. At $25 < x/d < 80$ the model prediction was within 10% error (Figure 2-4a). The results obtained from the simulation indicate that the computed concentrations were in good agreement (i.e., 10% error) with the experimental observations. As mentioned earlier, the error in the simulation increases close to the nozzle, $x/d < 30$, and it reduces with increasing mesh resolution.

Momentum fluxes of the water phase and the sand phase of the 8.2 mm sand jets were calculated by means of numerical integration of both experimental and numerical results (See Figure 2-1b). According to Figure 2-1b, the total momentum flux increases from the initial momentum flux by the effect of gravitational force on the sand particles inside the control volume. Then the momentum flux transfers to the water phase due to the inter-phase drag force.

The total momentum flux of the sand jets (sand phase plus water phase) at any location from the nozzle will be the summation of the initial momentum flux and the gravitational forces (Eq. 2.17). The gravitational force at any location could be approximated by calculating the weight of a tube of sand which has a diameter of d and length of Δx (Eq. 2.18).

$$M_s + M_w = \rho_s (\pi d^2 / 4) c_o u_o^2 + F_g \quad (2.17)$$

$$F_g = g(\rho_s - \rho_w)(\pi d^2 / 4) c_o \Delta x \quad (2.18)$$

The initial sand momentum flux is known and the gravitational force, F_g , can be calculated at each location. Therefore the total momentum flux at each location can be calculated using Eq. 2.17. The sand momentum flux, M_s , can be calculated by integrating the measured sand velocity and concentration Gaussian profiles (Eq. 2.19).

$$M_s = \rho_s \int_0^{\infty} c_s u_s^2 2\pi r dr \quad (2.19)$$

$$M_w = \rho_w \int_0^{\infty} (1 - c_s) u_w^2 2\pi r dr \quad (2.20)$$

Then the water momentum flux, M_w , can be obtained knowing the total momentum flux and the sand momentum flux. The water velocity induced by the sand particles can also be estimated by using Eq. 2.20

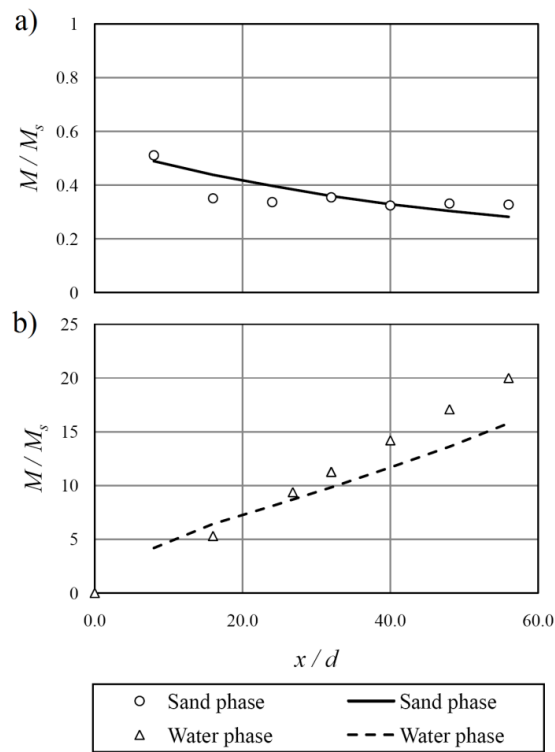


Figure 2-5: Variations of the measured sand and water momentum fluxes along the jet axis compared with the simulation outputs, $d = 8.2$ mm; (Open symbols are measurements and lines are simulation results).

The simulation results of the sand phase and the water phase momentum fluxes were compared with the measurements in Figure 2-5. Figure 2-5 shows that the numerical integration method provides relatively accurate results in prediction of sand phase momentum flux within 10 % error. But the numerical integration under-estimated the

momentum flux of the water phase by 15%. As can be seen from the simulation results (Figure 3a and 3b), the model under predicts the spread of the sand phase. This indicates that the sand phase zero-equation model for modeling the turbulent viscosity does not accurately predict the lateral spread of sand particles.

2.4 Effect of Particle Size on the Mean Properties of the Sand Jets

Numerical simulation of sand jets was performed using particles with a median size of 210 μm as used in the laboratory experiment of Hall et al. (2010). Two additional particle sizes of 460 and 780 μm were selected for simulation to study the influence of particle size on the behaviour of sand jets. These selected particle sizes were the same as those used in the experimental study on solid-gas turbulent jets by Sheen et al. (1994). Effect of particle sizes on jet void fraction was also reviewed using Hoffmann and Finkers formulation (1995). For sand particles with median diameters of 460 and 780 μm , the initial jet void fraction was also assumed to be 0.4, i.e., the change in the void fraction of sand particles is negligible in the size range of 210 to 780 μm .

Effect of particle size on the mean properties of the sand jets such as axial velocities of both phases was investigated in this part. The obtained results indicated that, having the same mass flux and initial concentration, particle size introduced significant changes in the mean properties of the sand jets. Figure 2-6 shows the effect of particle size on the axial velocities of both phases at different cross sections ($x/d = 24.4, 48.8, 73.1$). Both sand and water axial velocities were normalized with the centreline velocity, u_m , of the single-phase jet suggested by Papanicolaou and List (1988) (Eq. 2.15 & 2.16). Figure 2-6a shows that the peak value of the axial sand velocity at each cross section increases with increasing particle size. Close to the nozzle at $x/d = 24.4$, the computed maximum sand velocities using particle size of 210, 460 and 780 μm were respectively

1.08, 1.12 and 1.19 times of the single-phase water velocity. At $x/d = 48.8$, the sand axial velocity of $210 \mu\text{m}$ was approximately 6% higher than the single-phase buoyant jets. The sand axial velocities of 460 and $780 \mu\text{m}$ were respectively 17% and 26% higher than the single-phase buoyant jets. Far away from the nozzle ($x/d = 73.1$), particles velocity decays at a lower rate compared to the buoyant plume. Therefore, sediment velocities of particles with 210 , 460 and $780 \mu\text{m}$ were respectively 3%, 23% and 33% higher than the single-phase buoyant jets. Due to the dependence of the interaction forces on particle size, water phase velocity varies with particle size and the variation was found to be less significant compared to the sand phase (Figure 2-6b).

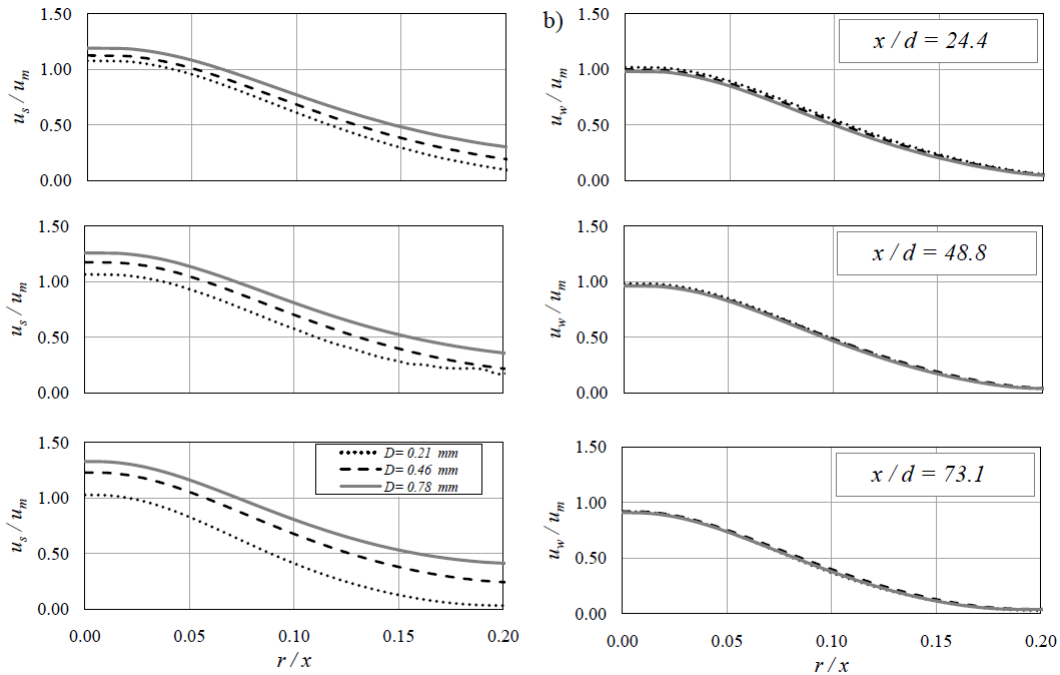


Figure 2-6: Effect of particle size on the axial velocity of the sand phase and the water phase; a) Sand phase velocity; b) Water phase velocity.

The computed radial velocities of both sand phase and water phase with different particle sizes are shown in Figure 2-7. Figure 2-7a indicates that, the radial velocity of the sand phase increased by particle size. A parameter r_v is introduced here for the distance between the jet centerline and the location of the maximum sand phase radial velocity. It was found that far away from the jet nozzle ($x/d = 64$), the value of r_v increases with

increasing particle size. The reason for having larger value of r_v may be due to the inter-particle spacing. With the same buoyancy flux of the sand phase, the space between the larger particles will be bigger, and larger eddies can form.

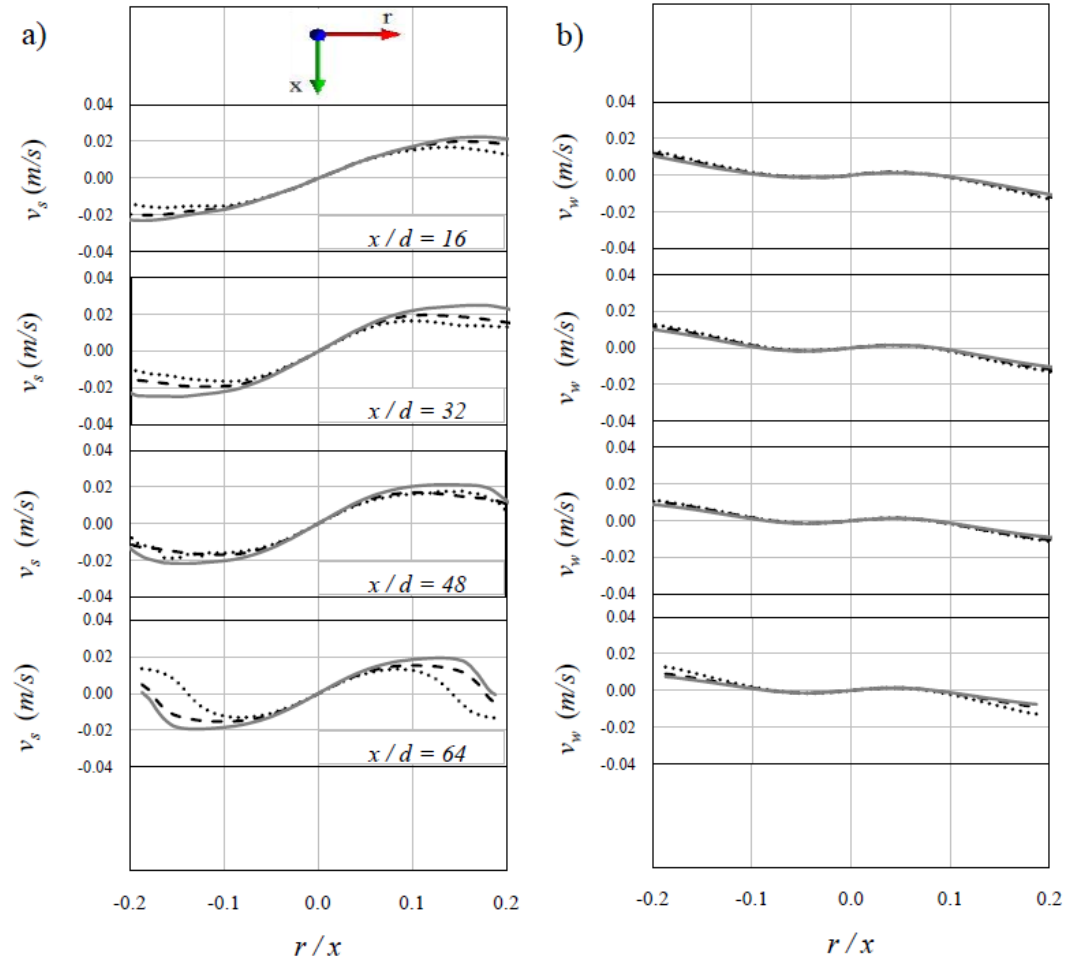


Figure 2-7: Effect of particle size on the radial sand and water phase velocity distributions at different cross sections, $x/d = 16, 32, 48, 64$, ($d = 8.2$ mm); a) Sand velocity distributions; b) Water velocity distributions.

The radial velocities obtained from this computational study were compared with a two-phase turbulent jet experiments of Arai et al. (2003). They carried out a series of experiments with a low initial particle volume ratio of 0.21% and used 389 μm particles. Their experimental observations of the radial velocity of the dispersed phase showed the same trend with the presented numerical outputs (Figures 2-7a). Variations of the water

phase radial velocity, v_w , was depicted in Figure 2-7b. The behaviour of the water phase radial velocity was found to be independent of the location.

Figure 2-8 illustrates the contour plots of the sand phase velocity and the effect of particle size on the spreading rate of the jet. It is interesting to note that, the normalized jet half-width b/x which represents the spreading rate of the jet was not constant in those cases. In these particle size ranges, jets with larger particle size have a larger spreading rate. The normalized jet half-width was calculated to be 0.095 for sand jets with 210 μm particles. The obtained spreading rates for jets with 460 and 780 μm were 0.105 and 0.12.

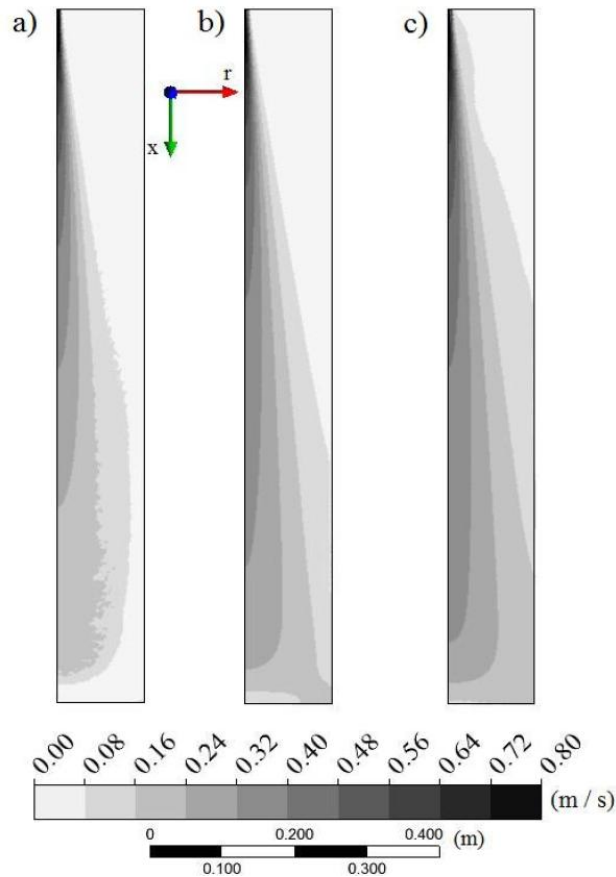


Figure 2-8: Contour plots of the sand phase velocity with different particle size, a) $D = 210 \mu\text{m}$, b) $D = 460 \mu\text{m}$, c) $D = 780 \mu\text{m}$.

The reason for observing higher spreading rate for jets with larger particle size may due to the fact that, larger particles have higher level of potential energy which

transforms to kinetic energy through the jet. Higher kinetic energy, in turn, creates more particle fluctuations which leads to particle dispersion and higher spreading rate.

2.5 Effect of Particle Size on the Turbulent Characteristics of the Sand Jets

Due to the limitation on using the turbulent model for the dispersed phase, the following detailed information on the turbulent characteristics of the sand jets were presented only for the water phase. The specific turbulent kinetic energy per unit mass of the water phase, k_w is defined as:

$$k_w = 0.5 (\overline{u'^2} + \overline{v'^2} + \overline{w'^2}) \quad (2.21)$$

Earlier experimental investigation on low concentrated solid-liquid turbulent jets indicates that the velocity fluctuations in all directions have close values which can be classified as isotropic turbulence (Parthasarathy and Faeth, 1987). In their experimental study the jet had a diameter of 5 mm and relatively high initial particle volume fractions of 2.4% and 4.8%. It was observed that close to nozzle, at $x/d = 8$, the turbulent fluctuations, the axial fluctuation u' , and the radial fluctuations v' are equal and at $x/d = 16$, u' was 25% higher than v' . The difference in the magnitude of fluctuations reached 50% at $x/d = 40$. Accordingly, the assumption of isotropic turbulence provides relatively reasonable results close to nozzle and inaccurate prediction for $x/d > 40$. In anisotropic turbulence, the averaged turbulent intensity of the jet can be calculated as

$$I_w = \frac{(2k_w/3)^{1/2}}{u_w} \quad (2.22)$$

The influences of particle size on turbulent characteristics of the sand jets were illustrated in Figure 2-9. The water phase turbulent kinetic energy, k_w , rate of energy dissipation, ϵ_w , turbulent eddy frequency, f_w , were normalized with the nozzle diameter, d ,

and initial velocity, u_o . The turbulent eddy frequency of the jet was calculated by the model as follows (Ansys, 2009):

$$f_w = \frac{k_w}{\nu \cdot (\mu_T / \mu)} \quad (2.23)$$

where ν is the kinematic viscosity and μ_T/μ is the eddy viscosity ratio. Figure 2-9a shows that the location of the maximum rate of turbulent energy dissipation is at $x/d = 8.6$ for sand jets. It was found that larger particles create less dissipation through the sand jets. The dissipation rate of the jets with 210 μm particles was higher than those with 460 and 780 μm particles by 5.3 and 11.6%, respectively. Small particles tend to follow the turbulent eddy for a part of their lifetime and the eddy's energy will transfer to the particles through the drag force which leads to particle movement. Therefore, small particles dissipate the continuous phase energy more than large particles. The results of the turbulent kinetic energy are shown in Figure 2-9b. The kinetic energy increases with x and reaches the maximum value at $x / d = 11.5$. After that, it starts to decrease. It is interesting to note that the location of the maximum k_w is approximately the same regardless of the particle size.

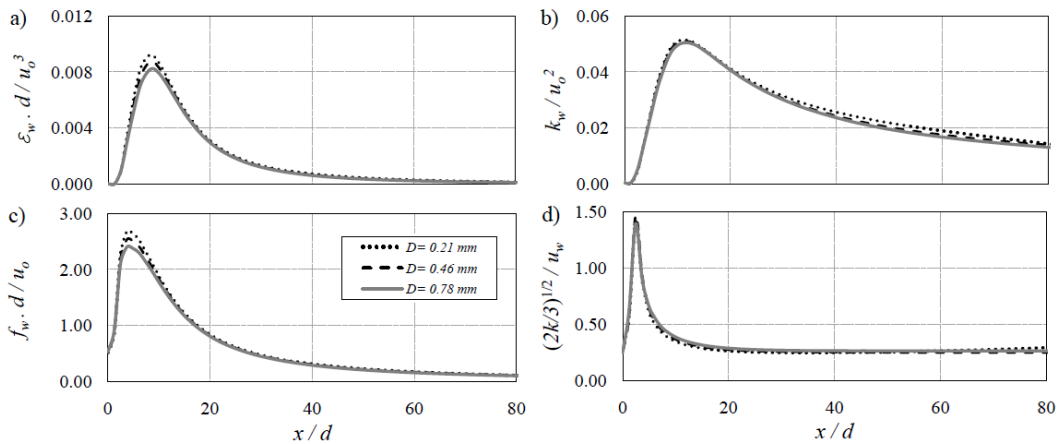


Figure 2-9: Effect of particle size on variations of the water phase turbulent characteristics along the jet axis; a) Rate of turbulent energy dissipation; b) Turbulent kinetic energy; c) Turbulent eddy frequency; d) Turbulence intensity.

Figure 2-9c illustrates the effect of particle size on the turbulent eddy frequency (Eq. 2-23). The eddy frequency of the jet decreases when the sand jet moves through the water and it stays constant further downstream of the nozzle regardless of the particle size. The extent to which the particles will follow the turbulent eddies of the fluid phase can be estimated by the Stokes number, S_t , which is the ratio of particle response time, τ_s , to the carrier phase characteristic time scale, d/u_o .

$$S_t = \frac{\tau_s u_o}{d} \quad (2.24)$$

The particle response time was defined by Crowe et al. (1985) as the time required for a particle released from rest in a constant velocity flow to achieve 63% of the free stream velocity. Assuming Stokes drag, the response time is given by:

$$\tau_s = \frac{\rho_s D^2}{18\mu} \quad (2.25)$$

Since the particle Reynolds number in all cases was above unity, a correction was required to calculate the response time. The correction is based on an empirical particle drag relationship for $Re_p < 700$, cited in Torobin and Gauvin (1959).

$$\tau_s^* = \frac{\tau_s}{1 + 0.15 Re_p^{0.687}} \quad (2.26)$$

The above mentioned time scales and non-dimensional parameters were calculated and results are shown in Table 2-2. Characteristic time scales and non-dimensional parameters identifying the dynamics of particles were calculated for sand jet and results are shown in Table 2-1. As can be seen from Table 2-2, the value of Stokes number for sand jets with small particles (i.e., 210 μm) is less than unity, which shows the particle response time is less than the carrier phase characteristics time scale. Thus

those particles follow the dominant eddies generated by the jets. On the other hand, particles with 780 μm diameter has a Stokes number above unity, thus those large particles do not follow eddies. It was found that, near the jet nozzle, small particles generate higher frequency than the large one. The frequency of eddies of 210 μm particles was higher than 460 and 780 μm particles by 3.6 and 7.3%. With the same continuous phase kinetic energy, small particles have less inertia and follow the eddy faster than the larger one. This could be the reason for the higher frequency of the small particles compared to the large particles.

Table 2-2: Time scales and non-dimensional properties of sand jets.

Particle size (μm)	210	460	780
Re_p	5.18	30.6	91.3
τ_s (sec)	6.22×10^{-3}	29.8×10^{-3}	85.8×10^{-3}
τ_s^* (sec)	4.24×10^{-3}	11.6×10^{-3}	19.8×10^{-3}
S_t	0.356	0.975	1.667

Bombardelli and Jha (2009) studied the sediment-laden, open channel flows using the complete two-fluid models (CTFM) and partial two-fluid models (PTFM), and found that turbulent Schmidt number can effect on particle spreading. Their numerical results indicate a Schmidt number less than one for dilute mixtures. Chen and Wood (1986), however, recommended the Schmidt number larger than one for the two-phase jet studies. They used the Stokes number to predict the suitable value for turbulent Schmidt number in two-phase jets studies, $\sigma = 1 + S_t$. The effect of Schmidt number is examined by carrying out the simulations with different values of Schmidt number, σ . Similar numerical simulations were run having different turbulent Schmidt numbers of $\sigma = 0.5, 1.0, 1.5, 1.75$ and 2.0 . It was found that the effect of Schmidt number on prediction of

sand concentration and spreading rate was negligible. The maximum change on sand velocity and concentration using the mentioned range of σ was found to be less than 1.2%. Similar result was found in steady state solid-liquid flows (Montante and Magelli, 2007).

The effect of the particle phase on the turbulence of the continuous phase is known as the turbulent modulation (Crowe et al., 1998; Gore and Crowe, 1989). For examining the impact of particle phase on turbulent sand jets, the averaged turbulent intensity of the jet was calculated based on the turbulent kinetic energy and the centerline water phase velocity at the same location (Eq. 2-22). The effect of particle size on the turbulent intensity of the continuous phase, I_w , was investigated and the obtained results were presented in Figure 2-9d. The maximum change in the turbulence intensity of the water occurs at $x/d = 2.5$. The maximum turbulent intensity in the solid-gas jets was shifted downstream and the location of the maximum turbulence intensity was reported at $7 < x/d < 12$ (Tsuji et al., 1988). The reason for moving the high fluctuation area downstream in solid-gas jets may be attributed to the higher density difference and large initial gas velocity (i.e., 11-24 m/s). After the turbulence intensity passed the maximum value it decreased to a constant value far downstream of the water surface (i.e. $\approx 25\%$). Similar trend was observed in solid-gas turbulent jets (Tsuji et al., 1988). Interesting results were observed in this correlations which agree quite well with turbulent modulation theory, that is, small particles attenuate the turbulence while large particles augment the turbulence (Gore and Crowe, 1989).

Axial profiles of k_w , ε_w , along the jets were obtained from the simulation results, and the effect of particle size is considered in Figure 2-10. Both turbulent kinetic energy and rate of dissipation were normalized with the nozzle diameter and water velocity along the jet. Effect of particle size on ε_w is plotted in Figure 2-10a. It can be deduced

that, larger particles dissipate energy at a lower rate. According to Gore and Crowe (1989 & 1991), small particles can follow the turbulent eddies and absorb the flow kinetic energy. Therefore, small particles reduce energy level of the continuous phase, that is, small particles can dissipate more energy than relatively large particles. Obtained results of numerical simulations shown in Figure 2-10a support this idea. Figure 2-10a implies that, using 780 μm sand particles instead of 210 μm particles can reduce the rate of energy dissipation by 7.2% at $x/d = 24.4$. At $x/d = 48.8$, larger particles (i.e., $D = 780 \mu\text{m}$) dissipate the energy 16.9 % less than 210 μm sand particles. At $x/d = 73.1$, ε_w of small particles became 17.2% higher than large particles.

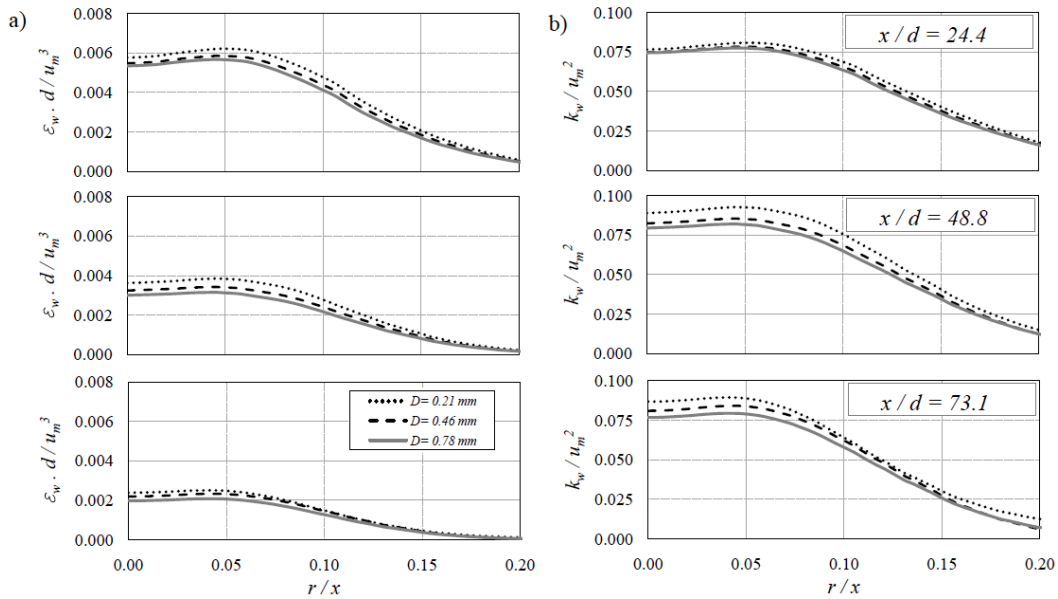


Figure 2-10: Effect of particle size on turbulent characteristics of the water phase at different cross sections; a) Rate of turbulent energy dissipation; b) Turbulent kinetic energy.

Effect of particle size on turbulent kinetic energy was studied at three locations and results were shown in Figure 2-10b. It was observed that k_w is symmetric in the radial position and the maximum kinetic energy was located at $r/x \approx 0.05$. Figure 2-10b implies that, the k_w varies with particle size and it reduces by increasing the particle size. The centreline k_w of small particles was 11.5% higher than centreline k_w of the larger sand

particles at $x/d = 73.1$. Close to the nozzle at $x/d = 24.4$, effect of particle size became less significant and the difference between the k_w was around 3%.

Effect of particle size on modulating turbulent intensity was investigated by Gore and Crowe (1989, 1991) and Crowe (2000). It was found that turbulence modulation is a function of length scale ratio of D / L_e where L_e is the characteristic length of the most energetic eddy in a single-phase condition. Integral length scale for a single-phase jet was found to be $L_e = 0.039 x$ (Wyganski and Fiedler, 1969). In their comparative study, turbulent intensity obtained from wide range of experimental studies such as bubbly flow and slurry flow in pipes, upward and downward particle laden jets were collected to explain the growth and the decline of turbulent intensity caused by the addition of particles. To study the turbulence modulation, turbulent intensity of a two-phase flow was normalized with the turbulent intensity of the corresponding single-phase flow.

$$\frac{I_{2P} - I_{1P}}{I_{1P}} \times 100 \quad (2.27)$$

where I_{2P} and I_{1P} are the turbulent intensity of two-phase flow, and one-phase flow, respectively. Based on a large number of experimental studies on two-phase flows, they concluded that small particles attenuate turbulence while large particles augment turbulence and the ratio of $D / L_e = 0.1$ was found as a critical value.

Change in turbulent intensity of sand jets as a function of length scale ratio was shown in Figure 2-11. Figure 2-11 shows that the numerical outputs of sand jets with different particle size follow the same trend as predicted by Crowe (2000). In all cases turbulent intensity augmented by increasing the length scale ratio but the critical value was not constant and it varied with particle size. The critical length scale values for sand jets with 210 μm particles was found to be 0.015 while this value for jets with 460 and 780 μm particles were 0.13 and 0.2, respectively. It was found that sand jets with 780 μm

particles attenuate turbulent intensity by 6% at $D / L_e < 0.1$ whereas sand jets with 460 μm particles attenuate turbulent intensity by 11% in this region. Notice that the two solid circles close to the simulation results of sand jets with 210 μm particles are from the experimental study of Shuen et al. (1985) on particle-laden gas-solid downward jets, which is consistent with our results on the turbulence modulation.

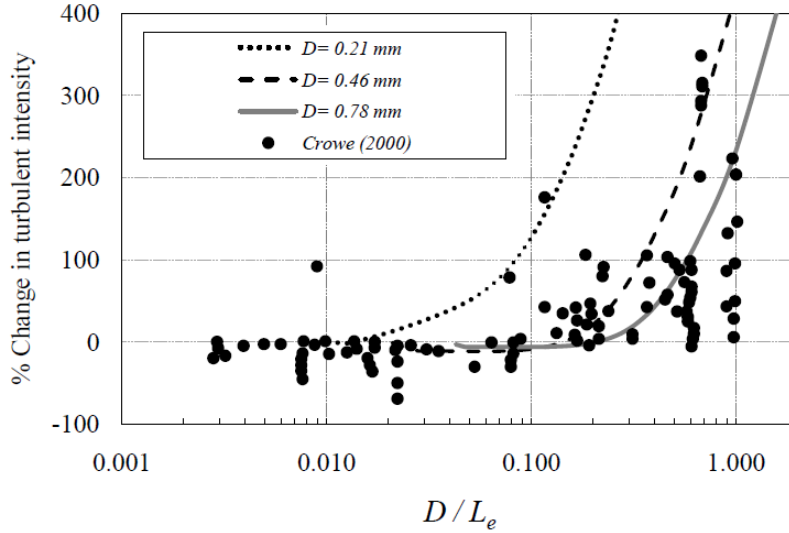


Figure 2-11: A comparison on turbulence modulation of sand jets with different particle size and experimental data collected by Crowe (2000).

The applicability of our numerical model and possible limitations of our results are discussed here. The CFD model was tested in dilute system and particle-particle interaction was considered to be negligible in simulation. The presented model is capable of obtaining detailed information on the water phase turbulence, such as turbulent kinetic energy and rate of energy dissipation but it is not capable of providing direct water velocity fluctuations. Simulation of the sand phase was also limited to the mean velocity and concentration and lack of information about turbulence since the model used zero-equation model for the sand phase. Since the inter-phase transfer of the turbulent kinetic energy and the rate of energy dissipation were omitted in this model, the model is not applicable for those studies that the inter-phase transfer of the turbulence is significant. A

relatively uniform particle size was tested in laboratory experiment and single size particle was employed in the numerical simulation. Therefore, our results are only applicable for uniform particle size. According to the obtained results from numerical simulation, the model is applicable over a particle sizes ranged between 0.21 to 0.78 mm, and the maximum volume fraction of 8% was compared with experimental observation.

2.6 Summary and Conclusion

A detailed computational fluid dynamics modeling was conducted to investigate the behaviour of the sand jets and the effect of particle size on the mean properties and turbulent characteristics of the jets. Computational capability and performance of ANSYS CFX 11.0 solver package for simulation of two-phase sand jets was evaluated. Sand phase axial velocity and concentration obtained from the numerical simulation were compared in different locations with laboratory experiments of Hall et al. (2010). Due to the experimental uncertainty, measurement inaccuracy, and the numerical model assumptions, a difference of 15% between the predictions and measurements is considered to be acceptable. Numerical outputs indicate that the model is able to simulate sand jets with acceptable accuracy.

The simulated sand velocity results close to the nozzle $x/d < 25$ were over-predicted by 5.4%. The accuracy of prediction was reduced at the middle of the jet $25 < x/d < 80$ and the model predictions were within 10% error. The analysis shows that the model is capable of simulating the concentration in all locations within 10% error. Numerical integration of the momentum fluxes of the sand phase and the water phase indicate that this method provides relatively accurate results in the prediction of sand phase momentum flux (within 10 % error), and it under-estimates the water phase momentum flux by 15%. Considering the model performance far away from the nozzle, it

appears that the model results were less accurate at the outer 40% of the jet ($r/x > 0.09$). This is likely due to the inaccurate prediction of the sand spreading rate, the high uncertainty of the measurements in this region, and inaccuracy of the zero-equation model for modeling the turbulent viscosity and the lateral spread of sand particles.

Effects of particle size on the axial mean velocities of both phases at different locations along the jet axis were numerically investigated. It was found that the kinetic energy of the sand jets increases from the nozzle, reaches the maximum value at $x/d = 11.5$ and decreases gradually thereafter. Similar trend was found for the rate of dissipation but the maximum value is located at $x/d=8.6$. It was found that the turbulent kinetic energy of the water phase decreases with increasing particle size. Far away from the nozzle, the maximum water phase turbulent kinetic energy of the sand jet with 210 μm particle size was found to be 6.7 and 11.5 percent higher than the sand jets with particles sizes of 460 μm and 780 μm , respectively.

The present numerical simulation was compared with the results of experimental studies (Sheen et. al., 1994; Tsuji et. al., 1988). It was found that the location of the peak fluctuation is located at $x/d = 2.5$ and independent of the particle size. Variation of turbulent intensity of sand jets with particle size was studied. Similar trend was found in variation of turbulent intensity with the length scale ratio but the critical value introduced by Gore and Crowe (1989) and Crowe (2000) was found to be varied in sand jets with different particle size. The effect of Schmidt number was examined by carrying out the simulations with different values of Schmidt number, σ . The maximum change on sand velocity and concentration was found to be less than 1.2% showing that the effect of Schmidt number on simulation of sand jets was negligible.

2.7 Notation

The following symbols are used in this chapter

A_{CD} = Interfacial area density

b = Jet half-width

B_o = Initial buoyancy flux

c_m = Centreline concentration

c_o = Initial volumetric concentration

c_s = Sand jet concentration

C_D = Drag coefficient

C^{TD} = Favre averaged drag coefficient

C_{VM} = Virtual mass coefficient

d = Nozzle diameter

D = Sand size

f_w = Turbulent eddy frequency

F_C^D = Drag force per unit volume

F_g = Gravitational force

F^{TD} = Favre averaged drag force

F_C^{VM} = Virtual mass force

g = Acceleration due to gravity

I_{1P} = Turbulent intensity of one-phase flow

I_{2P} = Turbulent intensity of two-phase flow

I_w = Averaged turbulent intensity

k_w = Turbulent kinetic energy per unit mass of water phase

l_m = Momentum length scale

L_e = Characteristic length of the most energetic eddy

M_C = Interfacial forces

M_o = Initial momentum flux
 M_s = Momentum flux of the sand phase
 M_w = Momentum flux of the water phase
 P_{kb} = Buoyancy production term
 P_{stat} = Static pressure
 P_{tot} = Total pressure
 r = Radial distance for the jet axis
 r_C = Volume fraction of the continuous phase
 r_D = Volume fraction of the dispersed phase
 r_v = Radial length scale
 \vec{r} = Vector from the upwind node to the ip
 Re_p = Particle Reynolds number
 S_t = Stokes number
 $T_{CD}^{(k)}$ & $T_{CD}^{(\varepsilon)}$ = inter-phase transfer for k and ε
 u_C = Velocity of continuous phase
 u_m = Centreline velocity
 u_o = Initial sand jet velocity
 u_s = Velocity of sand phase
 u_w = velocity of water phase
 u' = Axial velocity fluctuation
 v_s = Radial velocity of sand phase
 v_w = Radial velocity of water phase
 v', w' = Radial velocity fluctuations
 x = Axial distance from the water surface
 α = Particle volume fraction
 β = Blend factor
 $\nabla\phi$ = Gradient of a parameter
 ε_w = Rate of turbulent energy dissipation

- ϕ = Variable
- ϕ_{ip} = Value of a variable at a node
- ϕ_{up} = Value of a variable at the upwind node
- μ = Water molecular viscosity
- ν = Kinematic viscosity
- ν_{iC} = Continuous phase kinematic viscosity
- ν_{iD} = Dispersed phase kinematic viscosity
- ρ_C = Density of continuous phase
- ρ_s = Sand density
- ρ_w = Water density
- σ = Turbulent Schmidt number
- τ_s = Particle response time
- τ_s^* = Corrected particle response time

Chapter 3

Computational Investigation on Vertical Slurry Jets in Water

3.1 Introduction

Turbulent jets are commonly used in engineering applications such as waste disposals and industrial processes to enhance mixing processes and heat transfer. Single-phase turbulent jets have been studied for several decades. Detailed information about the mean and turbulent properties of single-phase jets are available in several books [Albertson et al., (1950); Abramovich (1963); Rajaratnam (1976); Fischer et al., (1979) and Lee and Chu (2003)]. Presence of sand particles as a second phase in water jets produces slurry jets and these are also referred as solid-liquid jets or particle-laden jets in the literature. Slurry jets can be found in many industrial and environmental applications such as in hydro-power systems, wastewater disposal, stirring vessels and marine bed capping. Theoretical study of the underlying physics of multi-phase flows is complicated. Consequently, understanding the dynamic interactions of particles and the surrounding water through experimental investigation and numerical modeling is important for engineering design.

Experimental studies of slurry jets have indicated that many parameters such as particle size, D , particle concentration, c_o , initial jet velocity, u_o , and nozzle diameter, d , are important. Influence of particles on the mean properties of the jets such as axial and radial velocities, particle distribution and jet spreading rate has been studied by many researchers [Brush (1962); Fan et al. (1990); Mazurek et al. (2002); Arai et al. (2003); Virdung and Rasmuson (2007) and Azimi et al. (2012)].

A paper based on the content of this chapter has been submitted for publication in the *International Journal of Multiphase flow*, as Azimi et al. (2012b)

Particles in slurry jets also affect the turbulent characteristics of the water-phase, known as turbulent modulation. Turbulent modulation of two-phase turbulent jets has been investigated by Tsuji et al. (1988); Gore and Crowe (1989 & 1991); Luo et al. (2005) and Azimi et al. (2008, 2011b).

Most of the laboratory experiments have been carried out to investigate slurry jets with low particle concentration (with an initial volume concentration $c_o < 1\%$) and relatively small particle sizes (see Table 3-1). In such dilute slurry jets, the effect of particle-particle interaction is negligible. In addition, in slurry jets with small particles, particle slip velocity is small and the inter-phase forces become negligible. While a number of experimental and numerical studies looked at dilute slurry jets and jets with small particles, less attention has been paid to highly concentrated slurry jets with a wide range of particle sizes.

Table 3-1: Experimental conditions under which previous two-phase solid-gas and solid-liquid turbulent jet investigations were conducted.

Experimental Study	Jet Type	d (mm)	x/d	u_o (m/s)	D (mm)	ρ_s (kg/m ³)	c_o (%)
Arai et al. (2003)	Solid-Liquid	5.0	15	1.84	0.389	2590	0.21
Azimi et al. (2011b)	Solid-Liquid	8.2-12.5	80	0.69	0.21-0.78	2540	60
Azimi et al. (2012)	Solid-Liquid	2-10	150	0.07-0.19	0.137-0.507	2540	60
Cerecedo et al. (2009)	Solid-Gas	12	15	15	0.05-0.1	2340	0.015
Fan et al. (1990)	Solid-Gas	42	20	15-25	0.075	1250	0.02-0.08
Hall et al. (2010)	Solid-Liquid	9-15.5	65	0.98-2.19	0.21	2540	5.5-12.4
Hardalupas et al. (1989)	Solid-Gas	15	30	11	0.04	2420	0.005-0.03
Jiang et al. (2005)	Solid-Liquid	5.5	50	0.56	0.075	1510	0.19
Modarress et al. (1984)	Solid-Gas	20	30	10.2	0.2	2290	0.04
Muste et al. (1998)	Solid-Liquid	47×4	49	0.83	0.5-0.6	2650	0.04
Parthasarathy & Faeth (1987)	Solid-Liquid	5.08	50	1.66-1.72	0.505	2450	2.4-4.8
Prevost et al. (1996)	Solid-Gas	10	45	20	0.05	2540	0.004
Sheen et al. (1994)	Solid-Gas	15	90	20	0.21-0.78	1020	0-0.43
Tsuji et al. (1988)	Solid-Gas	20	20	11-24	0.17-1.4	1020	0.05-0.2
Virdung & Rasmuson (2007)	Solid-Liquid	17	11.2	1.45-1.52	1.5	2500	0-1.9
Wang et al. (2009)	Solid-Gas	20	25	12.25	0.075-1.232	2450	0.14-0.24

For a range of low particle concentrations, Sheen et al. (1994) conducted a series of experiments to study the effect of particle size on solid-gas turbulent jets. Polystyrene particles of 210, 460 and 780 μm were used with the mass loading ratio (i.e. ratio of particle mass flux to the gas/fluid mass flux) ranging from 0 to 3.6 ($c_o \approx 0.43\%$). They found that for $x/d > 10$, the decreasing of the centerline axial velocity for the two-phase jet flow is smaller than that of the corresponding single-phase jet. They also reported that the turbulent intensity of the jet increases by increasing particle size and decreases by increasing particle concentration. Their results were consistent with observations of Tsuji et al. (1988). Experimental observations of Arai et al. (2003) on solid-liquid turbulent jets were also limited to dilute slurry jets ($c_o = 0.21\%$). They measured the axial and radial velocities of both phases close to the nozzle ($x/d = 15$ where d is the nozzle diameter). Experimental observations of Jiang et al. (2005) on dilute slurry jets ($c_o = 0.19\%$) with small particle size ($D = 75 \mu\text{m}$) indicated that the centreline velocity of sand-phase is higher than the water-phase and can be predicted as the summation of the water-phase velocity and particle settling velocity.

Difficulties arise in measuring the characteristics of slurry jets at large particle concentrations. Due to particle-particle and particle-liquid interactions, separation of two phases becomes very challenging for measurement techniques such as Particle Image Velocimetry. To the Author's knowledge, the highest particle concentration in a slurry jet at which sand-phase and water-phase were separately measured is the study of Parthasarathy and Faeth (1987). They employed a uniform particle size of 505 μm and initial volume fraction of $c_o = 2.4$ and 4.8%. These results are used to validate the present numerical model.

Some experimental investigations were successful in partially measuring the characteristics of highly concentrated slurry jets. Hall et al. (2010) were able to measure

sand-phase velocity and concentration of slurry jets with small particle size but, no turbulent measurements were made. Azimi et al. (2012) investigated the effect of nozzle size and particle size on the mean and turbulence of the frontal of highly concentrated slurry jets by measuring sand-phase velocity field. They found that the particle grouping effect enhances the axial velocity and changes the growth rate of the particle cloud.

It has been theoretically and experimentally established that the width of single-phase jets grows linearly with the axial distance of x from the nozzle [Abramovich (1963); Rajaratnam (1976); Fischer et al., (1979) and Lee and Chu (2003)]. Observations on the growth rate of particle cloud close to the nozzle indicated a linear relationship between the width of the particle cloud and x . This relationship becomes non-linear far from the nozzle and the growth rate decreases until the particle cloud reaches the swarm condition [Bush et al., (2003); Noh and Fernando (1993), and Azimi et al., (2012)]. In this condition the width of particle cloud remains constant and particles descend with their settling velocity. In order to properly study the growth rate of slurry jets, it would be useful to conduct experiments to cover larger values of x/d , since in most experimental investigations, measurements have been made for relatively small values of x/d (see Table 3-1). Numerical modeling could be effective in increasing the range of x/d .

Fewer attempts have been made to investigate experimentally the effect of particle concentration on slurry jets, since controlling the exact particle concentration and maintaining a uniform and proper mixture of particles can be a challenge. This difficulty can be resolved by employing a validated numerical model. Two-equation models such as $k-\varepsilon$ model have been developed to simulate more engineering related turbulent flows. Although, Large Eddy Simulation (LES) and Direct Navier-Stokes (DNS) models provide more accurate results on turbulence properties, they require much smaller cell size and time step for proper operation which directly increases the time and expense of

simulation. For engineering applications, working with two-equation models can save a lot of time and expense while still providing reasonable results if the model is properly validated with experimental data.

Several numerical studies have been carried out to simulate slurry jets by using two-equation models [Angst, (2001); Ochieng and Lewis (2006); Colaciti et al. (2007) and Azimi et al. (2011b)]. Virdung and Rasmuson (2007) used a numerical model to simulate dilute slurry jets (see Table 3-1 for detail). It was found that the CFD solver (Fluent 6.2) slightly under-estimated the water-phase centerline velocity in the vicinity of the nozzle and over-estimated the velocity further downstream. A previous numerical study performed by the authors (Azimi et al., 2011b) focused only on the effect of particle size on hydrodynamics of sand jets. This chapter is aimed at investigating the influences of other parameters such as, nozzle size, initial velocity, particle concentration and particle size on dilute and highly concentrated slurry jets. In addition, the present study attempts to numerically compute highly concentrated slurry jets and then use these results to calculate some of the integral properties of slurry jets such as entrainment coefficient and averaged drag coefficient.

This chapter is structured as follows. In section 2, the numerical model is validated with measurements found in the literature. For model validation, the simulated mean properties such as axial and radial velocities of sand-phase and water-phase, particle concentration and turbulent kinetic energy of the water-phase are compared with measurements. In section 3, a series of numerical experiments are performed to study the effects of nozzle size, particle concentration, particle size and initial velocity on the mean and turbulence characteristics of the jets. Conclusions of this numerical investigation are presented in section 4.

3.2 Model Convergence and Validation

3.2.1- Governing Equations and Modeling Parameters

Ansys CFX solver package with modified k - ε turbulent model was used in this study. In simulating particle-laden flows, both homogeneous or inhomogeneous models can be used depending on particle concentrations. For relatively high particle concentrations, where the particle-phase accelerates through the background flow, inter-phase forces are generated and the effects of particle motion on the water-phase become dominant. In these circumstances, the inhomogeneous model should be used. Employing inhomogeneous equations in numerical models involves inter-phase forces and slip velocities. On the other hand, homogeneous models are used for dilute systems and they neglect the influence of particle movement through the system.

The governing CFD equations and the validated magnitude of the inter-phase forces (i.e. drag, lift, added mass force, etc.) for simulation of the two-phase turbulent jets were presented in numerical study of Azimi et al. (2011b). The equation for turbulent kinetic energy k , and the equation for energy dissipation rate ε were employed to simulate water-phase and provide closure (Launder and Spalding, 1974). An algebraic equation known as the dispersed phase zero equation (Ansys, 2009) was applied to predict the sand-phase.

The turbulence kinematic viscosity of the sand-phase ν_s is correlated with the water-phase turbulent viscosity ν_w by the coefficient Sc known as turbulent Schmidt number ($\nu_w = Sc \nu_s$). To study the effect of turbulent Schmidt number, a sensitivity analysis was performed and Sc was compared with similar studies in the literature. Similar numerical cases of sand-jets with different turbulent Schmidt number, varying from 0.5-2.0 were performed by Azimi et al. (2011b). They found that the maximum

change on sand-phase velocity and concentration was less than 1.2%. A Schmidt number of 0.9 was used for this study and a widely used Schiller & Neumann inter-phase drag model was chosen for simulation (Wörner 2003).

3.2.2- Computational Domain and Mesh Analysis

Detailed information on the computational domain size and the jet characteristics is presented in Table 3-2. Three different computational domains were designed according to the measurement locations. A half-cylinder domain connected with 350 mm pipe was designed for the case number 1. The measured cross sections were close to the jet nozzle having the maximum distance of 7.5 cm. Consequently, a half-cylinder can provide enough resolution for the numerical simulation. Initial jet velocity normal to the nozzle was specified for the inlet boundary condition of both phases and the medium initial turbulent intensity was set for the water-phase ($I_o = 5\%$).

Table 3-2: Domain characteristics and mesh refinement properties of the numerical simulation.

Experimental Study	Mesh Resolution	Mesh Dimensions (mm)			Mesh Refinement (mm)				Number of Nodes	Number of Elements	Refinement Ratio (R_R)
		B_S	Max	Min	L_T	R_T	L_B	R_B			
Arai et al., (2003)	Coarse	2.5	2.5	0.5	0.50	2.5	1.00	30	268,023	1,251,920	1.25
	Medium	2.5	2.5	0.5	0.27	2.5	1.00	30	335,293	1,633,443	1.25
	Fine	2.5	2.5	0.5	0.27	2.5	0.86	30	415,536	2,092,244	1.25
Parthasarathy & Faeth (1987)	Coarse	50	50	5.0	1.00	2.5	5.00	30	182,679	874,136	1.50
	Medium	30	30	5.0	0.75	2.5	0.40	30	273,923	1,396,457	1.50
	Fine (Case 1)	30	30	5.0	0.70	2.5	2.85	30	412,276	2,198,016	1.50
¼ Ellipse	Very fine (Case 2)	10	10	2.5	0.35	2.5	2.50	50	416,996	2,246,079	---
Hall et al., (2010)	Fine ($R=9$ mm)	50	50	5.0	1.00	2.5	5.00	60	370,071	1,815,586	---
	Fine ($R=15.5$ mm)	50	50	5.0	1.00	2.5	4.00	60	347,160	2,060,155	---

According to the experimental condition of Parthasarathy and Faeth (1987), in the second validation test, the exact tank dimensions were modeled and the excess water was simulated to overflow from the domain to a reservoir. The outer boundary of the domain was set as wall boundary condition with an outlet boundary at the top of the domain. Similarly, the initial velocities of both phases were specified at the inlet boundary. As mentioned by Parthasarathy & Faeth (1987) the injecting pipe reached the fully-developed pipe flow condition and the initial turbulence intensity of the water-phase was set as 3.7% with the initial length scale same as the pipe diameter (Ansys, 2009).

Experimental study of Hall et al. (2010) was conducted in a large tank with dimensions of 210x125x116 cm. According to the memory limitation and the axisymmetric behaviour of the jets, the computational domain was reduced systematically to a smaller size (see Azimi et al. (2011b) for detail). The designed domain was relatively large in size compared to other cases. Consequently, to enhance the accuracy of simulation, a one-tenth cylinder domain was generated. Schematics of a slurry jet with computational boundary conditions, computational domain and element networks at the inlet of all three cases are illustrated in Figure 3-1. Opening boundary conditions were applied for the top and the outer boundary of the domain in cases number 1 and 3. In this boundary condition the flow is allowed to cross the boundary in either direction. For those cases that a portion of a domain was simulated, the symmetry boundary condition was chosen to model the symmetry plane.

Mesh refinement method was applied to enhance the local resolution of the computational domain. The uniform body spacing, B_s , was selected as an initial cell size of the entire domain. Then, the mesh was refined by introducing a new cell size and the radius of resolution expansion. Two spheres were specified for the local resolution at the top and the bottom of domains. The top sphere was designed with the cell size of L_T and

radius of R_T to increase the resolution of the initial part of the jets. The second sphere was located at the bottom of the domain and the cell size was reduced from B_s to L_B . The radius of expansion at the bottom of the domain, R_B , was selected based on the estimated width of the corresponding single-phase jets. Detailed information on the mesh resolution parameters are shown at Table 3-2. In all cases, the water density was 998 kg/m^3 and the sand density was set to 2540 kg/m^3 .

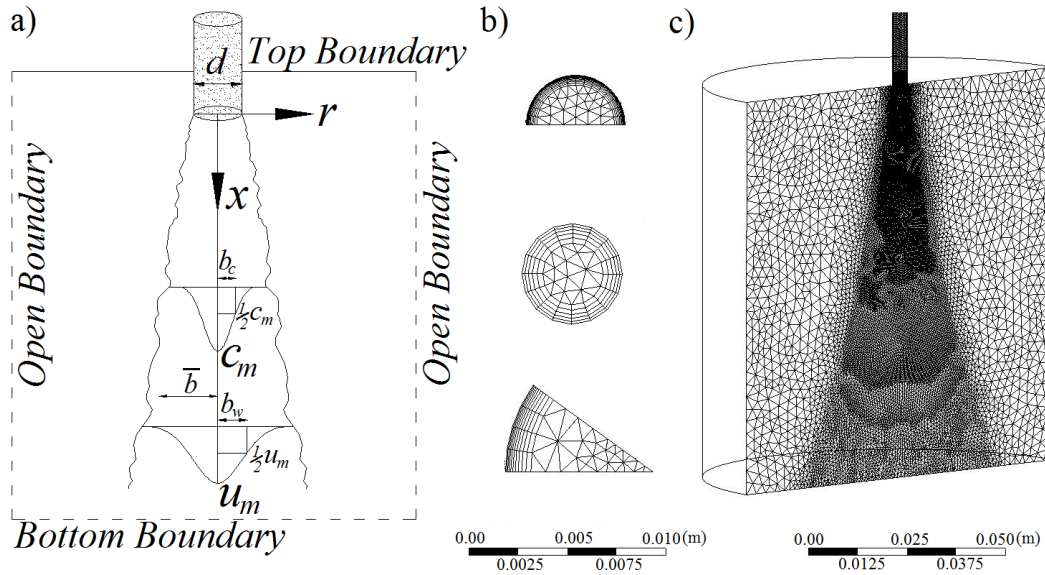


Figure 3-1: Schematic of a slurry jet with computational boundary conditions and computational domain. a) Definition sketch of a jet with coordinate system. b) Computational elements arrangement at the nozzle. Top: Experiment No. 1, Middle: Experiment No. 2, Bottom: Experiment No. 3. b) Half cylindrical computational domain with mesh resolution used for simulation of Experiment No. 2.

In order to find the resolution criteria, mesh sensitivity analysis was carried out for all cases. Domain structures were designed first by a reasonable number of nodes and labelled as Coarse mesh structure. Then the number of nodes increased systematically by the refinement ratio R_R , of 1.25 or 1.5 and generated the Medium and the Fine mesh structures. Mesh sensitivity has been analysed for case number 3 in the previous study (Azimi et al., 2011b), therefore the Fine mesh structure was directly applied for simulation. Mesh sensitivity analysis of the experiment No.1 (see Table 3-2) was shown

in this chapter. Figure 3-2 illustrates the simulated turbulent viscosity and the radial velocities of both phases which were monitored using different mesh structures and target levels. In this case the simulation iterated to reach the root mean square (r.m.s) residual of 10^{-4} , 10^{-5} and 10^{-6} .

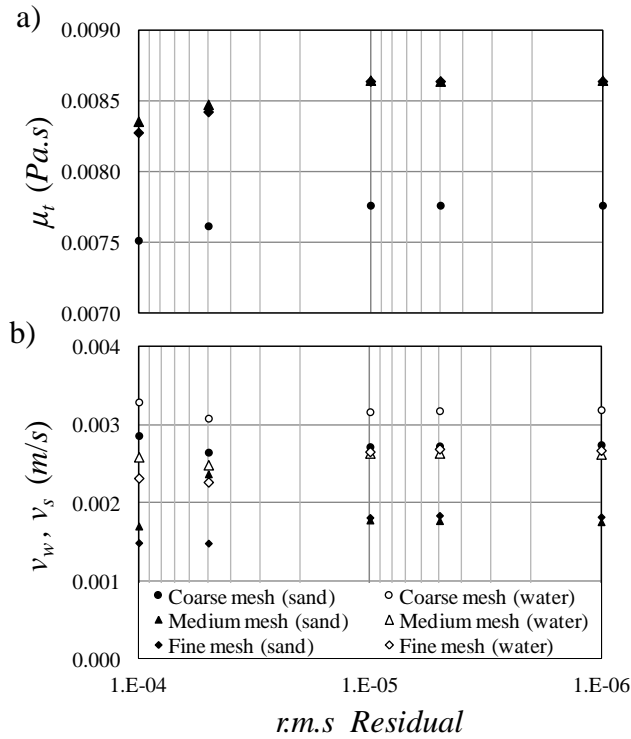


Figure 3-2: Mesh sensitivity analysis and correlations of the computed parameters with mesh structure and residual target level of Experiment No. 1. a) Turbulent viscosity. b) Radial velocities.

It can be seen from Figure 3-2 that the selected parameters varied with the target levels and reached the asymptotic regime as the computational residual became smaller. Moreover, the predicted results become similar as the mesh becomes finer. The total computational time to reach the highest target level was between 23-27 hours for each simulation using a computer work station that has two separate CPU each having eight processing core running at 3.00 GHz. The system has a random access memory of 16 GB and is capable of running up to eight simultaneous simulations. The convergence of the

numerical solution for all three cases is shown in Figure 3-3. The r.m.s residual of the water velocity in all directions was reduced at each time step. The best convergence (i.e., the lowest r.m.s residual) was found for case number two since the domain was smaller compared to the other setups.

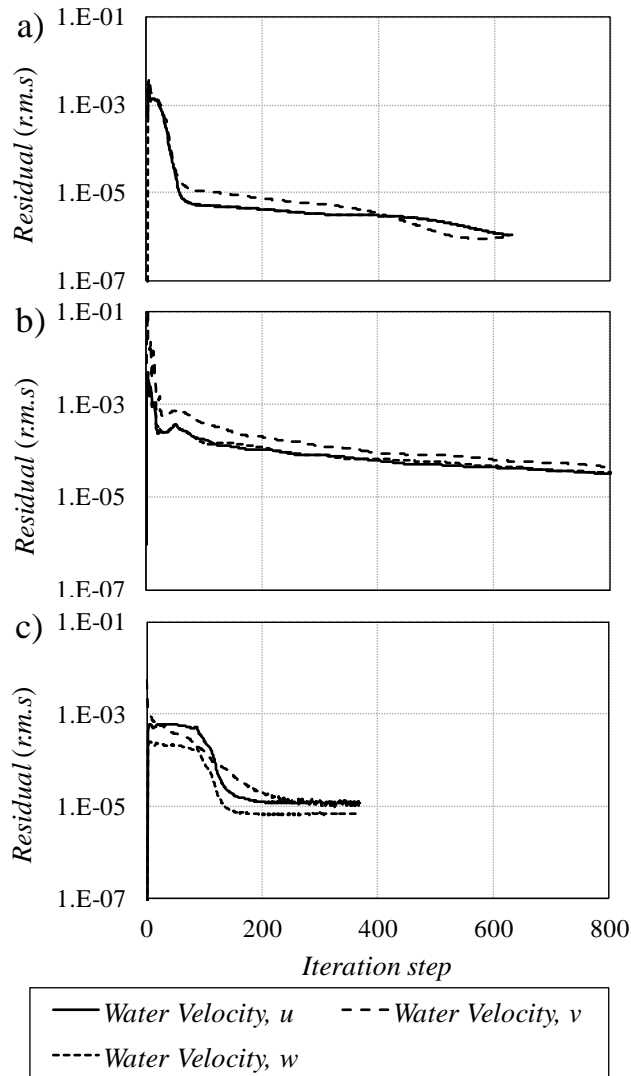


Figure 3-3: Effect of total computational time steps on the accuracy level of numerical simulation. a) Validation of axial and radial velocities, Experiment No. 1. b) Validation of turbulent kinetic energy per unit mass, Experiment No. 2. c) Validation of sand concentration, Experiment No. 3.

3.2.3- Effect of Mesh Resolution on Simulation Accuracy

Performance of the numerical model was evaluated by comparing the model outputs with three laboratory measurements. Effect of mesh resolution on the accuracy of the numerical results was also considered. Most of the CFD models are able to predict the velocity profile of the fully-developed pipe flow with high accuracy.

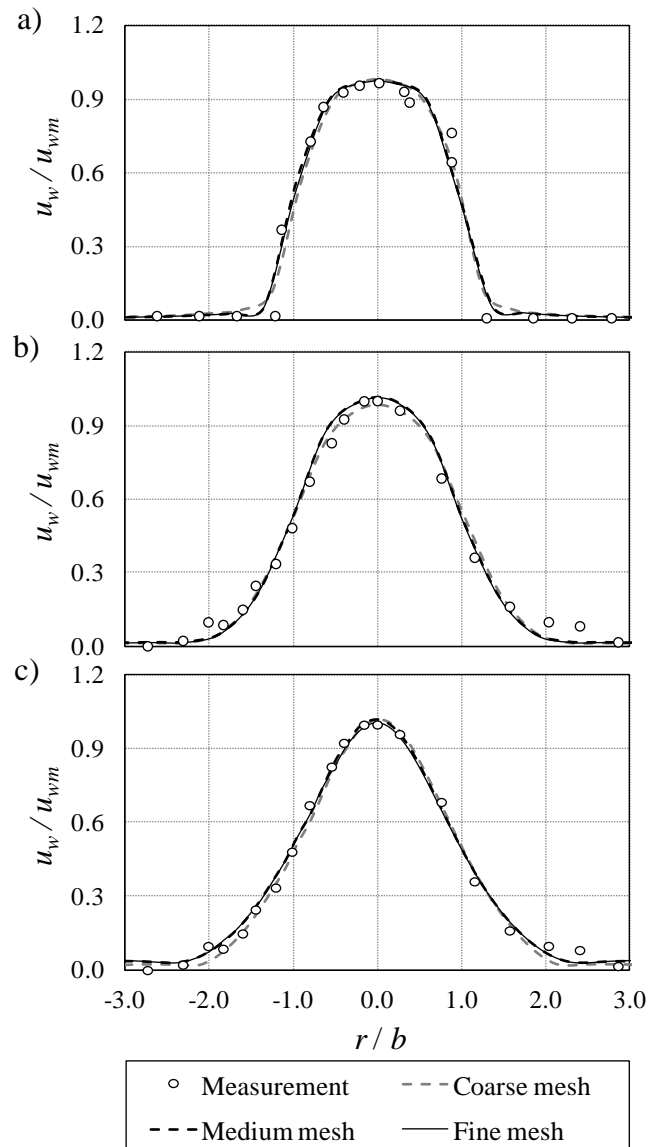


Figure 3-4: Comparison of the simulation outputs of the axial velocity using different mesh resolution with measurements of Experiment No. 1 (Arai et al., 2003) at three cross sections. a) At the injection pipe, $x/d = 0$. b) $x/d = 3$. c) $x/d = 15$.

The obtained simulation results of the fully-developed pipe flow were compared with the measurements to check the initial and boundary conditions of the model. Figure 3-4a shows the comparison of the numerical simulation results with the water velocity measurements of case 1 from Arai et al. (2003)-(see Table 3-2). In this figure, the axial velocity distribution of the water-phase, u_w , was normalized with the centreline velocity of the jet, u_m . Numerical results at the jet entrance obtained from different mesh structures were found to be similar since very small cell sizes were employed for all cases, i.e., $d = 10 - 18$ times of the cell size at the nozzle (see Table 3-2). Figure 3-4(b-c) illustrates the mean velocity properties at the locations of $x/d=3$ and 15. Comparing the obtained numerical simulation with the measurements indicates that the model predicted axial velocity accurately. Effect of mesh resolution on simulation of sand-phase axial velocity was found negligible.

Figure 3-5 shows the radial velocity distribution of water-phase, v_w , and sand-phase, v_s , normalized with the initial velocity of the jet, u_o (Arai et al., 2003). Considering the obtained radial velocity results it may be deduced that the model can provide relatively more accurate predictions of the water-phase than the sand-phase. The calculated bias error of simulation for sand-phase and water-phase at $x/d=3$ was -14.2% and +11.8%, respectively. At $x/d=15$, the model under-estimated the radial velocity of the two phases by -15.2% and -5.2%, respectively. Employing higher order closure model for the water-phase ($k-\varepsilon$ turbulent model) compared to the relatively simple model for the sand-phase (zero-equation model) may be the reason of having more accurate predictions for the water-phase than the sand-phase. Considering predictions close to the nozzle ($x/d=3$) it may be deduced that the domain with low mesh resolution was not able to predict the radial velocities at the trough (Figure 3-5a). It is interesting to note that the

mentioned shortcoming of the Coarse mesh became negligible at $x/d=15$, that is, the influence of the mesh resolution becomes less significant far from the nozzle.

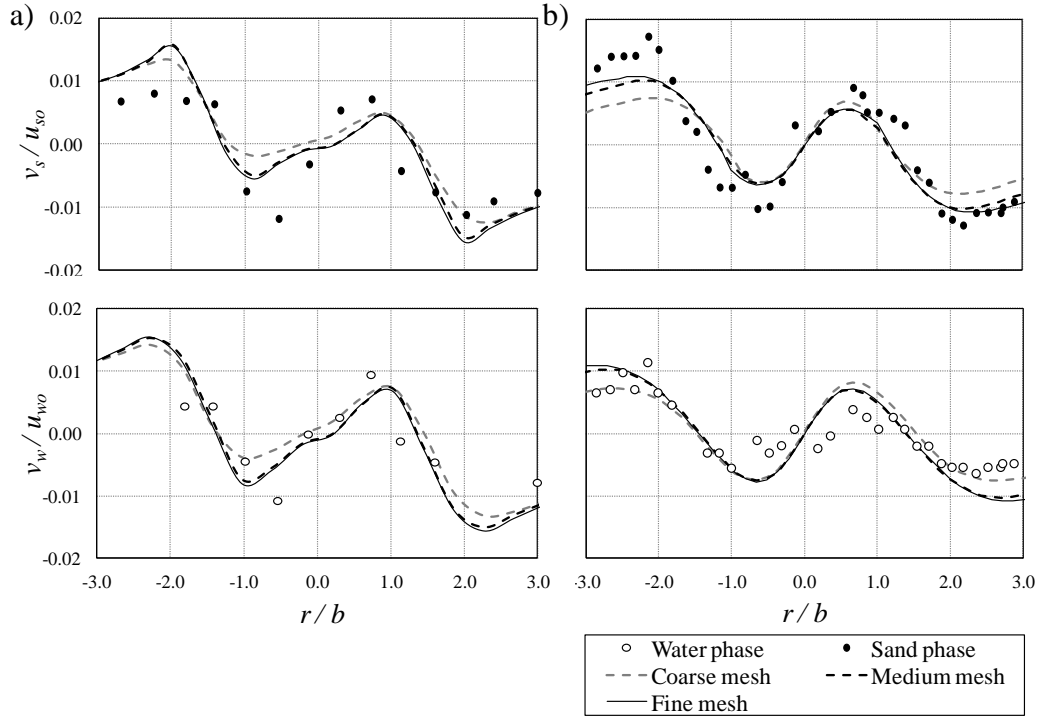


Figure 3-5: Comparison between numerical results and laboratory measurements of sand-phase and water-phase radial velocities of Experiment No. 1 (Arai et al., 2003). a) $x/d = 3$. b) $x/d = 15$.

Capability of the model to simulate sand-phase axial velocity and volumetric particle concentration was validated with the laboratory experiments of Hall et al. (2010). The simulation results of the mean properties of sand-phase at different cross sections ($x/d = 12.9, 25.8$ and 38.7) are shown in Figure 3-6. In this case, the radial distance from the jet axis, r was normalized with the half width of the jet, b (defined as the distance where the axial velocity is half of the maximum velocity) and the sand-phase axial velocity, u_s , was normalized with the centreline axial velocity, u_m . The obtained results presented in Figure 3-6 require mirror duplication to cover the negative abscissa axis since the $1/10$ cylindrical domain was employed for this case. Comparison of the obtained

numerical predictions with the measurements indicates that the model is capable of accurately predicting the sand axial velocity.

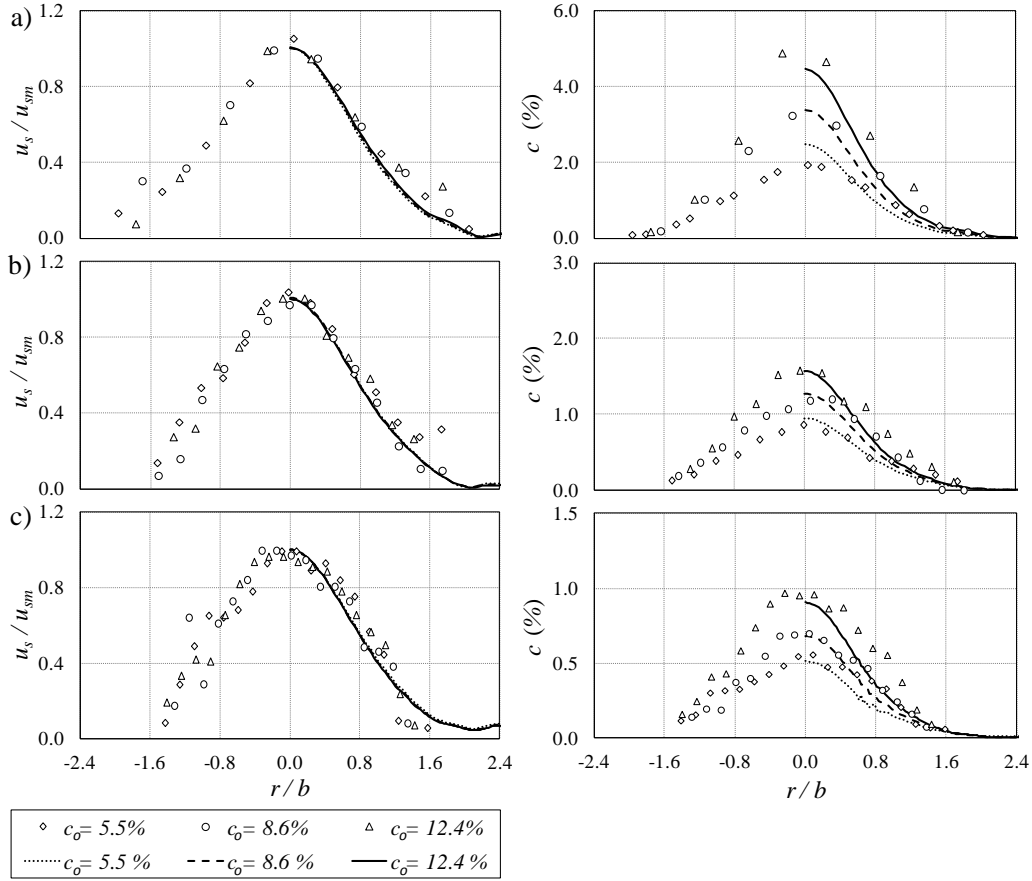


Figure 3-6: Model performance on prediction of the sand-phase axial velocity (Left) and the sand volumetric concentration (Right) of Experiment No. 2 (Hall et al., 2010) at three cross-sections. a) $x/d = 12.9$. b) $x/d = 25.8$. c) $x/d = 38.7$.

Volumetric concentration of the sand particles was computed at different cross sections and the model performance was evaluated with the laboratory measurements. The validated results are shown in Figure 3-6(a-c). Regarding the computed concentration profiles, it appears that the accuracy of predictions decreases with increasing c_o . With increasing c_o in slurry jets, effect of the particle-particle interaction becomes prominent and predictions deviate more from measurements. It was found that for highly concentrated slurry jets, the model predictions become less accurate close to the nozzle.

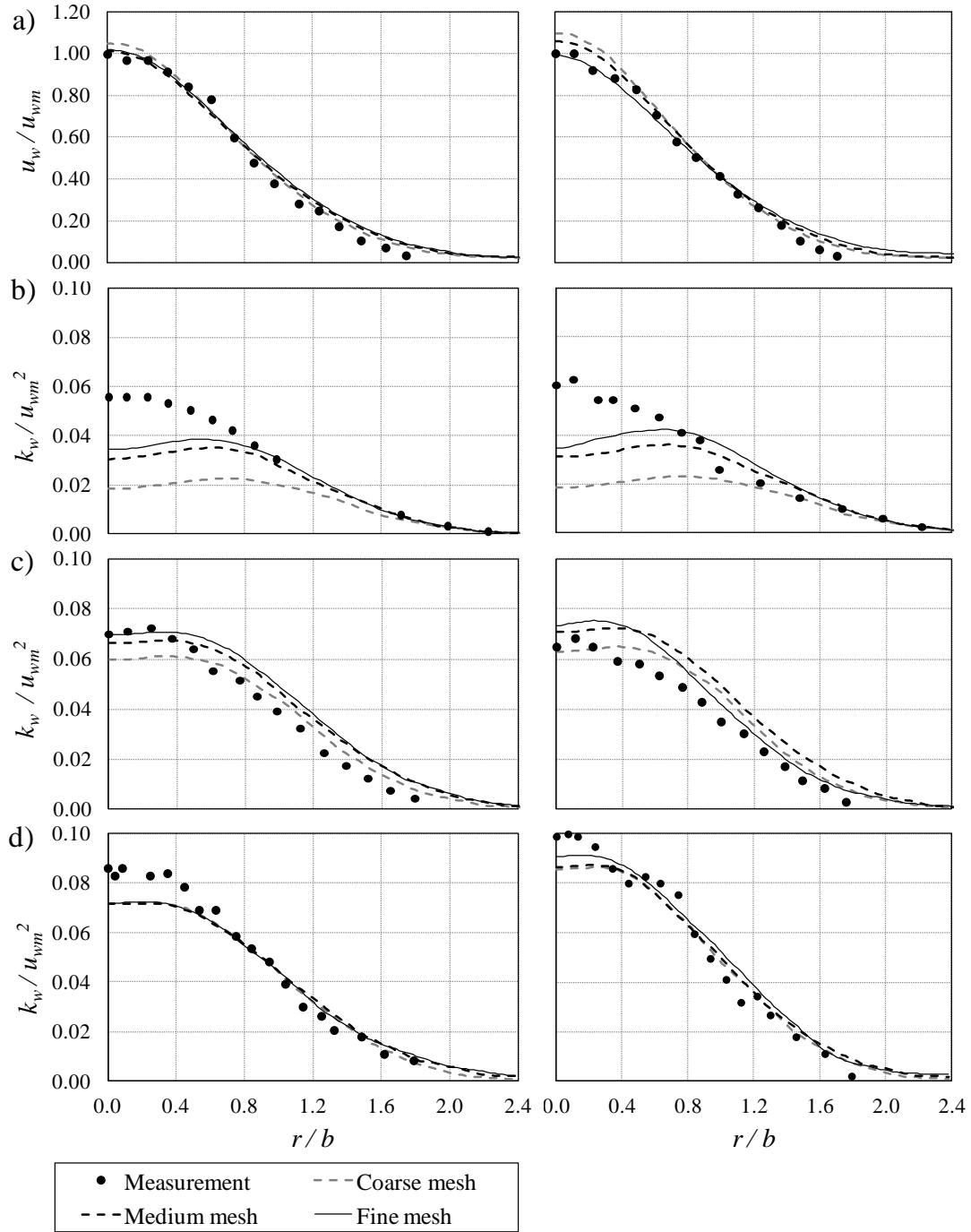


Figure 3-7: Comparison between model outputs and experimental observations of the normalized water-phase axial velocity and turbulent kinetic energy per unit mass (i.e., TKE) of Experiment No. 3 (Parthasarathy & Faeth, 1987) at three cross sections and two different initial concentration of $c_o = 2.4\%$ (Left) and $c_o = 4.8\%$ (Right). a) Axial velocity at $x/d = 16$. b) TKE at $x/d = 8$. c) TKE at $x/d = 16$. d) TKE at $x/d = 40$.

Reliable results were obtained at $x/d = 25.8$ which indicates that the jet spreading reduces the effect of particle-particle interactions. In general, the model predictions under-estimate the measurements by 10-15% and have the standard deviations between 8-20% which is reasonable considering the 15% standard deviation of measurements (Hall et al., 2010).

The simulated mean water- phase velocity and the turbulent kinetic energy (TKE) were validated with the experimental observations of Parthasarathy and Faeth (1987). Slurry jets with two initial volumetric particle concentrations of 2.4 and 4.8 percent were simulated. Figure 3-7 presents a comparison of numerical outputs with laboratory measurements. Effects of mesh resolution on the accuracy of the model results were also studied at three cross sections ($x/d = 8, 16$ and 40). Simulated results of the slurry jet axial velocities are shown in Figure 3-7a for both concentrations. By comparing the obtained results of the simulation for TKE close to the nozzle (i.e., $x/d=8$), we find that the resolution of the finest mesh was not enough to capture the peak value of k . Parthasarathy and Faeth (1987) compared their measurements with two of their numerical models and their models also under-estimated the peak TKE of the slurry jets.

Comparing the numerical results obtained from present simulation indicates that all mesh structures provided reliable results at $x/d=16$ and 40 (Figure 3-7c and d). Far away from the nozzle, as the slurry jets spread and the particle concentration reduces, the obtained computational results become more accurate. It was found that at $x/d = 40$, effect of mesh resolution becomes less important and model provided reliable predictions. The present model under-estimated the peak value of k by 15% regardless of the initial particle concentration (Figure 7d).

3.3 Results of Numerical Experiments

Accuracy of the numerical model to simulate the mean and turbulence properties of the slurry jets was evaluated in the validation part of this chapter. A series of numerical experiments were conducted by employing the validated model and varying the main parameters of the jet (nozzle size, particle concentration, particle size and initial velocity). The detailed flow characteristics of laboratory measurements and selected numerical simulations are shown in Table 3-3.

Performance of the model was tested by comparing the numerical results with laboratory measurements for the initial nozzle size of 5, 9 and 15.5 mm. In order to increase nozzle size range, an extra case (case d1) with the nozzle diameter of 3 mm was added to the numerical experiments. Validated simulations covered a relatively large range of initial particle concentration c_o , from 0.21 up to 12.4 percent. Since particle concentration can predominantly change the dynamics of slurry jets, eight numerical tests with the concentration range of 0.3 to 12 percent were chosen to study the effect of volumetric concentration of particles (see Experiment No. 5 (Series c) in Table 3-3).

The selected experimental studies had a narrow range of particle size variation ($D = 210, 389$ and $505 \mu\text{m}$). Since the balance between the length scale of the surrounding fluid and particle size plays a significant rule on the properties of slurry jets, two numerical cases with particle sizes of 100 and $780 \mu\text{m}$ were added to investigate the influence of particle size on slurry jets (see Experiment No. 6, (Series D) in Table 3-3). In order to investigate the effects of particle size and concentration on spreading of the jet, another series of simulations were performed for very dilute slurry jets ($c_o=0.3\%$) and small sand particles, $D=50-100 \mu\text{m}$ (see Series S in Table 3).

Table 3-3: Selected computational domain and the initial flow characteristics of laboratory measurements.

No	Experimental Study	Domain Size (cm)	Case Number	Nozzle Size		c_o (%)	D (μm)	u_o (m/s)	m_s (g/s)	m_w (g/s)	l_m (cm)	F_r	R_o
				d (mm)	Length (mm)								
1	Arai et al., (2003)	Half Cylinder $R=5$, $h=10$	---	5.00	350	0.21	389	1.84	0.2	36.0	68.8	6.68	9200
2	Parthasarathy and Faeth (1987)	41x91x53 (x, y, z)	I (d2, c4, D4, U4, S5)	5.08	350	2.40	505	1.66	1.90	32.7	19.0	5.98	8430
			II (c5)	5.08	350	4.80	505	1.72	3.80	32.7	13.8	6.20	8740
3	Hall et al., (2010)	Cylinder $\theta = 36^\circ$ $R= 15$ $h= 100$	B1	15.5	500	5.50	210	1.00	26.30	177.6	13.6	2.07	15500
			B2	15.5	500	8.60	210	0.98	40.55	168.8	11.0	2.02	15190
			B3	15.5	500	12.4	210	0.98	58.40	161.6	9.6	2.02	15190
			C1	9.00	150	12.2	210	2.19	43.20	122.3	16.4	5.94	19710
4	Numerical Experiment (Study the effect of nozzle size)	41x91x53 (x, y, z)	d1	3.00	350	2.40	505	1.66	1.90	32.7	14.6	7.78	4980
			d3	9.00	350	2.40	505	1.66	1.90	32.7	25.3	4.50	14940
			d4	15.50	350	2.40	505	1.66	1.90	32.7	33.1	3.42	25730
5	Numerical Experiment (Study the effect of particle concentration)	41x91x53 (x, y, z)	c1	5.08	350	0.30	505	1.66	0.24	32.7	52.4	5.98	8430
			c2	5.08	350	0.60	505	1.66	0.48	32.7	37.2	5.98	8430
			c3	5.08	350	1.20	505	1.66	0.95	32.7	26.5	5.98	8430
			c6	5.08	350	7.20	505	1.66	5.70	32.7	11.5	5.98	8430
			c7	5.08	350	9.60	505	1.66	7.60	32.7	10.2	5.98	8430
			c8	5.08	350	12.0	505	1.66	9.50	32.7	9.4	5.98	8430
6	Numerical Experiment (Study the effect of particle size)	41x91x53 (x, y, z)	D1	5.08	350	2.40	100	1.66	1.90	32.7	19.0	5.98	8430
			D2	5.08	350	2.40	210	1.66	1.90	32.7	19.0	5.98	8430
			D3	5.08	350	2.40	389	1.66	1.90	32.7	19.0	5.98	8430
			D5	5.08	350	2.40	780	1.66	1.90	32.7	19.0	5.98	8430
7	Numerical Experiment (Study the effect of initial velocity)	41x91x53 (x, y, z)	U1	5.08	350	2.40	505	0.40	1.90	32.7	4.6	1.44	2000
			U2	5.08	350	2.40	505	0.80	1.90	32.7	9.2	2.88	4000
			U3	5.08	350	2.40	505	1.20	1.90	32.7	13.7	4.32	6000
			U5	5.08	350	2.40	505	2.00	1.90	32.7	22.9	7.21	10000
8	Numerical Experiment (Study the spreading of the jet)	41x91x53 (x, y, z)	S1	5.08	350	0.30	50	1.66	0.24	32.7	52.4	5.98	8430
			S2	5.08	350	0.30	100	1.66	0.24	32.7	52.4	5.98	8430
			S3	5.08	350	0.30	210	1.66	0.24	32.7	52.4	5.98	8430
			S4	5.08	350	0.30	389	1.66	0.24	32.7	52.4	5.98	8430
			S6	5.08	350	1.20	100	1.66	0.95	32.7	26.5	5.98	8430
			S7	5.08	350	4.80	100	1.66	3.80	32.7	13.8	5.98	8430
			S8	5.08	350	12.0	100	1.66	9.50	32.7	9.4	5.98	8430

The jet centreline velocity, flow entrainment rate and turbulence level of slurry jets can be related to the jet initial momentum flux. The balance between u_o , nozzle size d , fluid absolute viscosity μ , and/or buoyancy can be shown by dimensionless parameters. Reynolds number, $R_o = \rho_w u_o d / \mu$ can be used to consider the effects of inertial force versus viscous force with ρ_w being the density of water. In addition, the balance between inertial force and gravitational force can be described by densimetric Froude number, $F_r = u_o / (gd(\rho_s - \rho_w) / \rho_w)^{1/2}$ with ρ_s being the density of sand and g being the gravitational acceleration. Initial velocities of the selected laboratory experiments were within 0.98 to 2.19 m/s. Numerical tests of series U were modeled to investigate the effect of inertial force on properties of slurry jets with jet initial velocity range of $0.4 < u_o < 2$ m/s (see Series U in Table 3-3 for details).

Computational domain and initial boundary conditions in all numerical experiments were consistent with the validated numerical simulation of the Parthasarathy and Faeth (1987) and the domain with Fine mesh structure was selected for simulation. The validated model with case I of Parthasarathy and Faeth (1987) was selected as a reference simulation with $d=5.08$ mm, $c_o=2.4\%$, $D= 505$ m and $u_o=1.66$ m/s. Effects of nozzle size, particle concentration, particle size and initial velocity were investigated by changing one of the parameters at a time while the other three parameters were kept constant. Hence, the numerical results of the reference simulation were presented in all analysis (d2=c4=D4=U4=S5).

3.4 Spreading of the Jet

It is generally accepted that the spreading of a single-phase water jet in water is linear with the distance from the nozzle x , and it is independent of nozzle diameter (Rajaratnam, 1976; Fischer et al., 1979; Lee and Chu, 2003). In some measurements, the half-width of the jet, b , was calculated as a distance where the axial velocity is $1/e$ of the

maximum velocity. The spreading rate, db/dx of a single-phase water jet has been measured by many researchers to range from 0.104 to 0.115 (Wang and Law, 2002).

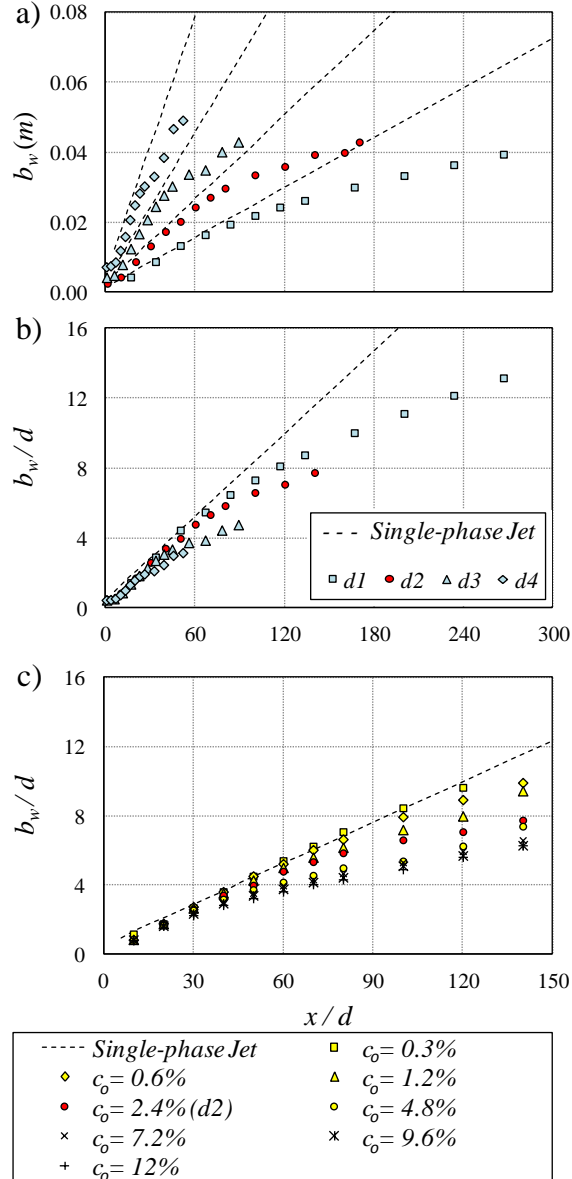


Figure 3-8: Effects of sand concentration and nozzle size on spreading of slurry jet. The spreading is calculated from the water-phase velocity profile width at $\frac{1}{2}$ the maximum velocity. a) Variation of the jet half-width along the axis of the jet for particle concentration of 2.4%. b) The jet spreading was normalized with nozzle diameter ($c_o=2.4\%$). c) Effect of sand concentration on the spreading of the jet for nozzle diameter of $d=5$ mm. Numerical results were compared with spreading of a single-phase water jets.

In this study, the half-width of the jet, b_w , was computed as a radial distance from the axis of the jet to the point where the water-phase velocity is half of the maximum water-phase velocity, u_{wm} (see Figure 3-1a). The half-width of the sand-phase b_s can be calculated similarly. Figure 3-8a shows the variation of the half-width along the axis of the slurry jet with different nozzle diameters. The dashed lines show the calculated spreading rates of a single-phase water jet (i.e., $db/dx=0.114$) as recommended by Wygnanski and Fiedler (1969).

As can be seen from Figure 3-8a, the spreading of slurry jets are similar to the single-phase jets close to the nozzle. This similarity is valid for $x/d < 40$ for large nozzle ($d=15.5$ mm) and $x/d < 100$ for small nozzle ($d=3$ mm). The axial distance from the nozzle and the half-width of the jet were normalized with the nozzle diameter. Variation of the normalized half-width with distance was plotted in Figure 3-8b. It was found that in contrast with single-phase water jet, the spreading of slurry jets along the axial distance shows nozzle size dependence. For $x/d < 40$, the spreading of slurry jet can be predicted by the single-phase correlation but, far from the nozzle (i.e. $x/d > 40$), effect of other parameters such as particle concentration and particle size on spreading of the jet must be taken into account. Variation of the jet spreading with particle concentration was studied and results were shown in Figure 3-8c. Comparison between the half-width of slurry jets having different concentrations with the spreading of single-phase water jets indicates that, slurry jets with very low concentration (i.e., $c_o=0.3\%$) the growth is almost similar to a single-phase water jet. The width of the jets becomes smaller with increasing the particle concentration. Figure 3-8c shows that the classical spreading rate value can be used for very dilute jets for x/d up to 120 whereas for slurry jets with 12% concentration, the classical value provides reasonable results only for $x/d < 20$ and deviation from single-phase formulation begins afterwards.

Figure 3-9 illustrates a typical velocity and concentration profiles of slurry jets with high volumetric concentration and large particle size (Case c8) at $x/d=160$. Velocities of both sand-phase and water-phase profiles were normalized with their corresponding centreline velocities and their half-width. The difference between normalized velocity profiles occurs at $r/b=1.4$. This indicates the buoyancy effect between two phases away from the axis of the jet. The concentration profile was normalized with c_m and b_w . Comparison between velocity and concentration profiles revealed that particles in slurry jets with high concentration tend to fall close to the centre of the jet and spread less than the velocity profile.

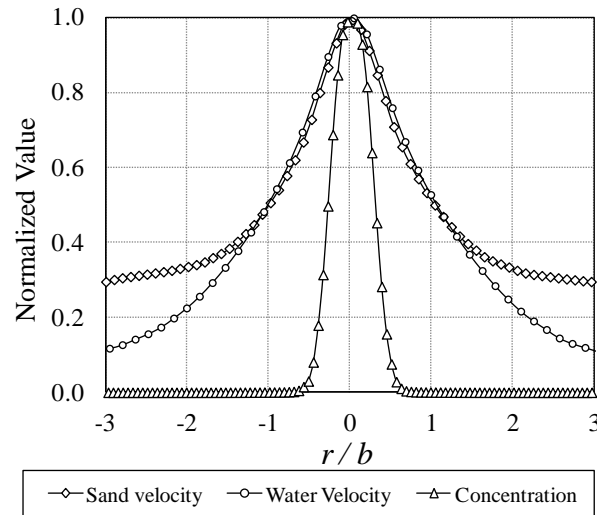


Figure 3-9: Normalized concentration, sand-phase and water-phase velocity profiles at $x/d=160$ for numerical test of c8 ($D=0.505$ mm and $c_o=12\%$). The radial distances of the sand-phase were normalized with b_s and the radial distances of the water-phase and particle concentration were normalized with b_w .

Effect of particle size and concentration on the spreading of particles can be investigated by comparing the ratio between the spreading rate of concentration b_c and the spreading rate of the water-phase velocity profile b_w . Defining λ as $\lambda=b_c/b_w$, the variation of λ for both single-phase and two-phase slurry jets has been studied by many

researchers (Papanicolaou and List, 1988; Hall et al., 2010). For single-phase jets and plumes, the spreading rate of the concentration profile was reported to be larger than that of the velocity profile. The value of λ was reported to be 1.2 for round jets (Fischer et al., 1979) and 1.19 for round plumes (Lee and Chu, 2003). For two-phase turbulent jets, Brush (1962) indicated that the width of the concentration profile is smaller than that of the velocity profile with the average value of $\lambda = 0.86$ for sand jets. Lima Neto et al. (2007) conducted a series of experiments on bubbly jets and found the λ value of 0.6 for bubbly jets. A typical λ value between 0.5-0.9 was also reported for bubbly jets by Socolofsky (2001). Recent experimental study on slurry jets with relatively small particles indicated that the spreading ratio can be close to one (Hall et al., 2010). Variation of λ can be function of many parameters such as particle size, particle concentration and relative density between two phases. For jets with very small and diluted particles (case S1-S2), the spreading ratio can approach the value recommended for single-phase jets. On the other hand, for jets with very large particles and highly concentrated slurry jets λ can be small (Case c7-c8).

Since the spreading rate can be influenced by both particle size and concentration, effect of each parameter was studied separately. Effect of particle size on slurry jets with moderate particle concentration ($c_o=2.4\%$) is shown in Figure 3-10a. It was found that, larger particles reduced the concentration half-width. Close to the nozzle ($x/d=10$), λ has a value between 0.7-0.8 but this value reduced in the axial direction and reached a plateau for $x/d>70$ with a value between 0.22-0.3. Variations of λ in this condition indicated that for relatively high concentration, effect of particle size can be negligible. In order to investigate the effect of particle size in slurry jet with very dilute concentration ($c_o=0.3\%$), variations of λ for jets having particle size ranging from 0.05 mm to 0.505 mm were plotted against the axis of the jet (Figure 3-10b). The spreading

ratio for very dilute slurry jets with small size particles was found to be similar to a single-phase plume, whereas for larger particles λ was significantly affected.

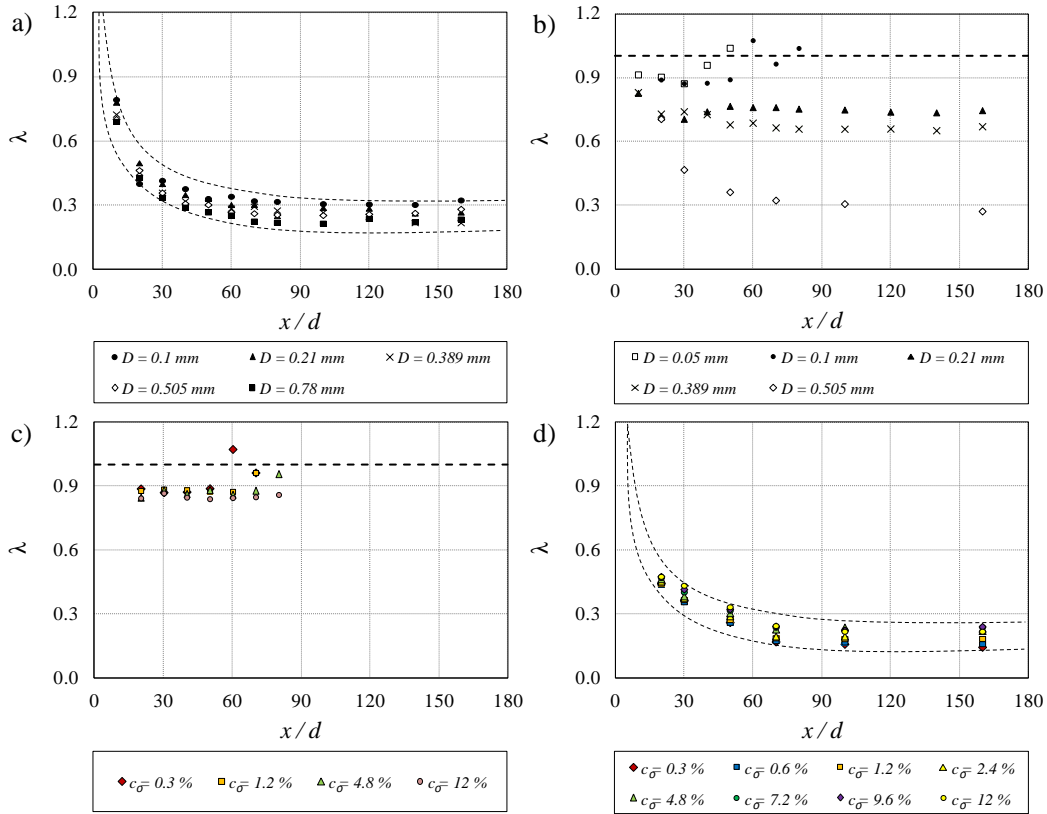


Figure 3-10: Variation of the ratio between the spreading rate of the concentration, b_c and the spreading rate of the water-phase velocity profiles, b_w (i.e., $\lambda=b_c/b_w$) along the axis of the jet with the effects of sand volumetric concentration and particle size on λ in slurry jets. a) Effect of particle size on λ for slurry jets with $c_o=2.4\%$ (Series D). b) Effect particles size on λ for very dilute slurry jets with $c_o = 0.3\%$ (Series S). c) Effect of particle concentration on λ for slurry jets with small particle size ($D=0.1$ mm). d) Effect of particle concentration on λ for slurry jets with relatively large particle size with $D=0.505$ mm (Series C).

Effect of particle size on the spreading rate of dilute slurry jets was found to be significant. For jets with small particles, λ reached a value close to unity whereas this value for jets with large particles can be as low as 0.3. Figure 3-10c shows the effect of particle concentration for slurry jets with small particle size ($D=100 \mu\text{m}$). It was found that the effect of particle concentration in this condition is negligible and λ was invariant

along the axis of the jet with the value of 0.88. Effect of c_o on the spreading ratio of slurry jets with large particle size ($D=505 \mu\text{m}$) is shown in Figure 3-10d. Close to the nozzle at $x/d=20$, the value of λ for slurry jets with 0.3% sand concentration was 0.44 whereas this value was 0.48 for slurry jets with $c_o=12\%$. Figure 10d shows that λ decreased from the nozzle and reached a plateau with the value between 0.17-0.245 after $x/d=70$.

3.5 Centreline Velocity

It is generally accepted that the centreline velocity of a single-phase jet decays at a rate of x^{-1} . Classical formulation for velocity decay of water jets was reported by Fischer et al. (1979) where u_m being the centreline velocity of the jet and u_o is the initial velocity.

$$u_m / u_o = 6.2/(x/d) \quad (3.1)$$

Presence of a second phase with different density can change the hydrodynamics of a jet to form a forced plume. In this case the buoyancy force dominates and plays as the main driver of the flow. The centreline velocity decay of a plume varies as $x^{-1/3}$. Papanicolaou and List (1988) introduced a formulation to predict the centreline velocity decay of a single-phase plume as:

$$u_m / u_o = 3.85B_o^{1/3} x^{-1/3} \quad (3.2)$$

where $B_o = (\pi d^2/4)u_o(\rho_s - \rho_w)g/\rho_w$ is the initial specific buoyancy flux. Centreline velocity decay of single-phase water jets and plumes has been measured by many researchers and somewhat different values have been reported for the coefficient in Equations 3.1 and 3.2. Those proposed coefficients for both jets and plumes were listed by Wang and Law (2002). The extent to which a jet starts to behave as a plume can be predicted by the

length scale of l_m (Fischer et al., 1979) defined as $l_m = M_o^{3/4} / B_o^{1/2}$ where $M_o = (\pi d^2 / 4) u_o^2$ is the initial specific momentum flux. The momentum length scale of l_m was calculated for all simulations (see Table 3-3).

Centreline velocities of both sand-phase and water-phase of slurry jets obtained from laboratory measurements are compared with simulation results and velocity decay of single-phase jet and plumes (Figure 3-11). According to the calculated momentum length scale l_m , all slurry jets behaved like plumes after a maximum distance of 0.19m from the nozzle (see Table 3). As can be seen from Figure 3-11, observations of Hall et al. (2010) fall in plume-like regime where $x/l_m > 1$ and those sand-phase centreline velocities decay almost at the rate of $x^{-1/3}$. The observations of Parthasarathy and Faeth (1987) fall in jet-like regime ($x/l_m < 1$) and those centreline water-phase velocities decay at the rate of x^{-1} . Effect of particle size on the variation of centreline velocity for a dilute slurry jet with $c_o=2.4\%$ is shown in Figure 3-11. It was found that, for $0.1 \text{ mm} < D < 0.78 \text{ mm}$, particle size has little impact on velocity decay and slurry jets with smaller particle sizes decay at a slightly faster rate. Far from the nozzle, the centreline velocity can reach a constant value of particle group fall velocity.

Azimi et al. (2012) measured the particle group fall velocity of the frontal of sand jets ($c_o=60\%$). They found that the particle group fall velocity was five times the settling velocity of individual particles. The curve fit of velocity decay along the axis of the jet for simulation results of series D ($c_o=2.4\%$) is shown in Figure 3-11. The proposed formulation is valid for the range of $10 < x/d < 170$ and gives the value of 0.114 m/s for the centreline velocity at one meter from the nozzle which is 1.6 times of the settling velocity of individual particles.

$$u_{wm} / u_{wo} = 0.04[2(x/d)^{-1/3} + (x/d)^{-1}] \quad (3.3)$$

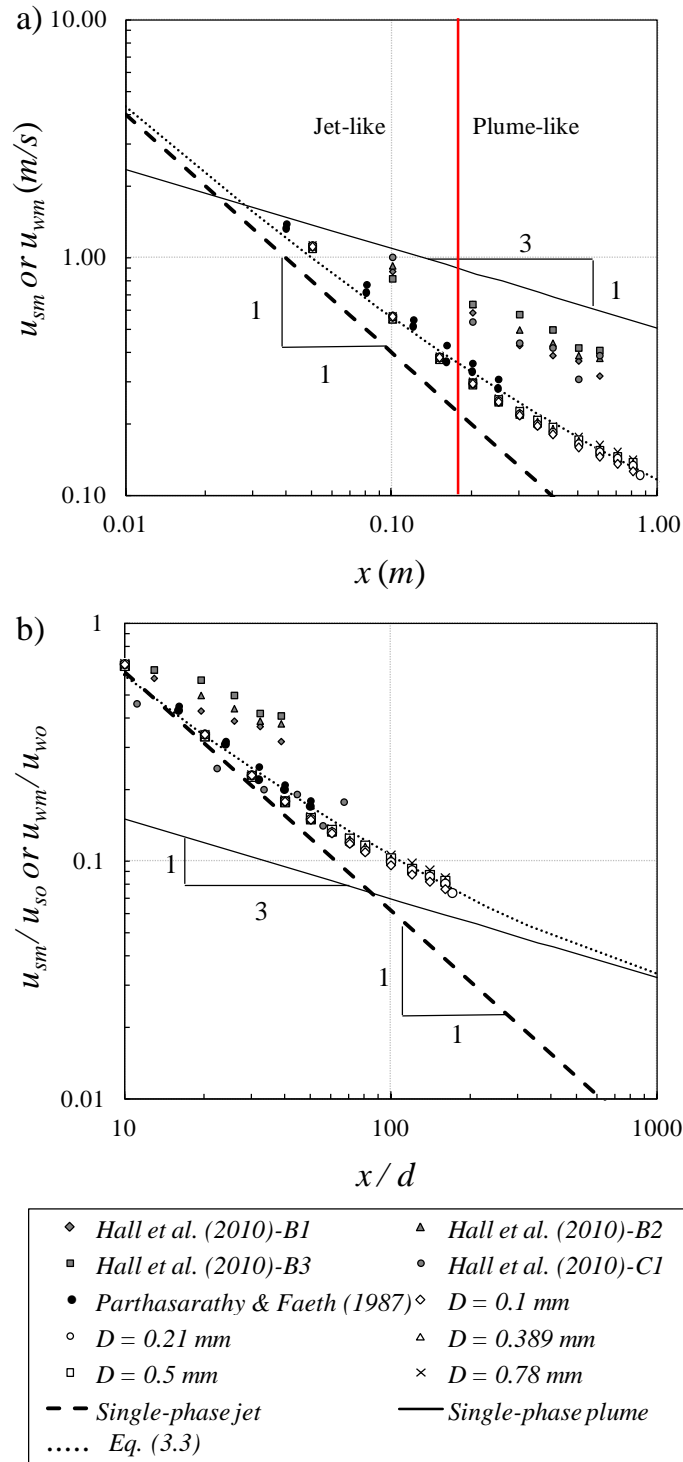


Figure 3-11: Variation of the sand-phase and water-phase centerline velocities of slurry jets along the axis of the jet. a) Velocities along the axis of the jet were compared with those single-phase water jets and plumes. b) Axial distance was normalized with nozzle diameter and centerline velocities were normalized with the initial velocity of the jets.

Effects of nozzle size and initial velocity on the centreline velocity of slurry jets were investigated and the results are plotted against the axial distance from the nozzle in Figure 3-12a. Velocity decay of a single-phase jet and plume was also plotted for comparison. Depending on the nozzle size and initial velocity of the jet, centreline velocity of slurry jets decays at a rate of $x^{-\gamma}$ where $1/3 < \gamma < 1$.

Centreline velocity of slurry jets with relatively low initial velocity (case U1, $l_m=4.6$ cm) decays at a rate of $x^{-1/3}$ similar to a single-phase plume. On the other hand, centreline velocity of slurry jets with large nozzle size and high initial velocity (case d4, $l_m=33.1$ cm) decays at a rate of x^{-1} similar to a single-phase jet.

Figure 3-12b shows the decay of the centreline velocity normalized with the initial jet velocity and the axial distance normalized with nozzle diameter. The difference in the variation of the centerline velocity indicates that other parameters may affect this velocity. Strong correlation was found by employing Froude number to generalize the velocity decay of slurry jets along the axis of the jet.

Increasing the initial particle concentration causes an increase in the sand-phase mass flux which enhances the potential energy of the system. The excess potential energy contributed by particles causes an increase on the mean velocity of the water-phase through the effect of inter-phase drag. The obtained results from computational simulation indicate that the water-phase centreline velocity increased with increasing particle concentration. Figure 3-12c shows the decay of the water-phase centreline velocity normalized Froude number, F_r . As can be seen from this figure, the normalized water-phase centreline velocity of slurry jets with different particle size, nozzle size and initial velocity collapsed in a single curve. The general formulation for modeling the centreline velocity was shown in Eq. 3.4.

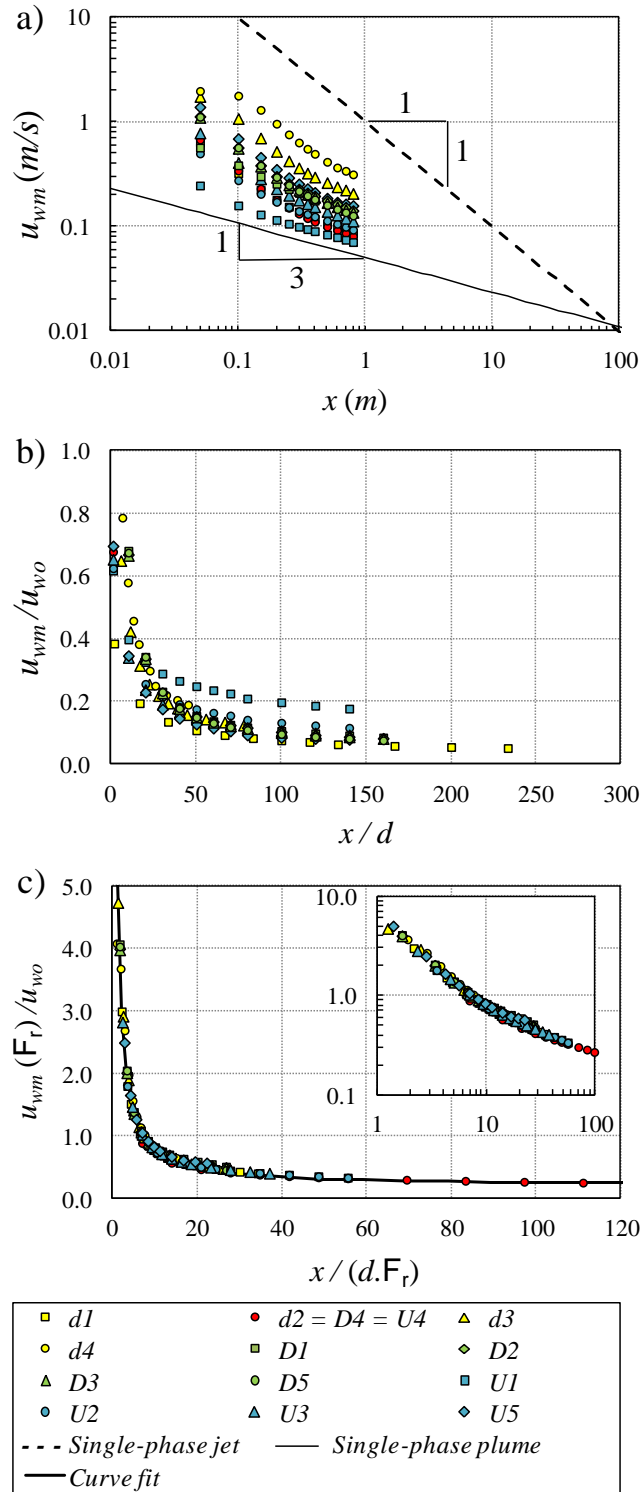


Figure 3-12: Correlations of the water-phase velocity along the axis of the jet with the effects of nozzle size variation (Series d), sand particle size variation (Series D) and initial velocity variation (Series U). a) Variation of the centerline velocity with distance from the nozzle. b) Variation of the normalized centerline velocity with normalized axial distance. c) Correlations of the centerline velocity of the water-phase with Froude number, F_r .

Particle concentration can also impact on the rate of velocity decay as shown in Figure 3-13a. As can be seen from this figure, the centreline velocity decay of dilute slurry jets ($c_o < 1\%$) is similar to single-phase jets, whereas centreline velocity of particle-laden jets with relatively high concentration decays similar to single-phase plume at the rate of $x^{-1/3}$. Normalized centreline velocities of slurry jets of Series c were plotted against normalized distance. This indicates that the classical velocity decay formulation for single-phase water jets (Eq. 3.1) is suitable for prediction of u_{wm} for dilute slurry jets.

In order to generalize the decay of u_{wm} for slurry jets with high sand concentration, effect of both F_r and c_o were included in the prediction and the following curve fit was found to be a suitable model for estimating the centreline velocity of a high concentrated slurry jets (see Figure 3-13c):

$$\frac{u_{wm} F_r}{u_o} = \frac{2}{3} c_o^{2/5} \left(\frac{x}{d F_r} \right)^{-1/3} + 3 \left(\frac{x}{d F_r} \right)^{-1} \quad (3.4)$$

The R.H.S of the proposed formulation consists of two parts. The first part is correlated with the velocity decay of a single-phase plume and the second part shows the effect of particles on the centreline velocity. Considering the second part of the proposed formulation to predict the centreline velocity of slurry jets, provides prediction results with an accuracy of 20% for $x/(dF_r) > 40$. As the distance from the nozzle increases, the error of prediction decreases.

Far from the nozzle at $x/(dF_r) = 100$ the single-phase formulation under-estimates the centreline velocity by 11%. Second part of the proposed formulation can be used to consider the effect of particles far from the nozzle. This part plays an important role in slurry jets with high particle volumetric concentration.

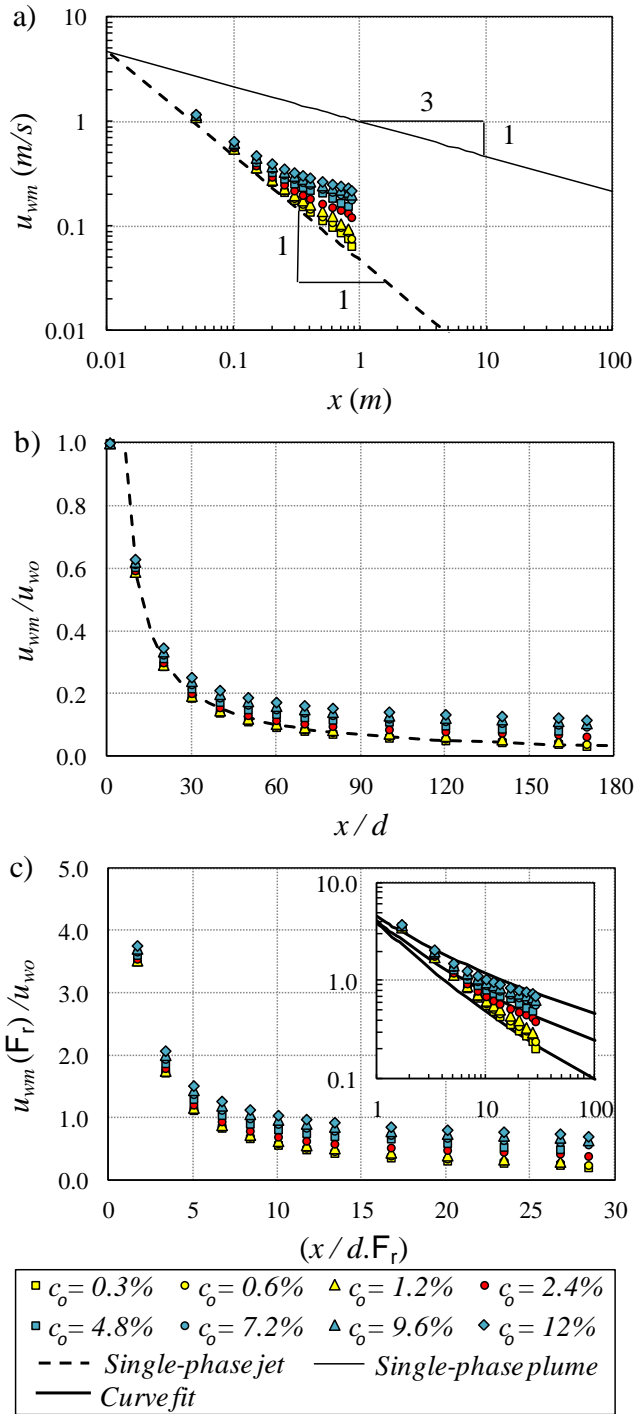


Figure 3-13: Correlations of the water-phase velocity along the axis of the jet with the effects of sand volumetric concentration (Series c). a) Numerical results were compared with the centerline velocity decay of a single-phase water jet and plume. b) Variation of the normalized centerline velocity with normalized distance from the nozzle. c) Centerline velocity of the water-phase was normalized with Froude number, F_r .

Centreline velocity of water jets and plumes can be studied in general form by incorporating the normalized distance of x/d and the normalized velocity of u_m/u_o in form of $M_o^{1/2}/(xu_m)$ (Wang and Law, 2002). Figure 3-14a shows the variation of $M_o^{1/2}/(xu_m)$ with x/l_m . By considering the value of l_m , jet-like and plume-like regimes can be identified. In jet-like regime ($x/l_m < 1$), u_m decays with x^{-1} which makes $M_o^{1/2}/(xu_m)$ invariant with x/l_m . By employing the classical equation for single-phase water jets (Eq. 3.1), the constant value of $M_o^{1/2}/(xu_m)$ in log-log scale becomes -0.844. Figure 3-14a shows that in plume-like regime, u_m decays at a slower rate.

A comparison between slurry jets and single-phase water jets indicates that, the decay of slurry jets follows the same trend as single-phase jets but, in plume-like regime the decay of slurry jets is slower than single-phase plume. Decay of centreline concentration in both jet-like and plume-like regimes was shown in Figure 3-14b. The averaged particle concentration \bar{c} at a cross-section can be computed by employing the following integration.

$$\bar{c} = \frac{2}{b_c^2} \int_0^{\bar{b}_c} c r dr \quad (3.5)$$

where c is the volumetric concentration of sand particles and \bar{b}_c is an indicator for the width of the jet where $\bar{b}_c = 2b_c$. Concentration variation in single-phase jets indicated that in jet-like regime, the averaged concentration decays at the rate of x^{-1} , whereas in plume-like regime \bar{c} decays at a faster rate. Since in a single-phase plume, concentration spreads even faster than velocity ($\lambda > 1$), the cross-section averaged concentration decays dramatically. Therefore, in plume-like regime, the growth rate of c_o/\bar{c} becomes larger than the growth rate of x/d , which causes a growth in the normalized value of $(c_o Q_o)/(x \bar{c}$

$M_o^{1/2}$) shown in Figure 3-14b. Particle concentration in slurry jets spreads much slower than the water phase with $\lambda < 1$, and the averaged concentration changes slightly along the jet axis. A balance between the normalized distance and the decay rate of particle concentration indicates that the normalized value of $(c_o Q_o) / (\bar{c} M_o^{1/2})$ decreases along the axis of the jet and the decay rate becomes faster for slurry jets with higher concentration.

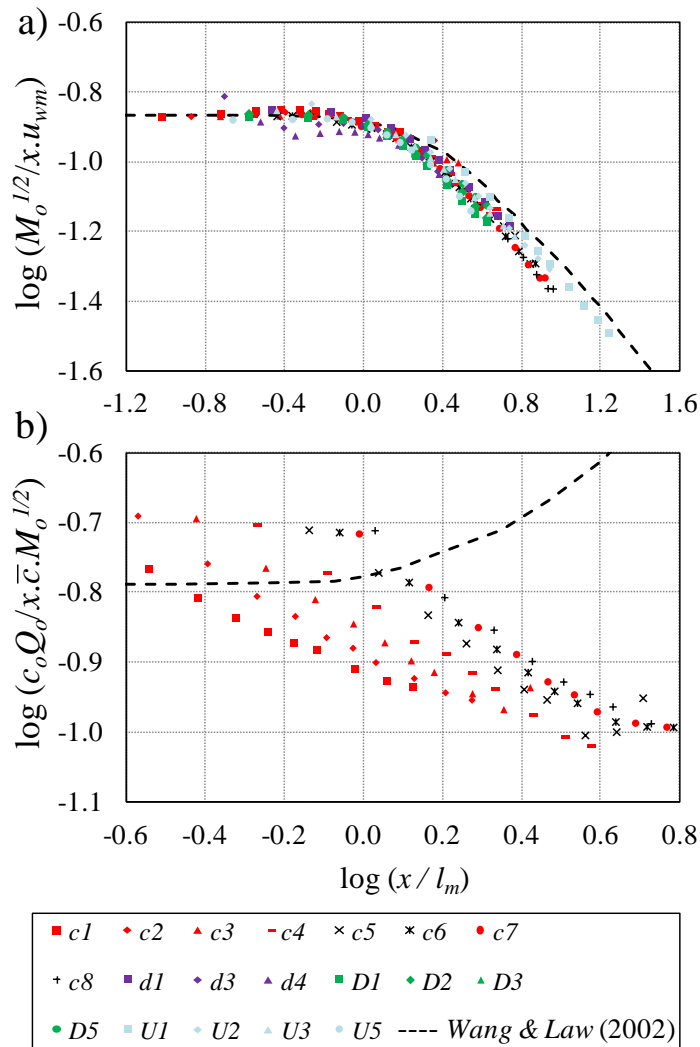


Figure 3-14: Centerline decay of the water-phase velocity and the mean sand concentration along the axis of the jet. Computational results were compared with proposed curve fit for buoyant jets used by Wang and Law (2002). a) Variation of the centerline water-phase velocity with x/l_m in log-log scale. b) Variation of centerline volumetric concentration with x/l_m in log-log scale.

3.6 Ambient Entrainment of Slurry Jets

It is generally known that jets and plumes entrain the surrounding fluid. Both sand-phase and water-phase mass fluxes of any section can be calculated by integrating velocity and concentration profiles at these cross-sections.

$$m_s = \rho_s \int_0^{\bar{b}_c} c u_s 2\pi r dr \quad (3.6)$$

$$m_w = \rho_w \int_0^{\bar{b}_c} (1-c) u_w 2\pi r dr \quad (3.7)$$

where m_s and m_w are the sand-phase and water-phase mass fluxes, respectively, u_s and u_w are the velocities of sand-phase and water-phase.

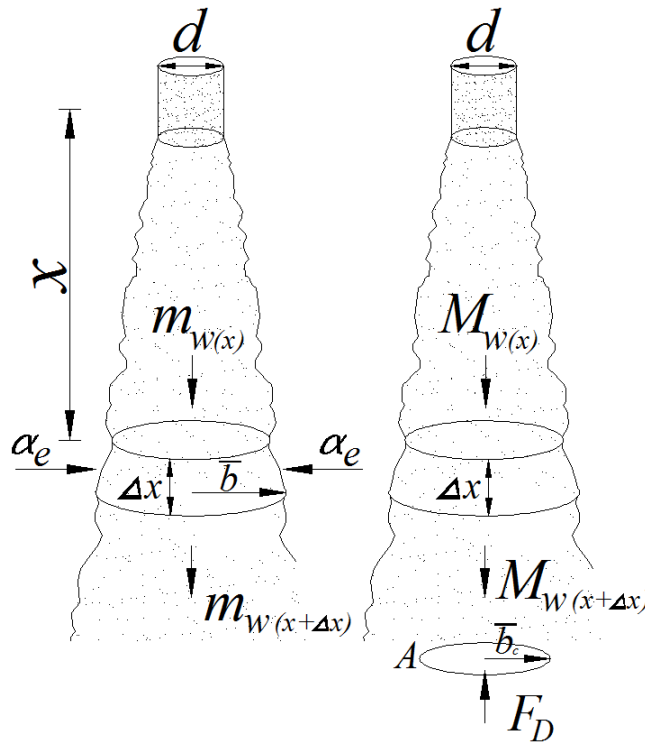


Figure 3-15: Schematic of the change on the mass and momentum fluxes of slurry jets in differential form for prediction of a) Entrainment coefficient and b) Averaged drag coefficient of the particle cloud along the axis of the jet.

By calculating the change in the water-phase mass flux m_w , in a disk-shaped control volume with a thickness of dx (see Figure 3-15a), the entrainment coefficient of the water-phase α_e , can be calculated by the following equation.

$$\frac{dm_w}{dx} = 2\pi \frac{d}{dx} \rho_w \int_0^{\bar{b}} (1-c)u_w r dr = 2\pi \rho_w \bar{b}(\alpha_e u_{wm}) \quad (3.8)$$

For single-phase water jets List (1982) summarized the values of α_e for a round jet and proposed a value of $\alpha_e = 0.0535$. For single-phase jets, the entrainment coefficient is constant along the axis of the jet since the width of the jet grows linearly with x and centreline velocity decays at x^{-1} . Variations of the entrainment coefficient of slurry jets with x/d and effect of particle concentration on α_e are shown in Figure 3-16.

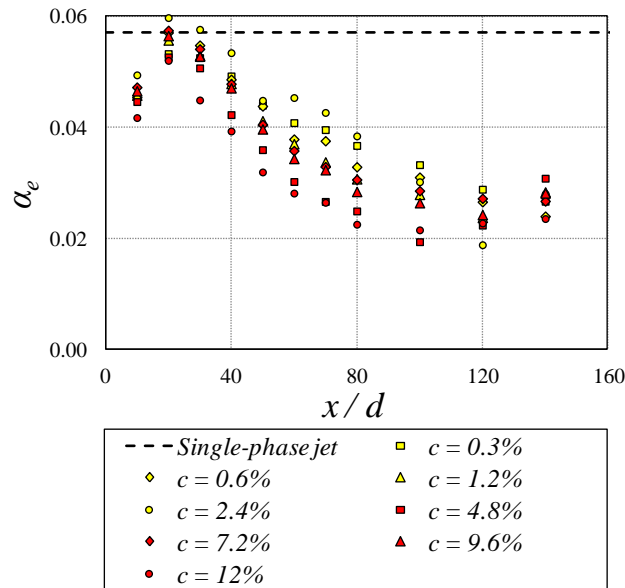


Figure 3-16: Effect of sand volumetric concentration on variation of entrainment coefficient along the axis of the jet. The computed entrainment coefficients were compared with the entrainment coefficient of a single-phase water jet.

Since in slurry jets u_{wm} decays at a slower rate with x and the growth rate of the width of the jet decreases with increasing particle concentration (see Figure 3-8c), the

calculated entrainment coefficient of slurry jets becomes smaller than the corresponding single-phase jet and varies along the axis of the jet. It was found that the entrainment capability of slurry jets reduced by particle concentration and far from the nozzle ($x/d > 120$) the value of entrainment coefficient reached a plateau with a value of approximately 50% of the α_e of single-phase water jets.

The entrainment velocity is usually normalized with the centreline velocity at that section. Since the decay of axial velocity in slurry jets is strongly correlated with many parameters such as, nozzle size, particle size, initial velocity and sand concentration (see section 3.2), a comprehensive comparison of the entrainment value of slurry jets can be carried out by normalizing the entrainment velocity with u_o . The computed entrainment coefficient in this method is referred to as the absolute entrainment coefficient, α_o .

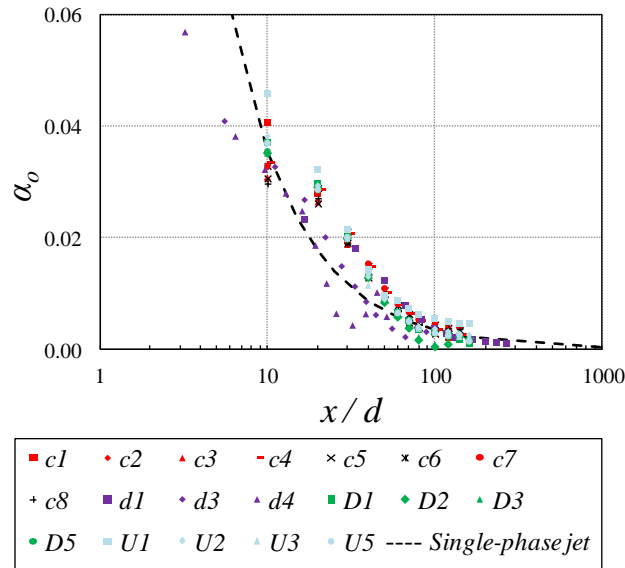


Figure 3-17: Effects of sand volumetric concentration, nozzle size, sand particle size and initial velocity on variation of the absolute entrainment coefficient, α_o along the axis of the jet. The absolute entrainment coefficient of slurry jets were compared with α_o of a single-phase water jet.

Figure 3-17 shows the impact of jet parameters on the entrainment capability of slurry jets with x/d . The absolute entrainment coefficient of a single-phase jet was computed and plotted as a reference for comparison. Figure 3-17 shows a strong nozzle size dependence on the absolute entrainment coefficient close to the nozzle ($x/d < 40$). Slurry jets with small nozzle size ($d=3$ mm) have higher entrainment capacity than a single-phase water jet whereas jets with larger nozzles entrain less flow into the jet. As can be seen from Figure 3-17, the mixing properties of the jet enhances by addition of the second phase in the water jet. It was found that α_o of slurry jets has higher values than the corresponding single-phase water jets for $x/d < 80$ and beyond that region the absolute entrainment coefficient of slurry jets is almost equal to that of the single-phase water jets.

3.7 Drag Reduction of Group Particles

The averaged drag force F_D , exerted by the surrounding fluid on particles at each cross-section can be computed by balancing the change in the momentum flux of the water-phase in a disk-shaped control volume. Schematic of the change in the momentum flux and forces exerted on a disk-shaped control volume for computing the averaged drag coefficient is illustrated in Figure 3-15b.

$$F_D = M_w(x + \Delta x) - M_w(x) \quad (3.9)$$

Momentum fluxes of water-phase M_w at each cross-section can be computed by integrating velocity and concentration profiles. The size of the disk-shaped control volume was set large enough to neglect the addition of the water-phase momentum from the sides of the disk.

$$M_w = \rho_w \int_0^{\bar{b}} (1 - c) u_w^2 2\pi r dr \quad (3.10)$$

The averaged drag coefficient at each cross-section along the axis of the jet can be calculated for a disk with a thickness of Δx equal to D by employing the following equation.

$$F_D = \frac{1}{2} \rho_w C_D^* \int_0^{\bar{b}_c} 2\pi r c (u_s - u_w)^2 dr \quad (3.11)$$

In order to compare the averaged drag coefficient of particles in a disk-shaped control volume computed from Eq. (3.11) with the drag coefficient of a single particle, the computed drag force can be divided by the estimated number of particles in control volume and it can be calculated as:

$$N = \frac{\pi \bar{b}_c^2 \bar{c} \Delta x}{\pi D^3 / 6} \quad (3.12)$$

where the bar signs on b and c denotes those parameters being averaged over the entire cross-section. By averaging the integral of the product of concentration and velocity over the cross sectional area of particles and introducing the N in equation (3.12), the relative drag coefficient of C_D can be defined as:

$$F_D = \frac{1}{2} \rho_w \frac{\pi D^2}{4} \frac{N}{\pi \bar{b}_c \bar{c}} C_D \int_0^{\bar{b}_c} 2\pi r c (u_s - u_w)^2 dr \quad (3.13)$$

The averaged drag coefficients of particles at different cross-sections were computed by equation (3.13), and the results were plotted against Reynolds number R , defined as

$$R = \frac{\rho_w [(\bar{u}_{s(x)} + \bar{u}_{s(x+\Delta x)}) - (\bar{u}_{w(x)} + \bar{u}_{w(x+\Delta x)})] D}{2\mu}$$

(3.14)

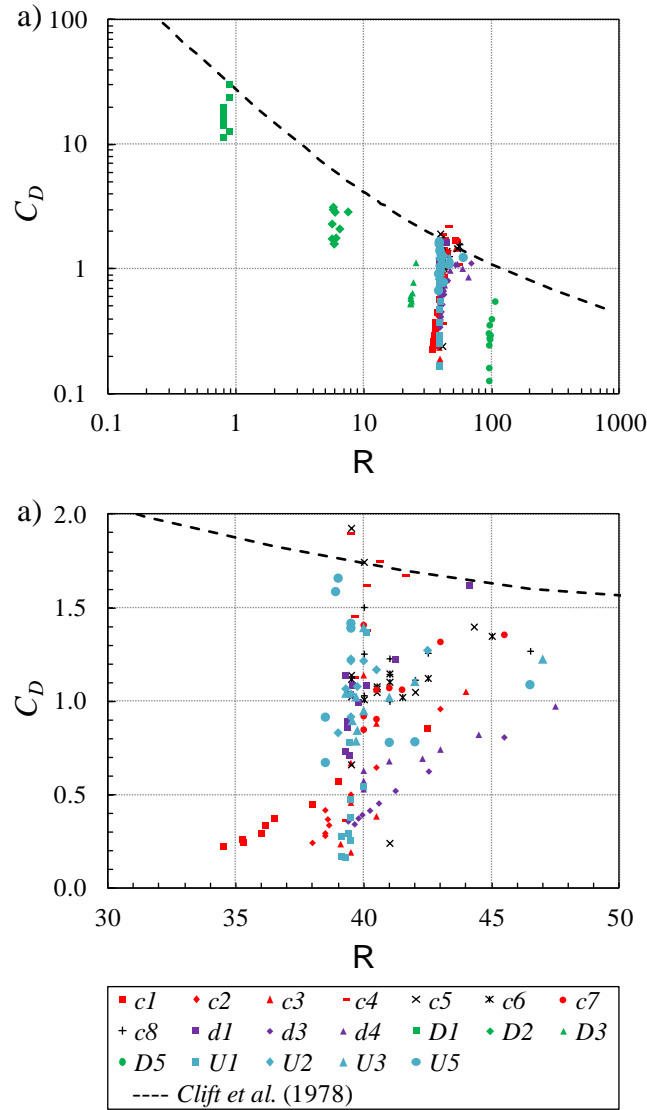


Figure 3-18: Effects of sand volumetric concentration, nozzle size and sand particle size on variation of the averaged drag coefficient with Reynolds number, R . a) Variations of the averaged drag of particle cloud with R in logarithmic scale. b) Effects of particle concentration, nozzle size and initial velocity of the jet on variation of C_D with R .

Figure 3-18a shows the variation of the averaged drag coefficient of particles with R . Variation of drag coefficient with R for a spherical particle, according to the classical work of Schiller and Naumann (Wörner, 2003), is plotted as a reference in Figure 3-18a. As can be seen, close to the nozzle ($x/d=10$) the averaged drag coefficient of particle cloud has similar value with individual particles, but grouping effect becomes

significant as particles descend far from the nozzle. For slurry jets with small particle size (e.g., case D1), descent of particles occur in a region close to laminar condition (i.e., $R \approx 1$). In this regime, grouping effect can significantly reduce C_D from 13.5, close to the nozzle, to 3.8 at $x/d=120$. For slurry jets with relatively large sand size ($D = 0.78$ mm), C_D was reduced from 0.72, close to the nozzle, to 0.25 at $x/d=120$. Effect of particle concentration on the drag coefficient of particle is shown in Figure 3-18b. It was found that particle concentration can reduce the averaged drag coefficient as particles tend to travel in the wake generated by the frontal particles. As can be seen from Figure 3-18b, grouping effect in particle cloud at high Reynolds number (case D5) can significantly reduce the averaged drag coefficient of particle groups.

3.8 Turbulence Characteristics of Slurry Jets

Effects of nozzle size, particle size and particle concentration on the turbulent characteristics of slurry jets along the axis are shown in Figure 3-19. Variation of turbulent kinetic energy (TKE) of the water-phase along the axis of the jet was shown in Figure 3-19a. Several numerical simulations of single-phase water jets with different nozzle sizes were performed to compute the values of TKE. The centreline turbulent kinetic energy of slurry jet k_w at each cross-section was normalized with TKE of the single-phase water jet, k_{w0} . As can be seen from Figure 3-19a the computed TKE increases with nozzle diameter. The value of k_w at the nozzle is equal to that of the single-phase jet ($k_w/k_{w0}=1$). For slurry jets with small nozzle diameter ($d=3$ mm), k_w increased by 6% at $x/d=25$. For relatively larger nozzle size ($d=15.5$ mm) k_w increases by 20% at the same location ($x/d=25$).

A turbulent length scale can be defined as $l=k_w^{3/2}/\varepsilon$ where ε is the rate of energy dissipation (Pope, 2000). The defined turbulent length scale can be normalized with the most energetic length scale of turbulence ($l=0.0385x$) defined by Wygnanski and Fiedler

(1969). It was found that the turbulent length scale of l is three times larger than the integral length scale of A with the value of $0.1155x$ ($db/dx=0.114$). This value indicates that the largest eddy in the jet can be as large as the jet half-width, b . This ratio was found to be almost constant along the axis of the jet at $x/d > 40$ and invariant with the nozzle size.

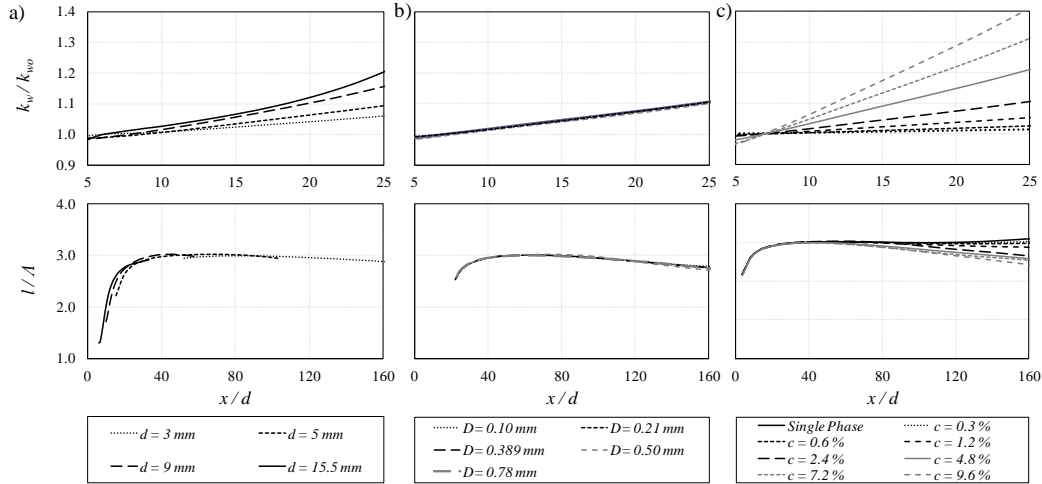


Figure 3-19: Effect of nozzle size, sand particle size and sand volumetric concentration on the normalized turbulent kinetic energy per unit mass and normalized turbulent length scale. a) Effect of nozzle size. b) Effect of particle size. c) Effect of sand volumetric concentration.

Variation of the normalized TKE and length scale with particle size are shown in Figure 3-19b. By considering the simulated results of series D, it can be deduced that the CFD model may not be able to simulate the effect of particle size on the turbulence of slurry jets, since no variations on k_w and l/A were found by particle size. Effect of particle concentration on TKE and turbulent length scale was studied and variations of those parameters along the axis of the jet are plotted in Figure 3-19c. It was found that particle concentration can increase k_w significantly. At $x/d=25$, the water-phase TKE of the slurry jet with $c_o=2.4\%$ (i.e., case d2=c4=D4=U4=S5) increased by 10% from the TKE at the

nozzle, whereas for slurry jet with higher concentration ($c_o=9.6\%$) TKE was found to be 38% higher than k_{wo} .

The excess potential energy of particles due to gravity can transform to the kinetic energy of the mean flow. The growth of turbulent level by the effect of particle concentration can be explained by the formation of wakes generated behind relatively large particles (Gore and Crowe, 1989). According to this hypothesis, the kinetic energy of mean flow can transfer to turbulent kinetic energy of the system with relatively higher rate. The normalized turbulent kinetic energy along the axis of the jet can be described by the following equation.

$$k_w / k_{wo} = 0.0023c_o(x/d) - 0.016c_o + 1 \quad (3.15)$$

The computed correlation coefficients, of all curves were between 0.97-0.99. By increasing the initial particle concentration, more particles are released into the system and consume more energy through their eddy circulations. The amount of work done by particles increases with increasing particle concentration and this elevates the energy dissipation rate. Effect of c_o on the size of turbulent length scale has shown that the length scale ratio of l/λ begins to deviate from single-phase curve at $x/d = 60$, (Figure 3-19c). Far from the nozzle ($x/d > 160$) this ratio was found to be around three for dilute slurry jets and it was reduced to 2.43 for slurry jets with high particle concentration ($c_o=9.6\%$). Relatively small eddy size in this condition (i.e. $l=0.0935x$) may be due to the smaller inter-particle spacing in highly concentrated slurry jets.

Contour plots of the computed turbulent viscosity of the sand-phase, $\mu_{t(s)}$ were shown in Figure 3-20. Effect of particles volumetric concentration on the turbulent viscosity of the sand-phase can be studied using those contour plots. It was found that slurry jets with higher particle concentration generate higher turbulent viscosity.

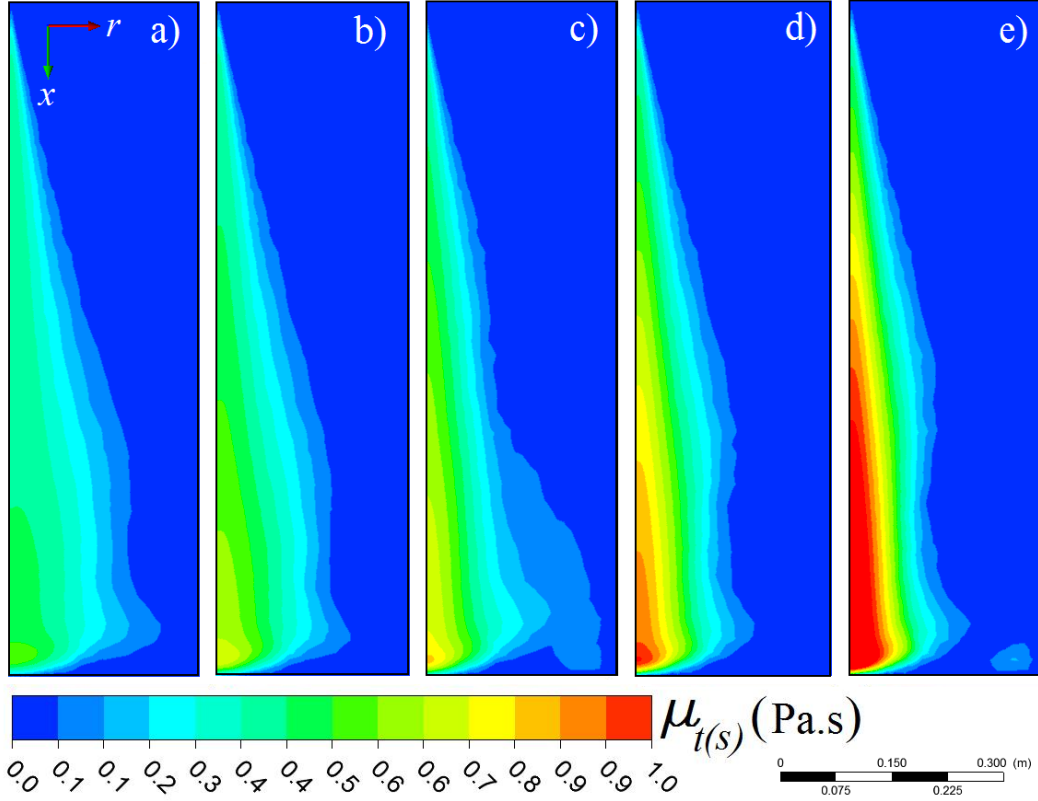


Figure 3-20: Contour plots of the computed turbulent viscosity of the sand-phase, $\mu_{t(s)}$ show the effect of particles volumetric concentration on $\mu_{t(s)}$. a) $c_o=0.3\%$, b) $c_o=1.2\%$, c) $c_o=2.4\%$, d) $c_o=4.8\%$ and e) $c_o=12\%$.

Turbulent shear stresses of sand-phase and water-phase can be calculated from the simplified mass and momentum equations of both phases. Continuity equation of both phases in cylindrical coordinate system can be written as

$$\frac{\partial(\bar{c}\bar{u}_s)}{\partial x} + \frac{1}{r} \frac{\partial(r\bar{c}\bar{v}_s)}{\partial r} = 0 \quad (3.16)$$

$$\frac{\partial[(1-c)\bar{u}_w]}{\partial x} + \frac{1}{r} \frac{\partial[r(1-c)\bar{v}_w]}{\partial r} = 0 \quad (3.17)$$

where v_s and v_w are radial velocities of sand-phase and water-phase, respectively. The bar sign on u and v denotes those parameters being averaged over time. Momentum equation

of both phases can be simplified by assuming steady-state condition, no swirl motion and using the boundary-layer approximation (Rajaratnam, 1976).

$$\rho_s \bar{u}_s \frac{\partial(\bar{c}\bar{u}_s)}{\partial x} + \rho_s \bar{v}_s \frac{\partial(\bar{c}\bar{u}_s)}{\partial r} = -\frac{\rho_s}{r} \frac{\partial}{\partial r} (rc\overline{u'_s v'_s}) + \rho_s cg \frac{\Delta\rho}{\rho_w} - F_D \quad (3.18)$$

$$\rho_w \bar{u}_w \frac{\partial[(1-c)\bar{u}_w]}{\partial x} + \rho_w \bar{v}_w \frac{\partial[(1-c)\bar{u}_w]}{\partial r} = -\frac{\rho_w}{r} \frac{\partial}{\partial r} (rc\overline{u'_w v'_w}) + F_D \quad (3.19)$$

Using the continuity equations in simplified jet equations and considering the drag as the main inter-phase force, turbulent shear stress of both phases can be computed (Rajaratnam, 1976). To reduce numerical errors of computations, 1000 data points were extracted from velocity and concentration profiles at each cross section which increased the resolution of integration to $\Delta x \approx 0.1$ mm. A five-point stencil scheme was used for calculating the derivatives of axial and radial velocities (Morton and Mayers, 2005).

$$\frac{\partial\phi}{\partial x} = \frac{-\phi_{i+2} + 8\phi_{i+1} - 8\phi_{i-1} + \phi_{i-2}}{12\Delta x} + O(\Delta x^4) \quad (3.20)$$

where ϕ_i is the value of velocity or concentration at point i . The computed water-phase turbulent shear stress of cases c4 and c5 was normalized with u_{wm} and results are plotted against the normalized radial distance at two cross-sections of $x/d=16$ and 40 (Figure 3-21). Computed results are compared with the slurry jet measurements of Parthasarathy and Faeth (1987) at $x/d = 16, 40$. At $x/d=16$. The simplified numerical model performs well for $0 < r/x < 0.06$ but a deviation between measurements and computed results was observed after the peak value (see Figure 3-21a). Parthasarathy and Faeth (1987) introduced two numerical schemes to model $\overline{u'v'}$ but, that deviation from measurements was also observed in their numerical results. Predictions of $\overline{u'v'}$ were in agreement at $x/d=40$.

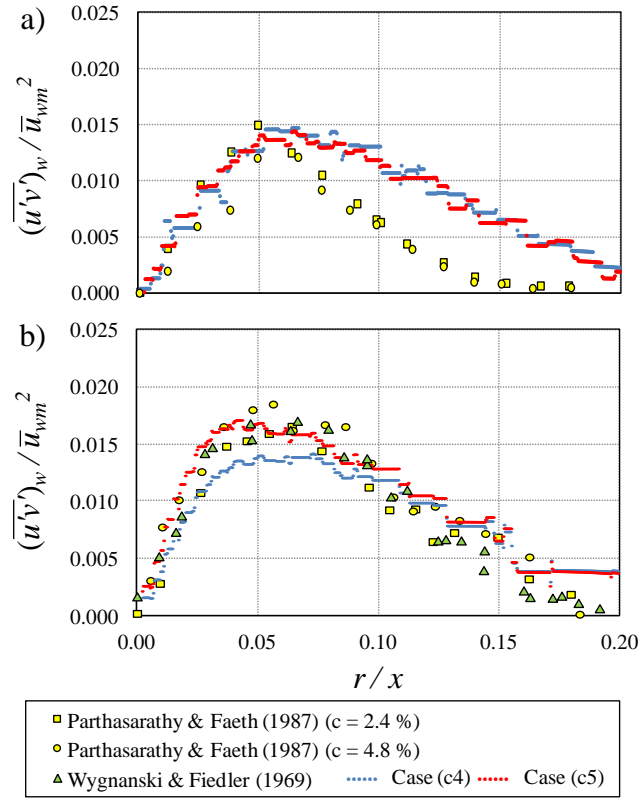


Figure 3-21: Cross-sectional variation of the computed normalized water-phase turbulent shear stress at a) $x/d = 16$. b) $x/d = 40$. The computed turbulent shear stresses were compared with experimental results of slurry jets (Parthasarathy & Faeth, 1987) and single-phase water jets (Wagnanski & Fiedler, 1969).

Turbulent shear stress of single-phase water jet was measured for $50 < x/d < 75$ by Wagnanski and Fiedler (1969) and their measurements showed that $\overline{u'v'}$ was almost invariant for $50 < x/d < 60$ and it became smaller at $x/d=75$. Comparison of the measured $\overline{u'v'}$ of slurry jet and single-phase jet at $x/d=40$, shows that the presence of the second phase with relatively high concentration ($c_o=4.8\%$) can slightly increase the water-phase turbulent shear stress by 8%.

The computed results indicated that the particle concentration can enhance the water-phase turbulent shear stress by 17% whereas experimental observations of Parthasarathy and Faeth (1987) showed an increase of 10.8% at the peak location.

To study the effect of particle concentration on turbulent shear-stress of the sand-phase, $\overline{u'v'}$ was computed for four cases having concentration range of 0.6 to 9.6 percent. Computed results at cross-sections of $x/d=16, 40, 50$ and 60 are plotted in Figure 3-22 and these results are compared with measurements of single-phase buoyant jets (Wang and Law, 2002) and dilute slurry jets with $c_o=0.19\%$ from experimental study of Jiang et al. (2005).

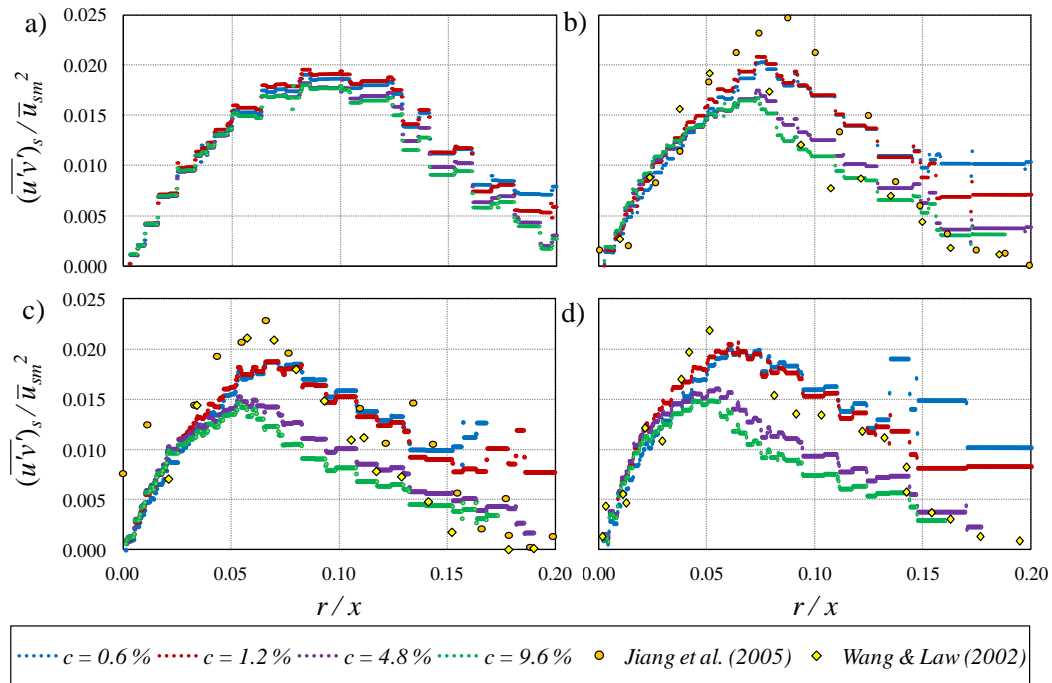


Figure 3-22: Cross-sectional variation of the computed normalized sand-phase turbulent shear stress at a) $x/d = 16$. b) $x/d = 40$. c) $x/d = 50$ and d) $x/d = 60$. The computed turbulent shear stresses were compared with experimental results of dilute slurry jets ($c_o=0.19\%$), (Jiang et al., 2005) and single-phase buoyant jets (Wang & Law, 2002).

It was found that particle concentration reduces the normalized sand-phase turbulent shear stress. This may be due to the fact that higher concentration causes a faster increase on the centreline sand-phase velocity than the turbulence. A comparison between the experimental results of a single-phase buoyant jet and a dilute slurry jet at $x/d=40$ is shown in Figure 3-22b. The difference between the turbulent shear stress

profiles in Figure 3-22b indicates the effect of particles on the sand-phase turbulent shear stress. Similar to the water-phase, the peak value of $\overline{u'v'}$ in sand-phase is larger than the corresponding single-phase by 28.5%. The location of the peak $\overline{u'v'}$ in single-phase jet was found to be at $r/x=0.078$. This location was found to be at $r/x=0.087$ for dilute slurry jets showing that the peak $\overline{u'v'}$ at $x/d=40$ was shifted away from the axis of the jet. The higher peak value of the dilute slurry jets found by Jiang et al. (2005) may be due to the low concentration and smaller particle size (particle size in study of Jiang et al. (2005) was 50-75 μm whereas particle size in numerical study was 505 μm .) Presence of particles in slurry jets showed a slight increase on the peak value of $\overline{u'v'}$ at $x/d=50$ by 9.5% (see Figures 3-22c). A relatively large drop in the peak $\overline{u'v'}$ with high c_o can be seen in Figures 3-22 (b-d). This may be due to the fact that the decay of u_{sm} in slurry jets with high concentration occurs at a slower rate as discussed in section 3.3.2 (see Figure 3-13).

3.9 Summary and Conclusion

A computational investigation was performed to study the effects of nozzle size, initial particle concentration, initial velocity and particle size on the hydrodynamics of sand-water slurry jets. The numerical model was validated with experimental results from the literature: for the nozzle size of 5, 9 and 15.5 mm, particle concentration in the range 0.21-12 percent, particle sizes of 210, 389 and 505 μm and initial velocity ranging from 0.98 to 2.19 m/s. The computed mean properties of sand-phase and water-phase axial and radial velocities, volumetric concentration and turbulent kinetic energy (TKE) along the jets axis and at different cross sections were compared with laboratory measurements. It was found that the model performs well for the specified conditions. It was concluded that, the model provides accurate predictions at low particle c_o . Close to the nozzle and at

the core region of the jets ($r/x < 0.06$), numerical results under-estimated the measured TKE. Validated results indicated that the model predictions were less reliable very close to the nozzle ($x/d=10$).

It was found that in contrast with single-phase water jet, the water-phase spreading of slurry jets is function of nozzle size. For $x/d < 40$, the spreading of slurry jet can be predicted by the single-phase correlation but, far from the nozzle ($x/d > 40$), effect of other parameters such as c_o and D must be considered. The spreading rate of single-phase jet can be used for very dilute jets for $x/d < 120$ whereas for slurry jets with $c_o=12\%$, the classical value provides reasonable results only for $x/d < 20$. It was found that the ratio between the jet half-width for the sand phase to water phase, λ , became independent of x for $x/d > 70$ with a value between 0.22-0.3.

Effect of nozzle size and particle concentration on spreading of slurry jets was investigated. It was found that for slurry jets with moderate concentration ($c_o=2.4\%$), larger particles reduced the concentration half-width but, the effect of particle size was not significant. In contrast, effect of particle size on the spreading ratio of dilute slurry jets was found to be significant. For dilute slurry jets with small particles, λ reached a value close to unity whereas this value for jets with large particles can be as low as 0.3. Effect of c_o on the spreading ratio of slurry jets with large particle size ($D=505 \mu\text{m}$) was investigated. The value of λ in these cases increased with increasing sand concentration and reached a value of 0.48 for the highest concentration. It was found that the spreading ratio became independent of distance from the nozzle for $x/d > 70$.

The variations of the centreline velocity of slurry jets were investigated. It was found that the water-phase centreline velocity increased with increasing particle concentration. Strong correlations were found between F_r , c_o and velocity decay. These

correlations were shown with empirical formulations to describe the decay of slurry jets along the axis of the jet.

Effect of c_o on the computed entrainment coefficient indicated that, α_e becomes smaller than the corresponding value for single-phase jet. It was found that the entrainment capacity of slurry jets reduced with increasing particle concentration and far from the nozzle ($x/d > 120$) α_e reached a plateau with approximately 50% of the α_e of single-phase water jets. An absolute entrainment coefficient, α_o was introduced by normalizing the entrainment velocity with u_o . It was found that α_o of slurry jets has higher values than the single-phase water jets for $x/d < 80$ and beyond that region the absolute entrainment coefficient of slurry jets is almost equal to that of single-phase water jets.

The averaged drag coefficients of particle cloud at different cross-sections were computed and variations were studied along the jet axis. It was revealed that, close to the nozzle ($x/d=10$), C_D has similar value with individual particles and grouping effect becomes significant as particles descend further from the nozzle. It was found that particle concentration can reduce C_D since particles tend to travel behind the wake generated by frontal particles. The grouping effect in particle cloud at high Reynolds number can significantly reduce the averaged drag coefficient of cloud.

Effects of the controlling parameters on the turbulence of slurry jets was investigated by introducing the turbulent length scale defined as $l=k_w^{3/2}/\varepsilon$. It was found that this turbulent length scale l is three times larger than the integral length scale of Λ . This ratio was almost constant along the axis of the jet at $x/d > 40$ and invariant with the nozzle diameter and particle size. For slurry jet with higher concentration ($c_o=9.6\%$) TKE was found to be 38% higher than k_{wo} .

Turbulent shear stress of both phases was computed from velocity and concentration profiles. The computed results indicated that c_o enhanced the water-phase turbulent shear stress by 17% whereas experimental observations showed an increase of 10.8% at the peak location. The peak value of $\overline{u'v'}$ in sand-phase was found to be larger than the corresponding single-phase by 28.5% and the peak location was shifted away from the peak location of single-phase jet at $x/d=40$.

3.10 Notation

b = half width of the jet (m)

B = specific buoyancy flux of the jet (m^4/s^3)

B_s = body spacing of the computational domain (mm)

c = particle concentration by volume (%)

C_D = Drag coefficient

d = nozzle diameter (mm)

D = particle size (μm)

F_D = drag force (N)

F_r = densimetric Froude number

g = acceleration due to gravity (m/s^2)

I = turbulence intensity (%)

k = turbulent kinetic energy per unit mass (m^2/s^2)

l = turbulent length scale (m)

l_m = length scale (m)

L = local resolution cell size of the domain (mm)

m = mass flux (g/s)

M = specific momentum flux (m^4/s^2)

r = radial distance from the centreline of the jet (m)

Q = volume flux (m^3/s)

R = radius of local resolution of the domain (mm)

R = Reynolds number

R_R = refinement ratio

Sc = turbulent Schmidt number

u = axial velocity (m/s)

v = radial velocity (m/s)

x = axial distance from the nozzle (m)

α_e = entrainment coefficient

α_o = absolute entrainment coefficient

γ = coefficient

ε = turbulent energy dissipation rate per unit mass (m^2/s^3)

ϕ_i = value of velocity or concentration at point i

λ = half width ratio

L = Integral length scale of turbulence (m)

μ = fluid absolute viscosity (kg/m.s)

μ_t = turbulent viscosity (kg/m.s)

ν = kinematic viscosity (m^2/s)

ρ = density (kg/m^3)

Subscripts and Superscripts

B = value at the bottom of domain;

c = concentration;

m = centreline value;

o = value at the nozzle;

s = sand-phase;

T = value at the top of domain;

v = velocity;

w = water-phase;

$'$ = fluctuation quantity;

$\bar{\quad}$ = mean quantity;

Chapter 4

Experimental Study of Sand Jet Front in Water

4.1 Introduction

Particle-laden jets are commonly observed when particles are released instantaneously into water bodies such as in marine bed capping, dredged material disposal, as well as aqueous industrial waste disposal [Buhler and Papantoniou (1999); Bush et al. (2003)]. The behaviour of these jets is determined by the size, concentration and density of the suspended particles. A number of experimental and numerical studies have been conducted to investigate the hydrodynamic behaviours of steady-state particle-laden jets [Virdung and Rasmuson (2007), Wang et al. (2009a); Hall et al. (2010); Gan and Nickels (2010), and Azimi et al. (2011b)] but less attention has been devoted to study the starting of particle-laden jets with relatively high particle concentrations.

Mean axial and radial velocities, turbulent fluctuations and Reynolds stresses of the solid-liquid jets with low solid concentration (e.g., solid concentration of less than 0.2%) were measured by many investigators such as Muste et al. (1998), Aria et al. (2003), Jiang et al., 2005 and Virdung and Rasmuson (2007). In the presence of low solid concentration effect of particle-particle interaction was assumed to be negligible. But in slurry jets with high solid concentration, particle-particle interaction can play an important role in the hydrodynamics of the jet (Hall et al., 2010). Therefore, effect of particle-particle interaction on the averaged axial and radial velocities and turbulent fluctuations of the slurry jets with high particle concentration need to be explored. Earlier studies by Muste et al. (1998) tried to include the effects of particles on the turbulence of particle-laden jets.

A paper based on the content of this chapter has been published in the *International Journal of Multiphase flow*, as Azimi et al., (2012), Vol 40, pp. 19-37.

Influence of particles on the turbulence of the carrier phase is known as turbulence modulation. The physics of turbulence modulation has been discussed by many researchers [Gore and Crowe, 1989, 1991; Wang et al. 2009a]. A comprehensive comparison of turbulence modulation effects of two-phase flow in pipes, bubbly flows and particle-laden jets was made to investigate the influence of particles in variations of turbulence intensity (Crowe, 2000).

The unsteady behaviour and the development of the two-phase liquid-air jets were studied by Hill and Ouellette (1999), Rottenkolber et al. (2002) and Marugán-Cruz et al. (2009). Experimental investigation of the transient jets indicated that the time scale of the jet evolution could be formulated as a function of momentum and buoyancy fluxes (Pantzlaff & Lueptow, 1999). In the release of a fixed amount of particles in stagnant water, the evolution of particle cloud and its velocity were correlated with the buoyancy force exerted by the particles whereas the frontal evolution of a continuous release of particles can be correlated with the buoyancy flux of the jets [Noh and Fernando (1993); Noh (2000) and Bush et al. (2003)]. The condition under which the particle cloud settles as a thermal or as a swarm of individual particles was investigated by Bush et al. (2003). The dependence of the normalized cloud velocity on the normalized buoyancy force of a particle cloud was correlated and it was found when the normalized buoyancy is less than 0.1, particles descended as a swarm of individual particles and for the normalized buoyancy above 0.1, settlement of particles behaves as thermal. Most experimental studies have been focused on the release of a fixed amount of particles to form a cloud thermal or swarm of particles [Noh and Fernando (1993); Noh (2000) and Bush et al. (2003)]. So far no attention has been made to study the particle cloud due to continuous release of particles. It will be useful to study the effect of initial momentum flux on the behaviour of particle clouds.

The unsteady behaviour of particle-laden jets/plumes and the evolution of particle cloud can be classified into different regimes by introducing some critical parameters such as particle Reynolds number, and particle Froude number. Nicolas (2002) classified the settling of particle cloud in water and glycerine into four different regimes: stable jet, unstable jet with blobs formation, spiral jet with dispersion and atomized jet. He found that a capillary-like instability with formation of blobs and dispersion of the jet particles occurs when a particle Reynolds number is over unity. Experimental studies have been performed to investigate the location of sedimentation after release of particles into a quiescent and cross flow ambient conditions (Ruggaber, 2000; Gensheimer, 2010). The physical mechanisms and the characteristic of the cloud of particles as it descended in the water column were investigated by Ruggaber (2000). In his experiments effects of practical release parameters such as release location (i.e., release height) and moisture content were investigated. He found that the thermal phase of particle clouds can be subdivided into turbulent thermals in the absence of spherical vortex and circulating thermals in the presence of vortices.

An interesting flow feature that has long been associated with starting jets is the formation of vortex structure. The formation of the vortex is largely due to the roll up of the jet shear layer as it is introduced into the ambient. The generation, formation, and evolution of vortex rings have been the subject of numerous experimental, analytical and numerical studies [Garib et al. (1998); Krueger and Gharib (2003); Arakeri et al. (2004); Pottebaum and Garib (2004); Bond and Johari (2005 & 2010)] but to the authors' knowledge, no experimental work has been devoted to study the vortex structure of a particle-laden starting jet. The formation of buoyant thermal and vortex rings was generated by the motion of a piston pushing a column of fluid of length of L through a nozzle of diameter d . Tube aspect ratio L/d was found to be a key parameter in the

prediction of vortex circulation and vortex translation velocity. Bond and Johari (2005) investigated the effect of tube aspect ratio ranging from 2 to 8. They found that the higher aspect ratio leads to higher circulation. Shusser and Garib (2000) proposed a direct correlation between the propagation velocity of a vortex ring and the vortex circulation.

Vortex structures and eddies can be extracted from two dimensional velocity vector field to provide more information about the effect of particles on the mixing mechanism and frontal entrainment of the starting sand jets. Reynolds decomposition is considered as the traditional method of vortex extraction; however, several other methods including Large Eddy Simulation (LES) and Galilean decomposition have been employed [Adrian et al. (2000); Wu and Christensen (2006); Natrajan et al. (2007)]. Besides the well-known Reynolds decomposition, identification of vortices in a velocity field can be accomplished by filtering the velocity fields such as Gaussian filter, LES method, or by translating the instantaneous velocity field with convection velocity (Galilean method). Adrian et al. (2000) investigated different turbulent extracting techniques to interpret the velocity field and vortex structures in the turbulent pipe and channel flows.

It should be mentioned that the Reynolds decomposition does not always provide the best visualising pattern of the turbulent mechanics of a flow and it removes large scale motions that are associated with the mean flow. Furthermore, in transient phenomenon that the time averaging is not permitted, Reynolds decomposition is not able to resolve the vortex structure. On the other hand, Galilean transformation was found as a simplest method of decomposition [Wu and Christensen (2006); Natrajan et al. (2007)]. In this method, the computed convection velocity corresponds to a different translational velocity of vortices embedded within the flow. When the convection velocity matches with a vortex's translational velocity, it becomes recognizable in the velocity vector pattern.

Local vortices can be identified by analysing the velocity gradient tensor and the three invariant of velocity gradient tensor. The symmetric and anti-symmetric parts of the velocity gradient tensor are called strain rate tensor and vorticity tensor, respectively. Local vortex identification techniques could be an excellent tool to assess the contributions of the small and large scale vortex structures in the overall dynamics of the flow [Jeong and Hussain (1995); Zhou et al. (1999)]. The reviews of Chakraborty et al. (2005) and Kolář (2007) describe much of the current understanding of vortex extraction techniques as well as some limitations in employing these techniques.

This Chapter is aimed at investigating the onset of particle-laden turbulent jets in still water with special emphasis on the effects of nozzle diameter and particle size on the hydrodynamics of the particle-laden jets. Effect of nozzle diameter and particle size on the shape and velocity of the front can help to understand the changes on vortex formation and the mixing capacity of the front jets. Since many factors involved in this study such as time, particle concentration, nozzle diameter, particle size and the excess momentum generated by particles, a close comparison between the results of this study with the results of the classical experimental studies having less complexity (i.e., the single-phase jet front, single-phase vortex, particle-laden turbulent jets and particle thermals) can address the effects of each controlling parameters on the characteristics of the front jets and their differences with the results found in the literature. Detailed simulation of the unsteady behaviour of the sediment-laden jets with high initial concentration is a challenge for CFD modellers. Consequently, the results provided in this chapter can also be used for validation of numerical models. Turbulent modulation is also one of the important parameters for the prediction of the mixing capability of such jets. Effect of particle size on turbulent modulation is investigated and correlations are introduced by a comprehensive comparison of other experimental studies in the literature.

The chapter is organized as follows: the experimental methods and the velocity measurement techniques are described in 4.2. In 4.3, dimensional analysis is used to investigate the effect of controlling parameters on the hydrodynamics of the jets. Experimental results including the study of the evolution of the frontal particle-laden jets, frontal velocity measurements and half-width growth rate are presented in 4.4. Effect of nozzle diameter and particle size on the axial and radial velocities, vortex structure and turbulence modulation are discussed in 4.5. Finally, a summary and conclusions of this study are presented in 4.6.

4.2 Laboratory Experiment

Experiments were conducted in a 133 cm square tank filled with tap water, and the water depth was fixed at 92 cm for all experiments using an overflow drain. A schematic view of the experimental setup is illustrated in Figure 4-1.

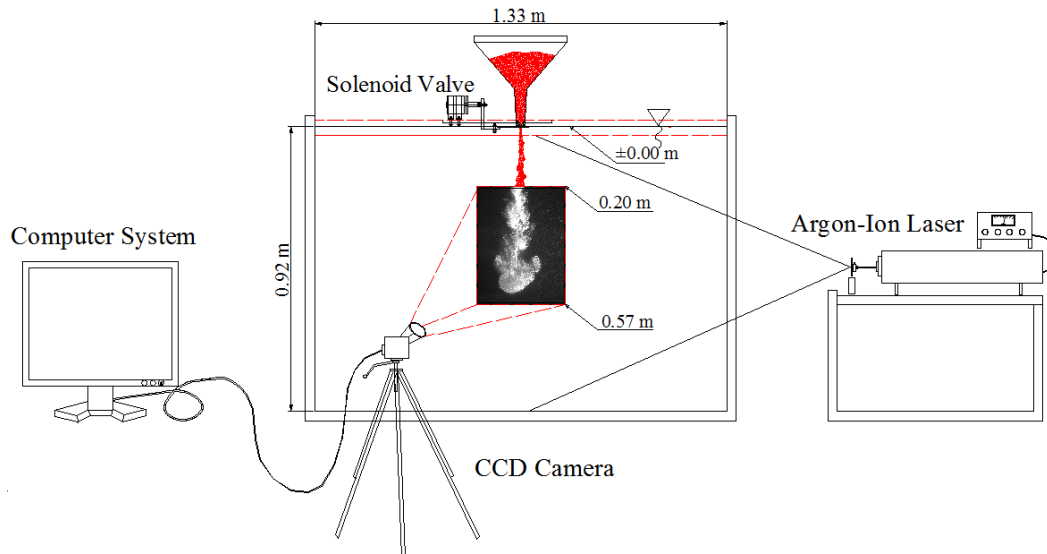


Figure 4-1: A schematic view of the experimental setup.

A sand hopper was held vertically above the tank, and a brass nozzle having different diameters was placed inside the funnel. In order to minimize the initial momentum of the jet, the release was kept at most 5 mm above the water surface. The

nozzle was controlled by a thin moveable plate which could pivot around a pin. The plate was actuated by a computer controlled solenoid valve and a spring for operating the nozzle without disturbing the jet and the water surface. The mass of sand particles passing through the nozzle was measured accurately and the sand mass flux, m_o , was calculated by correlation of mass with time.

Two series of experiments were carried out to study the effect of nozzle diameter (Series A) and particle size (Series B). Four nozzle sizes with a nominal diameter of 2, 3, 4.75 and 10 mm were used to study the effect of nozzle size. Fine blasting sand particles from Sil Industrial Minerals Inc., Edmonton, Canada with a median diameter, D_{50} of 206 μm and density of $\rho_p = 2540 \text{ kg/m}^3$ were employed in these experiments. The uniformity of particle sizes was evaluated by fitting the sand particle size distribution data with the lognormal probability curves. Sand particle sizes were considered uniform since the geometric standard deviation $\sigma_g = D_{84}/D_{50} = D_{50}/D_{16}$ was found to be smaller than 1.35 (Breusers and Raudkivi, 1991). The experimental details and non-dimensional parameters were given in Table 4-1.

Table 4-1: Experimental details of Series A with the particle size of $D_{50} = 206 \mu\text{m}$.

Test No.	d (mm)	m_o (g/s)	u_o (m/s)	R_o	F_o	Re_p	S_{to}	$u_{f\infty}$ (m/s)
A1	2.0	0.34	0.07	144	1.58	5.20	0.22	0.09
A2	3.0	0.84	0.08	243	2.03	5.20	0.17	0.11
A3	4.75	3.44	0.13	605	2.56	5.20	0.16	0.14
A4	10.0	22.9	0.19	1914	4.62	5.20	0.11	0.26

In order to study the effect of particle size, sand particles with the density of $\rho_p = 2540 \text{ kg/m}^3$ passed from a series of sieves ranging from 125 to 589 μm and 8 classes were identified in this setup. Particle size and the relevant characteristics of each setup are given in Table 4-2.

Table 4-2: Properties of the sand particles of Series B with the nominal nozzle size of 4 mm.

Test No.	D (μm)	Particle size range (μm) [Sieve No.]	d/D	m_o (g/s)	u_o (m/s)	u_{∞} (m/s)	R_o	F_o	Re_p	$u_{f\infty}$ (m/s)
B1	137.5	125-150 [120-100]	29.10	2.11	0.11	0.01	449	2.52	1.80	0.06
B2	165	150-180 [100-80]	24.24	2.08	0.11	0.02	442	2.24	2.90	0.07
B3	196	180-212 [80-70]	20.41	2.00	0.11	0.02	425	1.98	4.40	0.07
B4	231	212-250 [70-60]	17.32	1.93	0.10	0.03	410	1.76	6.50	0.07
B5	275	250-297 [60-50]	14.55	1.90	0.10	0.035	404	1.60	9.70	0.08
B6	327	297-354 [50-45]	12.23	1.84	0.10	0.045	391	1.41	14.4	0.09
B7	389.5	354-425 [45-40]	10.27	1.69	0.09	0.055	359	1.19	21.3	0.12
B8	507	425-589 [40-30]	7.89	1.64	0.09	0.075	349	1.00	37.6	0.13

Velocity of sand/water phase was measured using particle image velocimetry (PIV). A continuous 6 W Argon-Ion laser operating at 488 nm (Stabilite 2017, Spectra-Physics Laser) and optics (OZ optics) was employed to generate a light sheet. The laser sheet was launched from the side to illuminate the flow. A CCD camera (1392 x 1040 pixels) (TM-1040, Pulnix America Inc.) controlled by a computer frame grabber system (Stream 5, IO Industries Inc.) captured images of the particles with a frame rate of 30 frames per second and a resolution of 18 pixel/cm. The area of interest was a rectangle of 76 cm x 56.8 cm and located 3 cm below the water surface.

To measure the water velocity field, 50 grams of silver-coated glass particles (Potters Particles Inc.) with a density of 1.65 g/cm³ and the mean diameter of 15 μm were homogeneously distributed into the water provided the tracing particle concentration of

30.72 g/m³. A CCD camera (1600x1200 pixels) (DS-21-02M30-SA, DALSA) controlled by a computer frame grabber system (Video Savant Basic 4.5, IO Industries Inc.) captured images of the particles at a frame rate of 30 Hz and resolution of 43 pixel/cm. The area of interest was a rectangle of 37 cm x 27.75 cm and located 20 cm below the water surface.

The displacements of particles between subsequent images were computed with a standard PIV algorithm using the Davis program (Davis 7.2, La Vision, 2007). Davis computes the cross correlation between each subsequent images and according to the level of correlation it provides 4 vector choices. The percentage of the first vector choice and the percentage of spurious vectors could be a good measure of computation accuracy. The accuracy of vector computation is directly related to the background intensity fluctuations and it can be increased by employing sliding background subtraction. Subtracting the background with 10 pixels (~ 2.3 mm) sliding length provided the minimum missing vector of 2.56 % and the maximum first choice of 96.6 %. By employing the particle intensity normalization option with the scale length of 8 pixels, the missing vectors dropped to 2.1%.

Iterative multi pass method with deformable interrogation windows was applied for cross correlations of the subsequent images. The interrogation window size, windows overlapping, and number of iterations can be adjusted based on the image quality and area of interest. The interrogation window size of 64 x 64 pixels (1.48 x 1.48 cm) and 50% overlap between adjacent windows was selected for the first pass. For the second and the third passes, the window size was reduced to 32 x 32 pixels and 50% overlap. This enabled measurement of velocity fields with spatial resolutions always better than 4 mm. Vector validation algorithms were applied to eliminate the spurious vectors. For noise reduction, a four-pass regional median filter was used. Vectors with 1.5 times larger

than the root mean square (r.m.s) of the neighbours were removed from the velocity vector field. Those can be reinserted with filtered vectors if they were smaller than three times of the r.m.s of neighbours. Applying the above post processing method can reduce the spurious vectors to 0.43%. The position of the correlation peak can be measured to sub-pixel accuracy. In PIV technique, the velocity field computation has a bias toward integer velocity values called peak locking. The peak locking effect was monitored during PIV computations and computed values were in the acceptable range, i.e., peak lock < 0.1 (LaVision, 2007).

The front position at each image can be searched using an image processing method. The gray scaled images were first transformed to black & white images. Each pixel value in this matrix was either zero or one (i.e., white for particles and black for background). A searching procedure was set from each row and was started from the bottom row. Then the searching line was moved upward until reached the jet front. The pixel value at each row was added together and compared with a threshold value. The searching procedure was stopped when the summation of the pixel values in a row reached the threshold value. Similar searching method was employed from left side and right side of the image to detect the frontal boundary and the maximum value at each time step was recorded as the front width. This procedure detects the location of the front jet with a reasonable accuracy (i.e., 1 pixel \approx 0.7 cm/sec). The threshold value was obtained through direct comparison of the gray scaled images. The variations of the frontal position with time were plotted and the measured positions were fitted to a series of power law curves with intervals of $\frac{1}{2}$ second. Velocity profiles were obtained by taking the derivative of the fitted curve.

4.3 Dimensional Analysis

The parameters that control the particle cloud frontal velocity u_f and the frontal half-width b are

$$u_f = f_1(x, d, D, u_o, \mu, g\Delta\rho, \rho_w, c_o) \quad (4.1)$$

where x is the axial distance from the nozzle, d is the nozzle diameter, D is the particle size, u_o is the initial velocity of the sand jets, μ is the dynamic viscosity of water and $\Delta\rho = \rho_p - \rho_w$. Where ρ_p and ρ_w are the densities of the sand particles and water, respectively, and g is the acceleration due to gravity. c_o is the initial volumetric concentration of particles and it was constant with the value of $c_o = 60\%$. Based on dimensional analysis, effect of controlling parameters on the shape and evolution of sand jet front can be studied in a non-dimensional form.

$$\frac{u_f}{u_o} = f_2\left(\frac{x}{d}, \frac{u_o}{\sqrt{(g\Delta\rho/\rho_w)D}}, \frac{d}{D}, \frac{\rho_w u_o d}{\mu}, c_o\right) = f_2(x/d, F_o, d/D, R_o, c_o) \quad (4.2)$$

Considering the effect of gravitational acceleration and fluid viscosity, the initial velocity of particles can be normalized in the form of densimetric particle Froude number $F_o = u_o / (g\Delta\rho D / \rho_w)^{1/2}$ and Reynolds number $R_o = \rho_w u_o d / \mu$. For small particles where Stokes's regime is dominated, the relationship between terminal settling velocity of small particles, u_∞ , and the initial velocity of the jet can be manipulated by using the obtained non-dimensional parameters.

$$u_\infty = \frac{g\Delta\rho D^2}{18\mu} = \frac{u_o R_o}{18F_o^2} \quad (4.3)$$

Effects of fluid viscosity and the gravitational force on the formation of dense suspension jets were investigated by Nicolas (2002). Nicolas's experimental study

covered a variety of configurations but less attention was given to the two extremes. i.e., large and small values of R_o and F_o . The present experimental study was performed on relatively high values of R_o and F_o (see Tables 1 and 2 & Figure 3 in Nicolas, 2002). In accordance with Nicolas's classifications, the present experimental investigation falls in the spiral jet with dispersion regime.

Effect of particle inertia on the slurry jets over the viscosity of the ambient fluid can be expressed by particle Reynolds number, $Re_p = \rho_w u_\infty D / \mu$, where u_∞ is the particle settling velocity calculated using the Haywood tables (Holdich, 2002). It can be shown that the particle Reynolds number is a combination of R_o , F_o and the ratio of d/D

$$Re_p = \frac{\rho_w u_\infty D}{\mu} = \frac{1}{18} \left(\frac{d}{D} \right) \left(\frac{R_o}{F_o} \right)^2 \quad (4.4)$$

Equation 4.4 indicates that particle Reynolds number could be a suitable non-dimensional parameter to study the frontal velocity and can cover the influence of R_o , F_o and the ratio of d/D as well. By combining equations 4.2, 4.3 and 4.4 frontal velocity can be expressed as a function of

$$\frac{u_f}{u_\infty} = f_3(x/d, R_o, F_o, d/D, c_o) = f_4(x/d, Re_p, c_o) \quad (4.5)$$

The hydrodynamic behaviour of a continuous release of particles in water can be compared with a buoyant jet. The growth rate and velocity of the jet can be predicted by employing the initial mass, momentum and buoyancy of the jet.

$$u_m, b = f_5(m, M, B) \quad (4.6)$$

where u_m is the centreline velocity of the jet, $m = \rho_s(\pi d^2/4)u_o c_o$ is the initial mass flux, $M = \rho_s(\pi d^2/4)u_o^2 c_o$ is the initial momentum flux and $B = (\pi d^2/4)g'u_o$ is the buoyancy

flux of the jets. Dimensional consideration indicated that the frontal half-width b , and frontal velocity u_f , must evolve according to

$$b \sim x, \quad u_f \sim B^{1/3} x^{-1/3} \quad (4.7)$$

Papanicolaou and List (1988) introduced a formulation for predicting the centreline velocity in steady single-phase buoyant jets.

$$u_m = 3.85 B^{1/3} x^{-1/3} \quad (4.8)$$

A fixed amount of particles can be released into the ambient water to form a cloud of particles or thermal. Therefore, the evolution of a turbulent thermal can be prescribed by the buoyancy force F_B exerted by the particle cloud, $F_B = V_o g'$, where V_o is the volume of particles. The net force in the plume can be calculated by considering the weight of a sand column with a length of L as a downward force and the weight of ambient fluid displaced by the sand column as an upward force. Therefore, F_B can also be written as

$$F_B = (\pi d^2/4) L c_o g \Delta \rho \quad (4.9)$$

Bush et al. (2003) determined experimentally the frontal velocity of a turbulent thermal as a function of buoyancy force F_B , settling velocity of particles u_{∞} , and x . They found that their measurements are consistent with the following scaling relationship

$$u_f \sim F_B^{1/2} x^{-1} u_{\infty}^{-1} \quad (4.10)$$

Frontal velocity of circular single-phase turbulent jets, u_b was found to be 0.54 times of the centreline velocity of a steady jet, u_m (Rajaratnam and Yasmin, 1992). In fact, by introducing a time scale of $\tau^* = x / u_{\infty}$, we can rewrite the proposed equation to

predict the front velocity of a turbulent thermal in form of the corresponding frontal velocity of a single-phase buoyant jet, u_b .

$$\left(\frac{B}{xu_\infty^3}\right)^{1/2} = C\left(\frac{u_b}{u_\infty}\right)^{3/2} \quad (4.11)$$

The energy transfer between particles and ambient water is characterised by the particle relaxation time, τ_p (Wang et al., 2009a; Muste, et al., 1998). When $\rho_p > \rho_w$, the Stokesian particle relaxation time can be calculated as

$$\tau_p = \frac{\rho_p D^2}{18\mu} \quad (4.12)$$

The jet initial velocity u_o , and the nozzle diameter d , can be a good measure to estimate the initial characteristic time of the fluid. The ratio of the particle relaxation time τ_p , and the characteristic time of the fluid $\tau_f = d/u_o$, called the initial Stokes number S_{to} , and it plays an important role in particle motion. In other words, the extent to which the particles will follow the vortex motion and turbulent eddies of the carrier phase can be estimated with the initial Stokes number. The initial Stokes numbers of experiments Series A & B were tabulated in Tables 4-1 and 4-2, respectively.

$$S_{to} = \frac{\tau_p}{\tau_f} = \frac{\rho_p D^2 u_o}{18\mu d} \quad (4.13)$$

4.4 Evolution of Sand Jet Front

A cylindrical coordinate system (x, r) with the origin on the jet centreline at the nozzle exit is used for all data presentation. In most of the plots in this section, these coordinates are normalized by the nozzle exit diameter d . The initial particle velocity, u_o , at a hopper exit is found to be $u_o = c (gd)^{1/2}$. Cai et al. (2010) reported a coefficient of

0.68 for the d/D ratio between 40 and 300. According to our experimental condition and particle sizes, the value of d/D in present experiment ranged between 7 and 49. The reported coefficient provided by Cai et al. (2010) gave accurate prediction for the initial velocity of the jet in the range of $d/D > 40$. For $d/D < 40$, from correlation between the nozzle size and the initial mass flux the coefficient of c was found to be 0.6.

It has been observed by many researchers that the particle cloud velocity decelerates from the nozzle and reaches a plateau far away from the nozzle [Noh and Fernando (1993); Noh (2000); Bush et al. (2003); Bond and Johari (2005)]. A cloud of heavy particles with high concentration and low settling velocity, u_{∞} , may fall as a buoyant blob of finite size considered as the frontal part of the jet. In the case of large particles with low concentration, the frontal part of the cloud can descend as a swarm of individual particles (Turner 1962, 1969). Close to the nozzle, large amount of particles released to the ambient water and cause a significant entrainment with the surrounding fluid due to generation of a vortex ring within it. Far from the nozzle, the ambient fluid is relatively undisturbed by the sediment.

Figure 4.2 shows the images of sand jets passing from different nozzle sizes. The visualizations were obtained using a laser sheet as light source and recording the light scattered by the sand particles introduced in the jet with a digital camera. These images were taken two seconds after the release of particles and they were turned to negative images for better visualization. As can be seen from Figure 4-2, particles issued from a 2 mm nozzle almost reached the plateau regime (see Figure 4-5, $x/d = 150$) whereas particles issued from larger nozzle (i.e., 10 mm) still located in the thermal region.

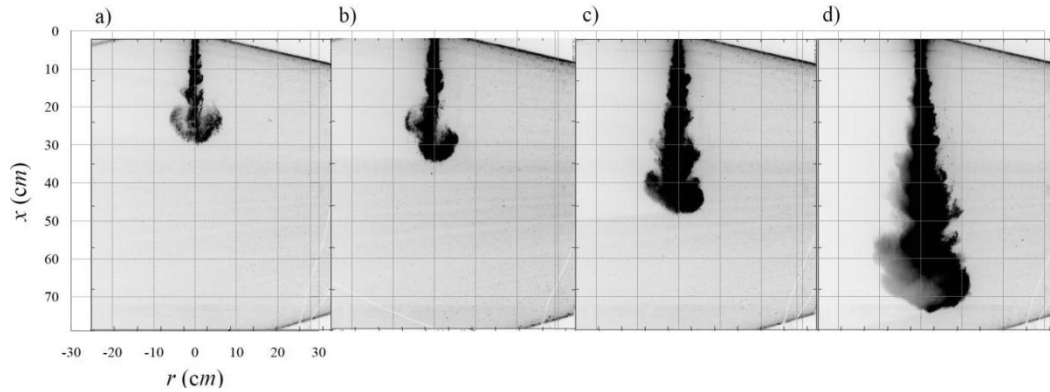


Figure 4-2: Images of the sand jets with different nozzle sizes in water at $t = 2$ sec. [Exp. A1 - A4] a) $d = 2$ mm; b) $d = 3$ mm; c) $d = 4.75$ mm; d) $d = 10$ mm. Images turned to negative for better visualization.

The jet front velocity at the plateau can be called as the jet front terminal velocity, $u_{f\infty}$ and can be used as a velocity scale. In order to study the transitional behaviour of the sand jets a dimensionless time scale, $t^* = u_{f\infty} t / d$ was defined (see Tables 4-1 & 4-2).

Effect of particle size on hydrodynamics of a transient jet at non-dimensional time of $t^* = 60$ was shown in Figure 4-3. As can be seen clearly, the transient particle-laden jets could be considered to be comprised of two simple parts. The first part of the jets is a spherical traveling head. It consisting of a vortex ring which continuously grows by the effect of mass and momentum of the jet. The second part is a quasi-steady state jet referred as the trailing jet which transfers the mass and momentum from the nozzle to the jet front. Similar definition was proposed for buoyant plumes by Turner (1969). In this experimental setup, these two parts are more obvious when the nozzle size is smaller (see Figure 4-2a).

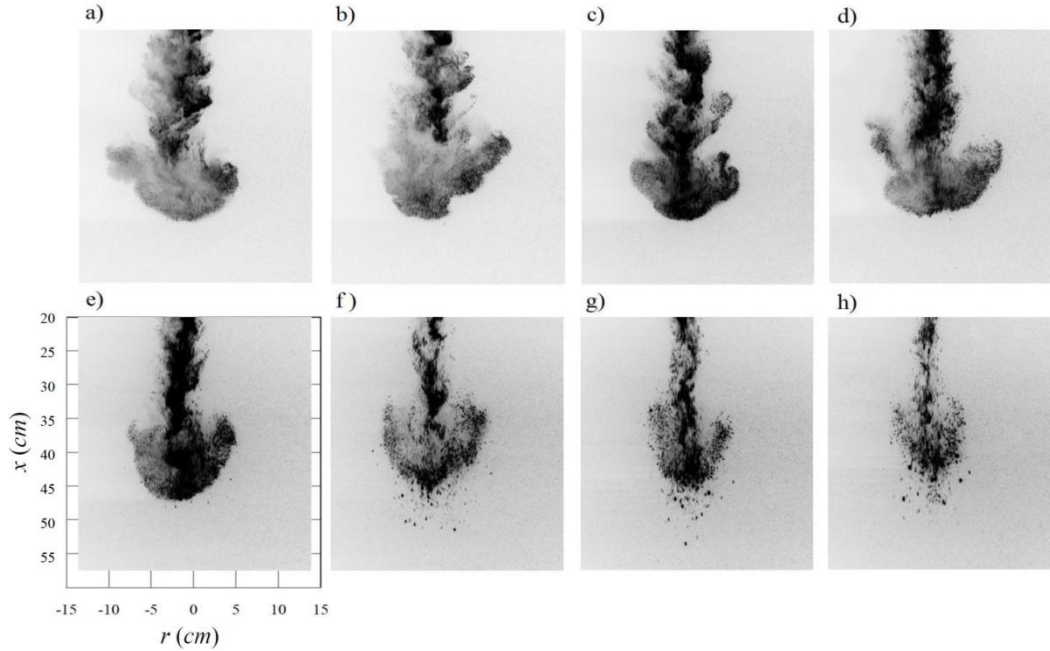


Figure 4-3: Effect of particle size on sand jet front behavior of experiments B1 – B8 at $t^* = 60$. a) Experiment B1 ($D=137.5 \mu\text{m}$), b) Experiment B2 ($D=165 \mu\text{m}$), c) Experiment B3 ($D=196 \mu\text{m}$), d) Experiment B4 ($D=231 \mu\text{m}$), e) Experiment B5 ($D=275 \mu\text{m}$), f) Experiment B6 ($D=327 \mu\text{m}$), g) Experiment B7 ($D=389.5 \mu\text{m}$), h) Experiment B8 ($D=507 \mu\text{m}$). Particles fall out of the cloud and the front head become narrower and sharper in experiments B5 – B8. Images turned to negative for better visualization.

It is possible to subdivide the evolution of particles into three subsections. Regarding the visual investigation of the transient jets and in accordance with the particle size variation, three different behaviours were observed. Considering the images illustrated in Figure 4-3[a-d], particle cloud behaves like thermal when $Re_p < 10$. Particles fall out of the cloud in the form of a bowl-shaped swarm when $Re_p \approx 10$ (Figure 4-3e). When the particle Reynolds number become greater than 10, the front head become narrower and sharper and particles begin to fall with a group velocity of $u_{f\infty}$ (Figure 4-3 [f-h]).

The evolution of the sand jets at different non-dimensional times i.e., $t^* = 10, 30, 50$ and 70 was shown in Figure 4-4. Three jets were selected to represent the mentioned subclasses (i.e., thermal, bowl-shaped and narrow frontal head). Particle clouds act as

thermal when $Re_p < 10$ (Figure 4-4a). Relatively low superficial velocity between ambient water and particle cloud provides enough time for particles to follow the water eddies which disperse particles from the jet center. As a result of velocity shear, a series of vortices similar to the Kelvin-Helmholtz instability can be seen clearly in the trailing jet.

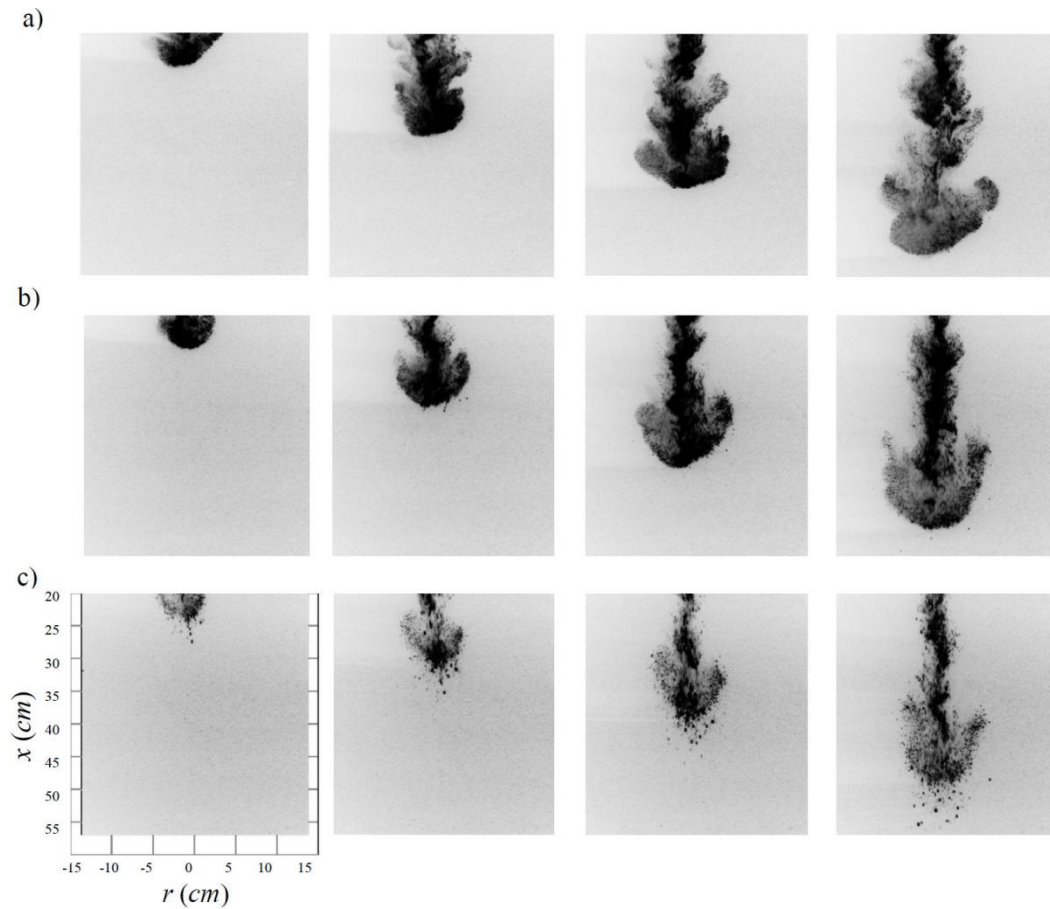


Figure 4-4: The evolution of sand jet front at $t^* = 10, 30, 50$ and 70 for experiments B3, B5 and B7. a) Experiment B3 ($D=196 \mu\text{m}$), b) Experiment B5 ($D=275 \mu\text{m}$), c) Experiment B7 ($D=389.5 \mu\text{m}$). Images turned to negative for better visualization.

The initial vortex ring in the jet front generates turbulence in the background water field causing additional dispersion. Figure 4-4b presents the movement of particle clouds at $Re_p \approx 10$. In this case, particles fall out of the cloud in the form of a bowl-shaped swarm. The frontal vortex ring was shifted upward and becomes less effective on

turbulence generation of the water phase. Particles in this regime require longer time to respond to the water phase fluctuations hence, less dispersion resulted in the trailing section. When the particle inertia is relatively larger than the fluid viscous force (i.e., $Re_p > 10$), particle clouds can penetrate through the water at a faster rate. In this category, the frontal head becomes narrower and the vortex ring becomes weaker. Consequently, effect of jet front and its vortex structure is negligible on the flow entrainment and the turbulence generation of the water phase.

4.5 Frontal Velocity of the Sand Jets

Frontal velocity of a cloud of sand particles with $D_{50} = 206 \mu\text{m}$ passing from nozzle size of 2, 3, 4.75 and 10 mm is shown in Figure 4-5a. As can be seen from this figure, frontal velocity of the jet decelerates and reaches a plateau far away from the nozzle. This qualitative trend is in consistent with the observation of Noh and Fernando (1993); Noh (2000) and Bond and Johari (2005).

Variations of the front location were plotted with time, and power law curves were fitted for every $1/2$ second of data. The average exponent for the power law fit of the particle cloud velocity was reported as 0.6 in experimental study of Bond and Johari (2005). The power law exponents for experiments with nozzle diameter ranged from 2 to 10 mm were found to be between 0.57 - 0.63. The regression coefficients of correlation were $R^2 = 0.975 - 0.99$ in all cases. The velocities of sand jet front u_f were normalized with the settling velocity of particles u_s , and variations of normalized frontal velocity with x/d were shown in Figure 4-5b. This figure shows the possible effect of nozzle diameter on the frontal velocity of the sand jet.

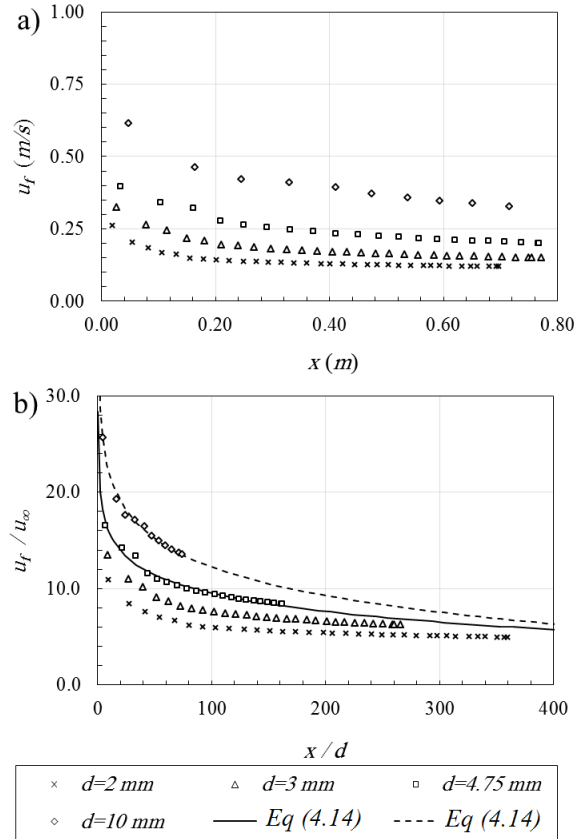


Figure 4-5: Effect of nozzle size on the frontal velocity of the sand jets, u_f , along the jet axis, x for experiments A1 ($d=2$ mm), A2 ($d=3$ mm), A3 ($d=4.75$ mm) and A4 ($d=10$ mm). a) Variations of the frontal velocity along the jet axis. b) Correlations of the frontal velocity normalized with the sand terminal velocity, u_∞ with the normalized distance of x/d . The proposed logarithmic equation of 4.14 corresponding for experiments A3 and A4 were included for comparison.

As can be seen from this figure, close to the nozzle, the frontal velocity of the jet issued from a 2 mm nozzle was 10.8 times of the corresponding particle settling velocity. The ratio of the jet front velocity to the particle settling velocity close to the nozzle was found to be 13.5, 16.6 and 25.6 for nozzles with diameter of 3, 4.75 and 10 mm, respectively. Considering the variation of the normalized frontal velocity along the jet axis indicates that the frontal velocity issued from small nozzles reached the plateau almost after $x/d = 200$. At this location, the frontal terminal velocity becomes almost 5 times of the particle settling velocity. The frontal velocity issued from a 10 mm nozzle

was measured from the nozzle up to $x/d = 75$. As can be seen from Figure 4-5b, the measured frontal velocity did not reach the plateau regime and the jet front located in decelerating stage. The sand frontal velocity issued from larger nozzles (Exp. A3 & A4) can be predicted far from the nozzle, i.e., $x/d > 200$, by fitting the trend line of measurements. A logarithmic equation can be proposed to estimate the normalized frontal velocity for the nozzle diameters used in this study

$$\frac{u_f}{u_\infty} = -\frac{1}{4} \left(\frac{D}{d} \right)^{-0.75} \ln \left(\frac{x}{d} \right) + 3.8 \left(\frac{D}{d} \right)^{-0.55} \quad (4.14)$$

The extrapolated trend lines indicate that the effect of nozzle size was diminished at $x/d \approx 400$. The frontal velocity at $x/d \approx 400$ issued from all nozzle sizes were found to be around 5 times of the particle settling velocity.

Effect of particle size on the frontal velocity of the sand jets is shown in Figure 4-6. As expected, larger particles produced higher frontal velocities. As can be seen from Figure 4-6, the velocity profiles of sand jets with larger particles reached the plateau regime in relatively early stages. In Figure 4-6b, the frontal velocity of the jet was normalized with the particle settling velocity. It was found that the frontal velocity reached the plateau at $x/d > 125$ for Exp. B3 to B8 whereas jet front with smaller particles reach the plateau further downstream ($\sim x/d = 200$).

The particle cloud fall velocity, $u_{f\infty}$ was found to vary with particle size. The variations of the normalized cloud fall velocity with particle size and particle Reynolds number are shown in Figure 4-7. For small particles, the ratio of $u_{f\infty}/u_\infty$ could be as large as 5 times of the individual settling velocity. This is consistent with the observations found on the effect of nozzle diameter (see Figure 4-5b).

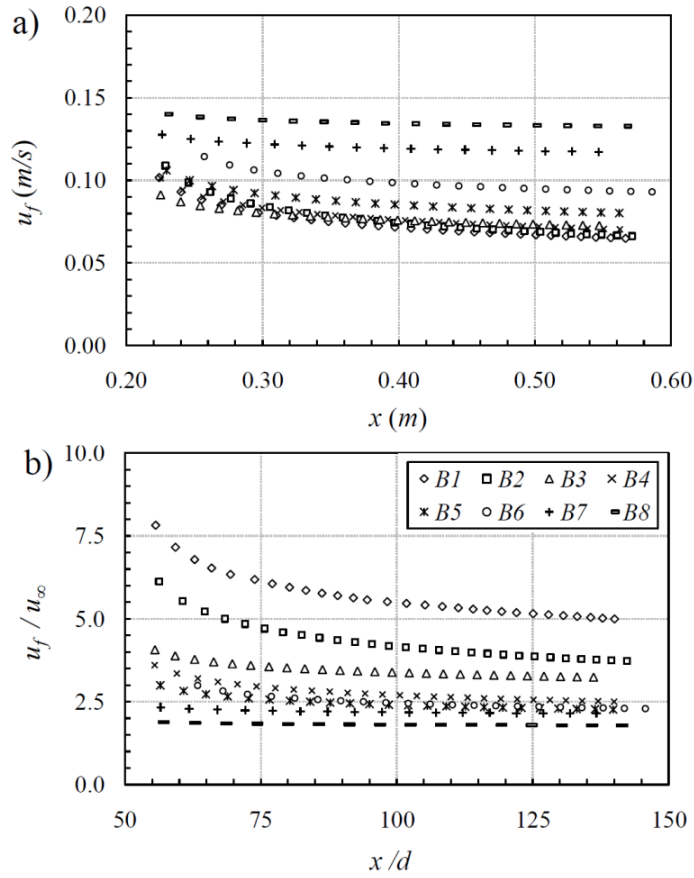


Figure 4-6: Effect of particle size on the frontal velocity of the sand jets, u_f , normalized with sand terminal velocity, u_∞ , for experiments B1 to B8.

However the ratio of u_{f0}/u_∞ become smaller and reaches the value of one for relatively large particles. This indicates that the grouping effect for larger particles diminishes close to the nozzle, and particles fall with velocity close to their individual settling velocity. A power law equation can describe the variation of cloud fall velocity, $u_{f0}/u_\infty = D^{-3/4}$ with the R^2 value of 0.94. The proposed equation is valid for particles up to 1mm in diameter and indicates that particles with 1mm size fall almost with its individual settling velocity. Variation of particle cloud velocity in comparison with settling velocity can be studied in non-dimensional form. Particle Reynolds number was found to be an important parameter to describe the particle cloud velocity. Similar power law equation

can be formulated to show the variations of cloud fall velocity with particle Reynolds number, $u_{f\infty}/u_{\infty}=5.35Re_p^{-1/3}$.

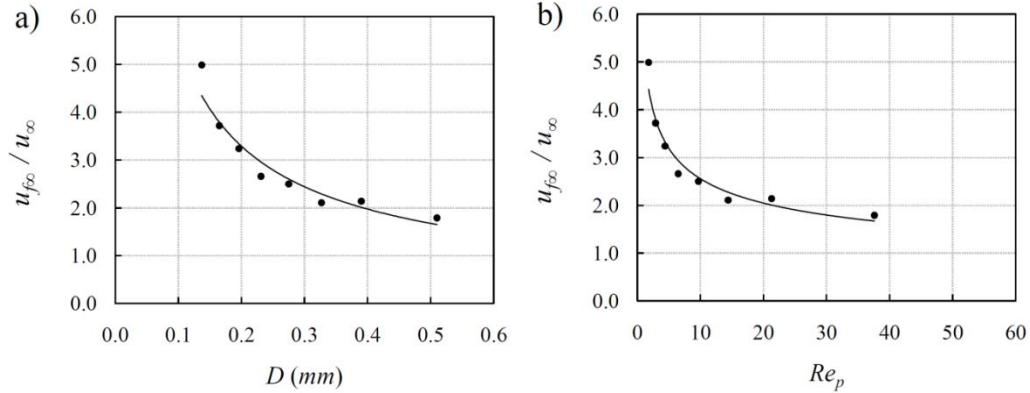


Figure 4-7: Variations of the settling velocity of the sand jet front, $u_{f\infty}$ with the effect of particle, D and particle Reynolds number, Re_p corresponding to experiments B1 to B8.

Effect of nozzle diameter and particle size on the frontal velocity of sand jets u_f , can be studied by comparing the corresponding frontal velocity of a single-phase water jet u_b , having the same initial buoyancy flux, B . Rajaratnam and Yasmin (1992) found that the frontal velocity of a water jet is 0.54 times of the centreline velocity of a steady jets u_m (Eq. 4.8). Figure 4-8 shows the ratio of the frontal velocity of sand jets to the frontal velocity of water jets. As can be seen from Figure 4-8a, this ratio is close to one at the nozzle but, it increased up to the value of 3 far from the nozzle. Since particles concentrated at the jet's center, the wake generated by particles enhanced the frontal velocity of sand jets. Consequently, the frontal velocity of sand jets at $x/d = 300$, become 3 times greater than its corresponding frontal velocity of a single-phase buoyant jet (Figure 4-8a). Figure 4-8b shows that particle size can have a significant effect on the frontal velocity of sand jets. At $x/d = 100$, small particles can only increase the frontal velocity of the sand jet 50% more than the corresponding single-phase water jet. Whereas at the same location, larger particles can enhance the frontal velocity almost 3 times of

the corresponding single-phase water jets. The logarithmic plots of u_f / u_b versus x/d were shown in Figures 4-8c and 4-8d. Effect of nozzle size on the frontal velocity in logarithmic scale shown in Figure 8c indicated that the sand jet front velocity decelerates at the rate of $-1/5$ whereas this value for a single phase buoyant jet was $-1/3$ (Papanicolaou and List, 1988).

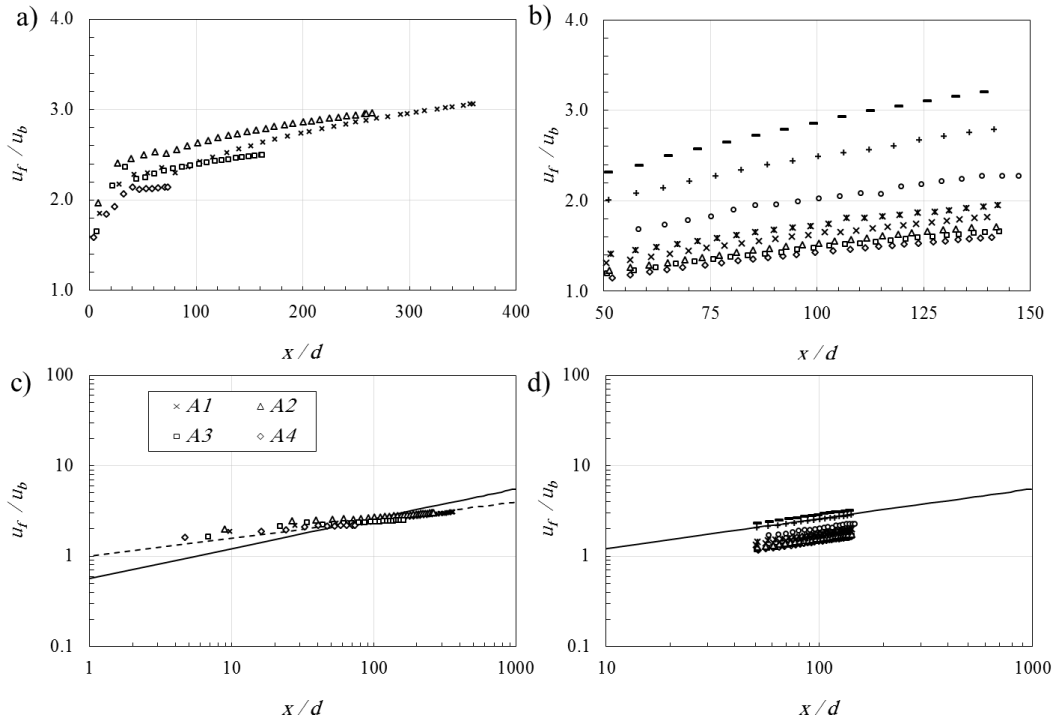


Figure 4-8: Effect of nozzle size and particle size on the frontal velocity of the sand jets, u_f , normalized with the frontal velocity of the water jet, u_b . a) Variations of the normalized frontal velocity along the jet axis for experiments A1 to A4. b) Correlations of the normalized frontal velocity along the jet axis for experiments B1 to B8. c) Effect of nozzle size on variations of the normalized frontal velocity plotted in logarithmic scale. d) Effect of particle size on development of the frontal velocity plotted in logarithmic scale.

Effect of particle size on frontal velocity is related to how particles respond to the vortex motion of the surrounding fluid which can be evaluated by the initial Stokes number, S_{i0} (Eq. 4.13). The initial Stokes number in this study ranged from 0.08 to 0.8. In release of particles with small diameter (i.e., small initial Stokes number), particles were

dragged by vortices generated by the jet's shear layer and were swept upward from the frontal region. This resulted in relatively smaller frontal velocity and larger front head (see Figure 4-3). Whereas larger particles with higher relaxation time can not immediately respond to vortices and tend to concentrate at the core region of the frontal head. This causes the frontal velocity enhancement of the larger particles.

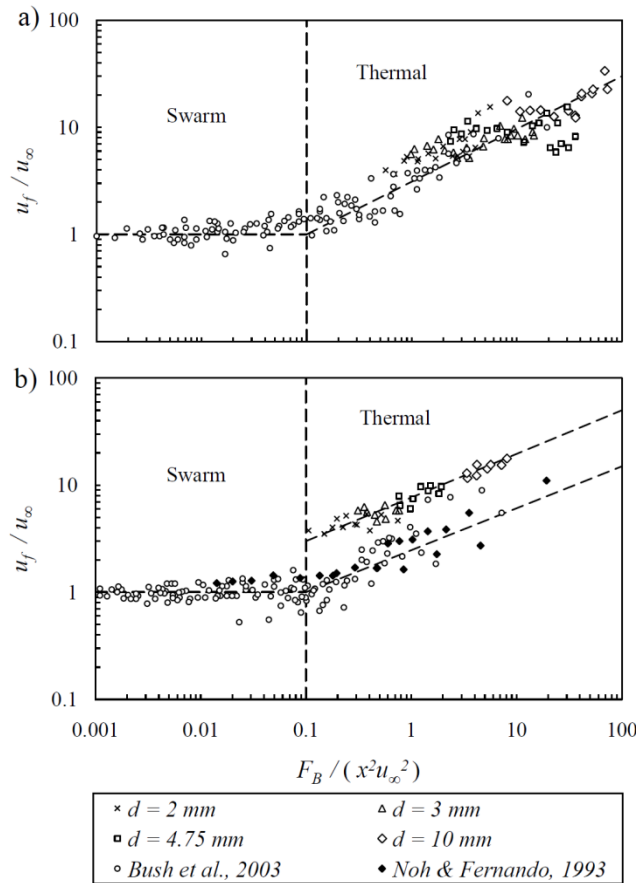


Figure 4-9: Effect of nozzle size on the correlation between normalized frontal velocity and normalized buoyancy at a) $10 < x < 30$ cm and b) $30 < x < 60$ cm. Dashed line distinguishes from the swarm and the thermal regimes.

Settlement of a particle cloud was classified into thermal and swarm regimes (Bush et al., 2003; Noh and Fernando, 1993). The dependence of normalized cloud frontal velocity on normalized buoyancy of particles passed through different nozzle sizes is shown in Figure 4-9. The experimental results of Bush et al. (2003) and Noh &

Fernando (1993) were added in this figure for comparison. Since Noh & Fernando (1993) employed a rectangular nozzle of 15.3 cm x 1.0 cm, the cloud velocities were normalized with the buoyancy force per unit width of the nozzle.

In order to be consistent with the other data, experimental observations of Noh & Fernando (1993) were renormalized with the total buoyancy force. Figure 4-9a illustrated the variation of the normalized cloud speed (u_f / u_∞) with normalized buoyancy, $F_B / (x^2 u_\infty^2)$ at $10 < x < 30$ cm. It can be seen from Figure 4-9a that the sand jet behaved as thermal at $10 < x < 30$ cm. The presented results appeared to collapse rather well with the particle cloud measurements found in the literature.

The correlation between the mentioned normalized parameters at $30 < x < 60$ indicated that the jet's frontal velocity was higher than the particle cloud velocity. The particle cloud velocity measured by Noh & Fernando (1993) in the swarm regime was found to be higher than the Bush's measurement (Figure 4-9b). This may be due to the fact that in Noh & Fernando's experiments, particles issued from a rectangular nozzle. This can reduce the cloud expansion rate in comparison with the release of particles from circular nozzle which resulted in a higher frontal velocity. Bush et al. (2003) found the dependence of parameters as

$$\frac{u_f}{u_\infty} = C_u \frac{F_B^{1/2}}{x u_\infty} \quad (4.15)$$

The scaling coefficient of C_u was reported as 3.0 ± 0.4 for the particle cloud velocity (Bush et al., 2003). C_u was also computed from our series B experiments. At $10 < x/d < 30$, $C_u = 2.48 \pm 0.5$ with a regression coefficient of 0.81. At $30 < x/d < 60$, $C_u = 5.65 \pm 0.2$ with the R^2 value of 0.93. Relatively higher value of C_u at $30 < x/d < 60$ could

be related to the continuous release of particles in the present study in comparison with Bush et al. (2003) where a fixed mass of particles was released into the ambient water.

The relationship between particle mass and nozzle diameter in this study can be described by a gravity driven piston-tube arrangement. In piston-tube arrangement for generating a buoyant thermal and vortex rings, a strong correlation was reported between the frontal velocity of a vortex and the aspect ratio of the piston, L/d [Bond and Johari (2005); Shusser and Garib (2000)]. By calculating an equivalent tube height using the sand mass and assuming the void ratio of 0.4, the L/d ratio in this study ranged from 79 to 395. By considering the maximum payload mass of 50 g and funnel diameter of 1.9 cm in Bush et al. (2003) experiments, the maximum L/d ratio can be calculated as 11.8. The higher aspect ratio in this study could be the main reason for obtaining a relatively higher frontal velocity (i.e., larger scaling coefficient) in comparison with Bush's experiment. Relatively smaller nozzle diameter in this study reduced the inter-particle spacing and caused a grouping effect between sand particles.

In this condition, particles fell behind the wake of the frontier particles, resulted a higher frontal velocity. On the other hand, relatively large nozzle diameter and small payload masses in Bush et al. (2003) and Noh and Fernando (1993) experiments caused larger inter-particle spacing which prevented the grouping effect and caused lower cloud velocity. The extreme case with the small L/d ratio could be the spreading of a few particles on the water surface causing the settling of individual particles with the settling velocity from the moment of release.

4.6 The Growth Rate of Jet Front Width

The growth of the jet front width, b , during its movement is studied in this section. The frontal width of sand jet was measured using the image processing method

described earlier in section 4-2. In series A, the frontal width was measured along the jet axis and the growth rate of $db/dx=0.125$ was found. It was found that the effect of nozzle diameter on the growth rate of the front head was negligible. Since the frontal width was measured in a short distance in series B (i.e., ~37 cm), the growth rate of the jet front cannot be measured with a reasonable accuracy. The frontal width of sand jets with relatively small particles fluctuated along the jet axis due to the presence of strong vortex motion. The frontal width measured from series A experiments were compared with the growth rate of sand jet front and thermal front with small L/d ratio.

In order to study the effect of particles on the size of frontal head, the growth rate of sand jet front was compared with that of a water jet and that of a buoyant plume (Figure 4-10). The growth of a water jet front is about two times faster than the sand jet front. The proposed value of 0.25 for the growth rate (solid line in Figure 4-10) was obtained using thermal of heavy salt solution falling through fresh water as reported in Turner (1969). The spreading coefficient of a round thermal was calculated based on the project area entrainment hypothesis with the value of 0.36 (Lee & Chu, 2003).

Measurements were compared with similar experiments on thermal front with relatively lower L/d ratio (Bush et al., 2003; Noh and Fernando, 1993). In Bush's experiment mass loads of 1, 7 and 20 grams of 100 μm particles were used. Thermal with relatively large trailing part was observed in the release of large amount of particle, i.e., 20g. The excess momentum in the trailing jet pushed the jet front downward therefore, particles have less time to be dragged by the ambient eddies. As a result, low growth rate was expected in this regime. On the other hand, jets with low initial mass load (e.g., 1g) behave like a pure thermal and the growth rate would be significantly larger.

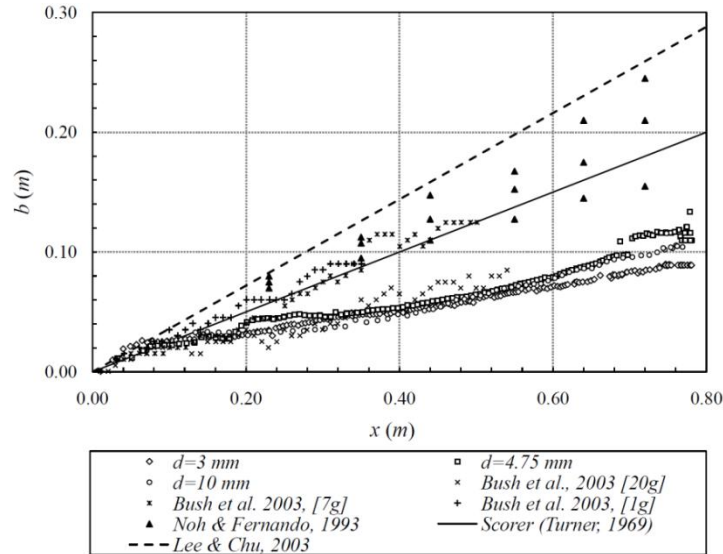


Figure 4-10: The growth rate of a sand jet front. Solid line is the growth rate of a starting water jet and dashed line is the growth rate of the thermal of a heavy salt. Numbers in brackets are the particles payload.

The spreading rate of the buoyant vortex decreases by increasing the circulation as explained by Turner (1962, 1969). Therefore, any extra momentum at the source (i.e., larger mass load in series A) which increases the circulation causes a reduction on the angle of spreading and less mixing with the environment. As an example, the instant release of 240 μm particles through a rectangular nozzle (15.3 cm x 1 cm) was compared with our experiment and the results are shown in Figure 4-10 (Noh and Fernando, 1993). As can be seen from Noh and Fernando's measurements the thermal growth rate is significantly larger than jet front growth obtained from experiments in series A. Comparison of the particle thermal growth with the water thermal growth shows that particle cloud generated by 240 μm particles can reduce the spreading rate from 0.36 to around 0.3.

4.7 Axial and Radial Velocities

Instantaneous velocities of the sand jets having different particle sizes were studied at three locations, $x/d = 75, 100$ and 125 and the results are shown in Figure 4-11. The instantaneous velocity measurements were started when the frontal head entered into the region of interest and were finished when the frontal head left the region of interest (see Figure 4-4).

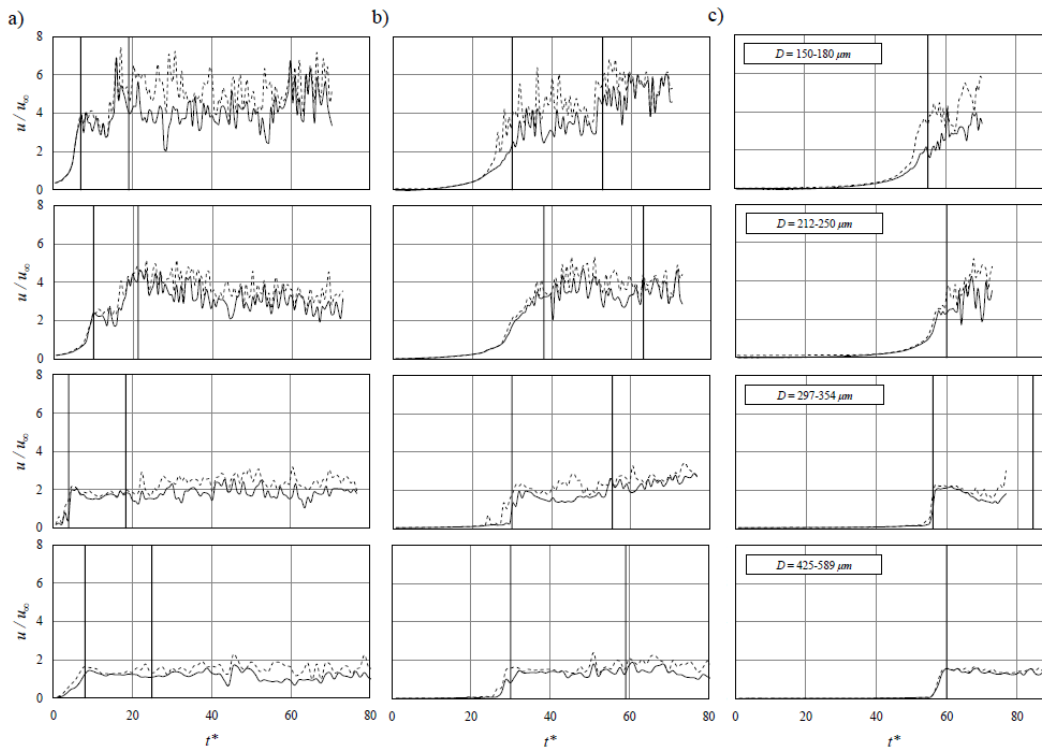


Figure 4-11: Axial frontal velocity at three fixed points located at $x/d = 75, 100,$ and 125 corresponding to cases B2, B4, B6 and B8. Solid line represents the axial velocity at the jet centreline and dashed line represents the maximum axial velocity at the cross section. The parallel lines indicate the times when the frontal head entered to and exited from those fixed locations of $x/d = 75, 100,$ and 125 .

The parallel lines indicate the times when the frontal head entered to and exited from those fixed locations of $x/d = 75, 100,$ and 125 . The instantaneous velocity at $x/d = 75$ (left column in Figure 4-11) shows the difference between the average velocity of the frontal head in comparison with the average velocity of the trailing part of the jet. This ratio was found to be larger than the single-phase case (i.e., 0.54) with the value of 0.69

and 0.64 for experiments B2 and B4, respectively. In sand jets with larger particles, the difference between the frontal head velocity and the velocity of the trailing part were found to be negligible ($u_f/u_b \approx 1$). This indicated that the frontal head velocity reached the velocity of the trailing part of the jet. In the presence of large particles, the frontal head vortices became weaker and particles fell vertically whereas, small particles can follow the front vortices and only the vertical component of particles can act as the frontal head velocity. The excess buoyancy force of the particles and the wake induced by particles can also result in the enhancement of the frontal velocity of sand jet. That changed the frontal head velocity of sand jet from 0.54 to 1.

The instantaneous velocity can be measured at the centreline of the jet, u_{axe} or the maximum velocity at that profile can be recorded, u_m . Solid lines in Figure 4-11 represent the front velocities obtained at the centre of the jets and dashed lines represent the maximum instantaneous velocities in the section. Low frequency movement of the frontal was observed during the experiments which can change the location of maximum axial velocity. Deviations between the obtained velocities at the jet's centre, u_{axe} and u_m with normalized time indicated that the maximum front velocities did not remain at the jet centre and meandered with time. The deviation of the peak axial and radial velocities from the axis of the jet can also be seen in Figure 4-12 where the axial and radial velocities studied at $t^* = 70$.

The water velocity induced by the falling frontal head of particle cloud can be formulated by approximating the frontal head as a solid ball with a radius of a passing through a potential fluid. By employing the potential flow theory,

$$u_r = u_m \left[1 - \frac{a^3}{r^3} \right] \cos \theta$$

(4.16)

Here u_r is the velocity of surrounding water, r is a radial distance from the ball and θ is the angle from the axis of flow. The velocity of surrounding water is zero far from the head and it increases to its maximum value at the front location. In order to apply the potential flow solution, the distance required for the jet to pick up the velocity from $0.1u_m$ to u_m was called the pickup distance and this distance was measured at $x/d = 100$ from Figures 4-11b. The thickness of the frontal head was measured from the corresponding images and those frontal thicknesses were shown with parallel solid lines in Figure 4-11.

The pickup distances for small and large particles were 4.62 and 2.2 cm, respectively. Considering the front location, e.g., 40 cm and the front growth rate of 0.125 for small and large particle cloud, the pickup distances for small and large particles become 0.924 and 0.44 times of the front radius, respectively. According to the potential flow solution, the pickup distance at $u_r / u_m = 0.1$ is 1.036 times of the front radius. This indicates that the solid sphere can influence on the ambient water further downstream. This difference on the pickup distance is mainly believed to be caused by the porosity of the front sphere. Larger amount of small particles can pass through the nozzle in comparison with large particles. Therefore, small particles can produce a front sphere with lower porosity compared to the larger particles and behave similar to a solid sphere (i.e., comparing 0.925 to 1.036). On the other hand, large particles produce a jet front with high porosity. Consequently, the effect of particle on ambient water would be less significant.

Axial and radial sand velocities were obtained from the experiments and the corresponding results at three cross-sections of $x = 30, 40$ and 50 cm from the nozzle are shown in Figure 4-12. The normalized time scale $t^* = 70$ was selected to observe the entire frontal head and the trailing jet (see Figure 4-4).

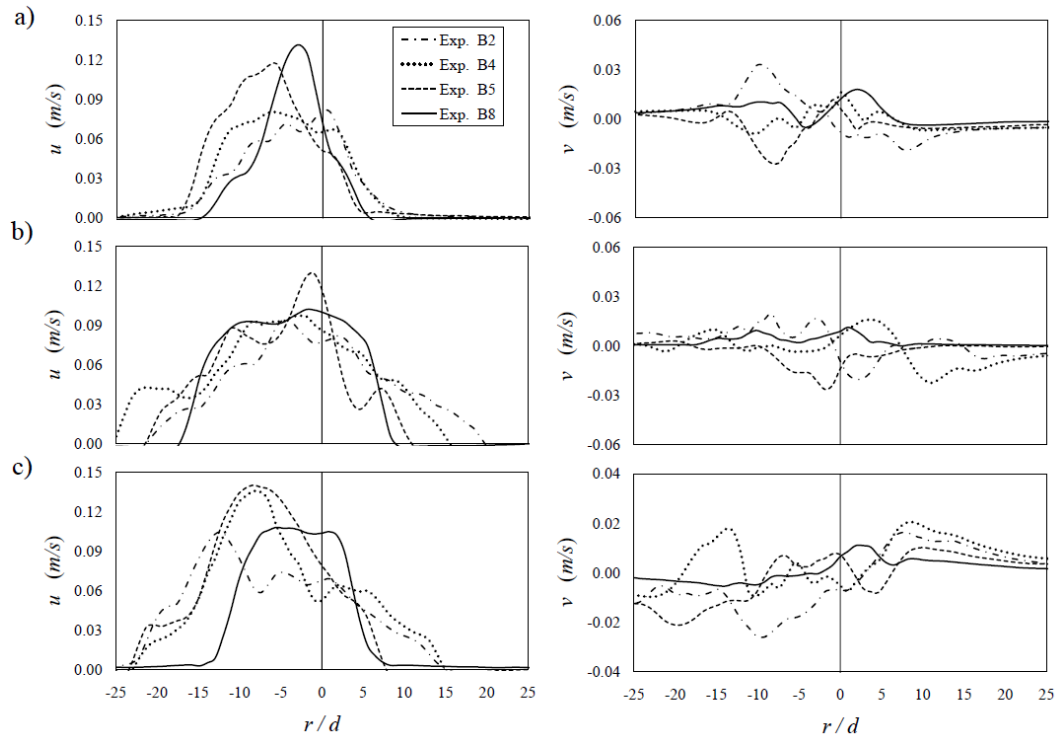


Figure 4-12: Instantaneous axial (left) and radial (right) velocities of experiments B2, B4, B5 and B8 at $t^* = 70$. a) $x/d = 75$, b) $x/d = 100$ and c) $x/d = 125$.

According to the selected normalized time in Figure 4-12, the cross-sectional views at $x/d = 125$ represent the instantaneous axial and radial velocities of the frontal head. Accordingly, the profile view at $x/d = 75$ and 100 indicate the effect of particle size on the trailing part of the sand jets. Semi-Gaussian profiles were observed on the instantaneous axial velocities even though no time averaging was performed. Considering the effect of particle size on the axial velocity of the trailing jets it may be deduced that, the jet spreading was affected by the particle size. Hence, larger particles tend to spread

less than smaller particles. In addition, as larger particles are able to generate stronger wakes behind them, following particles require less energy to overcome the drag force resulted in higher peak velocity. However, entrainment mechanism in particle clouds descendent can reduce the particle concentration significantly. Therefore, larger particles fallout with their settling group velocity, u_{fc} in relatively earlier stages.

Vortex size, its location in a transient jet can be studied by employing radial velocity at different locations. Figure 4-12 shows the variations of the instantaneous radial velocities of the frontal head and the trailing jets. It was observed that, sand jets with small particles can generate more vortices compare to that of the large particles. The radial velocity peaks indicated the existence of vortices at each location. As can be seen from the radial velocity profiles of the frontal head, i.e., $x / d = 125$, with small particles, large number of vortices were generated, and those vortices distribute over the entire area of the front as well as the trailing jet. The ratio between the radial to the axial velocities was found to be 0.25 for the smallest particle (Exp. B2). This ratio became smaller for the higher particle Reynolds numbers, (e.g., 0.15 for Exp. B4 and B5).

In the event of higher Re_p , the maximum radial velocity reached up to 10% of the corresponding axial velocity. In the presence of larger particles, strong shear layer was formed in the frontal edge and the trailing part of the jets. The vortices generated in the presence of larger particles were located at the boundary of the jet, therefore those particles were not able to generate sufficient circulation in the surrounding water. It was found that at $x / d = 100$, the ratio of radial to axial velocities were between 0.09 - 0.2. Sand jets with relatively small particles can also generate large number of eddies. The maximum size of the frontal vortex in Exp. B2 was measured from raw images and it was found to be around 15 times of the nozzle diameter (≈ 6 cm). This value for the largest particles (Exp. B8, $Re_p = 37.5$) was almost 5 times of the nozzle diameter.

The computed axial and radial velocities with non-dimensional time, t^* , at three locations, $x/d = 75, 100, 125$ are shown in Figure 4-13. The jet front passed $x/d = 75$ at $t^* = 10$ and the computed axial velocity in Exp. B2 was 4.2 times larger than the individual particle settling velocity.

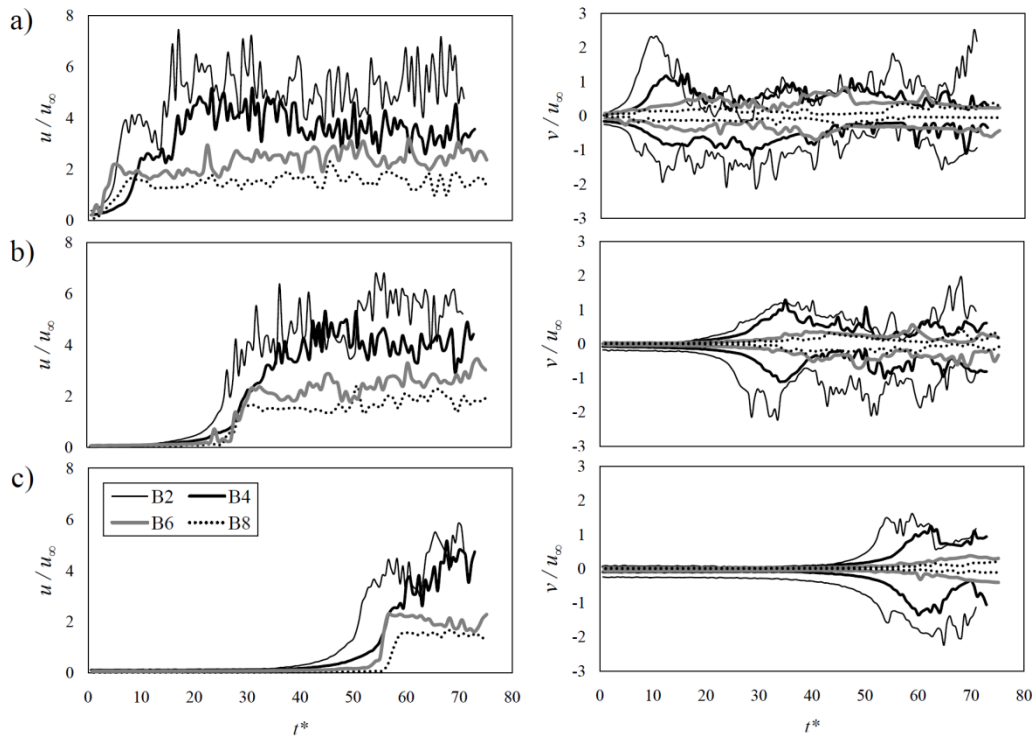


Figure 4-13: Variations of the axial (left) and the radial (right) water velocities with normalized time at a) $x/d = 75$, b) $x/d = 100$, and c) $x/d = 125$.

For relatively large particles (Exp. B8) the frontal velocity was 1.8 times of the individual particle settling velocity. A vortex ring formed by interaction of particles with the surrounding water increases the axial velocity right after the frontal head. Similar vortex profiles were observed from numerical study of starting buoyant jets (Wang et al., 2009b). Relatively large change in the axial velocity was observed after the jet front passed the observation point (i.e., $x/d = 75, 100$ and 125) and the changes become significant for the sand jets with small particle sizes. The obtained frontal velocity from

the PIV measurements at $x/d = 125$ with that from pixel search method indicated a good agreement within -11% to +16% errors. This indicates that the pixel search method can provide the frontal velocity measurements with reasonable accuracy.

The formation of the eddy structure was examined by considering the magnitude and the direction of radial velocities. Particles can influence on the vortex size as well as the magnitude of the radial velocities. Variations of the radial velocity with time were investigated at three locations and the computed results were illustrated in Figure 4-13. At $x/d = 75$, the frontal vortex ring can be detected at the location of the maximum radial velocity. Similar to the axial velocity, the radial velocity reached the peak value at around $t^* = 10$ and the computed radial velocity for the jet with $Re_p = 2.9$ was 2.3 times larger than the individual particle settling velocity. This ratio reduced to 1.3 when the jet front passed the point at $x/d = 125$.

An oscillatory behaviour was observed on the variations of the axial and radial velocities with time. These oscillations were more noticeable for the transient jets with small particle sizes (e.g., Exp. B2, $Re_p = 2.9$). The time scale of oscillation can be estimated by finding the peak values on the axial and radial velocities. The estimated time scale of oscillation for the trailing part of the sand jets with small particles, (e.g., Exp. B2), was found to be between 5.5 to 9 times of the non-dimensional time scale, t^* (see Figure 4-13a). Based on the measured oscillation time scale, the period of oscillation was found to be in the range of 0.34-0.55 sec.

Contour plots of the axial and radial velocities at $t^* = 60$ is shown in Figure 4-14. In the presence of small particles, large number of eddies generated in those regimes resulted in high spreading rate of the jet (Figure 4-14e and f). From the experimental visualisation, it can be observed that the transient sand jets formed a symmetrical bowl-

shaped front when $Re_p = 10$ (Figure 4-14c). Maximum axial velocity was observed in this class with almost symmetrical vortex structure (Figure 4-14 f).

The frontal head changed from a bowl-shaped to a cone, and the frontal tip became narrower and sharper when $Re_p > 10$ (Figure 4-14 d). It can be seen from contour plots of the axial velocity that, larger particles concentrated at the core region of the front jet, resulted in an increase of the axial velocity and reduction in radial velocity of the sand jet front with particle size (Figure 4-14d and h).

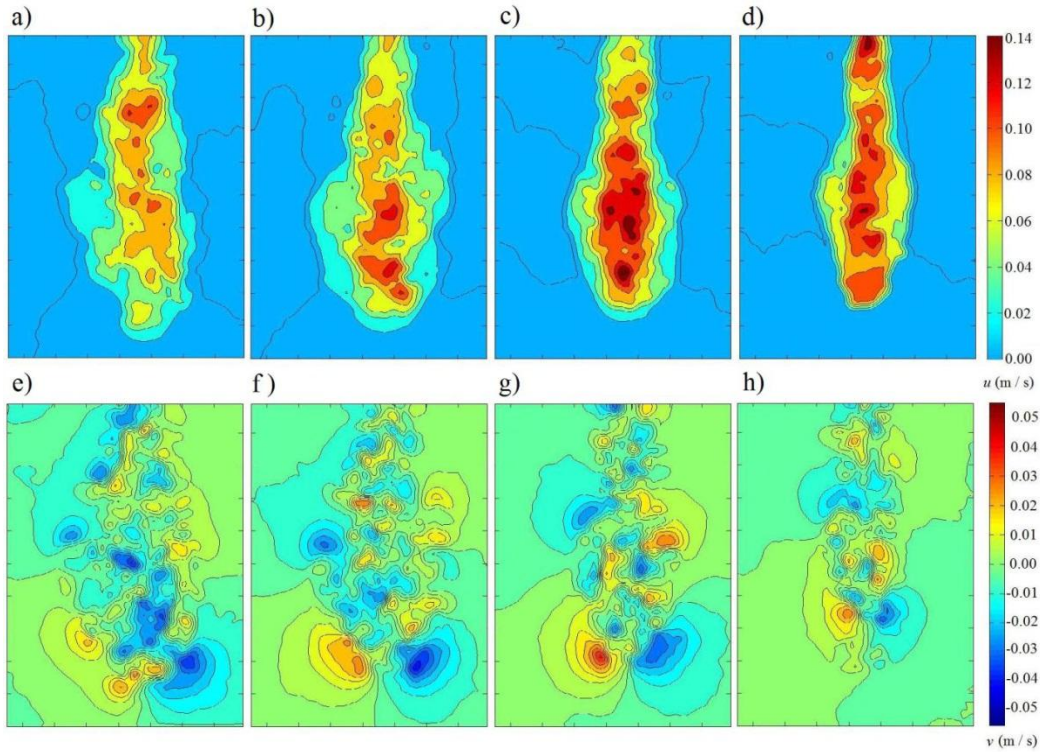


Figure 4-14: (Color online) Contour plots of the axial velocity, u , and the radial velocity, v , and effect of particle Reynolds number on the shape and speed of jet front at $t^* = 60$. a-h) Experiments B1 to B8.

4.8 Vortex Structure

Two dimensional velocity fields obtained from PIV measurements can provide new insight into the dynamics of the sand jets. Effect of particle size on the formation of the frontal head and the trailing jets was studied and the computed results are shown in Figure 4-15. Four cases of B2, B4, B5 and B7 were presented at $t^* = 60$ with the corresponding particle Reynolds number of $Re_p = 2.9, 6.5, 9.7$ and 21.3 , respectively (Figure 4-15a-d).

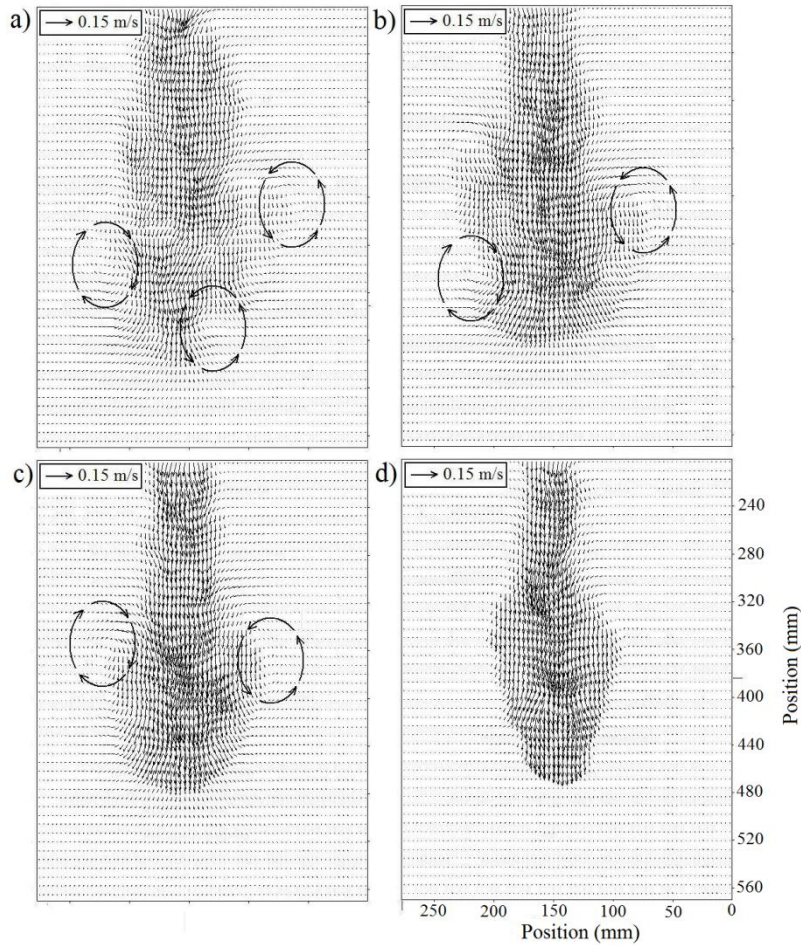


Figure 4-15: Two-dimensional velocity vector field obtained from PIV measurement technique at $t^* = 60$. a) B2, b) B4, c) B5 and d) B7.

As can be observed in the velocity field, small particles in the transient jets can follow the water eddies and generate stronger vortex field. Figure 4-15a illustrates the formation of vortices in the frontal head of the jets. It was found that small particles generated vortex field were reasonably symmetric about the axis at the critical value of $Re_p \approx 10$ (see Figure 4-15c). For particle clouds passing the critical value, i.e., $Re_p > 10$, particles tend to fallout vertically and the background flow tends to be less affected by the particle's movement. In this condition, weak vortex structure can be formed and the entrainment capacity drops to its minimum level.

The obtained velocity pattern of the transient sand jets having the particle size range of 212-250 μm (Exp. B4) was captured at $t^* = 60$. The detailed views of the jet's vortices obtained from the Galilean decomposition method with the location of each vortex in the velocity field illustrated in Figure 4-16. In order to extract vortex structure, a region of interest is selected in the velocity field, and axial and radial velocities are averaged over that selected region. The obtained averaged velocities can be used as the Galilean convectonal velocities.

According to the computed axial and radial convection velocities, the obtained vortex field can be classified into three categories. The first group of vortices can be resolved by employing the axial convection velocity, u_c , equal to 20% of the maximum axial velocity of the jet, u_m . The detailed views of this group are depicted in Figure 4-16 [b, c, d, e, and i]. Since the averaged axial velocities in these regions were small ($\sim 2\text{-}3$ cm/s) and small axial convection velocities were required for decomposition in this regime, the locations of the vortices can be detected in advance by visualizing techniques.

Adrian et al. (2000) reported that completely circular vortices have a perpendicular axes relative to the velocity vector plan whereas vortices making any angle

appear as ellipses. Depending on the radial convection velocity, the detected vortices could be circular or ellipsoidal. It should be mentioned that relatively circular vortices can be detected with small convection velocity in the radial direction, v_C .

Figure 4-16 [c and i] can be considered as an examples of semi-circular vortices ($v_C = 0$). Relatively large radial convection velocity i.e., $u_C = v_C = 0.17u_m$, provided an elongated ellipsoidal vortex (Figure 4-16e). The second class of vortices were observed behind the jet front, where high rotation was expected, and in the trailing jets, where the shear strength was significant.

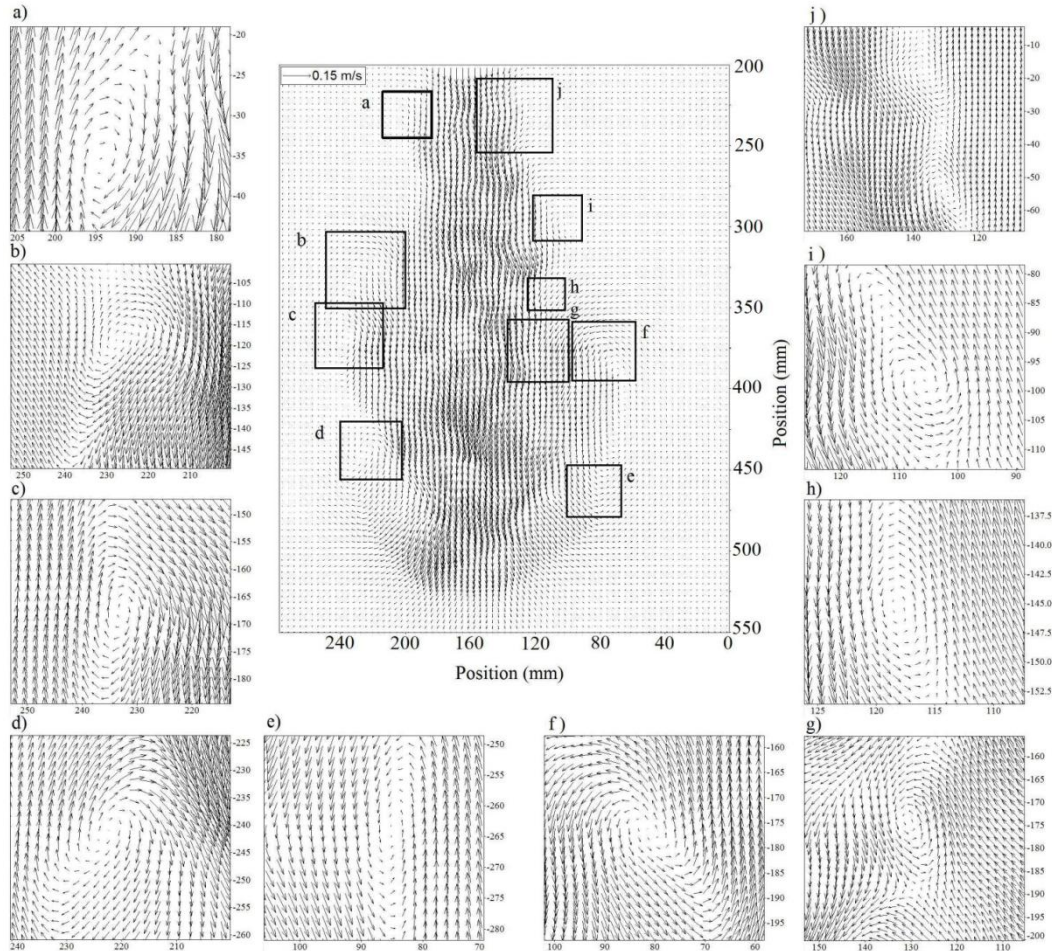


Figure 4-16: Velocity vector fields in transient turbulent sand jets illustrated at $t^*= 60$ (Exp B4).

The calculated convection velocities in those locations have fallen in the range of $0.2 u_m < u_c < 0.5 u_m$. The close-up views of this group are shown in Figure 4-16 [a, f, h, and j]. Vortices in this regime provided similar behaviour influenced with the radial convection velocity. Figure 4-16 [a and h] with $v_c = 0.02 u_m$, shows a semi-circular vortex structure whereas Figure 4-16f with $v_c = 0.125u_m$ indicate an elongated ellipsoid vortex. It is possible to resolve small vortices inside the turbulent jets with the Galilean decomposition approach, even though it seems all particles falling down in this region. Figure 4-16g presented a vortex structure that decomposed with $u_c = 0.83u_m$. After subtracting almost 83% of the axial velocity from the velocity vector field, the magnitude of axial and radial velocities become close to each other. Hence, completely circular vortex field was resulted.

The Galilean method is one of the most straightforward techniques amongst other vortex identification schemes but it has a main disadvantage that it requires knowledge of the core location of vortex and its velocity. The most widely used vortex identification methods are based on the analysis of the velocity gradient tensor into a symmetric and antisymmetric components, $\nabla u = S + \Omega$. where S is the strain rate tensor and Ω is the vorticity tensor (Kolář, 2007).

$$\nabla u = \frac{\partial u_i}{\partial x_j} = \frac{1}{2} \left(\frac{\partial u_i}{\partial x_j} + \frac{\partial u_j}{\partial x_i} \right) + \frac{1}{2} \left(\frac{\partial u_i}{\partial x_j} - \frac{\partial u_j}{\partial x_i} \right) \quad (4.17)$$

Many vortex identification techniques were proposed based on the local criterion schemes. Chakraborty et al. (2005) analysed the current vortex identification schemes such as the work of Hunt et al. (1988), Jeong and Hussain (1995), Chong et al. (1990) and swirling strength identification method, λ_{ci} , (Zhou et al., 1999). A recent comparison of different vortex identification techniques and their limitations was made by Kolář

(2007). In swirling strength computation, the strength of any local swirling motion can be quantified by computing the imaginary part of the complex conjugate eigenvalues of the velocity gradient tensor to identify vortices. Vortex identification based on swirling strength is frame independent and prior choice of convection velocity is not necessary.

Figure 4-17 shows the identified vortices embedded in the sand jet front of experiment B4 at $t^* = 60$. Vortices were identified by employing the swirling strength technique. In order to capture all various vertical structures and reduce the background noise the value of λ_{ci}^2 was used (Zhou et al., 1999).

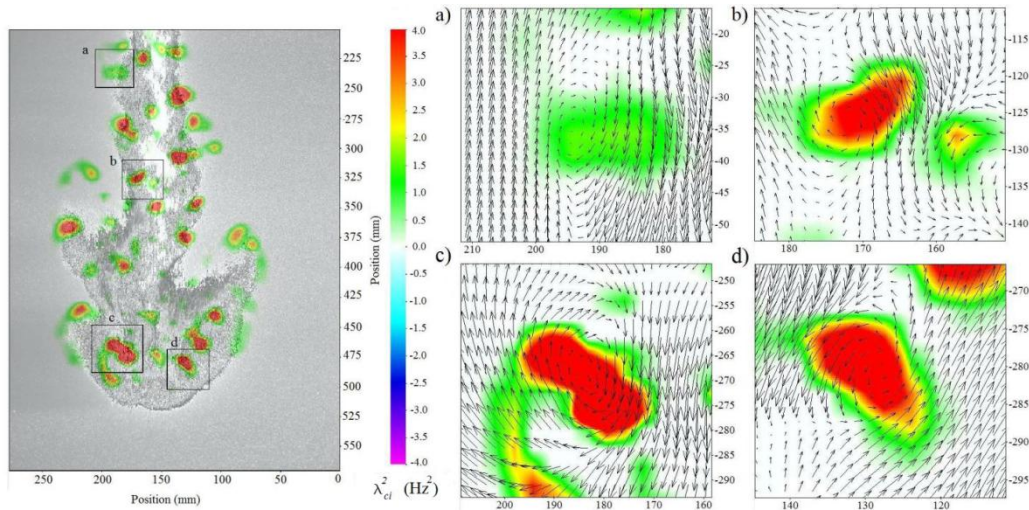


Figure 4-17: (Color online) Identification of vortices in sand jet front at $t^* = 60$ (Exp. B4).

A series of vortices were extracted in the trailing part of the jet indicating high shear flow at the interface of the jet with the ambient water. Since the shear flow in this region is high and the axial velocity is smaller than the central velocity of the jet, the magnitude of the convective velocities become similar resulted in formation of semi-circular vortices (Figure 4-17a-b). Strong vortices were formed at the edge of the sand jet front caused the majority of the flow entrainment. The contour plot of the swirling

strength can clearly show the roll up of the frontal vortices (Figure 4-17c). Effect of particles on the size, location and magnitude of the vortices was studied by extracting the vorticity from the velocity vector field at $t^* = 60$ for corresponding cases of B2, B4, B5 and B7.

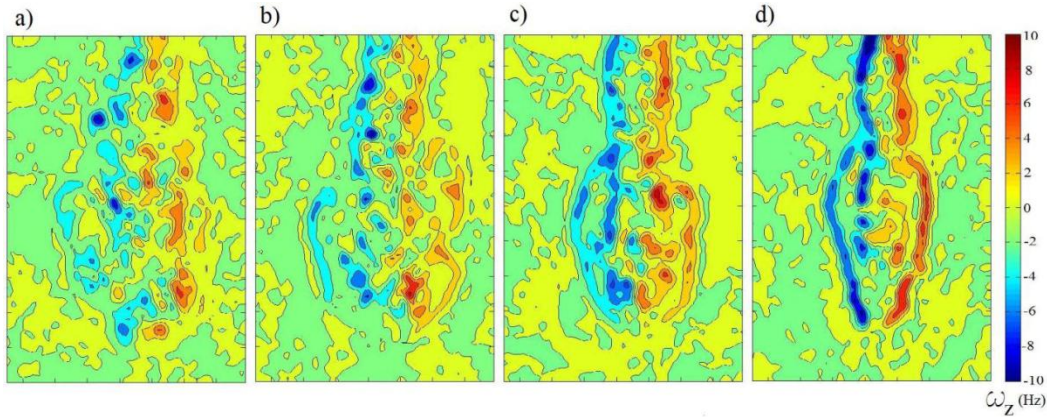


Figure 4-18: (Color online) Vortex structures generated by interactions of particles into the water bodies at $t^* = 60$. a) B2, b) B4, c) B5 and d) B7.

Figure 4-18 shows the contour plot of vortex structure generated by interactions of particles into the water bodies. As can be seen from the contour plot, maximum vorticity generated by particles was found to be 10 Hz.

Peak vorticity located at the boundary of the jets and centre of the front. Effect of particle size on the vortex structure of the transient jets was also depicted in Figure 4-18. As it is shown, small particles are not able to generate highly rotational fields but they can spread the vortex field over the entire area of the front. On the contrary, large particles can create a significant high shear layer in the boundaries between the jet and the surrounding fluid (Figure 4-18d).

4.9 Turbulence Modulation

The intensity of turbulence can be defined as the ratio of the velocity fluctuation, u' , to the mean velocity of the flow, u . Turbulent intensity can be shown as $I=u'/u$ which commonly expressed as a percentage of the mean velocity of the flow. Two major mechanisms determine the energy production and dissipation of turbulence in the particle-laden two-phase flows. Close to the nozzle, high velocity gradient generates strong shear, and particles enhance the flow instability and turbulent intensity in comparison with the corresponding single-phase flow. In this region, energy is transported from the particles to the carrier phase resulted in turbulence augmentation. Far from the nozzle, the filtering effect of particles consume the energy of small eddies of carrier phase and more turbulence energy is dissipated.

Turbulence intensity of the trailing region of the sand jets was measured and the effect of particles on turbulence modulation of two-phase turbulent jets was investigated in this section. The instantaneous axial velocities of the trailing part of the jet were averaged over time (i.e. 25-30 sec) and velocity fluctuations and turbulence intensities of the trailing jet were calculated. Effect of particle size was normalized with the most energetic eddy L_e , when only one phase is present. Wygnanski and Fiedler (1969) determined the integral length scale of the jet as $L_e = 0.0385 x$. The percentage change in turbulence intensity (CTI) can be calculated as $CTI = [(I_2 - I_1) / I_1] \times 100\%$. Here I_2 and I_1 are the turbulence intensities of the two-phase and single-phase flows, respectively.

The change in turbulence intensity of the trailing part of the starting sand jets is shown in Figure 4-19a. Experimental results of series B were used and turbulence intensities were calculated at $x/d = 75$ and 100. The CTI values obtained from Crowe (2000) were added for comparison. A value of $D/L_e = 0.1$ was reported as a threshold

which classifies the turbulence attenuation and augmentation (Gore and Crowe, 1989, 1991).

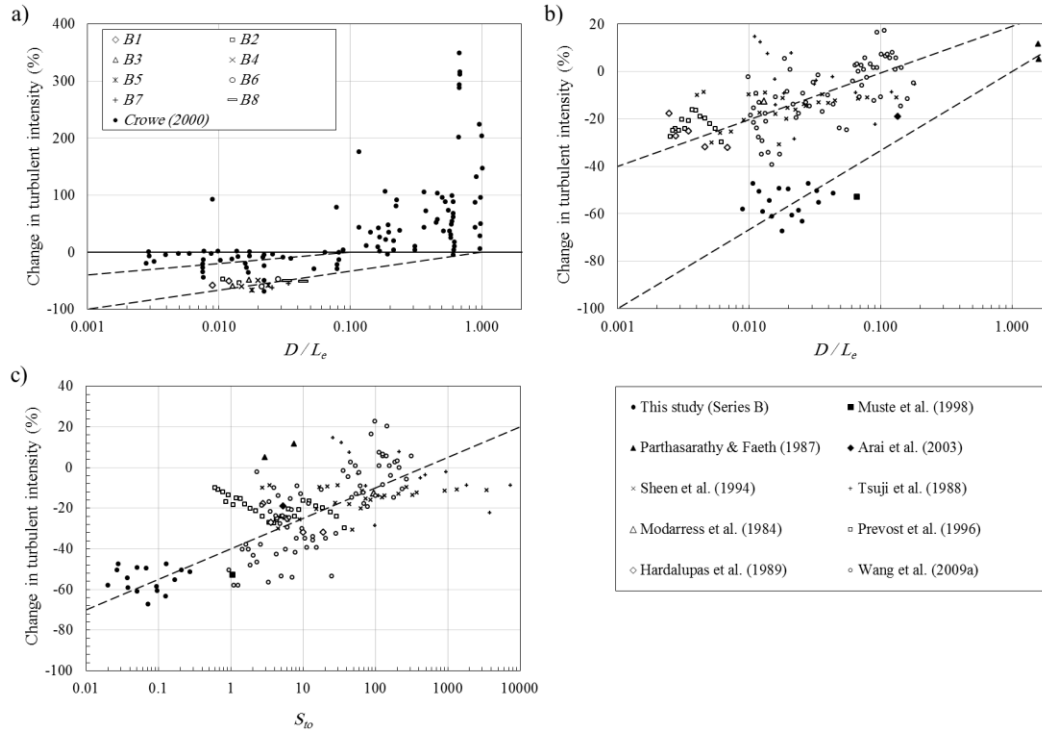


Figure 4-19: Turbulent attenuation of the two-phase turbulent jets. a) Change in turbulent intensity of a general two-phase system as a function of D/L_e , and the effect of particle size D , on turbulent modulation of solid-liquid jets. Dashed lines show the modulation of turbulence of the solid-liquid and the solid-air two-phase turbulent jets. b) Turbulent attenuation of the two-phase turbulent jets as a function of D/L_e . Open symbols are solid-air turbulent jets and solid symbols are solid-liquid turbulent jets. c) Effect of Stokes number on the turbulence modulation of the two-phase turbulent jets.

The energy transfer between particles and ambient water is characterised by the particle relaxation time (Eq. 4.12). Particles can only respond to the turbulent eddies with the same or longer characteristic time scales as the particle relaxation time scale. Consequently, smaller particles can respond to various range of turbulence fluctuation and dissipate more turbulent energy. As shown in Figure 4-19a, smaller particles (Exp. B1) dissipate more energy compared to the larger particles (Exp. B8). Crowe (2000)

correlated large numbers of laboratory experiments with different flow structures. This caused a difficulty to find a direct correlation between laboratory measurements. However, Crowe was able to show the trend between the normalized length scale of D/L_e and turbulent modulation.

A series of laboratory experiments on turbulent particle laden solid-gas and solid-liquid jets were chosen to study the effect of particles in turbulent modulation to find a possible formulation to describe the trend. The flow characteristics of each experiment were tabulated in Table 4-3.

Table 4-3: Principal characteristics of the two-phase solid-gas and solid-liquid turbulent jets.

Experiment	d (mm)	x/d	u_o (m/s)	D (mm)	ρ_p (kg/m ³)	c_o (%)	S_{to}
This study (Series B)	4.0	50 - 150	0.088- 0.115	0.138 - 0.507	2540	60	0.02 - 0.32
Muste et al., 1998	47x4	49	0.83	0.50 - 0.60	2650	0.04	1.07
Parthasarathy & Faeth, 1987	5.08	0 - 50	1.66	0.50	2450	2.4 - 4.8	3.0 - 7.60
Arai et al., 2003	5.0	0 - 15	1.84	0.389	2590	0.21	5.83
Sheen et al., 1994	15.0	0 - 90	20.0	0.21 - 0.78	1020	0.43	2.8 - 3560
Tsuji et al., 1988	20.0	0 - 20	11 - 24	0.17 - 1.40	1020	0.05 - 0.2	26 - 14810
Modarress et al., 1984	20.0	0 - 30	10.2	0.20	2990	0.04	96.8
Prevost et al., 1996	10.0	0 - 45	20.0	0.05	2540	0.004	4 - 38
Hardalupas et al., 1989	15.0	0 - 30	11.0	0.04	2420	0.005 - 0.03	2.8 - 19.6
Wang et al., 2009a	20.0	0 - 25	6.39 - 12.25	0.075 - 1.232	2450	0.14 - 0.24	0.94 - 315

Percentage changes in turbulence intensity of two-phase turbulent jets were plotted against length scale ratio of D/L_e and the results are shown in Figure 4-19b.

Higher dynamic viscosity of liquids (i.e., water) in comparison with gases (i.e., air) resulted in reduction of particle relaxation time which leads to the higher rate of turbulent dissipation. In addition, the wake generated by particles and particle fluctuations can die out quickly in viscous fluids. The following logarithmic equations were proposed to estimate the change in turbulence intensity of solid-gas (Eq. 4.18) and solid-liquid turbulent jets (Eq. 4.19), respectively.

$$CTI = 8.69 \ln(D / L_e) + 20 \quad (\text{for solid-gas turbulent jets}) \quad (4.18)$$

$$CTI = 14.48 \ln(D / L_e) \quad (\text{for solid-liquid turbulent jets}) \quad (4.19)$$

Data scatter presented in solid-gas turbulent jets could be due to the effect of particle concentration. Sheen et al. (1994) investigated the effect of particle concentration on the turbulence intensity of two-phase solid-gas turbulent jets. They found that increasing the particle concentration attenuates turbulence intensity. Therefore, particle-laden jets with higher particle concentration can result in smaller change in turbulence intensity. This is consistent with the experimental result of Tsuji et al. (1988) and Sheen et al. (1994).

Longmire and Eaton (1992) found that the local particle dispersion is mainly governed by the large-scale turbulent structure of the carrier flow. The Stokes number based on the time scale of the large structural eddy S_r , was employed to describe the effect of particles on turbulence modulation of particle-laden jets. The characteristic time scale of the large-scale turbulent structure along the jet's axis was then calculated by the axial velocity of the single-phase jet at any location u_c , and the dominant eddy length scale L_e as described by Wygnanski and Fiedler (1969). Different characteristics time scale can also be defined according to the study of Prevost et al. (1996). They selected the characteristic time as the ratio of $L = 0.1x$ to the standard deviation of the fluctuation

velocity on the jet axis $u'_{f,c}$. It can be shown that the Stokes number can be considered as a combination of the density ratio, the local Reynolds number and the critical length scale ratio of D/L_e at the same time.

$$S_t = \frac{\rho_p D^2 u_c}{18 \mu L_e} = \frac{1}{18} \cdot \frac{\rho_p}{\rho_f} \cdot \frac{u_c L_e}{\nu} \cdot \left(\frac{D}{L_e} \right)^2 \quad (4.20)$$

As can be seen from (Eq. 4.20), effect of particle concentration was not included in Stokes number which resulted in data scatter. Correlation between *CTI* and Stokes number was shown in Figure 4-19c. The measured *CTI* for 10 experiments on both solid-gas and solid-liquid turbulent jets collapsed onto a single logarithmic curve.

$$CTI = 6.5 \ln S_t - 40 \quad (4.21)$$

As can be seen in Figure 4-19c, the *CTI* values measured by Parthasarathy and Faeth (1987) indicated higher turbulent intensity in comparison with Arai et al. (2003). These two experimental studies were conducted in relatively similar conditions (see Table 4-3) except particle concentrations in Parthasarathy and Faeth study were 12-24 times higher than that in Arai et al. (2003). This indicates that the excess in particle concentration reduces the inter-particle spacing resulted in lower rate of turbulence attenuation. Experimental results of Tsuji et al. (1988), and Sheen et al. (2003) were consistent with our justification.

4.10 Summary and Conclusions

Experiments were conducted to study the effects of nozzle diameter and particle size on the behaviour of the starting sand jets and its associated fluid motion. Experiments were employed to investigate the effect of nozzle size with a range between 2 to 10 mm (series A) and with a relatively wide particle size range, i.e., 125-589 μm (series B).

The frontal shape and its formation were classified into three categories. Particle clouds act as a particle thermal when particle Reynolds number $Re_p < 10$. Kelvin-Helmholtz instability can be developed in the trailing jets since a strong shear layer was established in the jet boundaries and particle were relatively light enough to follow the water eddies. In the second class at $Re_p \approx 10$, particles fall out of the cloud in the form of a bowl-shaped swarm. Particles in this regime require longer time to respond to the water phase fluctuations. Hence, less dispersion resulted in the trailing section. For larger particles with $Re_p > 10$, particle clouds can penetrate through the water phase at a faster rate. As a result, the frontal head and vortex ring become narrower and weaker, respectively.

The jet frontal velocity was normalized with the particle settling velocity and was studied along the jets axis. It was found that this velocity is a function of nozzle diameter and particle size. The velocity ratio (u_f / u_{sc}) drops from the nozzle and approaches a constant far from the jet (i.e., $\sim x/d = 200$). Frontal velocity at this position called particle cloud fall velocity u_{fc} , and it was used as a velocity scale to normalize the duration time of experiment. It was found that the jet front terminal velocity of small particles were as large as 5 times of the individual particle settling velocity.

In order to study the effect of particles on the frontal velocity of the turbulent jets, the frontal velocities of the sand jets were compared with the measurement results of the frontal velocity of water jets found in the literature. It was found that close to the nozzle, there is almost no difference between those frontal velocities. However, effect of particles become significant along the jet axis resulted in increasing the particle cloud settling velocity. Variation of frontal velocity of sand jet along the jet axis can be formulated as a logarithmic function. The slope of correlation was found to be $1/5$ whereas this slope for a single-phase water jet was known to be $1/3$.

To investigate the effect of the particle excess momentum of the frontal velocity, the measured sand jet frontal velocities were also compared with the frontal velocity of particle thermals. The presented results at $10 < x/d < 30$ appeared to collapse rather well with the particle cloud measurements found in the literature. Whereas, at $30 < x/d < 60$, the measured frontal velocities were found to be higher than that of thermals. The excess frontal velocities of sand jets may be due to the effects of particle mass load and nozzle diameter.

The growth rate of front half-width was measured and the effect of nozzle diameter on the growth rate was studied. In order to investigate the effect of particles and the associated excess momentum generated by particles, the front half-widths measured in this study was compared with that of particle-laden thermal and single-phase front jets and thermals. It was found that the growth rate of the sand jet front is smaller than the growth rate of the water jet front.

Effect of particle cloud in surrounding water was studied by simulating the effect of a solid ball falling through a fluid using the potential flow theory. A pickup distance was introduced which is the distance measured from the sand jet front where the surrounding water velocity pickup from 10% of the sand jet front velocity. Effect of particle porosity on the particle cloud indicates that in presence of small particles, i.e., $D = 150\text{-}180 \mu\text{m}$, the pickup distance become 92.4% of the front radius whereas, this length is only 44% of the radius for relatively larger particles. The solution of Euler equations indicated that the identified pickup distance in potential flow is 3.6% larger than the front radius.

Vortex structure was identified by employing Galilean velocity decomposition and swirling strength method. Vortices were identified at each location by using the local axial and radial velocities as the Galilean convection velocities. Three regimes were

identified on the basis of magnitude of the employed convection axial velocity. The first category belongs to the group of vortices that requires small convection velocity to resolve. This group of vortices were obvious in the velocity vector fields. Moderate convection velocity was needed to detect vortices behind the jet front. In this case, the convection velocity were chosen in the range of $0.2 u_m < u_C < 0.5 u_m$, to resolve these types of vortices.

Relatively strong convection velocities were required to detect the vortices in the core region of the jets. In this study, the velocity fields decomposed with the 83% of the maximum axial velocity. Relatively circular vortices could be detected with small radial convection velocity whereas the large radial convection velocity was required to detecting an elongated ellipsoidal vortex. Vortices were identified by employing the swirling strength technique. Strong vortices were formed at the edge of the sand jet front caused the majority of the flow entrainment.

Velocity fluctuations and turbulent intensities of the tailing part of the sand jet were computed and the change in turbulent intensity from the corresponding single-phase flow was calculated to study the turbulence modulation. It was found that smaller particles attenuate the turbulence much faster than larger particles. A logarithmic formula was developed for prediction of turbulent modulation on solid-gas and solid-liquid turbulent jets. It was concluded having the same length scale ratio of D/L_e , particles in solid-liquid jets can attenuate the turbulence faster than solid-gas jets since the carrier phase has higher viscosity.

Effect of particles on turbulence modulation was found to be strongly related to the ratio between particle relaxation time and the integral time scale of turbulent jets along the jet axis; this ratio known as Stokes number. Effect of the Stokes number of the jet on

turbulence modulation was shown that particle-laden jets with lower Stokes number can provide larger turbulence attenuation. Turbulence modulation can be predicted with higher level of accuracy by including the effect of particle concentration in future studies.

4.11 Notation

a = Radius of a solid ball, m

b = Frontal half-width, m

B = Initial buoyancy flux per unit weight, m^4/s^3

c = Coefficient used to calculate initial particle velocity

c_o = Initial volumetric concentration, %

C = Coefficient correlates the buoyancy flux to the frontal velocity

CTI = Change in turbulence intensity, %

C_u = Scaling coefficient

d = Nozzle diameter, m

D = Diameter of sand particles, μm

D_{16}, D_{50}, D_{84} = Sand diameters at which 16%, 50% or 84% of the sand particles present are finer, respectively, μm

F_B = Buoyancy force, kgm/s^2

F_o = Densimetric particle Froude number

g = Acceleration due to gravity, m/s^2

I = Turbulence intensity, %

L = Length of piston, m

L_e = Most energetic eddy, m

m = Initial mass flux, kg/s

m_o = Sand mass flux, kg/s

M = Initial momentum flux, kgm/s^2

r = Radial distance from the axis of the jet, m

R^2 = Coefficient of correlation

R_o = Reynolds number
 Re_p = Particle Reynolds number
 S = Symmetric component of ∇u , s^{-1}
 S_t = Stokes number
 S_{to} = Initial Stokes number
 t = time, s
 t^* = Dimensionless time scale
 u = Axial velocity, m/s
 u_{axe} = Velocity of the jet's centre, m/s
 u_b = Frontal velocity of single-phase jet, m/s
 u_c = Axial velocity of the single-phase jet, m/s
 u_C = Axial convection velocity, m/s
 u_f = Frontal velocity of sand jet, m/s
 u_{fo} = Jet front terminal velocity, m/s
 u_m = Centreline velocity of the jet, m/s
 u_o = Initial velocity of the sand jet, m/s
 u_r = Velocity of surrounding water, m/s
 u' = Velocity fluctuation, m/s
 $u'_{f,c}$ = Fluctuation velocity on the jet axis, m/s
 u_∞ = Terminal settling velocity, m/s
 v = Radial velocity, m/s
 v_C = Radial convection velocity, m/s
 V_o = Volume of particles, m^3
 x = Axial distance from the nozzle, m
 θ = Angle from the axis of flow, Radian
 λ_{ci} = Swirling strength, s^{-1}
 μ = Dynamic viscosity, kg/ms
 ρ_p = Density of sand, kg/m^3

$\rho_w =$ Density of water, kg/m³

$\tau^* =$ Non dimensional time scale of the jet

$\tau_f =$ Characteristic time of the fluid, s

$\tau_p =$ Particle relaxation time, s

$\omega_z =$ vorticity, s⁻¹

$\Omega =$ Antisymmetric component of ∇u , s⁻¹

$\nabla u =$ Velocity gradient tensor, s⁻¹

Chapter 5

An Experimental Study of Sand Deposition from Slurry

Wall Jets

5.1 Introduction

Study of sediment deposition in a quiescent ambient is important in the planning phase of building submerged sand mounds, artificial islands and covering underwater waste material in marine environment (Shields et al., 1984). Mound formation is caused by sediment deposition and it is used for developing artificial beaches near the shorelines. In these cases, sediment particles can be transported as a slurry flow through pipes and can be released horizontally into the bottom of water bodies.

Investigation on the dynamics and deposition of sediment particles issued from horizontal slurry jets can be used for designing the cover layer of sediment waste materials disposed underwater. Accurate design and prediction of the deposition shape and its dimensions depend on the release conditions and can prevent any significant environmental risk. Sediment mound can be generated and developed by the release of particle-laden jets into the ambient water. The deposition shape, size and development rate can be directly related to the flow configuration. In stagnant ambient water, slurry jets can be introduced either vertically or horizontally.

A paper based on the content of this chapter is currently being prepared for submission to the *Journal of Hydraulic Engineering, ASCE*, as Azimi et al., (2012c).

Many experimental investigations have been carried out to study the development of particle cloud and its entrainment efficiency (Ruggaber, 2000; Bush et al., 2003; Azimi et al., 2012). The onset of sediment deposition and its location can be affected by the ambient current. According to experimental studies on the dynamics of particle clouds in cross flow, the shape and development of particle cloud can be influenced by several release variables such as, particle size, release height and water content (Gu et al., 2008; Bhuiyan et al., 2010; Gensheimer III, 2010).

A series of experiments were conducted to study the formation of sand mounds under vertical sediment-laden jets, impinging on a horizontal bed (Rajaratnam and Mazurek, 2006). They found that the normalized profile of the sediment deposition can be described well by a cosine function. The deposition formed by a continuous release of coarse materials in flowing water was investigated by Bhuiyan et al. (2010). The deposition length scales during the development phase of the mounds was found to be an exponential function of time.

Effects of bed slope and water level on mound formation were studied through a series of experiments (Azimi et al., 2011a). Longitudinal and transverse profiles were measured during the mound development. In their study, deposition profiles were normalized with the maximum mound height and a radial length scale. They defined the radial length scale as a distance from the jet axis to the point where the height of the mound was equal to half of the maximum height (see Figure 5-1b). It was found that the sediment mound can be developed in proportion in both upstream and downstream sides until the deposition height reaches its maximum value.

A series of laboratory experiments were carried out to investigate the effects of submergence on a local scour and deposition by plane turbulent wall jets (Deshpande et

al., 2007). Submergence was defined as the ratio of the tail water depth, y_t to the nozzle thickness/diameter and it varied from 4 to 20. Two distinct types of flow fields were observed for low and high submergence.

Effects of sediment concentration, bed slope and flow discharge on sediment deposition rates was studied by Beuselinck et al. (1998). In their laboratory experiments, a mixture of water and silty soil was introduced into a sloped flume. The upper part of the flume had 1.0 m length and 10% slope and the lower part of the flume had 2% slope and 1.6 m length. The deposition rates were measured at different conditions and a threshold discharge was found which beyond that point, the deposition rate decreased significantly. A series of laboratory experiments have been carried out to study the effect of initial momentum of the jet on the deposition shape and the grain size decay (Hoyal et al., 2003). In their experimental study, sediment depositions formed by slurry jets were classified into four regions of bed erosion, strong bed load deposition, weak bed load deposition, and suspended load deposition. The settling of particles in reservoir can also form sediment deposition.

The growth of sediment mound in these conditions is an important aspect of reservoir planning and design. Imran et al. (2002) conducted an experimental study on the formation of submarine fans. A slurry flow of suspended sediment with 2% concentration and two different sediment sizes with a nominal diameter of 0.071 mm and 0.11 mm was released from an opening of 8 cm x 5 cm. The mound bed profiles were measured and those profiles were compared with a 2D depth averaged numerical model. It was found that the model was generally in good agreement with experimental observations.

The discharge of particle-laden flow into natural streams can cause sediment deposition in river deltas and develops submarine fans. As the jet expands and its velocity decelerates from the nozzle, the submerged density of the sediment begins to dominate the inertial forces. In this condition, a gravity-dominated plume will form which can cause the deposition of the fine grains. It was noticed that, the dominant mechanism controlling the geometry of most classic deposits is the deceleration associated with flow separation and the development of turbulent shear layers (Allen, 1982).

Stability of the sediment deposition and formation of the sand dunes and ripples in the nature can be influenced by the wind or current history. Deposition patterns and the ripple formation induced by settling of particles in natural streams and reservoirs have been studied by many researchers (Schieber and Southard, 2009; Reffet et al., 2010). Reffet et al. (2010) studied the effect of current on formation of the sand dunes and ripples by means of experimental studies and numerical modeling. They found that the longitudinal dunes are more stable than transverse dunes.

A number of numerical models have been developed and used to study the growth of sediment deposition by horizontal particle-laden flows. Development of sediment deposition in a shallow reservoir formed by low concentrated channel flow was investigated by means of numerical modeling and laboratory experiment. Souza et al. (2010) employed a two dimensional model (MIKE 21C) which vertically integrated Navier-Stokes equations to simulate the development of sediment deposition in shallow reservoirs. In their laboratory experiments, sediment with a nominal diameter of $D=0.12$ mm and concentration of $C=0.04\%$ were introduced to a tank by a rectangular channel and deposition patterns were measured after 72 hrs. They found that the 2D model is capable of accurate simulation while no high dunes were presented. It was reported that, the increase in turbulent diffusion caused by development of dunes cannot be captured by

the 2D model. Syvitski et al. (1998) introduced a numerical model (PLUME 1.1) for the prediction of sediment deposition issued from a fluvial plume. The model solves a two dimensional advection-diffusion equation.

This chapter investigates the development of sand mound as affected by the initial velocity, bed slope and particle concentration. The results of this experimental study would be useful for predicting mound development and to find the end state of material dumped from dredging operations into flat and sloped shorelines. In the next section, experimental setup and flow configurations are described. Laboratory results of sediment deposition and effects of initial momentum, bed slope and sediment concentration are studied in part 5.3. Finally, a summary and conclusions are provided in section 4.

5.2 Experimental Setup

Experiments were conducted in a square Plexiglas tank with 1.12 m sides and 0.285 m height. The water in the tank was kept at a certain level (i.e., $h = 0.20$ m) by using a control valve. Sediment particles were fed from a funnel-shaped sand hopper with a mechanical vibrator and mounted at the top of the water tank. Figure 5-1a shows the test setup and the adopted coordinate system. Sand particles with a nominal diameter, D of 0.21 mm and density of $\rho_s = 2540$ kg/m³ were released from the hopper and sediment particles were fully mixed with the water in a cylindrical chamber. The water level in the chamber was 27 cm and it was kept constant during the experiment. The mixed slurry flow was pumped by a progressive cavity pump into the system through a nozzle with a diameter, d of 12 mm. According to Deshpande et al. (2007), the present slurry wall jet is classified as highly submerged wall jet since the ratio of $h/d > 8$ (i.e., $h/d_o \approx 17$).

The generated slurry flow at early stage was directed to a temporary bucket until a uniform mixture of flow was formed by the system. The slurry flow was then switched to the tank for a period of time and the mixture was injected as a slurry wall jet to form a sediment mound. The water level in the tank was kept at the initial level during the release of the slurry jets. The duration of the slurry flow injection at each step, t_p is related to the initial velocity of the jet and the sediment concentration. The value of, t_p was determined as low as $\frac{1}{2}$ minute for high sand concentration and low velocity flows (Case A7). For high jet velocity low sand concentration t_p was up to 5 minutes (Case C4).

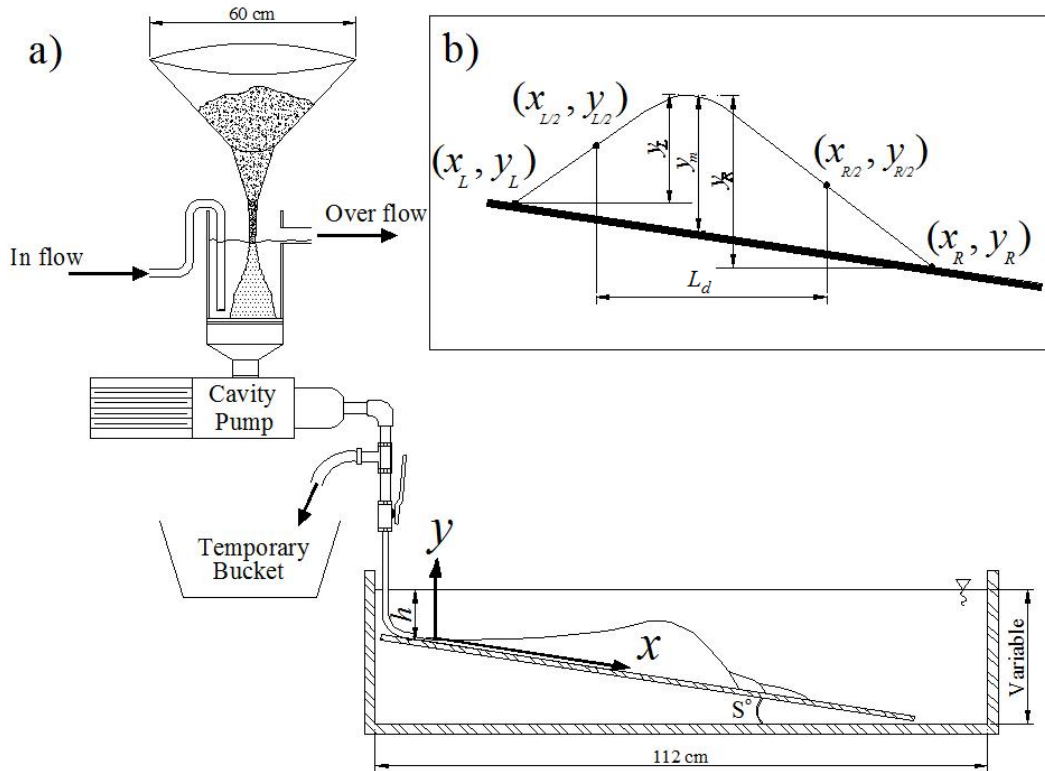


Figure 5-1: a) Experimental setup and coordinate system, b) Sketch for deposition length scales.

After the time step, t_p the slurry flow was switched back to the temporary bucket. In most cases, experiments were continued until the sediment deposition blocked the nozzle. The duration of each experiment, T_d can be calculated by summation of the time

durations, t_p at each step. The volume flux, Q and the sediment volumetric concentration, C were measured from samples of slurry flow from the nozzle. The details of the experiments and jets characteristics are given in Table 5-1.

The deposition heights along the axis of the jets were measured by employing a mechanical point gauge with an accuracy of 0.1 mm. At the peak of the deposition height, sediment deposition profiles in the transverse direction were also measured. Sediment mound length, width and base area were measured by using images taken from a high resolution digital camera. Images were imported to AutoCad software and scaled properly with the accuracy of 0.1 mm. The base area of deposition was obtained by tracing the boundary of deposition.

Deposition patterns and the development of sediment mounds were found to be related to the initial characteristics of slurry jets issued into the water tank. Effect of controlling parameters such as initial momentum flux of the jet M , bed slope S , and sediment volumetric concentration C , plays an important role on the development of the sediment mound. In this study, the initial momentum flux of the jet can be defined as $M = \pi d^2 / 4 [C\rho_s + (1-C)\rho_w] u_o^2$ where ρ_w is the density of the water and u_o is the initial velocity of the jet at the nozzle. A series of experiments were conducted in this study to investigate the effect of initial momentum (Series A), bed slope (Series B) and sediment concentration (Series C).

Since during each experiment slurry flow was released and stopped at several time steps, experiments with a continuous release time of, T_d were carried out to study the effect of the release mechanism. Cases A7 and C2 were conducted with the continuous release time of 2.5 and 32 minutes, respectively (see Table 5-1). It was found that the release/stop cycles did not significantly affect the deposition size. The deposition lengths in experiments with a continuous release of sediment particles were between 0.3 - 2.65 %

larger than the experiments with the release/stop mechanism whereas, the deposition widths were smaller by 1.3 - 1.75 % in the continuous release condition.

Table 5-1: Details of the laboratory experiments and jet characteristics (sediment size $D = 0.21$ mm, $d = 12$ mm and water depth $h = 0.20$ m).

Test	u_o (m/s)	C (%)	S (°)	t_p (min)	T_d (min)	T (ms)	M (kg.m/s ²)	F	R
A1 (C1)	1.60	6.00	0.0	1.0	2.5	5.9	0.32	28.3	19,200
A2	1.35	7.10	0.0	1.0	3.0	7.0	0.23	24.0	16,200
A3	1.22	7.90	0.0	1.0	5.0	7.7	0.18	21.6	14,600
A4 (B1)	1.09	8.80	0.0	1.0	7.0	8.7	0.15	19.3	13,100
A5	0.94	10.2	0.0	0.5-1.0	7.0	10.0	0.11	16.7	11,300
A6	0.80	12.0	0.0	1.0	7.0	11.8	0.09	14.2	9,600
A7	0.66	14.5	0.0	0.5-1.0	5.0	14.2	0.055	11.8	8,000
B1 (A4)	1.09	8.80	0.0	1.0	7.0	8.7	0.15	19.3	13,100
B2	1.09	8.80	2.5	1.0	6.0	8.7	0.15	19.3	13,100
B3	1.09	8.80	5.0	1.0	9.0	8.7	0.15	19.3	13,100
B4	1.09	8.80	7.5	1.0	9.0	8.7	0.15	19.3	13,100
B5	1.09	8.80	10.0	1.0	10.0	8.7	0.15	19.3	13,100
C1 (A1)	1.60	6.00	0.0	1.0	2.5	5.9	0.32	28.3	19,200
C2	1.60	2.50	0.0	3.0	32.0	5.9	0.30	28.3	19,200
C3	1.60	1.50	0.0	4.0	44.0	5.9	0.295	28.3	19,200
C4	1.60	0.50	0.0	5.0-6.0	60.0	5.9	0.29	28.3	19,200
Z1*	1.09	4.70	0.0	1.0	6.0	8.7	0.145	19.3	13,100
Z2*	1.09	4.70	5.0	1.0	12.50	8.7	0.145	19.3	13,100
Z3*	1.09	4.70	10.0	1.0	9.0	8.7	0.145	19.3	13,100

*Tests Z1-Z3 were added from experimental study of Azimi et al., (2011a) for comparison.

In Series A, 7 sets of tests were conducted with the initial velocity u_o , ranging from 0.66 - 1.60 m/s. The Reynolds number, $R = \rho_w u_o d / \mu$ was high with values ranging from 9,600 to 19,200 where μ is the dynamic viscosity of water.

In all cases, sediment particles with a constant rate were mixed with the water in the cylindrical chamber. For lower velocities the spin rate of the cavity pump was reduced but the dry sand flux was kept constant. Consequently, the volumetric

concentration of the slurry flow was increased from 6.0% to 14.5%. Five experiments were carried out to study the effect of bed slope.

An aluminum square plate of 0.9 m with a layer of sand paper with a roughness of $K_s = 0.53$ mm was employed as a false bed to provide different slopes (series B). The false bed was adjusted at different slopes of $S = 0, 2.5, 5, 7.5$ and 10 degrees from horizontal. The initial conditions of these sets were similar to the case A4 having the initial velocity of 1.09 m/s and volumetric concentration of 8.80%. Effect of sediment concentration on sand deposition was studied by reducing the sediment mass flux from the hopper (Series C). All cases in series C were conducted with a horizontal bed. Initial velocities of all cases were similar to case A1 with the initial velocity of 1.60 m/s.

5.3 Dimensional Consideration and Flow Visualization

Three different sets of experiments have been carried out to investigate the effect of jet characteristics and controlling parameters on development of sediment deposition issued from horizontal submerged jets. Based on physics of the problem, following parameters can be correlated with the advancement of the sediment mound

$$y_m, b_m \text{ and } L_m = f(t, d, u_o, \rho_s, \rho_w, \mu, C, D, S, K_s) \quad (5.1)$$

where y_m , b_m and L_m are the maximum height, width and length of deposition, respectively. Effect of bed roughness, K_s on the formation of horizontal sediment mound was investigated. Two plates with the roughness of $K_s = 0.21$ mm and 0.53 mm were tested and results were compared with the deposition pattern formed on top of a smooth bed (Azimi et al., 2011a). It was found that the effect of bed roughness on the mound length and width formed by a horizontal slurry wall jet is not significant. Since relatively high sediment concentration was used in this study, the first layer of sediment was built

up quickly and created a movable bed with a roughness similar to the sediment size (i.e., 0.21 mm).

In this study, the primary forces of sediment transport are the gravitational force and the local inertial force. Densimetric particle Froude number, $F = u_o / (g'D)^{1/2}$ shows the relative magnitude of the mentioned forces and it is an important non-dimensional parameter in erosion-sedimentation processes [Rajaratnam and Mazurek, (2006); Bhuiyan et al. (2010)]. Here $g' = g (\rho_s - \rho_w) / \rho_w$ is the reduced gravity and g is the acceleration due to gravity. The time dependent behaviour of the problem can be resolved by introducing a time scale, T , where T is related to the jet characteristics and can be defined as $T = Q / (d u_o^2)$. By introducing the time scale, T and densimetric particle Froude number F , the governing parameters can be reduced to

$$y_m, b_m \text{ and } L = f'(t/T, F, C, S, R, D/d, K_s/D) \quad (5.2)$$

The development of sediment deposition and ripple formation were studied by measuring dimensions of the sediment mound at different times during the experiments. Figure 5-2 shows the development of the sediment mound for experiment C2 where the initial velocity is $u_o = 1.60$ m/s and the initial volumetric concentration is $C = 2.5\%$. The obtained images were taken at different times and they were turned into negatives for better visualization. In this test, images were taken every 3 minutes and the deposition blocked the nozzle after 32 minutes. An angle of deposition, β can be defined as the angle between the two tangent lines of deposition. As can be seen from Figure 5-2, the maximum width of deposition b_m , occurs at the location of the maximum deposition height, x_m . Considering the development of ripples, a bimodal profile can be observed downside of the sand mound as shown in Figures 5-2(a-b). The advancement of ripples

can be related to the sediment fluctuations and can be correlated with the turbulent kinetic energy.

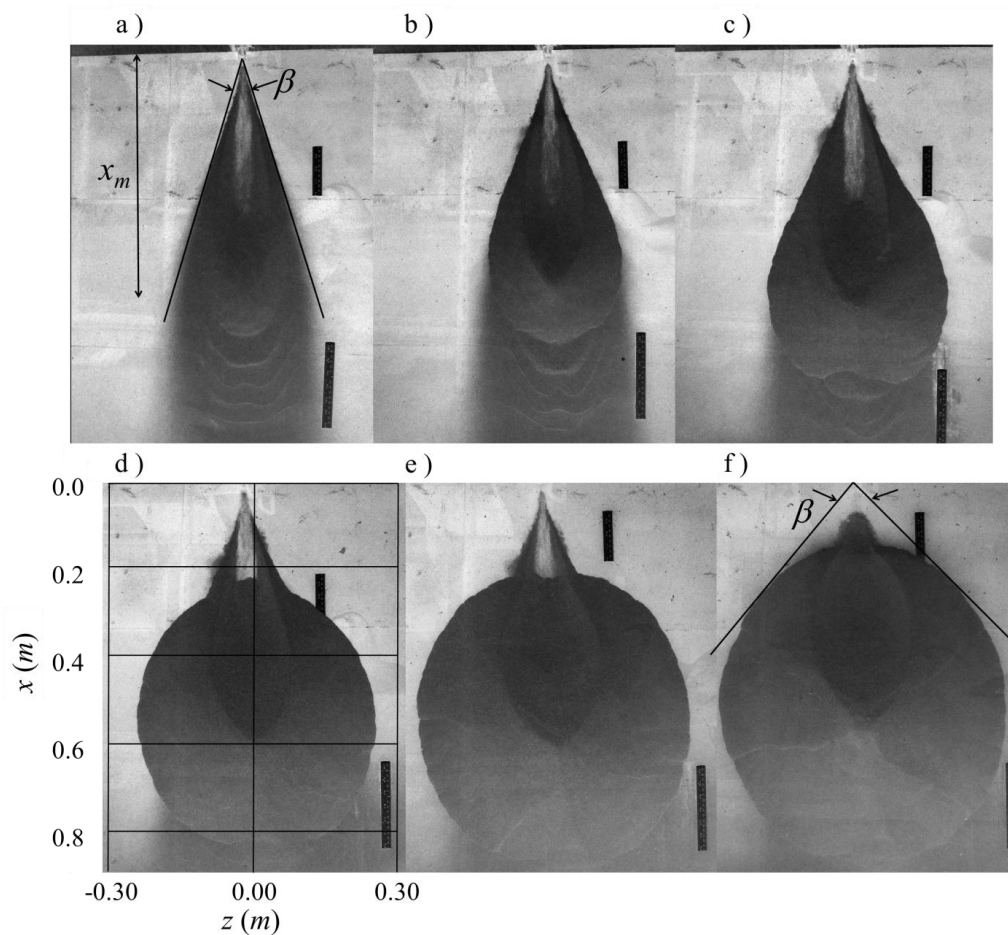


Figure 5-2: Images of the sediment deposition and ripples formed at different times for experiment C2. a) $t = 3$ min. b) $t = 6$ min. c) $t = 12$ min. d) $t = 21$ min. e) $t = 27$ min. f) $t = 32$ min. Images turned to negative for better visualization.

Since flow with higher fluctuations can push sediment particles further downstream, the peak advancement can be related to the location of the maximum turbulent kinetic energy. Numerical investigation of sand jets in water (Azimi et al., 2011b) showed the same bimodal profile for the turbulent kinetic energy.

According to the obtained images from experiments, three different regimes were observed during the mound development process and were named as developing regime,

spreading regime and backup regime. Figure 5-3 shows the development of sediment deposition from raw images taken from experiment A1. At the onset of sediment injection, all sediment particles were carried forward by the momentum of the wall jets. At this stage, sedimentation occurs due to jet spreading and decay of sediment velocity. During the deposition buildup, sediment mound was formed but most of sediment particles have enough momentum to pass over the peak of the mound. Then, the peak increased and a portion of sediment was diverted to the sides of the mound. The time duration from the onset of deposition to the stage when sediment particles were diverted to the sides of the mound, is classified as developing regime (Figure 5-3[a-b]).

The second deposition regime starts when a small portion of sediment deposit on the sides of the mound. This regime can be named as spreading regime since the mound develops more on the sides. Figure 5-3c illustrates a three dimensional view of the mound development in the spreading regime. In this condition, the energy of the jet is not enough to push particles over the mound and most of particles are transported to the sides of the mound. This caused an increase in the rate of growth of the width and the angle β .

The sediment flux of the two sides of the mound increases and the downside sand flux decreases until the mound height and width reach their maximum values, y_m^* and b_m^* . At this stage, almost no flow passed over the mound and all the incoming flow diverted to the mound sides (Figure 5-3d). This time is the onset of the third stage which is called the backup regime. Figures 5-3[e-g] show the development of deposition in the backup regime. At the beginning of this regime, sediment flow turns to the upper side of the mound and causes a continuous built up of the deposition in the upper side of the mound.

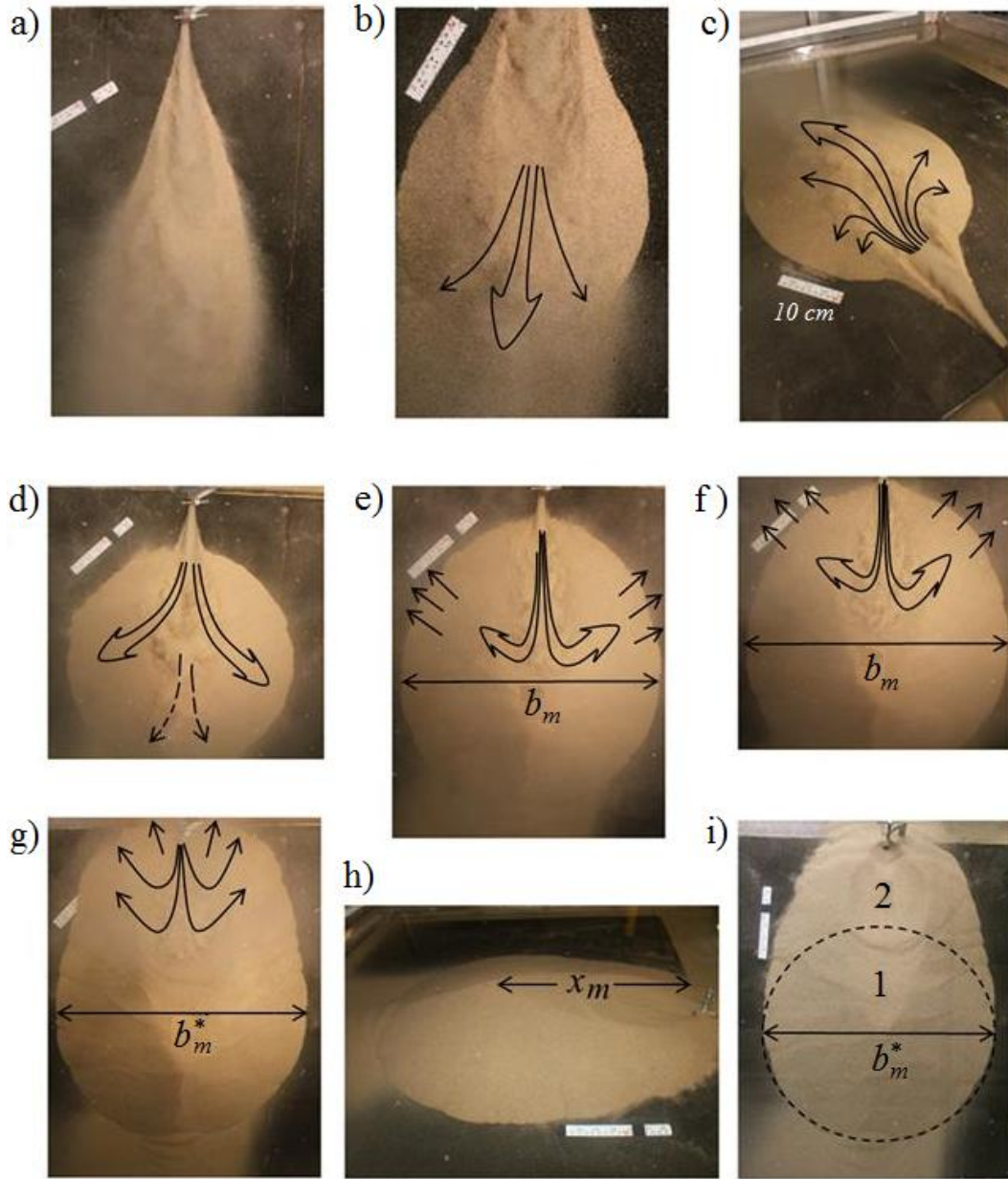


Figure 5-3: Raw images taken from experiment A1 show development of sediment deposition with time and illustrate different classifications of mound formation. a) Deposition in developing regime, b) Sediment mound development at the end of developing regime, c) Three-dimensional view of the spreading regime, d) End stage of the spreading regime, e) Beginning of the backup regime, f) Advancement of sediments toward the nozzle, g) End stage of the backup regime, h) Three-dimensional side view of the sediment deposition at the end of experiment, i) Top-view at the end of experiment shows the area of mound cone (1) versus the deposition area formed in the backup regime (2).

In this regime the maximum deposition height and width remain almost constant and the angle of deposition and the mound base area increase with a higher rate to reach its maximum value at the end of the experiment. The beginning of the third regime can be easily captured from images taken from the top (Figure 5-3e).

In the backup regime, the deposition base deforms from circular shape to elliptical and ends when the mound blocks the nozzle. Besides photographic studies, those mentioned regimes can be captured by analyzing the main characteristics length scales of y_m , b_m , x_m . Effects of the controlling parameters on the mound length scales and analysis of the mentioned deposition regimes are presented in sections 5.4-5.6.

According to dimensional consideration, experimental results are organized as follows. In section 5.4, effects of initial momentum on sediment deposition are studied. Since sediment concentration on those experiments varied over a wide range ($C=6.0-14.5\%$), variations of the sediment concentration produced by the cavity pump are included on those experiments. Deposition length scales and mound aspect ratio are correlated with the densimetric particle Froude number, F . Section 5.5 presents the effect of bed slope on the mound formation and section 5.6 focuses on the effect of slurry concentration and provides a general relationship between the dominant parameters.

5.4 Effect of Initial Momentum

Densimetric Froude number F was found to be an effective parameter on controlling the sediment deposition shape, height, and its length. F is a measure of the ratio of the inertial force acting on sediment to the submerged specific weight of the sand particle. Many experiments have been conducted to investigate sediment deposition and formulate its development rate at different flow configurations [Rajaratnam and Mazurek, (2006); Deshpande et al. (2007); Bhuiyan et al. (2010)]. In the current tests, the densimetric

particle Froude number, F was varied from 11.8 to 28.3. The mound length, L and the distance between the nozzle and the peak deposition height, x_m at the time t after starting sediment disposal can be normalized with the jet nozzle diameter and expressed as a linear function of densimetric Froude number (Figure 5-4).

$$x_m / d = 1.13F + 3.63 \quad (5.3)$$

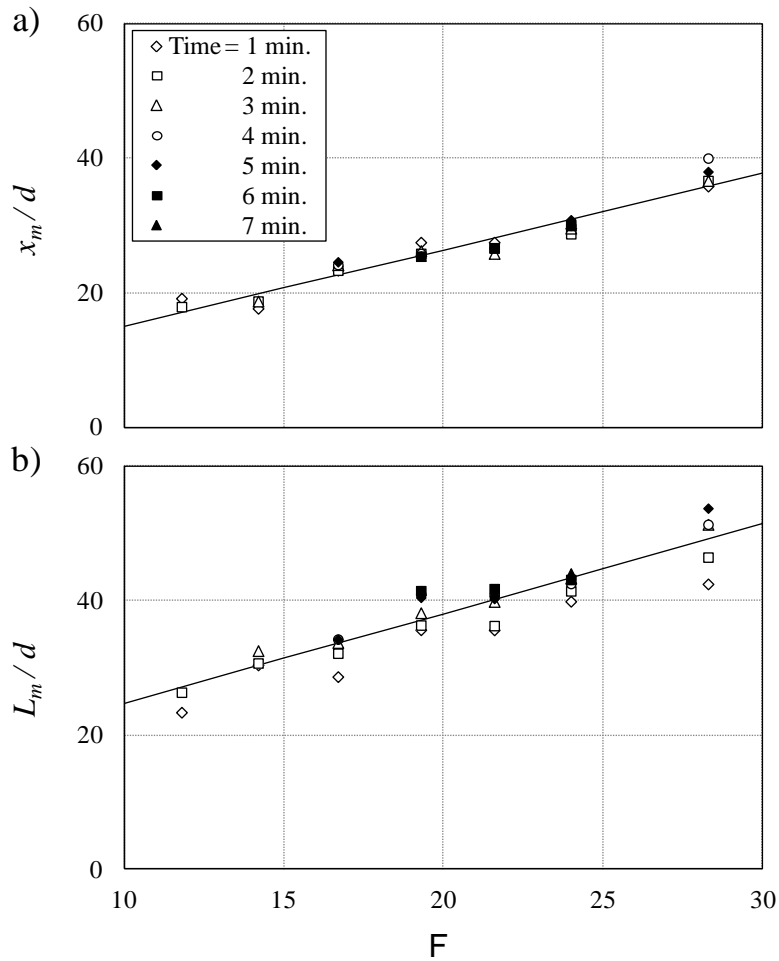


Figure 5-4: Correlation of the normalized deposition length scales with densimetric Froude number, F . a) Variation of the normalized length of the maximum deposition height from the nozzle, x_m with F . b) Variation of the normalized deposition length normalized with the nozzle diameter with F .

The location of mound peak can increase to a certain extent which was strongly related to the initial momentum of the jet and the sediment concentration. It can be also

seen from Figure 5-2 that the mound advancement can be started from the location of peak height, x_m and develops almost in all directions. At different stages of deposition, strong correlation was found between the densimetric Froude number and x_m , in terms of d , with a regression coefficient of 0.93 (Figure 5-4a).

The strong correlation indicates that the value of x_m is almost time independent and the peak locations are invariant with time until the beginning of the backup regime. Longitudinal profiles of the sediment mound presented later in this chapter were also independent of time before the backup regime. Figure 5-4b shows the correlation between the mound length and F . The slope and the intercept of the correlation were found to be 1.33 and 11.4, respectively. Data scatter in this plot shows a time dependency between the mound length and F , which indicates that the mound length increases with time. The slight growth of the sediment length can be due to a part of sediment flux which could pass over the mound during the spreading regime. The time dependency effect between L_m and F reduced the correlation coefficient to 0.84.

The angle of sediment mound, β was measured at each time step and variation of β with time was shown in Figure 5-5a. Regarding the initial parameters of the test and time, the mound angle increases linearly and it varies from 17 to 68 degrees. Since slurry jets with higher initial velocity can push sediment particles further downstream, it can be expected that jets with higher F would produce smaller β which is consistent with the measurements shown in Figure 5-5a. By employing Froude number of each experiment and plotting the results against the normalized time and C , a general trend for the angle of deposition can be introduced. Linear correlation was found between the normalized time and the angle of deposition. The slope and the intercept of correlation were 0.205 and 287.5, respectively with $R^2 = 0.86$.

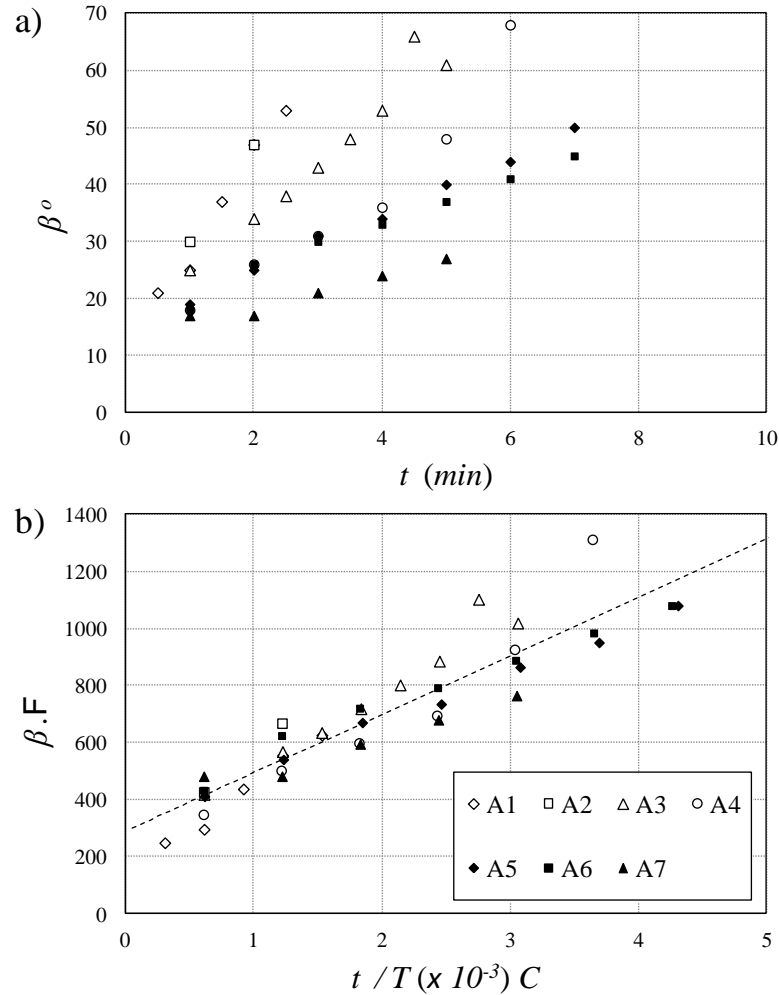


Figure 5-5: Effects of sediment concentration and densimetric Froude number, F on development of the mound angle of deposition, β , for experiments A1-A7. a) Growth of the angle of deposition with time. b) Effects of sediment concentration and F on correlation of the angle of deposition with normalized time.

Considering the images taken from top view of the mound at the end of experiment (Figure 5-3i), the sediment mound at the end of experiments can be divided into two sections. These areas are the cone area which is shown as area (1) and the deposition area formed in the backup regime and it is shown as area (2) in Figure 5-3i. The ratio between the total mound base area and the cone area of the mound (see Figure 5-3i) at each time can be a suitable indicator to study the onset of the backup regime. Variations of mound

base area with time was studied by normalizing the total mound base area with the cone area (i.e., $\pi b_m^{*2}/4$) and results were plotted against the normalized time in Figure 5-6.

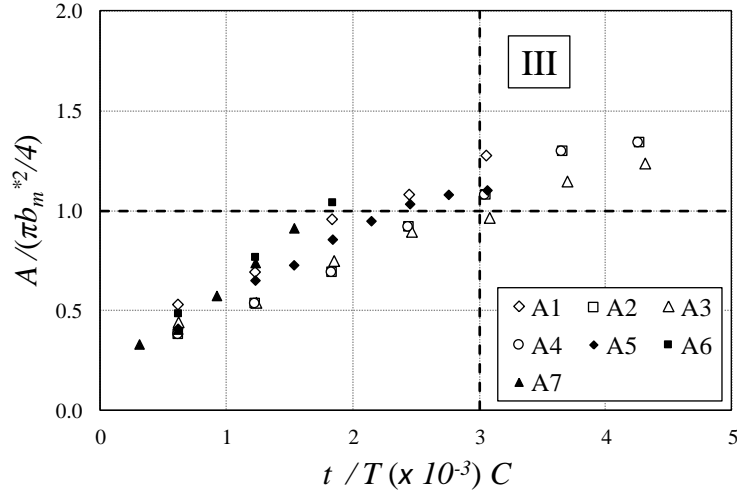


Figure 5-6: Development of the deposition base area with time for experiments A1-A7. Mound base area was normalized with the cone area of the mound, $(\pi b_m^{*2}/4)$ and time was normalized with the time scale of the slurry jet. Influence of sediment concentration on mound development was included in this plot (I is the developing regime, II is the spreading regime).

It was found that the mound base area increased almost linearly with time. The onset of the backup regime can be identified when the total mound base area becomes larger than the cone area of the mound. According to the normalized base area, the onset of the backup regime can be predicted and for these test series the onset of backup regime occurs at $[t/T (x10^{-3}) C] = 3$.

5.5 Effect of Bed Slope

In order to study the variation of the mound base area with time, the boundary of the deposition can be traced at each time. Effects of bed slope on the shape and formation of the deposition were investigated in this study. Variations of the mound base area with time and for different slopes are shown in Figure 5-7. Series of contour plots with the

time interval of one minute show the formation of deposition. The frontal ripples were formed due to flow separation and impingement of strong eddies on the bed as can be clearly seen in Figure 5-2. These ripples were plotted as a series of curved lines in Figure 5-7. Increasing the bed slope leads to the advancement of deposition front and caused an increase in deposition length. Consequently, the total time of experiment for beds with higher slope became longer than for the smaller slope. This indicated the effect of the horizontal component of the gravity force, $g_x = g \sin(S)$ on the growth of sediment mound. On the other hand, by increasing the bed slope, the peak deposition height, y_m reaches its maximum value faster and the deposition begins to advance in the upstream direction earlier.

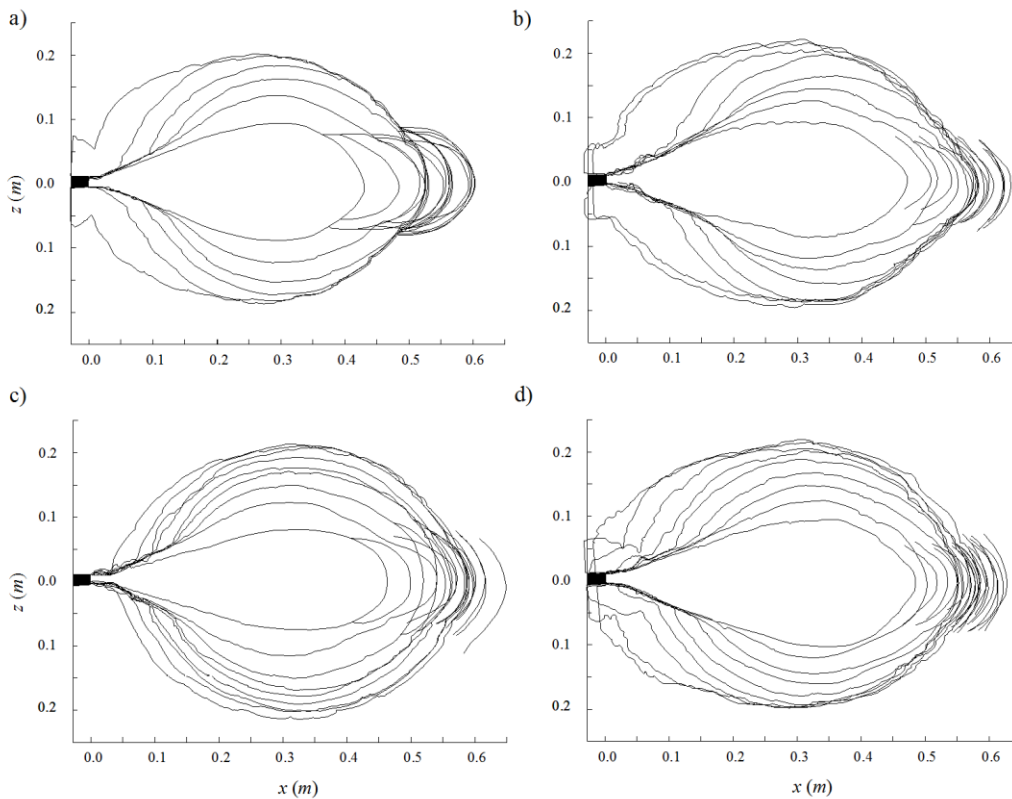


Figure 5-7: Contour plots of the sediment deposition at different times and effect of bed slope on the size and shape of the deposition. a) $S = 2.5^\circ$, b) $S = 5^\circ$, c) $S = 7.5^\circ$, d) $S = 10^\circ$. Contour lines were shown at one minute time interval.

Contour plots in Figures 5-7c and 5-7d show that the upstream deposition occurs at a faster rate for higher slopes (i.e. 2minutes earlier) whereas deposition backup advances gradually in relatively lower slopes. Effects of the initial momentum of the jets (Series A) and bed slope (Series B) on the mound characteristic length scales (i.e. height, width and length) with time are shown in Figure 5-8. Mound dimensions measured by Azimi et al. (2011a) named as test series Z (see Table 5-1) were added for comparison.

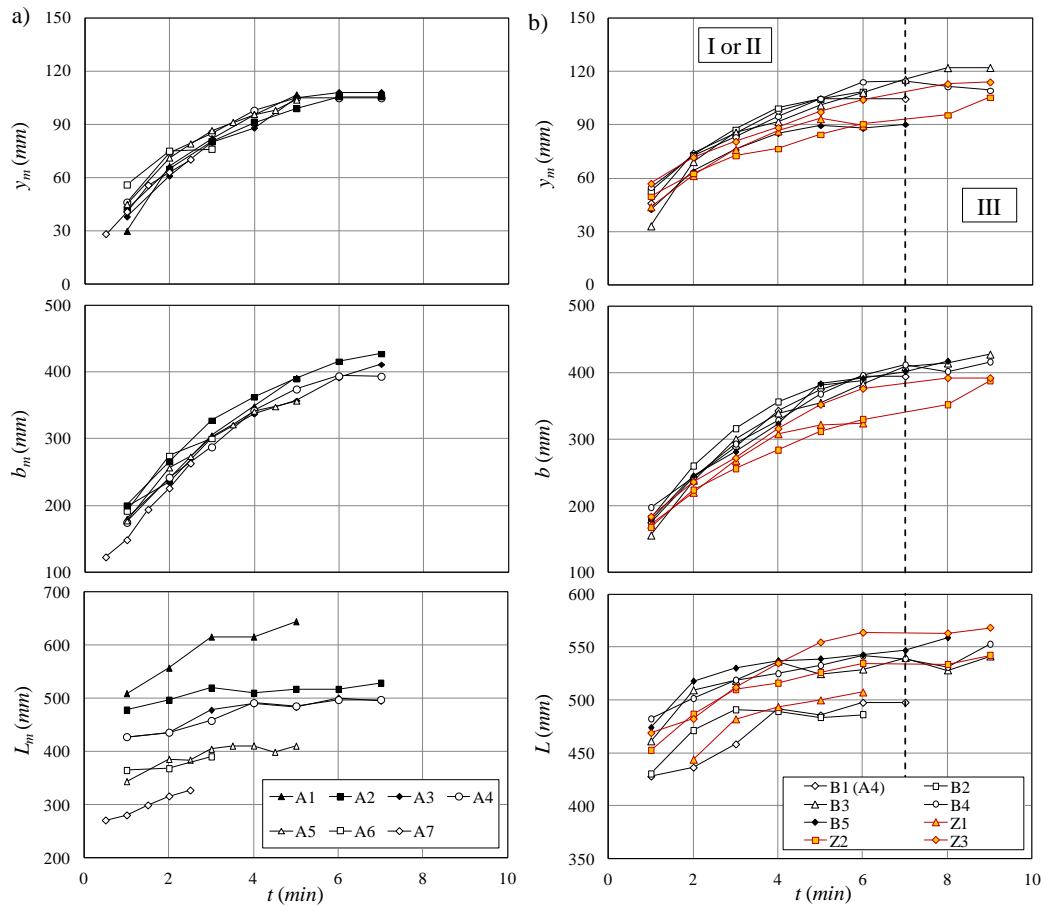


Figure 5-8: Effect of initial velocity and bed slope on development of the sediment mound length scales (Top: Maximum mound height, Middle: Mound width, Bottom: Mound length), a) Effect of initial velocity, b) Effect of bed slope. (I is the developing regime, II is the spreading regime).

Effects of the initial momentum on the mound size are shown in Figure 5-8a. It was found that the mound height and width were invariant with the momentum of the jets but,

they grow with time and reach their maximum value. Figure 5-8a also revealed that the mound length slightly increased with time and the initial momentum can significantly increase the mound length. Effect of bed slope on the characteristic length scales of the sediment mound with time were shown in Figure 5-8b. As can be seen, the peak deposition height increased with time and reached its maximum value in the spreading regime. Effect of bed slope on y_m was found to be minimal except for experiments B5, Z2 and Z3 with the bed slope of $S=5^\circ-10^\circ$. Since the mound peak height decreases with increasing bed slope, the deposition backup starts earlier for cases with higher slope.

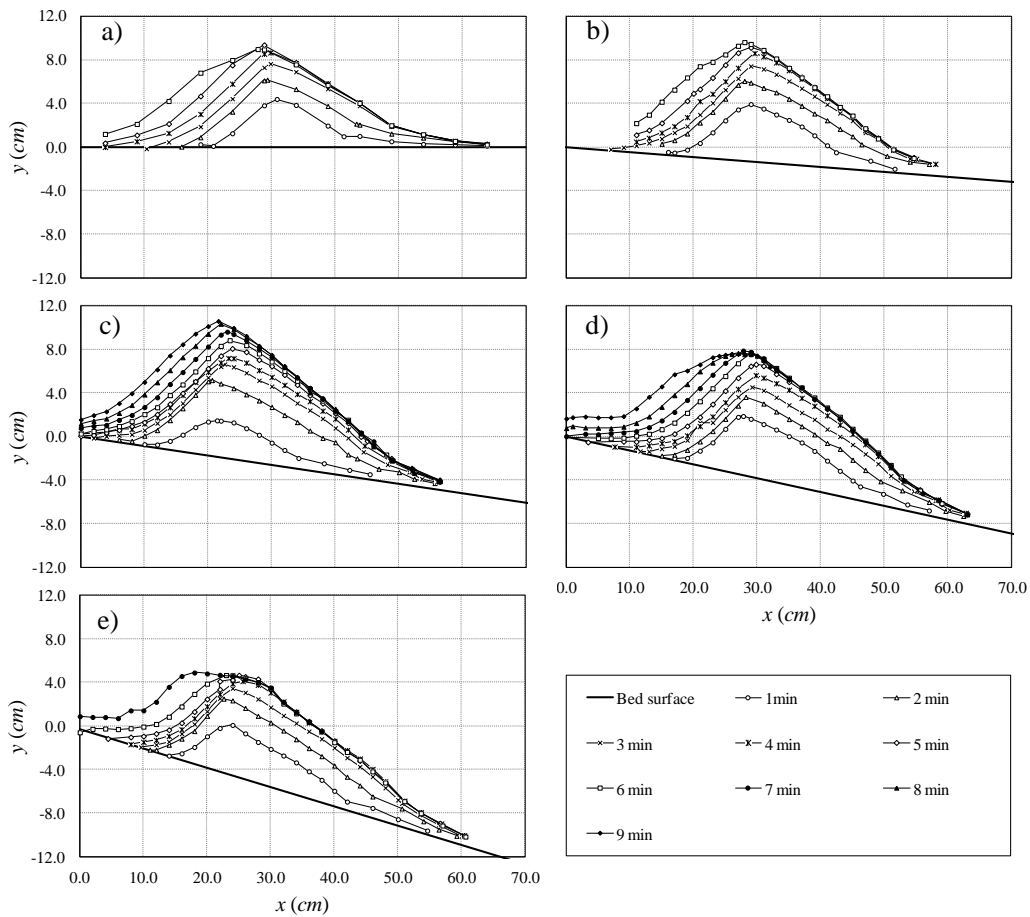


Figure 5-9: Variations of the longitudinal profiles of the sediment deposition with time and bed slope. a) $S = 0^\circ$, b) $S = 2.5^\circ$, c) $S = 5^\circ$, d) $S = 7.5^\circ$, e) $S = 10^\circ$.

Correlation between time and mound width can be expressed by a power law function with the base and exponent of 184 and 0.4, respectively. It was found that the effect of bed slope on the mound width was insignificant except for tests Z2 and Z3. Bed slope has a significant impact on the advancement of the deposition front. Increasing the mound dimensions indicated that the sediment deposition is a function of both time and bed slope.

A comparison between the results of this study (Series B) and the mound development of sediment with lower concentration used in previous investigation (series Z) shows that, sediment with lower concentration can build up a bit further downstream. This causes a relatively longer deposition length and narrower mound width. Effect of sediment concentration on the height of deposition on slope was found to be negligible. Longitudinal profiles of deposition are shown in Figure 5-9. This figure illustrates the variations of the longitudinal profiles of deposition with time and at different bed slopes. As can be seen, deposition advanced towards the upper side of the mound when the height of the mound reaches its maximum value. Deposition profiles can be normalized by utilizing the peak height and radial length scale (see Figure 5-1b) as it explained by Azimi et al, (2011a).

5.6 Effect of Sediment Concentration

Slurry wall jets with higher concentration can develop sediment deposition at a faster rate. By including the effect of sediment concentration and densimetric Froude number, variations of the deposition height, y_m and mound width, b with time can be formulated. Figure 5-10a shows the variation of the maximum deposition height, y_m with time. Experimental results of Azimi et al. (2011a) were added in this plot. In this correlation, y_m was normalized with the nozzle diameter. It was found that the maximum deposition

height is a function of sediment concentration and F . The computed correlation coefficient of $R^2 = 0.93$ indicated a strong correlation of y_m with time for all experiments and this correlation can be expressed as

$$(y_m / d) = 9[t / T(x10^{-3})C]^{3/5} F^{-1/4} \quad (5.4)$$

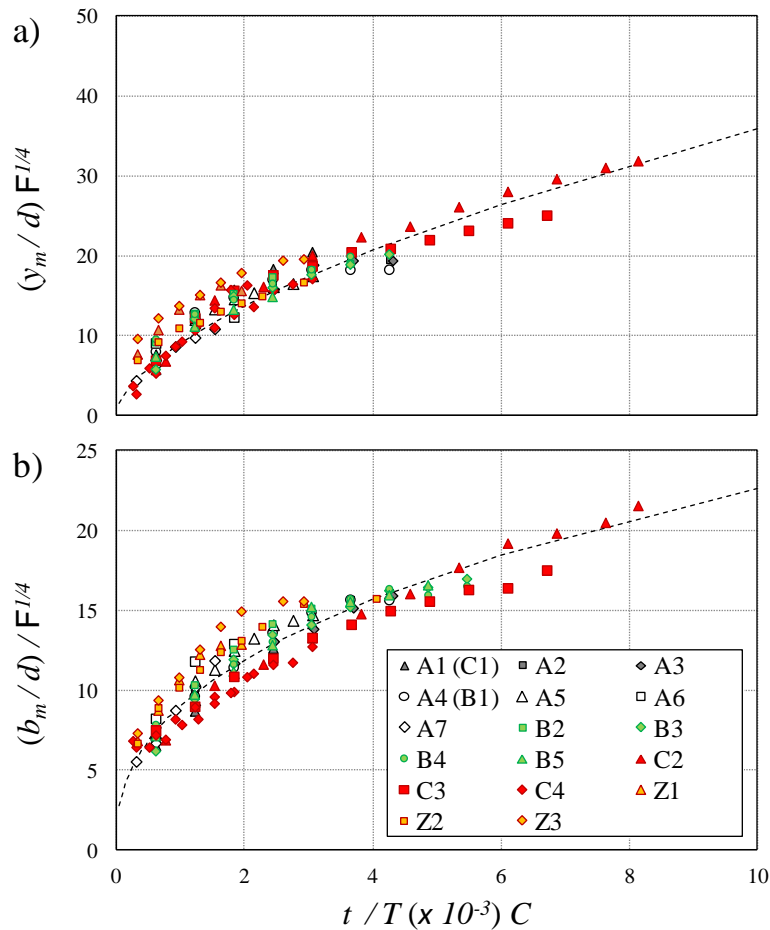


Figure 5-10: Effects of sediment concentration, C and densimetric Froude number, F on development of the characteristic length scales of the sediment deposition. a) Correlations of the maximum deposition height with normalized time, C and F . b) Variations of the mound width with time, C and F .

Effect of bed slope in equation 5.4 was not considered. As a result, by eliminating the test results of the highest bed slope (case B5 and Z3) from analysis, the coefficient of correlation can be improved to $R^2=0.95$. Similar equation was introduced to predict the mound width with the R^2 value of 0.94.

$$(b_m / d) = 9[t / T(\times 10^{-3})C]^{2/5} F^{1/4} \quad (5.5)$$

Slurry flow with higher densimetric Froude number having higher turbulent energy which can spread sediment into a larger area whereas sediment with lower initial velocity settles closer to the nozzle. In a fixed time frame and by considering the same initial sediment flux, tests with higher initial velocity can develop deposition with larger base area and consequently lower deposition height. Correlations formulated for the variations of y_m and b with time in equations 5.4 and 5.5 support the underlying physics and indicated that the characteristic length of y_m and b_m varied with $F^{1/4}$.

Equations 5.4 and 5.5 revealed that, the maximum mound height had an inverse correlation with F (i.e., $y_m \sim F^{-1/4}$) whereas the widths of the mound increase by increasing F with the same rate. This indicates that at a constant dimensionless time, slurry flow with higher F can spread sediment in a larger area due to higher initial turbulent energy. Therefore, the higher sediment spreading resulted in relatively smaller deposition height and larger deposition width. Consequently, tests with higher Froude number reach the maximum deposition height at longer dimensionless time.

The mentioned three stages of mound development (i.e., developing (I), spreading (II) and backup (III) regimes) can be analyzed by considering the variations of the mound dimensions in each regime. Correlations of the characteristic length scales and the base area of the sediment mound with time at different regimes were shown in Figure 5-11. From previous observations on the development of the height and width of the

mound, it appears that the relevant non-dimensional parameters for prediction of the mound dimensions are F and C . Since experiments with various initial momentum and sediment concentration were analyzed in Figure 5-11, F and C were used to formulate the mound development.

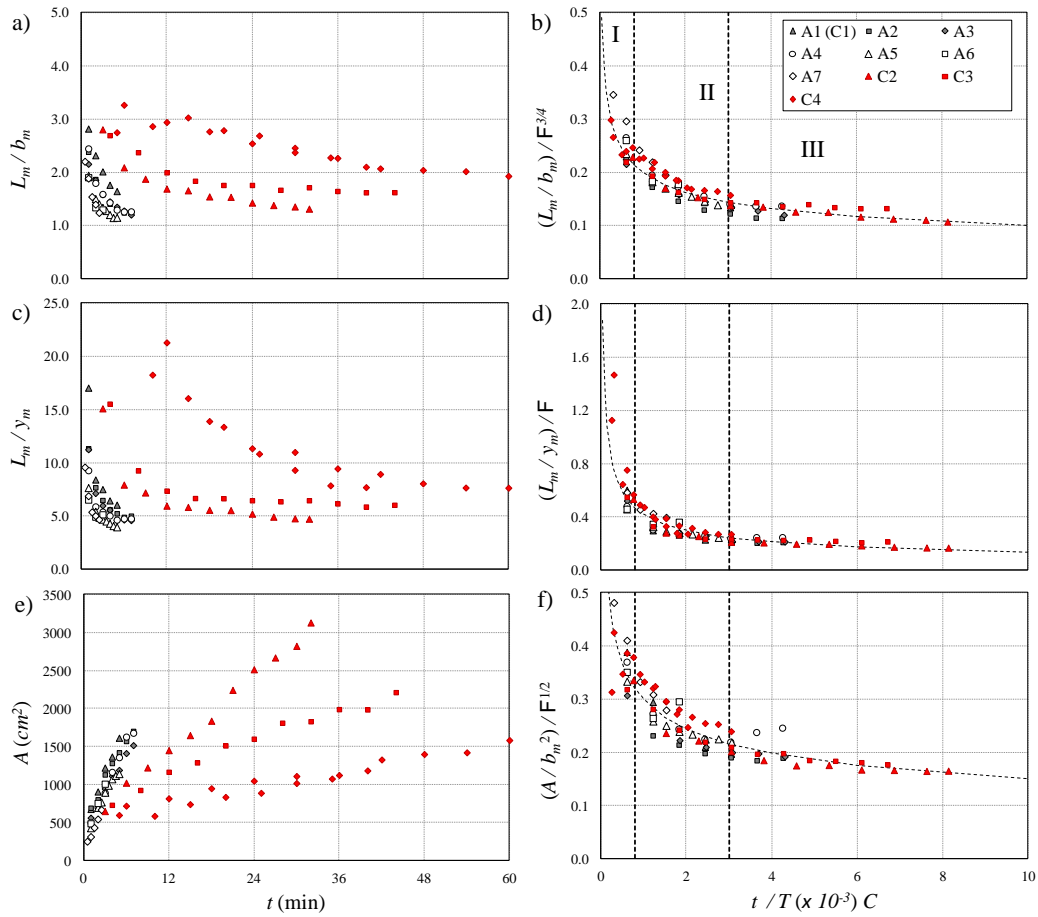


Figure 5-11: Variations of the mound aspect ratio and sediment base area with time at different regimes. (I is the developing regime, II is the spreading regime and III is the backup regime.) Deposition aspect ratios and the normalized mound base area were correlated with the mound time scale, T , sediment concentration, C , and densimetric Froude number, F .

Variations of the mound dimensions (i.e., length, width and height) with time were studied in the form of aspect ratios. Figure 5-11a illustrates the variations of the horizontal aspect ratio, L_m/b_m with time for two test series of A and C. According to

Figure 5-11a, the mound length was found to be three times larger than its corresponding width from starting of the sediment disposal. Deposition width develops at a faster rate in comparison with the mound length since the aspect ratio decreases from three at the starting stage and becomes close to one at the end of the experiment. Effects of F and C can be studied on the development of the horizontal aspect ratio of L_m/b_m with normalized time of t/T . The correlation of the horizontal aspect ratio with time can be described by a power law function with a correlation coefficient of $R^2=0.9$.

$$(L_m/b_m) = 0.2[t/T(\times 10^{-3}) C]^{-1/3} F^{3/4} \quad (5.6)$$

Figure 5-11b shows the correlation of L_m/b_m with the normalized time. The horizontal aspect ratio from the time of disposal decreased rapidly as sediment transported to the mound side until the backup regime started. In the backup regime the horizontal aspect ratios were almost constant since most of sediment deposited to the upper side of the mound and changed the deposition shape from circular to ellipsoid (see Figure 5-2f and 5-3f). Variation of the vertical aspect ratio of L_m/y_m with time was shown in figure 5-11c. As can be seen from this figure, the vertical aspect ratio decreased rapidly with time from the beginning of disposal up to a certain time. The ratio of L_m/y_m can be correlated with sediment concentration and densimetric Froude number. The following proposed formulation can describe the correlation between the vertical aspect ratio and the controlling parameters of F and C with time with $R^2= 0.87$.

$$(L_m/y_m) = 0.4[t/T(\times 10^{-3}) C]^{-1/2} F \quad (5.7)$$

According to experimental observations, variations of the aspect ratios of L_m/b_m and L_m/y_m with time can illustrate the three regimes in development of sediment mound. In the developing regime (Regime I), the vertical aspect ratio of L_m/y_m decreases rapidly, since y_m grows much faster than L_m . According to experimental observations, the

transition from developing to spreading regimes for test A1 occurred 4 minutes after the release of slurry jets (i.e., $t/T=0.041$) whereas this transition occurred for test A7 around 1.5 minutes (i.e., $t/T=0.0063$) after the starting of the experiment.

As the deposition height approaches to its maximum value, larger portions of slurry flow are blocked by the mound and sediment particles are detoured by the flow to the mound sides. This caused a slower deposition build up and showed a smaller slope in region II of Figure 5-11d. As a result, the mound height increases slowly in the second regime (i.e., spreading regime) and most of sediment builds the sides of the mound. This caused an increase in the mound width and a decrease in the horizontal aspect ratio. Figures 5-11b and 5-11d show the ratio of L_m/y_m is almost constant in regime II whereas L_m/b_m in this regime decreased with relatively higher slope. When the maximum mound height became constant with time, most of sediment particles spread either to the mound sides or the backup regime may occur. The behaviour of deposition width with time can be a good measure of defining the onset of backup regime. In the backup regime (Regime III), the mound height is almost constant and the mound width increases linearly with time. Therefore, the horizontal aspect ratio of L_m/y_m decreases with time with a very small rate. Development of the deposition base area with time was studied and the results were shown in Figure 5-11e. Correlation between the mound base area and the controlling parameters of deposition is shown in Figure 5-11f. The mound base area can be normalized with the mound width and a power law function can describe the relationship. A regression coefficient of 0.86 was obtained for the proposed formulation.

$$(A / b_m^2) = 0.3 [t / T(\times 10^{-3}) C]^{-1/3} F^{1/2} \quad (5.8)$$

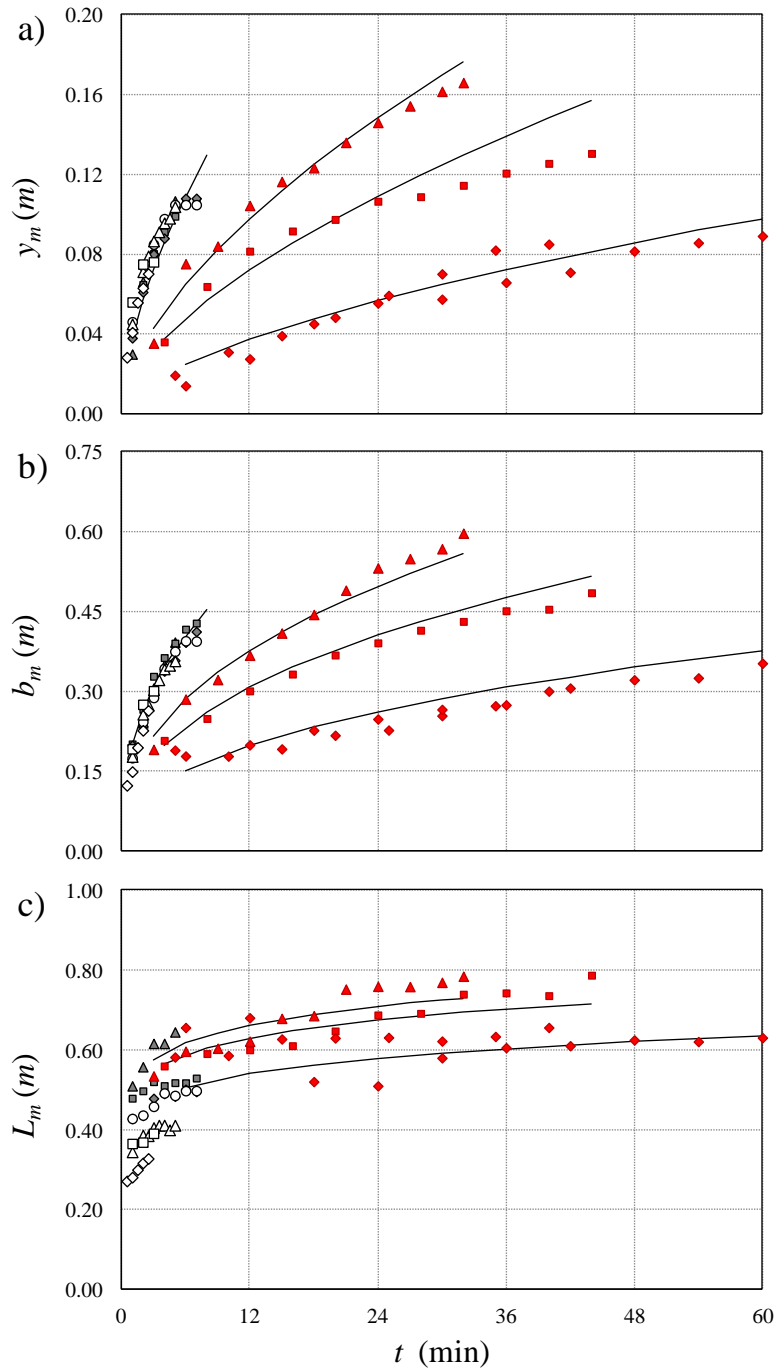


Figure 5-12: Comparison between predictions of the proposed equations and experimental measurements. a) Model performance on prediction of the maximum deposition height, y_m . b) Comparison between the computed deposition widths, b with measurements. c) Comparison of the computed mound length, L , with measurements.

Figure 5-12 shows a comparison between the prediction of the proposed equations and the measured deposition length scales (i.e., maximum deposition height, mound width and mound length). The solid lines in Figure 5-12a show the calculated mound peak height with equation 5.4. Equation 5.4 underestimated the maximum mound height on average by 3% and the maximum error of prediction was within $\pm 20\%$ especially at early stages of the mound development. The proposed equation for prediction of y_m can be used to estimate the deposition height with bed slope up to 10 degrees. In these cases the average error of prediction was found to be -3.60%. A comparison between the predicted values of the mound width, computed by equation 5.5 with measurements was shown in Figure 5-12b.

The proposed formula predicted the mound width with the average error of 1% and this model can also predict the width of the deposition on slope by the average error of 1.7%. The mound length can be estimated by employing equation 5.6 after prediction of the deposition width. A comparison with the mound length measurements and predictions of equation 5.6 are shown in Figure 5-12c. The estimated results calculated by the proposed equation agreed with measurements and the average error of the proposed empirical formula was found to be 2.4%. The proposed model can be employed for prediction of sediment mound length with slope up to 10 degrees with 4.8% error.

The initiation of the sediment deposition and the location of the bed erosion can be estimated by comparing the magnitude of the sediment fall velocity, u_{∞} to the shear velocity, u_* where $u_* = (\tau_o / \rho_w)^{1/2}$ and τ_o is the bed shear stress. Julien (2010) classified the sediment transport in three zones of bed load, mixed load and suspended load. He found that for the ratio of $u_*/u_{\infty} < 0.5$ almost all sediments were transported by bed load and no suspended load can be existed in the flow. For the ratio of $u_*/u_{\infty} > 2$ all sediments will suspend in the flow. These criteria can be employed to estimate the initiation of sediment

deposition and verify the location of bed erosion. Variation of the bed shear stress along the axis of a single-phase wall jets was studied by Rajaratnam and Pani (1974). They presented a non-linear curve to show the normalized shear stress with x/\sqrt{A} , where A is the cross-sectional area of the jet. For $x/\sqrt{A} < 60$ this correlation can be estimated by the following formulation

$$\frac{\tau_o}{1/2\rho u_o^2} = 0.004e^{-0.063(x/\sqrt{A})} \quad (5.9)$$

By assuming a similarity for the velocity and shear stress decay of single-phase wall jets and slurry wall jets along the axis of the jet and employing bed load and suspended loads criteria for the initiation of sediment erosion and deposition, the initiation of deposition can be calculated.

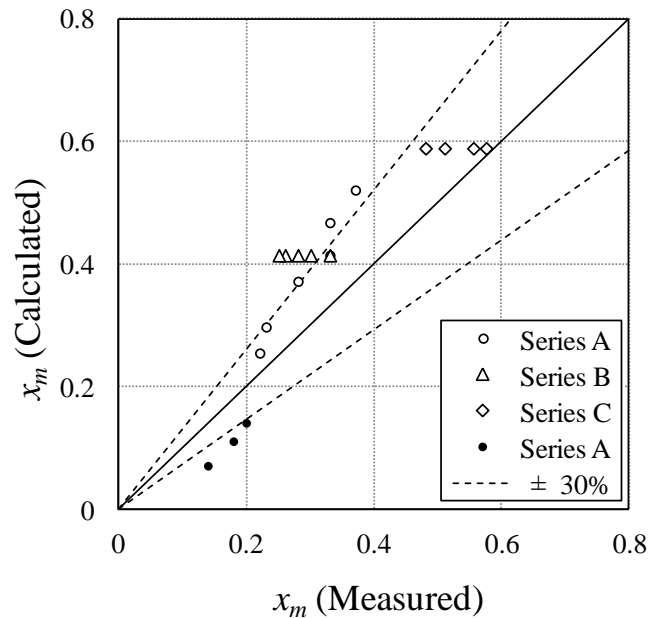


Figure 5-13: Comparison between the measured initiation of the sediment deposition and the location of bed erosion close to the nozzle with calculations for experiments series A, B and C. Open symbols show the initiation of deposition and solid symbols show the locations of erosion. Dash lines represent the $\pm 30\%$ accuracy of calculations.

Figure 5-13 shows the comparison between the measured erosion lengths and the locations of sediment initiation with estimations. Lines with $\pm 30\%$ variation were plotted to show the accuracy of calculation. It was found that the estimation provides reasonable results for slurry wall jets with lower concentration (Series C) but, for wall jets with bed slopes, calculation can have more than 50% error (Series B). Low accuracy level of calculation can be due to the difference between the decay of shear stress for slurry wall jets and single-phase wall jets. Effect of particle concentration can also impact the criteria of the sediment erosion and deposition.

5.7 Summary and Conclusion

A series of laboratory experiments were conducted to study the effects of initial velocity of the slurry jets, bed slope and sediment concentration on the sediment deposition shape and its development. Effect of initial velocity on mound development was shown by densimetric Froude number, F . The densimetric Froude number was found to be an effective parameter on controlling the sediment deposition height, width and its length. It was found that the location of maximum deposition height and mound length increased linearly with F . The deposition angle of sediment mound, β was measured at each time step. A linear correlation was developed between the normalized time, F and the angle of sediment mound.

Effect of bed slope on the shape and formation of the deposition was also studied. It was found that, by increasing the bed slope, the peak deposition height, y_m reached its maximum value earlier and deposition started to advance in the upstream direction. A comparison between the obtained results in this study (Series B) and the mound development of sediment with lower concentration used in a previous investigation (series Z) indicated that, sediment with lower concentration can build up a

bit further downstream. This causes a relatively longer deposition length and narrower mound width. (see Figure 5-8b). Effect of sediment concentration on development of deposition height on slope was found to be negligible.

According to our classification, deposition can develop in three stages named as developing regime, spreading regime and backup regime. In developing regime, deposition height increases with time. Hence the angle of deposition and the deposition width were increased slightly. In spreading regime the maximum deposition height remains almost constant and the angle of deposition begins to increase with a higher rate to reach its maximum value at the end of experiment. The backup regime sets in when the deposition height moved continuously towards the nozzle. It was found that in this regime, the maximum deposition height and width remain almost constant.

The mentioned three stages of the mound development were analyzed by considering the variations of the mound dimensions in each regime. Variations of the aspect ratios of L_m/b_m and L_m/y_m with time were studied and power law correlations were developed for prediction of the mound dimensions. Results of these proposed formulations were compared with measurements. It was found that empirical formulations were capable of predicting the mound dimension with a maximum error of $\pm 20\%$. Proposed models can be employed for estimating the mound dimensions on slopes up to 10 degrees with the average error of 4.8%.

5.8 Notation

A = Area of the deposition, m^2

b_m = Maximum width of deposition, m

b_m^* = Maximum width of deposition at the end of experiment, m

C = Sediment volumetric concentration, %

d = Nozzle diameter, m

D = Diameter of sand particles, mm

F = Densimetric particle Froude number

g = Acceleration due to gravity, m/s^2

g_x = horizontal component of the gravity, m/s^2

g' = Reduced gravity, m/s^2

h = water depth, m

K_s = Bed roughness, mm

L_d = Mound length scale, m

L_m = Maximum length of deposition, m

M = Initial momentum flux of the jet, kgm/s^2

Q = Slurry volume flux, m^3/s

R^2 = Coefficient of correlation

R = Reynolds number

S = Bed slope, degree

t = time, s

t_p = Duration of experiment at each step, min

T = Time scale

T_d = Duration of each experiment, min

u_o = Initial velocity of the sand jet, m/s

u_* = Shear velocity, m/s

u_{∞} = Settling velocity of particles, m/s

x_m = Distance between the nozzle and the peak deposition height, m

y_m = Maximum deposition height, m

y_t = Tail water depth, m

β = Angle of deposition, Degree

ν = Kinematic viscosity, m²/s

ρ_s = Density of sand, kg/m³

ρ_w = Density of water, kg/m³

τ_o = Bed shear stress, Pa

Chapter 6

General Conclusions and Recommendations for Future Research

6.1 General Conclusions

In the preceding chapters, the analysis and results of the laboratory experiments and numerical simulations were presented on the hydrodynamics of slurry jets and deposition developed from slurry wall jets.

In Chapter 2, a detailed numerical modelling of sand jets in water was conducted at high initial sand concentration ($c_o = 60\%$ volumetric concentration) using a computational fluid dynamics model (CFX 11.0). Due to the experimental uncertainty, measurement inaccuracy, and the numerical model assumptions, a difference of 15% between the predictions and measurements is considered to be acceptable. In this study, effects of particle size on the mean properties and turbulent characteristics of the jets were investigated and the following results were concluded:

- The simulated sand velocity results close to the nozzle ($x/d < 25$) were over-predicted by 5.4%.
- The accuracy of prediction was reduced at the middle of the jet $25 < x/d < 80$ and the model predictions were within 10% error.
- The accuracy of the water-phase velocity was also verified by employing the conservation of momentum.
- The model was able to predict the sand-phase momentum flux within 10 % error and it under-estimates the water phase momentum flux by 15%.

- The turbulent kinetic energy of the sand jets increases from the nozzle, reaches the maximum value at $x/d = 11.5$ and decreases gradually thereafter.
- Similar trend was found for the rate of energy dissipation but the maximum value was located at $x/d=8.6$.
- The turbulent kinetic energy of the water phase decreases with increasing particle size.
- The maximum TKE of the jet with 210 μm particle size was found to be 6.7 and 11.5 percent higher than the sand jets with particles sizes of 460 μm and 780 μm , respectively.
- The effect of Schmidt number on sand velocity and concentration was found to be less than 1.2% showing that the effect of Schmidt number on simulation of sand jets was negligible.

In Chapter 3, a computational investigation was performed to study the effects of nozzle size, initial particle concentration, initial velocity and particle size on the hydrodynamics of sand-water slurry jets. The computed mean properties of sand-phase and water-phase axial and radial velocities, volumetric concentration and turbulent kinetic energy (TKE) along the jets axis and at different cross sections were compared with laboratory measurements. The effect of sand particles on slurry jet spreading rate, axial velocity decay, decay of concentration and turbulence properties were studied, and the results were compared with the corresponding single-phase water jets and plumes. Following results were found in Chapter 3.

- In contrast with single-phase water jet, the water-phase spreading of slurry jets is function of nozzle size.

- Effects of other parameters such as c_o and D on the spreading of slurry jets were studied and results were shown as the ratio between the jet half-width for the sand phase to water phase, λ .
- For slurry jets with $D=505 \mu\text{m}$, λ became independent of x for $x/d > 70$ with a value between 0.22-0.3.
- For dilute slurry jets with small particles, λ reached a value close to unity whereas this value for jets with large particles can be as low as 0.3.
- The water-phase centreline velocity increased with increasing particle concentration. Empirical formulations were introduced to show these strong correlations between F_r , c_o and velocity decay.
- Effect of c_o on the computed entrainment coefficient, α_e , indicated that, α_e becomes smaller than the corresponding value for single-phase jet.
- An absolute entrainment coefficient, α_o , was introduced by normalizing the entrainment velocity with u_o .
- α_o of slurry jets has higher values than the single-phase water jets for $x/d < 80$.
- The averaged drag coefficients of particle cloud, C_D , at different cross-sections were computed. It was found that particle concentration can reduce C_D since particles tend to travel behind the wake generated by frontal particles.
- The turbulent length scale $l=k_w^{3/2}/\varepsilon$ is three times larger than the integral length scale of $A=0.0385x$ and this ratio was almost constant along the axis of the jet at $x/d > 40$ and invariant with the nozzle diameter and particle size.
- Turbulent shear stress of both phases was computed from velocity and concentration profiles and the computed results indicated that c_o enhanced the water-phase turbulent shear stress by 17% whereas experimental observations showed an increase of 10.8% at the peak location.

- The peak value of $\overline{u'v'}$ in sand-phase was found to be larger than the corresponding single-phase by 28.5% and the peak location was shifted away from the peak location of single-phase jet at $x/d=40$.

In Chapter 4, the behaviour of a sand jet front in water and its associated fluid motions with different sand particle sizes and different nozzle diameters were studied by using laboratory experiments. It was concluded that the particle size can significantly change the frontal shape of the jets and their mixing capacities. The obtained results of this chapter can be employed for designing and for optimizing the onset of mixing systems. The experimental results presented in this chapter can be used for validation of numerical models. In this experimental study the following results were found:

- The frontal shape and its formation were classified into three categories which particle Reynolds number, Re_p , was the parameter of classification.
- The normalized frontal velocity (u_f/u_∞) was a function of nozzle diameter and particle size and this ratio drops from the nozzle and approaches a constant far from the jet ($x/d = 200$).
- The jet front terminal velocities, u_{fo} , of small particles were as large as 5 times of the individual particle settling velocity, u_∞ .
- The slope of correlation between the normalized frontal velocity and axial distance was found to be $1/5$ whereas this slope for a single-phase water jet was known to be $1/3$.
- The decay of frontal velocity at $10 < x/d < 30$ is similar to the particle cloud measurements found in the literature but, at $30 < x/d < 60$, the measured frontal velocities were higher than that of thermals.

- The growth rate of the sand jet front is smaller than the growth rate of the water jet front.
- A pickup distance was introduced from the solution of Euler equation. For small particles, the pickup distance become 92.4% of the front radius whereas, this length is only 44% of the radius for relatively larger particles.
- Three regimes were identified on the vortex structure of the fronts using Galilean decomposition and the velocity ranges at each regime were reported.
- Vortices were extracted by employing the swirling strength technique.
- It was found that smaller particles attenuate the turbulence much faster than larger particles and logarithmic formulations were developed for prediction of turbulent modulation on solid-gas and solid-liquid turbulent jets.
- Particles in solid-liquid jets can attenuate the turbulence faster than solid-gas jets since the carrier phase has higher viscosity.
- Effect of the Stokes number of the jet on turbulence modulation was shown that particle-laden jets with lower Stokes number can provide larger turbulence attenuation.

In Chapter 5, the deposition of sand particles injected from sediment laden circular jets on a horizontal and inclined beds were studied. Laboratory experiments in this chapter can be used for prediction of the development of sediment mound with time. The obtained results can also be used to verify numerical models and optimize the current design of the submerged sand mounds and artificial islands. Following results were found in Chapter 5.

- Effect of initial velocity on mound development was shown by densimetric Froude number, F , and it was found that the location of maximum deposition height and mound length linearly increased with F .

- A linear correlation was developed between the normalized time, F and angle of sediment mound.
- The peak deposition height, y_m increased with bed slope.
- In presence of same bed slope, sediment particles with lower concentration can build up a bit further downstream which cause relatively longer deposition length and narrower mound width.
- Three regimes were classified in mound formation named as the developing regime, the spreading regime and the backup regime.
- In the developing regime, deposition height increases with time and angle of deposition and the deposition width were increased slightly.
- In the spreading regime, the maximum deposition height remains almost constant and the angle of deposition begins to increase with a higher rate.
- The backup regime is started when the deposition height continuously developed toward the nozzle and the maximum deposition height and width remain almost constant.
- Variations of the aspect ratios of L_m/b_m and L_m/y_m with time were studied and power law correlations were introduced for prediction of the mound dimensions.
- Proposed models can be employed for estimating the mound dimensions on slopes up to 10 degrees with the average error of 4.8%.

Overall, this thesis provides important results that advance the knowledge of two-phase solid-liquid flow dynamics in the mixing of sediment laden jets and sediment deposition. In addition, this thesis provides valuable information about the flow parameters that can be taken into account for accurate simulation of the sediment-laden jets with high initial sediment concentration.

6.2 Future Research Studies

Future research in this area can be classified in to two categories. Since hydrodynamics of solid-liquid two-phase flows especially in presence of high sediment concentration is complex, fundamental research can enhance our current understanding about the underlying physics and dynamics of the system. This provides detailed information about the flow and can be used to develop and define applied research topics. The knowledge gap on fundamental research in this area is shown in this chapter. Other topics can be proposed at this stage which can be categorized in the area of applied research. The out coming results could be directly employed in the industrial projects. Those results can be useful for designing purposes, optimization and monitoring of the current projects. A list of possible applied research topics with a brief introduction is described below.

6.2.1 Fundamental Research:

- *Experimental Study of the Pulsed Sediment-laden Jets:*

Series of experimental studies on the frontal of the slurry jets have been conducted in this thesis and the obtained results with the analysis of the jet front were shown in Chapter 4. In order to form a series of pulses, a fixed amount of particles can be released into the ambient water in sequence with a time lag. One extreme of this study is to reduce the time lag between each release to form a continuous release of sediment particles (slurry jet). Experimental investigations of the continuous release of sediment in water have been reported in the literature (see section 4.1) and the differences between the mixing mechanism of a slurry jet and the frontal of a slurry jet were clearly shown in Chapter 4. The other extreme in this study is to increase the time lag between each release to a large value. In this condition, a single thermal or a jet front will form (depend

of the duration of release). Even though, the physical understanding and the detailed measurements of the two extreme cases are available but, a gap of knowledge between two extremes requires more attention. Possible variations on the stop/release duration and the interfaces between each pulses need to be investigated. The out coming results of this study can be used for validation of numerical models and can be developed our current understanding about this subject.

- *Hydrodynamics of the Slurry Jet Front in Viscous and Non-Newtonian Ambient:*

The aim of this fundamental study is to understand the development and formation of the slurry jet front injecting into the oil-sand's tailing ponds. The rheological properties of the tailing ponds can be classified as highly viscous and non-Newtonian. To approach this goal, hydrodynamics of the frontal of the slurry jet in water was studied in this thesis. It was found that particle size as one of the controlling parameters can change the behavior and mixing capacity of the jet front in water. According to the experimental observations (Chapter 4), different hydrodynamic classes were found based on the effect of the particles' inertia and the ambient viscosity. A new series of laboratory experiments can be conducted by using fluids with different viscosity to study the effect of ambient viscosity on the jet front. The obtained results in this area can be compared with the results of the slurry jet front in water. In later stages, a non-Newtonian fluid with similar characteristics of the tailing ponds can be employed as an ambient flow.

The driving force of particles in this thesis was gravity. Initial momentum of particles released into viscous ambient can be increased by pumping. Effects of initial momentum, particle size and ambient viscosity can be studied to understand the underlying physics of the jet front in a highly viscous flow.

- *Investigation on the Formation of Sediment Mound:*

Formation and development of the sediment mound was investigated in this thesis. Effects of initial velocity, sediment concentration and bed slope were studied and the formation of sediment mound with time was classified into three regimes. Investigation on the concentration decay of slurry jets can provides more understanding about the formation of sediment deposition. Mound formation mechanism can be studied by measuring flow characteristics in detail such as velocity of the slurry flow passing over the mound. In addition, detailed velocity measurements can provide more information about sediment transport and variations of turbulence on the horizontal slurry jets. By knowing the obtained results from this study, development of deposition can be modeled more accurately and the effect of other parameters such as sediment sizes and their densities can be predicted by a validated model. Velocity field and sediment concentration can be measured by employing PIV technique and optical probes.

For velocity field measurements, PIV method can be used in this study. This measuring equipment can provide instantaneous two-dimensional velocity field which the averaged velocity, vortex structure, turbulence and other flow characteristics can be extracted from the PIV measurements. Optical probe can be employed to measure sediment concentration and velocity in locations of having high sediment concentration.

6.2.2 Applied Research

- *Numerical Simulation of Slurry Wall Jets and Sediment Deposition:*

Deposition of sand particles injected from sediment-laden circular jets on a horizontal and inclined beds were studied in Chapter 5 of this thesis. Effects of initial velocity, sediment concentration and bed slopes were investigated and developments of sediment

mound with time with the effects controlling parameters were analyzed. These studies can be performed by employing validated numerical models. The components of the governing equations that require to be taken into account in simulation of sediment-laden jets were studied carefully in Chapter 2 and 3 of this thesis. Mesh refinement strategy, simulation procedure, and model coefficients used in modeling of sand and slurry jets can be used to simulate slurry wall jets and sediment deposition. Outputs of the numerical model can be used to study the variations of mound dimensions with time and results can be compared with the results reported in Chapter 5 of this thesis. After model verification, influence of some other parameters such as, particle size, nozzle diameter and the characteristics of the ambient flow can be modeled. Numerical model has the capability to simulate velocity field around the sediment mound. This information could provide more insight into the hydrodynamics of slurry wall jets.

For industrial application, a series of nozzle could be used to form a manifold. In this condition the optimum distance between each nozzle can be designed by the verified numerical model. Since properties of slurry flow such as flow rate, sediment size and its concentration may varied with time, the verified model could be used as a monitoring tool to optimize operation.

- *Sediment Deposition Formed by Surface Slurry Jets:*

Experimental investigations reported in Chapter 5 of this thesis were focused on the deposition pattern formed by slurry wall jets. Laboratory experiment can also be carried out to study the formation of sediment mound issued from surface slurry jets. Since operation of slurry flow on the ground can be more efficient than the underwater release, a comprehensive knowledge on the mound formation by the slurry surface jets can save

time and expenses on building under water cover or artificial islands. The controlling parameters on development of sediment mound can be listed as follow.

- 1- Initial release conditions such as, nozzle diameter and its orientation to the horizon, initial momentum of the slurry flow. Slurry flow can also be released continuously or can be pulsed.
- 2- Sediment conditions such as, sediment size and sand concentration.
- 3- Ambient conditions could be stagnant, stratified or co-flow.

The combination of those parameters can deform the shape of the mound and affect the development of deposition. Numerical models can be verified with those laboratory studies and can be used in designing and operation of the submerged sand mounds.

- *Mound Formation in Non-Newtonian Ambient:*

Sediment deposition can be used to cover the underwater waste and sludge. Many hazardous and toxic materials have been settled in the lower layer of oil-sand's tailing ponds that can jeopardize the life of species in the vicinity of the pond. A layer of sediment with a designed thickness can prevent mixing of those toxic materials with the top water layer. The mound formation due to release of slurry flow can provide a sediment layer which can cover the hazardous materials at the bottom of the pond.

The sludge formed in tailing ponds behaves like a non-Newtonian fluid (i.e., Bingham plastic). The deposition development in this ambient can be different from the formation of sediment mound in water. Consequently, the obtained results of mound formation in water cannot be applied for this condition. Deposition development in non-Newtonian ambient can be studied by employing experimental studies. Properties of the non-Newtonian ambient can be adjusted for numerical model and the obtained results can be used for monitoring the operation.

Appendix 1

Slurry Jet Visualization

Photographic observations of turbulent sand jets in water were carried out using the 210 μm sand particles passing through three different nozzle size, 6, 12.5, and 19.2 mm. A high resolution CCD camera (Pulnix Tm-1040) controlled by a computer frame grabber system (Streams 5, I.O. Industries Inc.) captured images of the turbulent jets with a frame rate of 30 fps and exposure time of 1/60 sec. In order to eliminate the effect of distortion on photos, a Plexiglas plane with the mesh of 2.0 X 2.0 cm was located at the centreline of the nozzle and photographed. This image was used as a reference of both horizontal and vertical dimensions. The distorted mesh and the turbulent sand jet images were imported and redrawn in AutoCAD 2008. The exact location of the jet boundary was counted by the redrawn mesh.

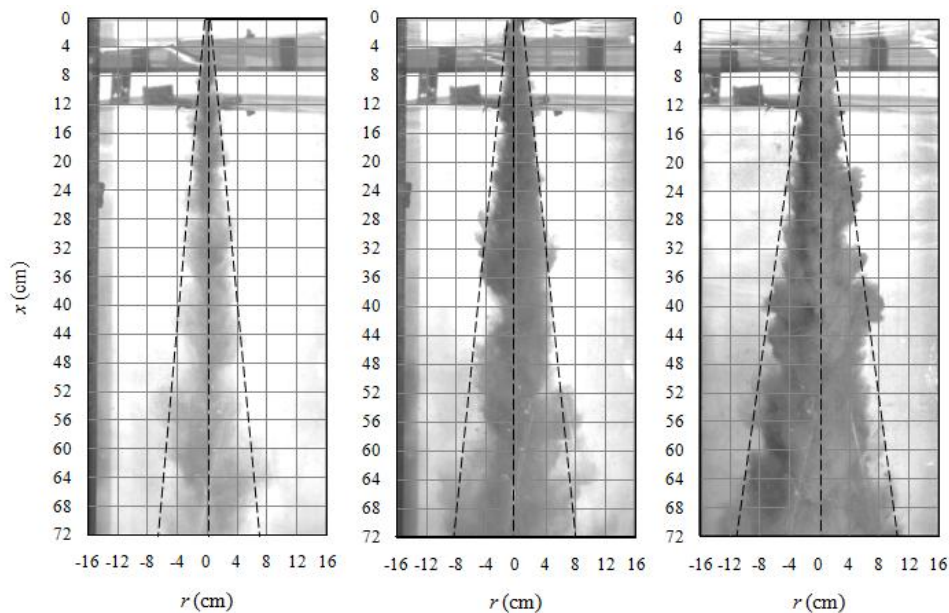


Figure A1-1: Photographical observation of the turbulent sand jet in water from the water surface to the 72 cm downstream; Left, $d = 6$ mm; Middle $d = 12.5$ mm; Right, $d = 19.2$ mm.

Figure A1-1 is illustrated the spreading of the 210 μm sand jet with different nozzle diameter. The width of jet was measured at 72 cm from the water surface. From Figure A1-1, it may deduce that, the turbulent sand jets has more spreading rate when the jet nozzle diameter increased. Similar experiments were conducted using an 8 mm jet nozzle diameter with the different sand particle size by Mazurek et al. (2002). They studied the effect of particle size on the jet spreading rate and found that, the larger particle size spread less than the smaller one.

Figure A1-2 presents the comparative relations between the particle size, D , and the jet nozzle diameter, d . Open symbols represented the Mazurek et al. (2002) observations and the solid symbols show the present photographical experiment results. Both the abscissa and the ordinate of the Figure A1-2 were normalized with the jet nozzle radius, r_o .

They have also demonstrated that, the ratio of the momentum flux from the nozzle, $M_o = \rho_s u_s^2 (1-n) \pi r_o^2$ to the buoyancy force $B = Ng \Delta\rho (4/3) \pi (D/2)^3$, plays an important roles on the turbulent jet spreading. Here g is the acceleration due to the gravity, $\Delta\rho$ is the relative density of the sand compared to the water and N is the number of the sand particles at any section. Base on the above expressions, parameter F_o was introduced to generalized the turbulent sand jets spreading data that is:

$$F_o = \frac{U_s}{\sqrt{gD \frac{\Delta\rho}{\rho}}} \quad (\text{A1-1})$$

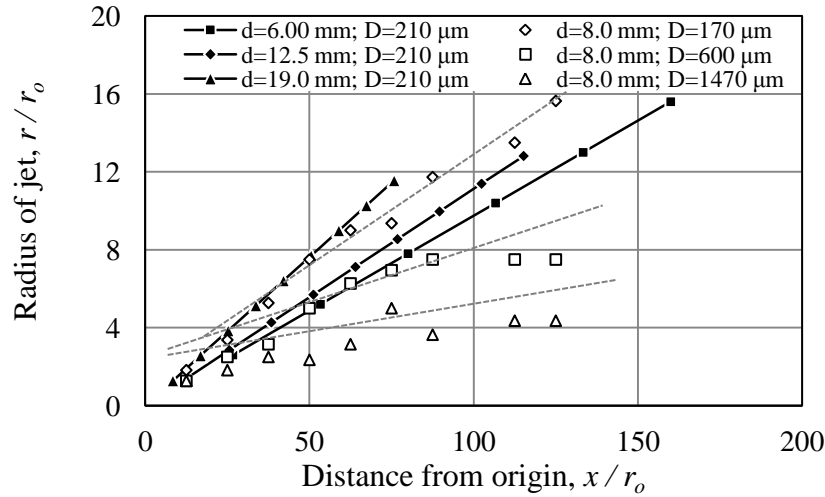


Figure A1-2: Observation results on the growth of the turbulent sand jets.

F_o was calculated from different setup in the present experiments and the initial velocities of the sand particles at the jet nozzle, u_s , were obtained from the simulation outputs. An assumption was made to determine the jet boundaries at any section from the numerical simulation outputs. The boundaries of the jet were located at the position which the volumetric concentration of the sand particles is equal to 1%, that is, outside of the jet boundaries have a concentration less than 1%. The growth rates of the simulated jet were then computed by measuring the radius of the jet at any location, r , respect to the distance from the nozzle, x .

The correlation of the nondimensional parameter, F_o , and the jet growth rate is depicted in Figure A1-3. Previous observations on the jet growth rate (Mazurek et al., 2002) were also presented in Figure A1-3 (open symbols). The results of four different jet nozzles and seven different particle sizes ranging from 0.17 mm to 1.47 mm are well correlated with F_o , since all points collapse approximately on one curve. A modified formulation of the Mazurek et al. (2002) study can be described by the following expression with a correlation coefficient of $R^2 = 0.82$.

$$\frac{r}{x} = 0.029 F_o^{0.685} \quad (\text{A1-2})$$

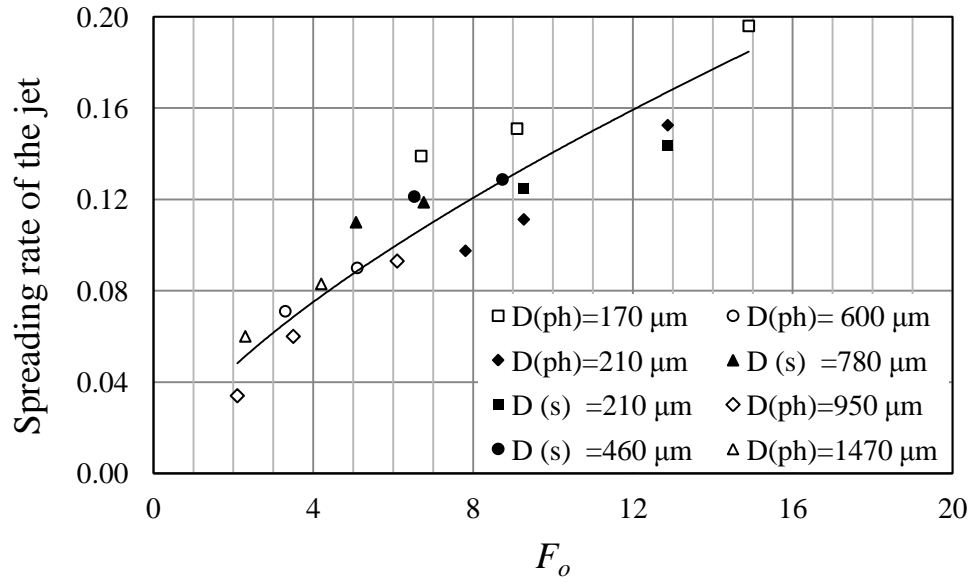


Figure A1-3: Correlation of the spreading rate of the turbulent sand jets with F_o . (ph) in the legend stands for the photographic observation, (m) stands for the measurement and (s) stands for the numerical simulation.

Appendix 2

Mass Flux Measurements

Sand particles instantly released from the nozzle ($d = 4$ mm) and collected into an Erlenmeyer flask. Time was recorded with stopwatch and sands were weighted with an accurate scale with the tolerance of 0.2 gr.

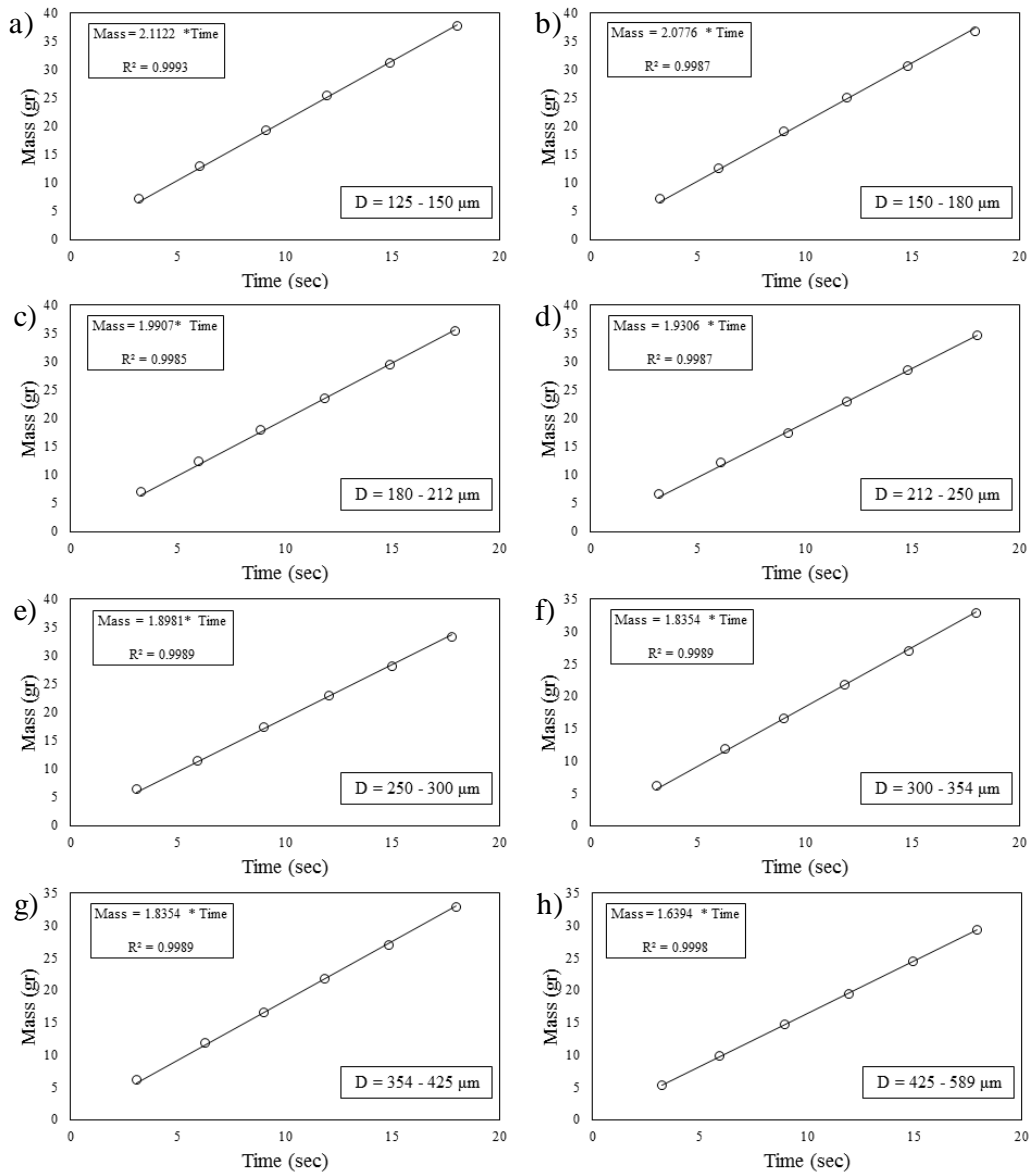


Figure A2-1: Mass - Time relationship for different particle sizes. a) $D=125-150 \mu\text{m}$, b) $D=150-180 \mu\text{m}$, c) $D=180-212 \mu\text{m}$, d) $D=212-250 \mu\text{m}$, e) $D=250-300 \mu\text{m}$, f) $D=300-354 \mu\text{m}$, g) $D=354-425 \mu\text{m}$, and h) $D=425-589 \mu\text{m}$.

The relationship between the time and sand mass were shown in Figures A2-1. A trend line was passed through the measurements and its slope was the mass flux of the sand particles. Sand particles passed through different nozzle size ranged between 2 to 10 mm and the mass fluxes were measured via the mentioned procedure. The results of mass flux measurement having size ranges between 210 to 850 μm and passed through different nozzles were shown in Figures A2-2.

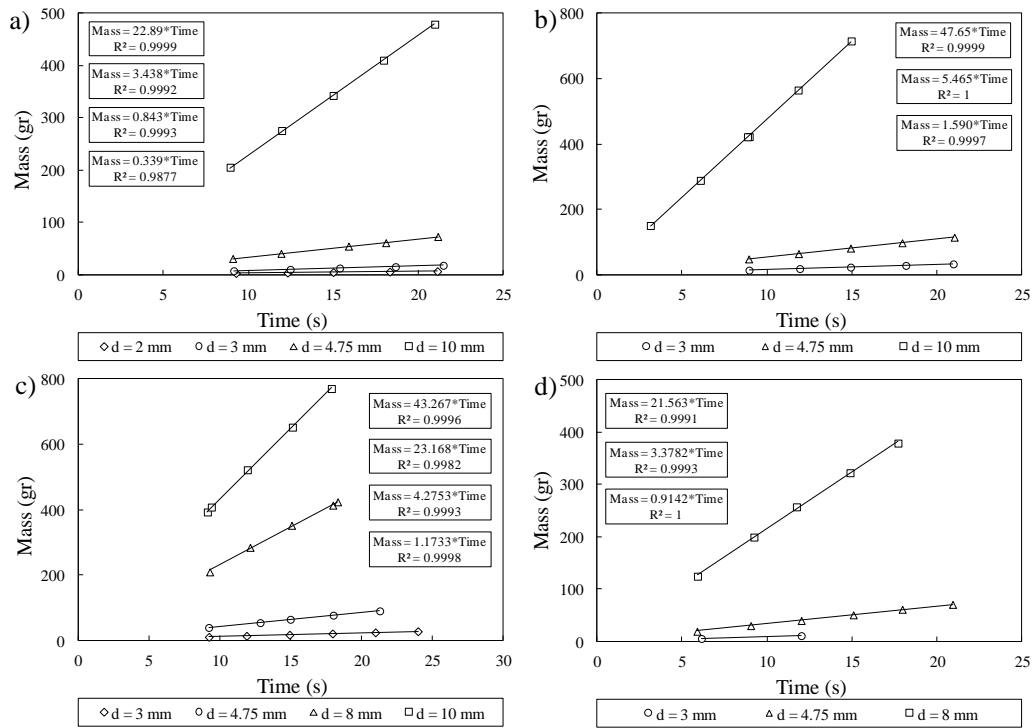


Figure A2-2: Effect of nozzle diameter on the mass flux of sand particles. a) $D = 210 \mu\text{m}$, b) $D = 300 - 425 \mu\text{m}$, c) $D = 425 - 707 \mu\text{m}$, and d) $D = 707 - 850 \mu\text{m}$.

References

- Abramovich, G. N., (1963). "The theory of turbulent jets" *MIT Press*, 671 p.
- Adrian, R. J., Christensen, K. T., Liu, Z., C., (2000), "Analysis and interpretation of instantaneous turbulent velocity fields." *Experiment in Fluids*, 29, pp. 275-290.
- Alberta Department of Energy, (1995), "Fine tails and process water reclamation." *Advances in Oil Sands Tailing Research, Alberta Department of Energy*, Oil Sands and Research Division, Edmonton, AB, pp. 317.
- Alberta Energy and Utilities Board, (2005), "Alberta's reserves 2004 and supply/demand outlook 2005-2014." Report No. ST98-2005. Alberta Energy and Utilities Board, Calgary, AB.
- Albertson, M. L., Dai, Y. B., Jensen, R. A. and Rouse, H., (1950), "Diffusion of submerged jets." *Trans. ASCE*, 115, pp. 639-697.
- Allen, J. R. L., (1982), "Sedimentation from jets and separated flows." Chapter 4, *Sedimentary structures their character and physical basis*, v. II: Amsterdam, Oxford, New York, Elsevier Scientific Publishing Company, pp. 133-171.
- Angst, R., Harnack, E., Singh, M., and Kraume, M., (2003), "Grid and model dependency of the solid/liquid two phase CFD simulations of stirred vessels." *11th European Conference on Mixing*, Oct. 14-17, Bamberg, Germany, 347-354.
- Angst, R., Mier, P., Kraume, M., (2001). "Simulation of the solid/liquid two-phase flow field in jet loop reactors." *Comp. Fluid and Solid Mech./2* Elsevier. Ltd. Netherlands, 1058-1061.
- Ansys. (2008). CFX-11 solver theory, ANSYS Canada Ltd.
- Ansys. (2009). CFX-11 solver theory, ANSYS Canada Ltd.
- Arai, T., Kudo, N., Ishima, T., Youssef, I. M., Obokata, T., (2003). "Turbulence structure of a liquid-solid two-phase jet by means of laser techniques."

Proc. of ASME FEDSM'03 4th ASME_JSME joint Fluid Eng. Conf.,
Honolulu, Hawaii, USA, July 6-10.

Arakeri, J. H., Das, D., Krothapalli, A., and Lourenco L., (2004), "Vortex ring formation at the open end of a shock tube: A particle image velocimetry study." *Physics of Fluids*, Vol. 16, 4, pp. 1008-1019.

Azimi, A., Zhu, D., Rajaratnam, N., (2008) "Numerical simulation of sand jet in water." *1st International Oil Sand Conference*, Edmonton, Dec. 2008. Pp. 183-191.

Azimi, A.H, Cai, J., Hall, N., Oshikawa, H., Zhu, D. Z., and Rajaratnam, N., (2011a), "Mound formation by slurry jets on a slope in a water pond." *34th IAHR world congress*, Brisbane, Australia, June 2011, pp. 3346-3353.

Azimi, A. H., Zhu, D. Z., and Rajaratnam, N., (2011b), "Effect of particle size on the characteristics of sand jet in water." *Journal of Engineering Mechanics*, Vol. 137, No. 12, pp. 822-834.

Azimi, A. H., Zhu, D. Z., Rajaratnam, N., (2012). "Experimental study of sand jet front in water." *Int. Journal of Multiphase flow*. Vol. 40, pp. 19-37.

Beuselinck, L., Govers, G., Steegen, A., and Hairsine, P. B., (1998), "Experiment on sediment deposition by overland flow." *Modeling Soil Erosion, Proceedings of Sediment Transport and Closely Related Hydrological Processes*, Vienna, IAHS Publishers, no. 249, July 1998, pp. 91-96.

Bhuiyan, F., Rajaratnam, N., Zhu, D. Z., (2010), "An experimental study of mounds formed by dumping coarse sediment in channel flow." *Journal of Hydraulic Research*, Vol. 48, No. 3, pp. 283-291.

Bombardelli, F. A., and Jha, S. K., (2009). "Hierarchical modeling of dilute transport of suspended sediment in open channels." *Environmental Fluid Mechanics*, Vol. 9, 207-235.

Bond, D., and Johari, H., (2005), "Effect of initial geometry on the development of thermals." *Experiment in Fluids*, 39, pp. 589-599.

Bond, D., and Johari, H., (2010), "Impact of buoyancy on vortex ring development in the near field." *Experiment in Fluids*, 48, pp. 737-745.

- Breusers, H. N. C., Raudkivi, A. J., and International Association for Hydraulic Research, (1991), *Scouring*, Balkema, Rotterdam, The Netherlands.
- Brush, L. M. J., (1962). "Exploratory study of sediment diffusion." *Journal of Geophysical Research*, Vol. 67, No. 4, pp. 1427-1433.
- Buhler, J., and Papantoniou, D. A., (1991), "Swarms of coarse particles falling through a fluid." *In Environmental Hydraulics* (ed. J. T. Lee & T. K. Cheung), pp. 135-140. Balkema, Rotterdam.
- Bush, J. W. M., Thurber, B. A., Blanchette, F., (2003), "Particle clouds in homogeneous and stratified environments." *Journal of Fluid Mechanics*, Vol. 489, pp. 29-54.
- Cai, J., Hall, N., Elenany, M., Zhu, D. Z., and Rajaratnam, N., (2010), "Observations on Sand Jets in Air", *Journal of Engineering Mechanics*, Vol. 136, No. 9, pp. 1181-1186.
- Cerecedo, L. M., Aisa, L., Ballester, J., (2009), "Experimental study on a non-dilute two-phase coflowing jet: Dynamics of particles in the near flow field." *Int. Journal of Multiphase flow*, Vol. 35, pp. 468-483.
- Chakraborty, P., Balachandar, S., and Adrian, R. J., (2005), "On the relationships between local vortex identification schemes." *Journal of Fluid Mechanics*, Vol. 535, pp. 189-214.
- Chen, C. P., and Wood, P. E., (1986). "Turbulence closure modeling of the dilute gas-particle axisymmetric jet. *AIChE J* Vol. 32, No. 1, 163-166."
- Chong, M. S., Perry, A. E., and Cantwell, B. J., (1990), "A general classification of three-dimensional flow fields." *Physics of Fluids A*, Vol. 2, pp. 765-777.
- Colaciti, A. K., Lopez, L. M. V., Navarro, H. A., Cabezas-Gomez, L., (2007). "Numerical simulation of a radial diffuser turbulent airflow." *Applied Mathematics and Computation*, Vol. 189, pp. 1491-1504.
- Crowe, C. T., (2000). "On models for turbulence modulation in fluid - particle flows." *Int. J. Multiphase Flow*, Vol. 26, 719-727.

- Crowe, C. T., Gore, R. A., Troutt, T. R., (1985), "Particle dispersion by coherent structures in free shear flows." *Particulate Science and Technology*, 3, pp. 149-158.
- Crowe, C. T., Sommerfeld, M., Tsuji, Y., (1998). "Multiphase flows with droplets and particles." *CRC press LLC*, 471p.
- Cuthbertson, A. J. S., Davies, P. A., (2008). "Deposition from particle-laden, round, turbulent horizontal buoyant jets in stationary and coflowing receiving fluids." *Journal of Hydraulic Engineering*, ASCE, Vol. 134, No. 4, 390-402.
- Deshpande, N., Balachandar, R., and Mazurek, K. A., (2007), "Effects of submergence and test startup conditions on local scour by plane turbulent wall jets." *Journal of Hydraulic Research*, Vol. 45, No. 3, pp. 370-387.
- Dominski, M. (2007), "Surface mined oil sand: tailings practices performance, and projections." Alberta Energy and Utilities Board, Proceedings of the 3rd International Heavy Oil Conference, March 57, 2007, Calgary, AB.
- Fan, J., Zhang, L., Zhao, H., and Cen, K., (1990). "Particle concentration and particle size measurements in a particle laden turbulent free jet." *Experiments in Fluids*, 9, pp. 320-322.
- Fischer, H.B., List, E. J., Koh, R. C. Y., Imberger, J., and Brooks, N. H., (1979). "Mixing in inland and coastal waters." *Academic press*, San Diego, California, USA. 483 p.
- FTFC. (1995), "Fine tailings and process water reclamation." Fine Tailings Fundamental Consortium, *Advances in oil sands tailings research*, Vol. II, Alberta Department of Energy, Oil Sands and Research Division, Edmonton, AB, pp. 1-52.
- Gan, L., and Nichels, T. B., (2010), "An experimental study of turbulent vortex rings during their early development." *Journal of Fluid Mechanics*, Vol. 649, pp. 467-496.

- Gensheimer III, R. J., (2010), "Dynamics of particle clouds in ambient currents with application to open-water sediment disposal." *MSc. Thesis*, Dept. of Civil and Environmental Engineering, MIT, Cambridge, MA, 260 p.
- Gharib, M., Rambod, E., and Shariff, K., (1998), "A universal time scale for vortex ring formation." *Journal of Fluid Mechanics*, Vol. 360, pp. 121-140.
- Gore, R. A., Crowe, C. T., (1989). "Effect of particle size on modulating turbulent intensity." *Int. J. Multiphase Flow* Vol. 15, No. 2, 279-285.
- Gore, R. A., Crowe, C. T., (1991). "Modulation of turbulence by a dispersed phase." *Transaction of the ASME*, Vol. 113, 304-307.
- Gu, J., Huang, J., and Li, C. W., (2008), "Experimental study on instantaneous discharge of unsorted particle cloud in cross-flow." *Journal of Hydrodynamics*, Vol. 20, No. 1, pp. 10-16.
- Hall, N., Elenany, M., Zhu, D. Z., and Rajaratnam, N., (2010) "Experimental study of sand and slurry jets in water." *Journal of Hydraulic Engineering*, ASCE, Vol. 136, No. 10, pp.727-738.
- Hardalupas, Y., Taylor, A. M. K. P., and Whitelaw, J. H., (1989), "Velocity and particle-flux characteristics of turbulent particle-laden jets." Proceedings of the royal society of London, Series A, Mathematical and Physical Science, Vol. 426, No. 1870, pp. 31-78.
- Hartmann, H., Derksen, J. J., van den Akker, H. E. A., (2006). "Numerical simulation of a dissolution process in a stirred tank reactor." *Chemical Engineering Science*, Vol. 61, 3025-3032.
- Hill, P. G. and Ouellette, P., (1999), "Transient turbulent gaseous fuel jets for diesel engines." *Journal of Fluids Engineering*. Vol. 121, pp. 93-101.
- Hoffmann, A. C., Finkers, H. J., (1995). "A relation for the void fraction of randomly packed particle beds." *Powder Technology*, 82, 197-203.
- Holdich, R. G., (2002), "Fundamentals of particle technology." Midland Information Technology and Publishing, 173 p.
- Hoyal, D. C. J. D., Van Wagoner, J. C., Adair, N. L., Deffenbaugh, M., Li, D., Sun, T., Huh, C., and Giffin, D. E., (2003), "Sedimentation from jets; A

- deposition model for classic depositions of all scales and environments.”, *AAPG Annual Meeting*, Salt Lake City, Utah., Search and Discovery Article #80081, 10 p.
- Hrenya, C. M. And Sinclair, J. L., (1997). “Effects of particle-phase turbulence in gas-solid flows.” *Fluid Mechanics and Transport phenomena, AIChE*, Vol. 43, No. 4, 853-869.
- Hunt, J. C. R., Wary, A. A. and Moin, P., (1988), “Eddies, stream, and convergence zones in turbulent flows.” Center for Turbulence Research Report, CTR-S88, pp. 193-208.
- Imran, J., Parker, G., and Harff, P., (2002), “Experiments on incipient canalization of submarine fans.” *Journal of Hydraulic Research*, Vol. 40, pp. 21-32.
- Jeong, J., and Hussain, F., (1995), “On the identification of a vortex.” *Journal of Fluid Mechanics*, Vol. 285, pp. 69-94.
- Jiang, J. S., Law, A. W. K., Cheng, N. S., (2005). “Two-phase analysis of vertical sediment-laden jets.” *Journal of Eng. Mechanics*, 131(3), 308-318.
- Julien, P. Y., (2010), “Erosion and sedimentation.” Cambridge University Press, Second edition, 371p.
- Kasperski, K. L., (1992), “A review of properties and treatment of oil sands tailings.” *AOSTRA Journal of Research*, Vol. 8, pp. 11-53.
- Kolář, V., (2007), “Vortex identification: New requirements and limitations.” *Int. J. of Heat and Fluid Flow*, Vol. 28, pp. 638-652.
- Krueger, P. S., and Gharib M., (2003), “The significance of vortex ring formation to the impulse and thrust of a starting jet.” *Physics of Fluids*, Vol. 15, 4, pp. 1271-1281.
- Lain, S., and Garcia, J. A., (2006), “ Study of four-way coupling on turbulent particle-laden jet flows.” *Chemical Engineering Science*, 61, 6775-6785.
- La Vision (2007), “DaVis flow master software manual for DaVis 7.2.” LaVision, GmbH, Germany.

- Launder, B. E., and Spalding, D. B., (1974). "The numerical computation of turbulent flows." *Computer Methods in Applied Mech. and Eng.*, 3, 269-289.
- Lee, J.H.W., Chu, V. H., (2003). "Turbulent jets and plumes; A Lagrangian approach." *Kluwer Academic Publishers Group*, The Netherlands, 390 p.
- Lima Neto, I. E., Zhu, D. Z., Rajaratnam, N., (2007) "Effect of tank size and geometry on the flow induced by circular bubble plumes and water jets." *Journal of Hydraulic Engineering*, ASCE, Vol. 134, No. 6, pp. 833-842.
- List, E. J., (1982) "Mechanics of turbulent buoyant jets and plumes." *Turbulent Buoyant Jets and Plumes* (ed. W. Rodi), *Pergamon*, pp. 1-68
- Longmire, E. K., and Eaton, J. K., (1992), "Structure of a particle-laden round jet." *Journal of Fluid Mechanics*, Vol. 236, pp. 217-257.
- Lopez de Bertodano, M. A., (1998). "Two fluid model for two-phase turbulent jets." *Nuclear Engineering and Design*, 179, 65-74.
- Luo, K., Fan, J., Cen, K., (2005). "Modulations on turbulent characteristics by dispersed particles in gas-solid jets." *Proc. R. Soc. A*, August 10, Vol. 461, pp. 3279-3295.
- MacKinnon, M. D, (2001), "Process-affected waters: impact of operating factors on recycle water quality [online]." Canadian Oil Sands Network for Research and Development (CONRAD), Oil Sands Water Usage Workshop, February 24-25, 2005.
- Marugán-Cruz, C., Rodríguez-Rodríguez, J., and Martínez-Bazán C., (2009), "Negatively buoyant starting jets." *Physics of Fluids*, Vol. 21, 117101-14.
- Mathiesen, V., Solberg, T., and Hjertager, B. H., (2000), "Prediction of gas / particle flow with an Eulerian model including a realistic particle size distribution." *Powder Technology*, 112, 34-45.
- Mazurek, K. A., Christison, K., and Rajaratnam, N., (2002). "Turbulent sand jet in water." *Journal of Hydraulic Research*, Vol. 40, no. 4, pp. 527-530.

- Modarress, D., Wuerer, J., and Elghobashi, S., (1984), "An experimental study of a turbulent round two-phase jet." *Chemical Engineering Communications*, Vol. 28, 4, pp. 341-354.
- Montante, G., Magelli, F., (2007). "Mixed solids distribution in stirred vessels: Experiments and computational fluid dynamics simulations." *Ind. Eng. Chem. Res.*, Vol. 46, 2885-2891.
- Morton, K. W., and Mayers, D. F., (2005), "Numerical solution of partial differential equations." Second edition, *Cambridge University Press*, U.K., 278 p.
- Muste, M., Fujita, I., Kruger, A., (1998). "Experimental comparison of two laser-based velocimeters for flows with alluvial sand." *Experiments in Fluids*, Vol. 24, 273-284.
- National Energy Board, (2006), "Canada's oil sands. Opportunities and challenges to 2015." An update National Energy Board, Calgary, AB.
- Natrajan, V. K., Wu, Y., and Christensen, K. T., (2007), "Spatial signatures of retrograde spanwise vortices in wall turbulence." *Journal of Fluid Mechanics*, Vol. 574, pp. 155-167.
- Nicolas, M., (2002), "Experimental study of gravity-driven dense suspension jets." *Physics of Fluids*, Vol. 14, 10, pp. 3570-3576.
- Noh, Y., Fernando, H.J.S., (1993), "The transition in the sedimentation pattern of a particle cloud." *Physics of Fluids A*, 5, 12, pp. 3049-3055.
- Noh, Y., (2000), "sedimentation of a particle cloud across a density interface." *Fluid Dynamics Research*, Vol. 27, pp. 129-142.
- Ochieng, A., Lewis, A. E., (2006). "Nickel solids concentration distribution in a stirred tank." *Minerals Engineering*, 19, pp. 180-189.
- Pantzlaff, L. & Lueptow, R. M., (1999), "Transient positively and negatively buoyant turbulent round jets." *Experiments in Fluids*, 27, pp. 117-125.
- Papanicolaou, P. and List, E.J. (1988). "Investigations of round vertical turbulent buoyant jets." *J. Fluid Mech.*, Vol. 195, 341-391.

- Parthasarathy, R. N., Faeth, G. M., (1987). "Structure of particle-laden turbulent water jets in still water." *Int. J. Multiphase Flow*, 13(5), 699-716.
- Pope, S. B., (2000), "Turbulent flows", *Cambridge University Press*, Cambridge, UK, 749 p.
- Pottebaum, T. S., and Gharib, M., (2004), "The pinch-off process in a starting buoyant plume." *Experiments in Fluids*, 37, pp. 87-94.
- Prevost, F., Boree, J., Nuglisch, H. J., and Charnay, G., (1996), "Measurements of fluid/particle correlated motion in the far field of an axisymmetric jet." *Int. J. Multiphase Flow*, 22(4), pp. 685-701.
- Rajaratnam, N., (1976). "Turbulent jets." Elsevier, Netherlands, 304 p.
- Rajaratnam, N., Mazurek, K. A., (2006), "An experimental study of sand deposition from sediment laden water jets." *Journal of Hydraulic Research*, Vol. 44, No. 4, pp. 560-566.
- Rajaratnam, N. and Pani, B. S. (1974). "Three-dimensional turbulent wall jets." *J. Hydraul. Div., Am. Soc. Civ. Eng.*, 100(1), 69-83.
- Rajaratnam, N., Yasmin, N., (1992), "Fronts of circular turbulent jets." *Proc. Instn Civ. Engrs Wat., Marit. & Energy*, Vol. 96, March, pp. 59-61.
- Reffet, E., Courrech du Pont, S., Hersen, P., and Douady, S., (2010), "Formation and stability of transverse and longitudinal sand dunes." *Geology*, Vol. 38, No. 6, pp. 491-494.
- Rottenkolber, G., Gindele, J., Raposo, J., Dullenkopf, K., Hentschel, W., Wittig, S., Spicher, U., Merzkirch, W., (2002), "Spray analysis of a gasoline direct injector by means of two-phase PIV." *Experiments in Fluids*, Vol. 32(6), pp. 710-721.
- Ruggaber, G. J., (2000), "Dynamics of particle clouds related to open-water sediment disposal." *Ph.D. Thesis*, Dept. of Civil and Environmental Engineering, MIT, Cambridge, MA, 242 p.
- Schieber, J. and Southard, J. B., (2009), "Bedload transport of mud by floccule ripples – Direct observation of ripple migration processes and their implications." *Geology*, Vol. 37, No. 6, pp. 483-486.

- Scott, J. D., Dusseault, M. B., and Carrier, W. D., III, (1985), "Behaviour of the clay/bitumen/water sludge system from oil sands extraction plants." *Journal of Appl. Clay Sci.*, Vol. 1, pp. 207-218.
- Sheen, H. J., Jou, B. H., Lee, Y. T., (1994), "Effect of particle size on a two-phase turbulent jet." *Experimental Thermal and Fluid Science*, Vol. 8, pp. 315-327.
- Shields, D. H., Domaschuk, L., Corkal, D. W., and MacCutchon, J. R., (1984), "Controlling sand placement during the building of artificial islands." *Can. Geo tech. J.*, Vol. 21 No. 2, pp. 371-375.
- Shuen, J. S., Solomon, A. S. P., Zhang, Q. F. And Faeth, G. M., (1985). "Structure of particle-laden jets: measurements and predictions." *AIAA J.*, Vol. 23, 396-404.
- Shusser, M., and Gharib, M., (2000), "Energy and velocity of a forming vortex ring." *Physics of Fluids*, Vol. 12, No. 3, pp. 618-621.
- Socolofski, S. A., (2001). "Laboratory experiments of multi-phase plumes in stratification and crossflow." *PhD thesis*, MIT, Massachusetts, 233p.
- Souza, L.B.S., Schulz, H.E., Villela, S.M., Gulliver, J.S. and Souza, L.B.S., (2010), "Experimental study and numerical simulation of sediment transport in shallow reservoir." *Journal of Applied Fluid Mechanics*, Vol. 3, No. 2, pp. 9-21.
- Syvitski, J. P. M., Skene, K. I., Nicholson, M. K., and Morehead, M. D., (1998), "Plume 1.1: Deposition of sediment from a fluvial plume." *Computer & Geosciences*, Vol. 24, pp. 159-171.
- Torobin, L., Gauvin, H., (1959), "Fundamental aspects of solid-gas flow.", *Canadian Journal of Chemical Engineering*, 37, (4-6), pp. 129-141.
- Tsuji, Y., Morikawa, Y., Tanaka, T., Karimine, K., Nishida, S., (1988), "Measurement of an axisymmetric jet laden with coarse particles." *Int. J. Multiphase Flow*, Vol. 14 (5), pp. 565-574.
- Turner, J. S., (1962), "The starting plume in neutral surroundings." *Journal of Fluid Mechanics*, Vol. 13, pp. 356-368.

- Turner, J. S., (1969), "Buoyant plumes and thermals." *Annul Rev Fluid Mechanics*, 1: pp. 29-44.
- Uchiyama, T., and Naruse, M., (2003), "Vortex simulation of slit nozzle gas-particle two-phase jet." *Powder Technology*, Vol. 131, pp. 156-165.
- Virdung, T., Rasmuson, A., (2007), "Hydrodynamic properties of a turbulent confined solid-liquid jet evaluated using PIV and CFD." *Chemical Engineering Science*, Vol. 62, pp. 5963-5979.
- Wang, B., Zhang, H., Liu, Y., Yan, X., and Wang, X., (2009a), "Particle modulations to turbulence in two-phase round jets." *Acta Mechanica Sinica*. Vol. 25, pp. 611-617.
- Wang, F., Mao, Z., Wang, Y., Yang, C., (2006). "Measurement of phase holdups in liquid-liquid-solid three-phase stirred tanks and CFD simulation." *Chemical Engineering Science*, Vol. 61, 7535-7550.
- Wang, H., and Law, A. W., (2002), "Second-order integral model for a round turbulent buoyant jet." *Journal of Fluid Mech.*, Vol. 459, pp. 397-428.
- Wang, R., Law, A. W., Adams, E. E., Fringer, O. B., (2009b) "Buoyant formation number of a starting buoyant jet.", *Physics of Fluids*, Vol. 21, 125104-9.
- Wörner, M. (2003), "A compact introduction to the numerical modeling of multiphase flows.", *Forschungszentrum Karlsruhe GmbH*, Karlsruhe, Germany. 38 p.
- Wu, Y., and Christensen, K. T., (2006), "Population trends of spanwise vortices in wall turbulence." *Journal of Fluid Mechanics*, Vol. 568, pp. 55-76.
- Wynanski, I., Fiedler, H., (1969). "Some measurements in the self-preserving jet." *Journal of Fluid Mech.*, Vol. 38, part 3, pp. 577-612.
- Zhang, D. Z., and Prosperetti, A., (1994). "Averaged equations for inviscid disperse two-phase flow." *J. Fluid Mech.*, Vol. 267, 185-219.
- Zhou, J., Adrian, R. J., Balachandar, S., and Kendall, T. M., (1999), "Mechanisms for generating coherent packets of hairpin vortices." *Journal of Fluid Mechanics*, Vol. 387, pp. 353-396.